NMR STUDIES OF CATHODE MATERIALS FOR LITHIUM ION BATTERIES

MULTINUCLEAR NMR STUDIES OF ION MOBILITY PATHWAYS IN CATHODE MATERIALS FOR LITHIUM ION BATTERIES

BY

LINDA J. M. DAVIS, B. SC.

A Thesis Submitted to the School of Graduate Studies in Partial Fulfillment of the

Requirements for the Degree Doctor of Philosophy

McMaster University

McMaster University DOCTOR OF PHILOSOPHY (2011) Hamilton, Ontario (Chemistry)

TITLE: Multinuclear NMR Studies of Ion Mobility Pathways in Cathode Materials for Lithium Ion Batteries

AUTHOR: Linda J. M. Davis, B. Sc. (McGill University)

SUPERVISOR: Professor G. R. Goward

NUMBER OF PAGES: xxi, 236

ABSTRACT

This thesis investigates the structure and ion mobility properties within the phosphate and fluorophosphate family of cathode materials for Li ion batteries using solid-state NMR. Developments in lithium ion battery technology are now directed towards automotive applications meaning that many of the cost and safety issues associated with current lithium ion battery technology need to be addressed. Within the current systems the high cost is largely attributed to the use of $LiCoO_2$ as the positive electrode. Many new and inexpensive Li intercalation materials have been put forward as alternatives to $LiCoO_2$, however the details concerning the structural and ion-transport properties of these new phases are not well defined. $^{6,7}Li$, ^{31}P, and ^{19}F NMR measurements are an ideal tool to study these properties, as $^{6,7}Li$ is able to probe the local environment and dynamics of the mobile ion while ^{31}P and ^{19}F monitor changes in the host framework. Materials selected for study in this thesis include olivine $LiFePO_4$, monoclinic $Li_3M_2(PO_4)_3$ (M = V, Fe), the tavorite-based Li_2VPO_4F and Li_2VOPO_4, and the novel layered $Li_5V(PO_4)_2F_2$. The fluorophosphates have been introduced as higher voltage cathode materials for lithium batteries, however our $^{6,7}Li$ 1D selective inversion and 2D EXSY measurements reveal timescales of ion hopping that are relatively slow when compared to those measured in the phosphates. This indicates that the improved power output from the voltage gains may be lost to slow charge/discharge rates.

Acknowledgements

I would like to thank my thesis advisor, Prof. Gillian Goward, for her guidance, patience, support, encouragement and friendship throughout my graduate degree. Moreover, I am very grateful to Prof. Goward for providing opportunities for me to travel across North America and Europe to attend scientific meetings and participate in research collaborations. I also wish to thank my committee members, Prof. Alex Bain and Prof. Yurij Mozharivskyj, for their helpful insight and recommendations. I am also very grateful to the NMR spectroscopy facility staff, in particular Dr. Bob Berno for his support and help with NMR equipment and experiments. Thank you as well to Dr. Ivo Heinmaa of the NICPB for his hospitality and mentorship during my time in Tallinn, Estonia. I also thank Dr. Darren Brouwer (Redeemer), Prof. Linda Nazar (University of Waterloo), Brian Ellis (University of Waterloo) and Jim Garrett (BIMR) for assistance with experimental work. I also wish to thank current and former Goward group members. Their enthusiasm, expertise and friendship made the lab an enjoyable place to work. I also am grateful for financial support through the Ontario Graduate Scholarship program.

This manuscript is dedicated to my parents, Reid and Thea.

Table of Contents

List of Tables

List of Figures

List of Abbreviations and Symbols

SSNMR	Solid State Nuclear Magnetic Resonance
MAS	Magic Angle Spinning
VT	Variable Temperature
REDOR	Rotational-Echo, Double-Resonance
EXSY	Exchange Spectroscopy
SI	Selective Inversion
NSI	Nonselective Inversion
SEDOR	Spin-echo, double-resonance
GHG	Greenhouse Gas
EV	Electric Vehicle
HEV	Hybrid Electric Vehicle
Ni-MH	Nickel Metal Hydride
μ_A	Redox potential of the anode
μ_C	Redox potential of the cathode

E_g	Band gap
V_{OC}	Open circuit voltage
V	Volt
Z	Atomic number
I	Spin quantum number
μ_N	Nuclear magnetic moment
μ_e	Electron magnetic moment
γ_N	Nuclear gyromagnetic ratio
γ_e	Electron gyromagnetic ratio
$\hbar$	Reduced Planck constant
B_0	Applied magnetic field strength
ω_0	Larmor frequency
τ_r	Rotor period
$\hat{H}$	Hamiltonian
$\left\langle S_z \right\rangle$	Unpaired electron spin density

D_{ij}	Dipolar coupling constant
CSA	Chemical Shift Anisotropy
C_q	Quadrupole coupling
σ	Chemical shielding
δ	Chemical shift
ppm	Part per million
FWHM	Full-Width at Half-Maximum
A_H	Hyperfine coupling constant
T_1	Spin-lattice relaxation rate
T_2	Spin-spin relaxation rate
BVS	Bond Valence Sum
k	Ion hopping rate
E_a	Activation energy
K	Equilibrium constant

Chapter 1: Introduction to Cathode Materials for Li Ion Batteries

1.1 Thesis Layout

This thesis details the use of Solid-State Nuclear Magnetic Resonance (SSNMR) techniques to investigate the structural features and lithium ion mobility pathways in a series of phosphate and fluorophosphate lithium intercalation materials used as positive electrodes in lithium ion batteries. Chapter 1 provides the project motivation with a description of current lithium ion battery technology and a summary of the structural and electrochemical properties of cathode materials selected for investigation in subsequent chapters. Chapter 2 outlines the properties of nuclear and electron spin with a description of the unique spectral features expected from SSNMR measurements. Also included is a description of Magic Angle Spinning (MAS) techniques and how it is used to minimize unwanted spectral features. Chapter 3 is a summary of specific SSNMR experiments used to unravel the structural and ion mobility properties of the materials summarized in Chapter 1. Chapter 4 details the use of variable temperature (VT) and $^{6}Li\{^{31}P\}$ rotational-echo, double resonance (REDOR) measurements to evaluate ion and electron mobility in Li_xFePO_4 ($0 \leq x \leq 1$). Chapter 5 demonstrates the use of ^{6}Li two-dimensional MAS exchange spectroscopy (2D MAS EXSY) to study Li ion hopping pathways in monoclinic $Li_3Fe_2(PO_4)_3$ and also characterizes the electrochemical extraction of a single lithium in $Li_3V(PO_4)_3$ using ^{6}Li MAS NMR. Chapter 6 introduces the use of ^{6}Li 1D selective-inversion (SI) measurements as a more efficient means of studying ion dynamics in the two-site system, Li_2VPO_4F. Also included is a detailed structural characterization of Li_xVPO_4F with x =1.0, 1.5, and 2.0, using $^{6}Li\{^{19}F\}$REDOR measurements as well as analysis of the sideband manifolds observed in ^{7}Li MAS spectra of the mixed phase $0.5LiVPO_4F:0.5Li_2VPO_4F$. Chapter 7 expands ^{6}Li 1D SI experiments to a three-site material, Li_2VOPO_4, where the reproducibility of the inversion method is tested. Chapter 8 is a further expansion of ^{6}Li 1D SI methods, where the many possible ion exchange pathways in $Li_5V(PO_4)_2F_2$ are discussed in terms of their structural bottlenecks, ion internuclear distances, as well as bond sum valence values. The final chapter provides a summary and proposes future work for research in this field.

1.2 Motivation for Using Li ion Batteries

Investigation into alternative energy storage and conversion systems is an important step towards not only reducing greenhouse gas (GHG) emissions but also minimizing the dependence of global economies on fossil fuels sourced from unstable regions. One area that has large potential for use of alternative energy conversion and storage systems is the transportation sector. Within Canada, the ground transportation sector (excluding freight transport) constitutes 9.6 % of total energy consumption.[1] Of that energy, 87 % is sourced from refined fossil fuels with gasoline (54.5 %) and diesel (32.5 %) being the most heavily consumed.[1] Moreover, use of these energy sources is accompanied by substantial GHG emissions where 11.8% of total emissions in Canada are from gasoline and diesel fueled passenger vehicles.[2] Advancing automotive technology towards zero-emissions through modification and/or replacement of the combustion engine, can have a significant impact on minimizing the economic and environmental hazards of fossil fuel consumption and combustion.

Electric and hybrid electric vehicles (EV and HEV, respectively) have an electric motor that either fully replaces or is paired with, a traditional combustion engine. To maximize the efficiency of EV and HEV motors, use of lightweight lithium ion battery systems is desired. **Figure 1.1** (from Tarascon et al.)[3] illustrates the higher volumetric and gravimetric energy density of Li ion batteries as compared to more traditional car batteries including lead-acid and nickel metal hydride (Ni-MH) systems

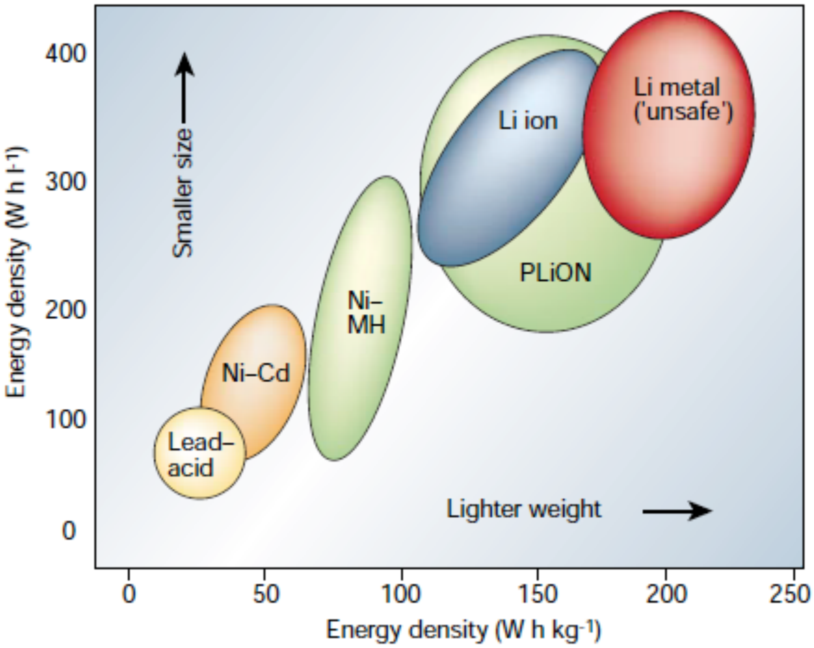

Figure 1.1 – Plot of the volumetric and gravimetric energy densities of different battery systems.[3]

The high energy density of these battery systems has resulted in their widespread application towards small electronic devices (laptops, mobile phones, etc.). To apply this technology towards larger scale applications such as HEV and EV's, many of the cost and safety issues of the current systems need to be addressed.

The remainder of this chapter outlines the current state of Li ion battery technology and highlights the chemical components that are targeted for improvement.

1.3 Description of a Li Ion Battery

A schematic of a Li ion battery is shown in **Figure 1.2**. Rechargeable lithium ion batteries involve a reversible insertion/extraction of lithium ions (the guest species) from a host matrix. This Li guest/host species is referred to as an intercalation compound and possesses a redox active metal center where the movement of the Li ions is accompanied by a flow of electrons through the external circuit. In the systems discussed throughout this thesis, the positive electrode material is the redox active Li intercalation compound while the negative electrode is comprised of a conductive layered material such as graphite.

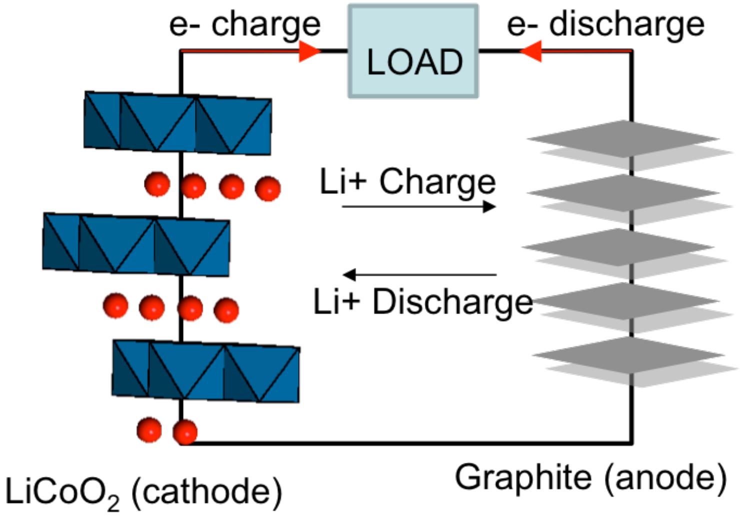

Figure 1.2 - Schematic of a Li ion battery having $LiCoO_2$ as the positive electrode and graphite (grey sheets) as the negative electrode. The $LiCoO_2$ structure has layers of CoO_6 octahedra (blue) interleaved with layers of Li ions (red spheres)

The performance of an electrode material is described by its gravimetric and/or volumetric energy capacity. Both values are a measure of the number of electrons transferred through a circuit either per gram of electrode material (mAh g^{-1}) or per unit volume (mAh cm^{-3}), respectively.[4] The gravimetric capacity is more often reported, as it is easier to measure in electrochemical experiments. The *theoretical gravimetric capacity* is calculated based on the number of charge transporters (in this case, the Li ions) that are intercalated into a unit mass of a given material. This makes the Li:anode and Li:cathode stoichiometry at the fully intercalated potential important. The *specific gravimetric capacity* is the measured number of charge transporters found at the fully charged or discharged potential. Under experimental conditions, irreversible capacity loss is often found and attributed to the reaction of the intercalated Li ions with the electrodes and/or the electrolyte.

The Li ions are shuttled from the anode to the cathode via the electronically insulating electrolyte, which is typically comprised of a Li salt dissolved in an organic solvent. The choice of electrolyte can impose limitations on the choice of electrode material, as the redox potentials of the anode (μ_A) and/or cathode (μ_C) must lie within the band gap (E_g) of the electrolyte (**Figure 1.3**, adapted from Goodenough et al.[5]). The most commonly used electrolyte, $LiPF_6$ has a decomposition voltage of 4.9 V at room temperature, limiting many electrode redox potentials to below this level.[6]

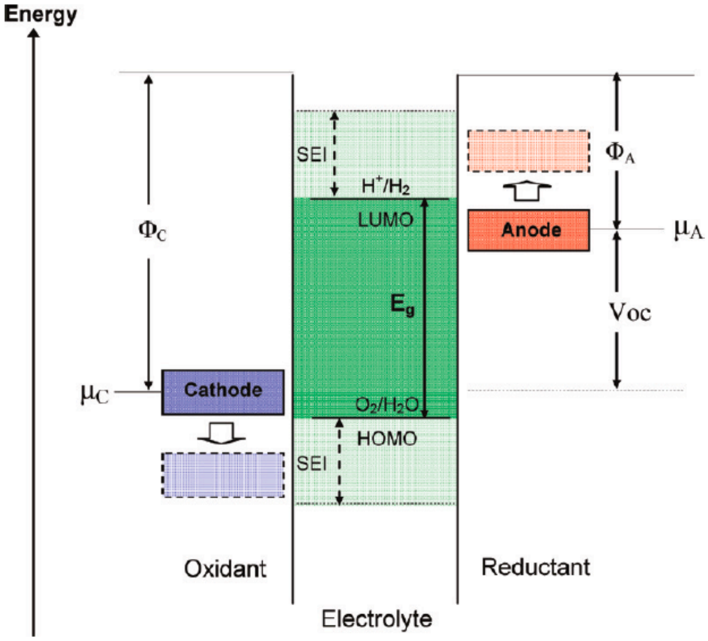

Figure 1.3 – Open-circuit diagram of an aqueous electrolyte from Goodenough et al.[5] Φ_A and Φ_C are the work function for the anode and cathode, respectively. V_{OC} is the open circuit voltage as defined by the redox potentials of the anode (μ_A) and cathode (μ_C)

The cycling rate capabilities are also an important parameter for describing the performance of an electrochemical cell. This is a measure of the time needed for the cell to charge or discharge. For example, a charge rate of C/100, indicates that a total of 100 hours is needed for a complete charge cycle. Fast charge/discharge rates are not only needed for high-power output, but also for fast recharging such that the battery can be used again in a reasonable amount of time.

The battery shown in **Figure 1.2** represents the most commonly used Li ion battery, with $LiCoO_2$ as the positive electrode and graphite as the negative electrode. Many of the cost, safety, and performance issues associated with this design need to be addressed in order to apply Li ion battery technology towards larger scale applications such as HEVs and EVs.[5,7] While most chemical components have been targeted for improvement, the high cost of the $LiCoO_2$ has singled it out as the economic crutch of the battery system. In addition to this, much structural instability is present in this material leading to poor electrochemical performance. Details of this are outlined in Section 1.4.

1.4 Layered $LiCoO_2$ and Spinel $LiMn_2O_4$

It was first observed in 1976 that Li could be reversibly intercalated between layers of TiS_2 in a paper by Whittingham *et al.*[8] Here, Li was reversibly intercalated in a solid solution phase with TiS_2 and $LiTiS_2$ end members. This occurred in a potential range of 2.5 V to 1.5 V against Li metal. It was later reported that higher cell potentials were obtained using metal oxides leading to commercialization of two major materials; layered $LiCoO_2$ and cubic spinel $LiMn_2O_4$.[9,10]

The $LiMO_2$ (M = Co, Ni, Mn) family of compounds crystallize in a layered $R\bar{3}m$ structure.[9] The Li^+ and M^{3+} ions sit in alternating (111) sheets within the rocksalt structure. This allows for two-dimensional movement of the lithium ions in and out of the structure (**Figure 1.2**). Despite its predominance in portable electronic devices, this material exhibits many shortcomings and its application to larger scale applications has been stalled. Aside from high cost, a significant limitation of $LiCoO_2$ is that only half of the 280 mAh g^{-1} theoretical capacity is reached, as the material becomes unstable and the structure degrades when Li is deintercalated below this level.[11-13] This drawback coupled with slow charge-discharge rates, high cost, and environmental toxicity prevent $LiCoO_2$ from being used in larger scale applications such as batteries needed for hybrid electric vehicles (HEV).[14]

This led to an interest in the low-cost cubic spinel phase of $LiMn_2O_4$ (space group *Fd3m*).[10,15] The edge shared MnO_6 octahedra create tetrahedral holes in which Li ions reside in the 8a crystallographic site (**Figure 1.4**). This is a mixed valent compound where the Mn ions in the +3 and +4 oxidation are equally populated with an average oxidation state of +3.5 observed due to the delocalization of the e_g electrons in the semi-conducting framework. Lithium extraction in $Li_xMn_2O_4$ occurs at 4 V opposite Li metal where the cubic structure is retained over the $0 < x < 1$ range.[15-18] For insertion of a second Li ion at a voltage of 2.96 V for $1 < x < 2$, the cubic structure irreversibly adopts a tetragonal $Li_2Mn_2O_4$ phase ($F4_1/ddm$) due to Jahn-Teller distortion around the Mn^{3+} centers.[10,19] The 4 V cycling range is also not immune to this phase transformation as fast cycling rates can lead to over lithiation at the surface of the $LiMn_2O_4$ cubic phase leading to formation of the tetragonal phase.[20]

Overall, the poor electrochemical performance of the two most popular metal oxide phases has prompted investigation into entirely new Li intercalation phases, where structural fatigue leading to capacity fading is not as severe. This thesis will investigate the structure and electrochemical properties of newer, inexpensive cathode materials, using multinuclear solid-state nuclear magnetic resonance experiments.

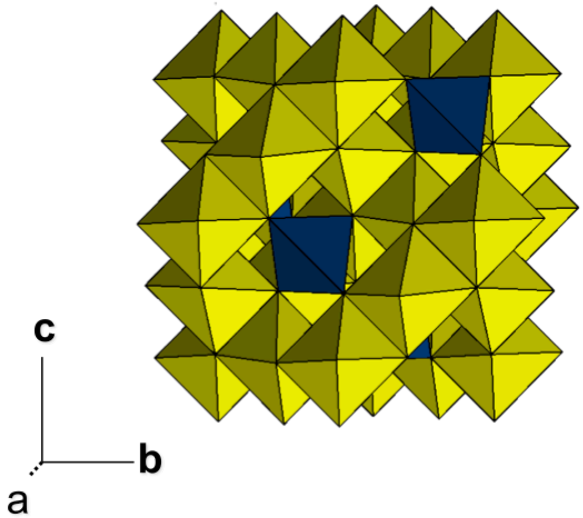

Figure 1.4 – Structure of cubic spinel $LiMn_2O_4$. Yellow octahedra are the MnO_6 sites with the tetrahedral Li environments shows a navy blue sites.

1.5 Materials Studied in this Thesis

For the positive electrode material, many new intercalation compounds have been introduced based on phosphates, and more recently fluorophosphates.[21,22] These newer cathodes show impressive cycling capabilities and are typically environmentally benign and economically accessible. The systems are built up of tetrahedral PO_4^{3-} and octahedral

MO_6 of MO_4F_2 groups where M = Ti, V, Mn, Fe, Co. The PO_4^{3-} groups create an inductive effect where the strongly covalent P-O bond results in greater ionic character of the Li-O bonds, opening up large interstitial space in which the Li ions can reversibly be (de)intercalated. The inductive effect also results in higher redox potentials of many important redox couples as compared to the potentials found in oxide lattices. This includes Fe^{2+}/Fe^{3+} and V^{2+}/V^{3+}, redox couples, which are two very low-cost transition metal centers. The phosphate groups also offer significant structural support such that a fully deintercalated phase is isostructural with its fully lithiated phase, which is key to retaining the full capacity and long lifetime of the material.

With these new materials however, in order to better understand cycling failure and/or successes, the behaviour of the mobile ion must be understood. While powder X-ray diffraction, as well as a variety of other spectroscopic techniques can provide useful information about structural changes to the lattice during chemical/electrochemical cycling, very few techniques can directly monitor the mobile ion. Solid-state nuclear magnetic resonance (NMR) is one of these few techniques, where ^{6,7}Li NMR is able to monitor the mobile guest species while ^{31}P and ^{19}F can monitor changes to the host-framework. Further to this, ^{6,7}Li NMR is sensitive to local site dynamics that take place on the NMR timescale. This includes site-specific rattling and site-to-site Li ion hopping.[23-26] Determination of these timescales is then correlated to structural constraints within the host framework, offering insight into what factors govern fast ion mobility within a given lattice.

The remainder of this chapter provides a summary of the bulk structure and electrochemical performance of the phosphate and fluorophosphate cathode materials that will be investigated in this thesis. This includes olivine Li_xFePO_4 ($0 \leq x \leq 1$), monoclinic $Li_3V_2(PO_4)_3$ and $Li_3Fe_2(PO_4)_3$, tavorite based Li_xVPO_4F and Li_xVOPO_4 ($1 \leq x \leq 2$), and layered $Li_5V(PO_4)_2F_2$. Many of these materials show impressive theoretical and specific capacities with improved reversibility over $LiCoO_2$ and $LiMn_2O_4$ (**Table 1.1**). Chapter 3 outlines the solid-state NMR techniques used to study the ionic and structural properties of these electrochemically promising materials.

Table 1.1– Summary of electrochemical performance of cathode materials investigated in this thesis.

Cathode Material	Highest Redox Potential (V)	Available Range (Δx)	Reversible Range (Δx)	Theoretical capacity (mAh g^{-1})	Specific capacity (mAh g^{-1})
$LiCoO_2$[9]	4.0	1.0	0.5	280	140
$LiMn_2O_4$[15-18]	3.8	2.0	1.0	148	120
$LiFePO_4$[21,27]	3.5	1.0	0.95	170	162
$LiMnPO_4$[28]	4.1	1.0	0.88	171	150
$Li_3Fe_2(PO_4)_3$[29,30]	2.8	2.0	2.0	128	116
$Li_3V_2(PO_4)_3$[31,32]	3.5	3.0	2.8	197	185
Li_2VPO_4F[22,33]	4.1	2.0	1.8	300	270
Li_2VOPO_4[34,35]	3.8	2.0	1.5	305	229
$Li_5V(PO_4)_2F_2$[36]	4.2	2.0	1.0	170	165

1.5.1 $LiFePO_4$

Olivine $LiFePO_4$ has been the most extensively studied cathode material proposed as an alternative to $LiCoO_2$. Structural and electrochemical details of this material were first published in 1997 by Padhi and associates.[21] It was shown that the environmentally benign, inexpensive, cathode material, had a reversible capacity of 162 mAh g^{-1} (theoretical 170 mAh g^{-1}) with a Fe^{2+}/Fe^{3+} redox potential of 3.5 V. The high degree of reversibility was attributed to structure retention of the fully delithiated heterosite phase, $FePO_4$ which experiences a reversible 7% decrease in cell volume upon Li removal. $LiFePO_4$ crystallizes in the *Pnma* space group where lithium ions occupy the M(1) octahedral sites forming a linear chain of ions that run parallel to the *b*-axis.[37] The Fe atoms sit on the M(2) sites with the octahedra forming a "zig-zag" plane of corner-shared environments supported by PO_4 tetrahedra. The Li ions are not able to diffuse through the FeO_6-PO_4 planes and are thus confined to one-dimensional mobility through a "tunnel" created by the Li ion octahedra (**Figure 1.5**).[38-40] Moreover, the two-phase (de)lithiation observed in the electrochemical cycling forms a phase interface that impedes Li ion diffusion and consequently restricts this material to slow cycling rates.[21,39,41-46] This resulted in $LiFePO_4$ being proposed as a material for low-power battery applications.

Despite this, the high electrochemical and thermal stability of $LiFePO_4$ as compared to $LiCoO_2$ and $LiMn_2O_4$ lead to extensive efforts to advance the performance of this material for high-power batteries needed for the automotive industry. Well over 1500 publications have emerged, detailing chemical and/or physical manipulation of the material in order to achieve faster cycling rates. Some more noteworthy results include coating of the particles in a conductive layer such as graphite and reducing the particle size to nanometric dimensions. [27,47-49] Both of these strategies lead to better contact between particles and resulted in high capacity retention at faster cycling rates (70% capacity retention at 5C). Another attractive feature of $LiFePO_4$ is the high temperature solid-state synthesis has been replaced by more environmentally benign hydrothermal methods.[50] Initial reports showed M(1) and M(2) site mixing where Fe atoms were found within the Li ion tunnels leading to diminished electrochemical performance. It was later shown that site mixing was limited when heating temperatures were set higher than 175 °C with 190-195 °C being the more commonly reported synthesis temperatures.[51-53] Moreover, it has been shown that nano-morphologies were easily obtained and controlled using this hydrothermal method.[53] Chapter 4 of this thesis will focus on better understanding the two-phase reaction as well as characterization of Li ions at the phase interface in hydrothermally prepared Li_xFePO_4 ($x \leq 1$) using solid-state $^{6,7}Li$ and ^{31}P NMR experiments. The samples studied were prepared both in the Goward research group and by collaborators at the University of Waterloo.

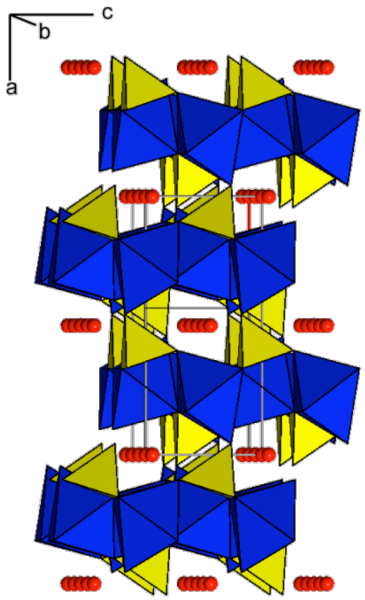

Figure 1.5 - Structure of olivine $LiFePO_4$ with space group *Pnma.* FeO_6 are shown as blue octahedral with yellow tetrahedra representing the corner-shared PO_4^{3-} units. Li ions are shown as red spheres occupying tunnels along the *b*-axis are shown as red-spheres.

1.5.2 Monoclinic $Li_3M_2(PO_4)_3$ (M = V, Fe)

To overcome the limits of 1D conduction in $LiFePO_4$, many phases of phosphate and fluorophosphate Li intercalation compounds with frameworks having a higher degree of dimensionality and larger theoretical capacities have been introduced. Included in this analysis are the $Li_3M_2(PO_4)_3$ (M = V, Fe) phases[29,54] Both $Li_3V_2(PO_4)_3$ and $Li_3Fe_2(PO_4)_2$ crystallize in either a monoclinic α-$Li_3M_2(PO_4)_3$ or a rhombohedral NASICON β-$Li_3M_2(PO_4)_3$ framework. For the V-analogue, α-$Li_3V_2(PO_4)_3$ is the more thermodynamically stable and therefore preferred phase.[55] For $Li_3Fe_2(PO_4)$ both the α and β phases show promising electrochemical performance. In this thesis, only the α-phase of both materials is discussed in order to easily compare the ion mobility results obtained from SSNMR experiments.

The α-$Li_3V_2(PO_4)_3$ phase has a three-dimensional framework created by the VO_6-octahedra sharing all six of its oxygen vertices with the PO_4^{3-} tetrahedral units. Similarly, each PO_4 unit has a corner shared VO_6 found at each of its oxygen vertices. Three crystallographically unique Li sites occupy the spaces between the MO_6 and PO_4 units. Li1 occupies the tetrahedral position and Li2 and Li3 both occupy distorted trigonal bipyramidal sites. The lithium polyhedra corner share with one another forming chains of Li ions along the *a*-axis (**Figure 1.6**).

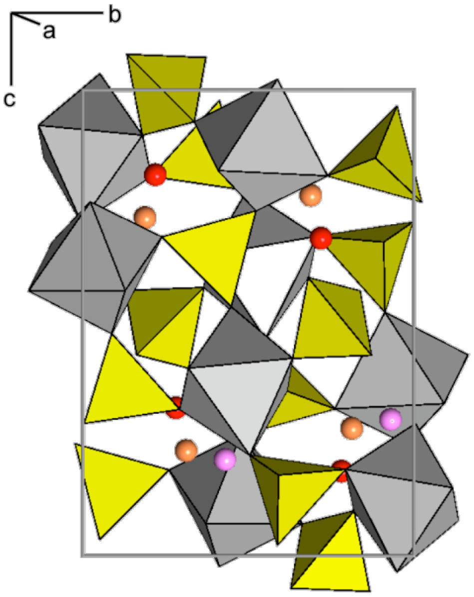

Figure 1.6 – Structure of $Li_3M_2(PO_4)_3$ where M = V or Fe. The MO_6 octahedra shown as grey square with PO_4^{3-} shown as yellow tetrahedra. The Li ions occupying the interstitial spaces as shown as pink, orange, and red spheres.

For $Li_3V_2(PO_4)_3$, all three lithium environments can be reversibly extracted approaching the theoretical capacity of 197 mAh/g.[31,32,56,57] The extraction of the first lithium takes place over two voltage plateaus of 3.61 V and 3.69 V. The second and third Li ions are extracted at voltages of 4.07 V and 4.6 V, respectively, with the latter voltage corresponding to the V^{4+}/V^{5+} redox couple. Reinsertion occurs with solid solution formation accompanied by a small amount of hysteresis.[32] Previous NMR studies have reported the timescales of both Li ion hopping as well as local Li-site rattling using advanced NMR methods.[23,24] Local lithium environments were also characterized upon extraction of materials electrochemically cycled to points between voltage plateaus. In this thesis, Chapter 6 evaluates the local lithium environment of materials prepared in the Goward group that are cycled and extracted at the first voltage plateau of the discharge curve.

For α-$Li_3Fe_2(PO_4)_3$, the Fe^{3+}/Fe^{4+} redox potential falls outside of the voltage window created by most lithium battery electrolytes (upper limit is ~ 5 V). Therefore reversible insertion of 1.8 Li has been reported for $Li_{3+x}Fe_2(PO_4)_3$ with two separate voltage plateaus of 2.85 V (for $0 \leq x \leq 1$) and 2.70 V (for $1 \leq x \leq 1.8$). The observed discharge capacity of 115-116 mAh/g for this insertion process comes close to the theoretical value of 128 mAh g^{-1}.[29,30] Again kinetic limitations are reported, similar to that observed in $LiFePO_4$. However the primary source of slow kinetics in this case is the slow electron and/or lithium transport found within each phase rather than due to slow phase-front migration.[58]

In this thesis, the timescales of ion mobility in $Li_3Fe_2(PO_4)_3$ were determined using solid-state ^{6,7}Li MAS NMR techniques and correlations of ion hopping rates made to structural constraints within the lattice. The materials studied were prepared using a high temperature solid-state reaction in the Goward research group. Results are compared to timescales of ion mobility in $Li_3V_2(PO_4)_3$ determined from MAS NMR studies.[24]

1.5.3 Li_xVPO_4F ($1 \leq x \leq 2$)

Lithium ion fluorophosphates represent a new generation of cathode materials for Li ion batteries. The addition of the electronegative fluorine atoms to the metal octahedra enhances the inductive effect resulting in higher redox potentials of the transition metal centers. $Li_2Ni(PO_4)F$ was the first fluorophosphate material reported for electrochemical applications. Its synthesis was first reported in 1999 where an ordered mixed anionic framework of chains of NiO_4F_2 octahedra are joined by PO_4^{3-} tetrahedra.[59] No electrochemical studies of this material were reported, nor for the isostructural Li_2CoPO_4F as the redox potentials were too high (> 5 V) for most liquid electrolytes.[60] More accessible redox potentials are found in tavorite-based $LiMPO_4F$ fluorophosphate compounds where M is either Fe or V. $LiVPO_4F$ which has a V^{4+}/V^{5+} redox potential of 4.1 V and theoretical capacity of 155 mAh/g, for the extraction of one Li, is a material proposed for high-power electrochemical applications.[22] This compound is isostructural with the naturally occurring minerals, tavorite $LiFePO_4OH$ and amblygonite $LiAlPO_4F$, which all crystallize in a triclinic space group.[22,61-63] These materials also have a 3D framework, created by corner sharing units of PO_4 tetrahedra and VO_4F_2 octahedra (**Figure 1.7**a).[64] Li-disorder is present over two crystallographic positions as shown from electrochemical results[64] and also through NMR measurements of the isostructural, $LiAlPO_4F$.[63] It was later shown that $LiVPO_4F$ could also intercalate Li at a potential of about 1.8 V yielding a higher capacity, Li_2VPO_4F cathode material for battery applications.[33] This reduced phase crystallizes in a monoclinic phase (space group *C2/c*) as recently reported by our collaborators at the University of Waterloo.[65] Although a different space group is found for the reduced phase, the structures of $LiVPO_4F$ and Li_2VPO_4F are closely related, where the PO_4 and VO_4F_2 continue their corner-sharing network, retaining the 3D framework. The Li ions now occupy two distinct crystallographic positions where Li1 takes on a position very similar to the disordered Li position of the parent $LiVPO_4F$ while Li2 is a completely new environment resulting from the electrochemical/chemical insertion (**Figure 1.7**b).

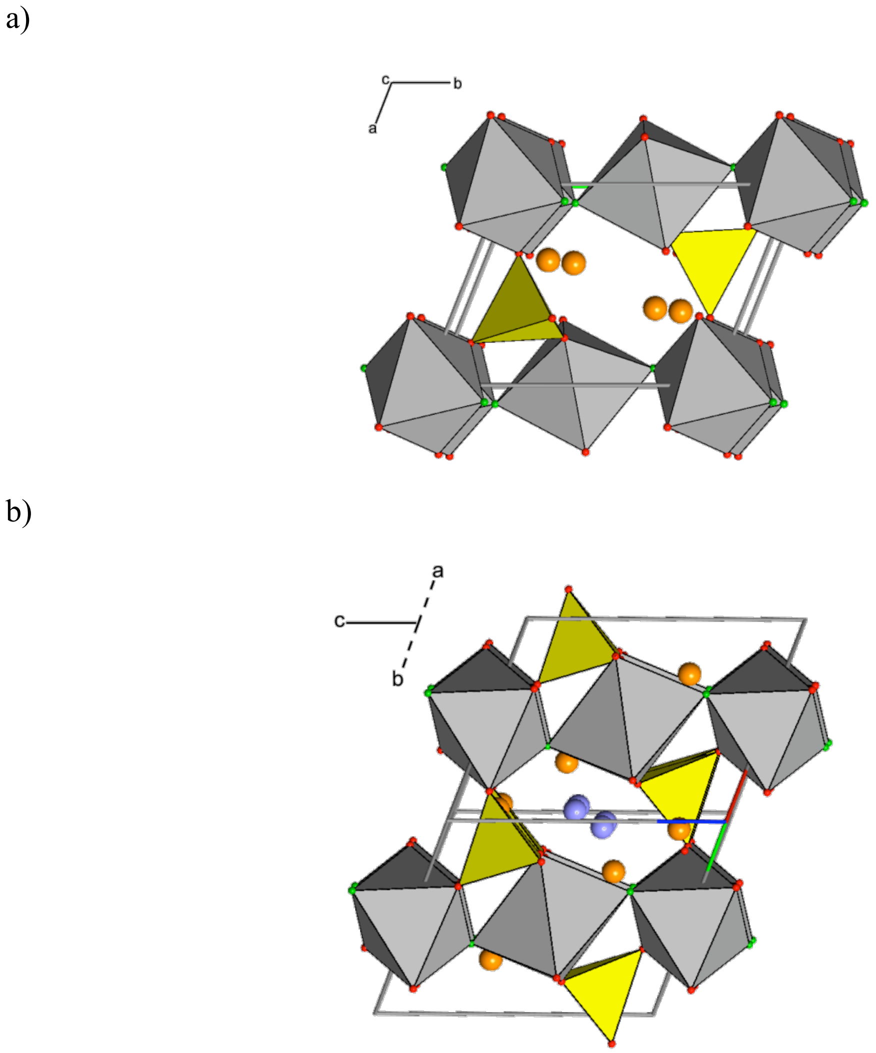

Figure 1.7 - Structures of a) $LiVPO_4F$ and b) Li_2VPO_4F. VO_4F_2 octahedra are shown in grey with red oxygen atoms and green fluorine atoms sitting at the vertices. Tetrahedral PO_4^{3-} groups shown as yellow with Li-atoms shown as orange and lilac spheres.

Chapter 6 of this thesis details the structural characterization of Li_xVPO_4F (x = 1, 1.5, or 2) using multinuclear MAS NMR techniques in samples prepared by collaborators at the University of Waterloo. Also presented is a study of the timescales of ion mobility and energy barriers in the reduced phase, Li_2VPO_4F using one and two-dimensional ^{6}Li exchange spectroscopy.

1.5.4 Li_xVOPO_4 ($1 \leq x \leq 2$)

Oxyphosphates are another class of compounds being considered for high-power battery applications. The synthesis of ε-$VOPO_4$ was first reported by Lim *et al.* in 1996 from the heating of hydrothermally prepared $VPO_4 \cdot H_2O$ in O_2.[66] The resulting ε−$VOPO_4$ has a monoclinic unit cell (space group $P2_1/n$) able to intercalate one Li in a two-phase process at 3.8 V with a specific capacity of 128 mAh/g (theoretical capacity is 159 mAh/g).[34] This new phase has the same structure as triclinic α-$LiVOPO_4$ (space group $P\bar{1}$) as reported from the high-temperature synthesis by Lavrov *et al.*[67] Chains of corner sharing VO_6 octahedra are connected in three-dimensions by $(PO_4)^{3-}$ tetrahedra (**Figure 1.8**). Two crystallographically distinct Li ions sit in the interstitial spaces opposite the phosphate groups.[34] Intercalation of the second Li was shown to occur at a V^{3+}/V^{4+} redox potential of ~ 2.5 V.[35]

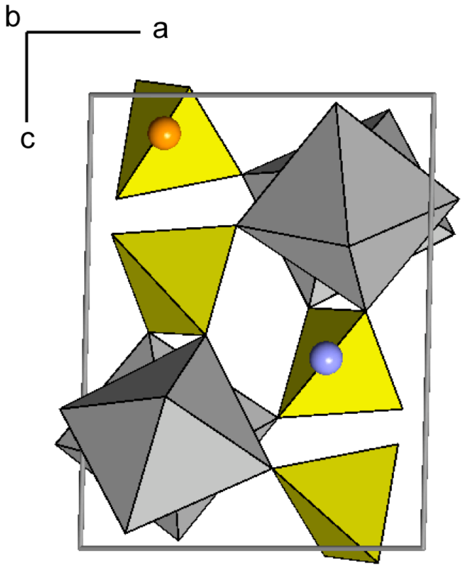

Figure 1.8 – Structure of $LiVOPO_4$. Grey polyhedra represent the VO_6 octahedral environments and yellow tetrahedra indicate PO_3^{3-} units. Lithium environments are shown as orange and lilac spheres.

Chapter 7 of this thesis offers the first solid-state $^{6,7}Li$ NMR study of Li_xVOPO_4 ($x = 1, 1.5$, or 2) samples prepared by collaborators at the University of Waterloo. The timescales of ion mobility in Li_2VOPO_4 were determined using one and two-dimensional $^{6,7}Li$ NMR techniques and reveal faster ion dynamics than its Li_2VPO_4F cousin.

1.5.5 $Li_5V(PO_4)_2F_2$

A newer fluorophosphate material, layered $Li_5V(PO_4)_2F_2$, is generated from the dimensional reduction of α-$Li_3V_2(PO_4)_3$ with LiF.[36] The term "dimensional reduction" is in reference to the structure being lowered from the 3D framework to a 2D layered framework.[68] $Li_5V(PO_4)_2F_2$ crystallizes in monoclinic $P2_1/c$ symmetry with two dimensional sheets of VO_4F_2-PO_4 interleaved with layers of Li ions. Six crystallographically distinct Li environments are found in this compound, many of which have distorted octahedral coordination. The exception is Li3 and Li5 which are only five coordinate. Li1, Li2, and Li5 comprise the layer of Li ions found between the metal-fluorophosphate sheets, while Li3, Li4, and Li6 occupy interstitial spaces within the metal sheets (**Figure 1.9**). The high theoretical capacity of 170 mAh/g for this layered phase is accompanied by the possibility of spanning the entire $V^{3+}/V^{4+}/V^{5+}$ redox couple by removal of two Li. A specific capacity of 85 mAh/g was observed for the extraction of one Li with an average voltage plateau of 4.15 V. A second voltage plateau of 4.65 V was reported in microcrystalline phases of $Li_5V(PO_4)_2F_2$/carbon composites raising the specific capacity to 165 mAh/g.[69] This second electrochemical process is not reversible due in large part to the structural instability of the $Li_3V(PO_4)_2F_2$ framework where V^{5+} is not stable in octahedral coordination.[70]

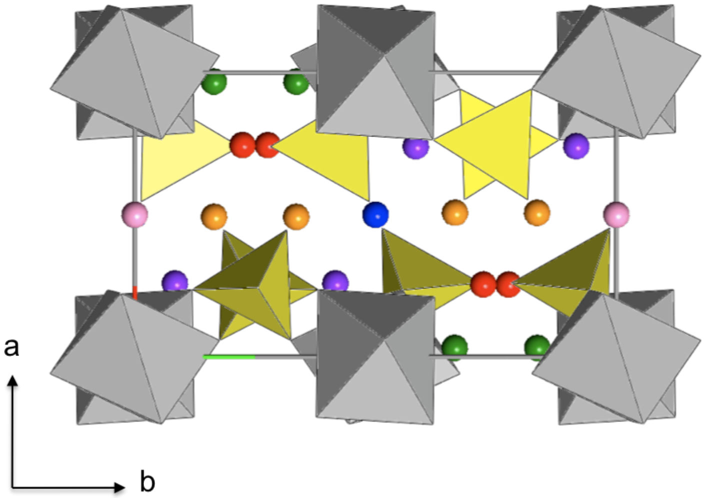

Figure 1.9 – Structure of $Li_5V(PO_4)_2F_2$. Vanadium centered octahedra (grey) corner share with PO_4 tetrahedra to create 2D layers sandwiching Li ions (coloured spheres)

Previous solid-state ^{6,7}Li NMR studies of this material in the Goward research group resolved all six crystallographic Li ion positions in $Li_5V(PO_4)_2F_2$ and showed ion exchange taking place between many of the environments.[69] A study of $Li_4V(PO_4)_2F_2$ showed qualitatively that the ion dynamics increased considerably upon removal of one unit of Li.[70] Chapter 8 of this thesis quantifies the timescale of ion hopping within the fully lithiated phase (prepared by collaborators at the University of Waterloo) using one-dimensional solid-state NMR techniques. Here the large number of possible exchange pairs with different geometries, reveals the structural properties that better accommodate fast ion mobility.

1.6 Summary

In order to better understand the success and failure mechanisms of many of these new cathode materials for Li ion batteries, greater detail regarding the local lithium structure and mobility pathways is needed. Moreover, determination of the timescales and energy barriers of these mobility processes will help to better understand what structural features can enhance or hinder ion diffusion. Multinuclear solid-state NMR is a tool that is sensitive to the local environments of both the mobile ion and the host framework, giving us a powerful tool for identifying these properties. The following chapters demonstrate how solid-state NMR techniques were applied to characterize formation of phase interface regions in $LiFePO_4$ as well as determine the timescales and energy barriers of ion mobility in the multi-Li site materials, $Li_3Fe_2(PO_4)_3$, Li_2VPO_4F and

Li_2VOPO_4, and $Li_5V(PO_4)_2F_2$. Overall, identification of the structural constraints that lead to fast or slow kinetics assists in a more targeted development of cathode materials with enhanced electrochemical performance.

1.7 References

(1) In *Comprehensvie Energy Use Databases*; Natural Resources Canada; Office of Energy Efficiency: 1990-2008.

(2) In *Sectoral Greenhouse Gas Emission Summary*; Environment Canada: 1990-2008.

(3) Tarascon, J.-M.; Armans, M. *Nature* **2001**, *414*, 359.

(4) Dahn, J. R.; Zheng, T.; Liu, Y. H.; Xue, J. S. *Science* **1995**, *270*, 590.

(5) Goodenough, J. B.; Kim, Y. *Chem. Mater.* **2010**, *22*, 587.

(6) Guyomard, D.; Tarascon, J. M. *J. Power Sources* **1995**, *54*, 92.

(7) Ellis, B. L.; Lee, K. T.; Nazar, L. F. *Chem. Mater.* **2010**, *22*, 691.

(8) Whittingham, M. S. *Science* **1976**, *192*, 1126.

(9) Mizushima, K.; Jones, P. C.; Wiseman, P. J.; Goodenough, J. B. *Mater. Res. Bull.* **1980**, *15*, 783.

(10) Thackeray, M. M.; David, W. I. F.; Bruce, P. G.; Goodenough, J. B. *Mater. Res. Bull.* **1983**, *18*, 461.

(11) Amatucci, G. G.; Tarascon, J. M.; Klein, L. C. *J. Electrochem. Soc.* **1996**, *143*, 1114.

(12) Reimers, J. N.; Dahn, J. R. *J. Electrochem. Soc.* **1992**, *139*, 2091.

(13) Manthiram, A.; Kim, J. *Chem. Mater.* **1998**, *10*, 2895.

(14) Whittingham, M. S. *Chem. Rev.* **2004**, *104*, 4271.

(15) Thackeray, M. M. *J. Electrochem. Soc.* **1995**, *142*, 2558

(16) Ohzuku, T.; Kitagawa, M.; Hirai, T. *J. Electrochem. Soc.* **1990**, *137*, 769.

(17) Tarascon, J. M.; Wang, E.; Shokoohi, F. K.; McKinnon, W. R.; Colson, S. *J. Electrochem. Soc.* **1991**, *138*, 2859.

(18) Gummow, R. J.; Dekock, A.; Thackeray, M. M. *Solid State Ionics* **1994**, *69*, 59.

(19) David, W. I. F.; Thackeray, M. M.; Depicciotto, L. A.; Goodenough, J. B. *J. Solid State Chem.* **1987**, *67*, 316.

(20) Thackeray, M. M.; Shao-Horn, Y.; Kahaian, A. J.; Kepler, K. D.; Skinner, E.; Vaughey, J. T.; Hackney, S. A. *Electrochem. Solid-State Lett.* **1998**, *1*, 7.

(21) Padhi, A. K.; Nanjundaswamy, K. S.; Goodenough, J. B. *J. Electrochem. Soc.* **1997**, *144*, 1188

(22) Barker, J.; Saidi, M. Y.; Swoyer, J. L. *J. Electrochem. Soc.* **2003**, *150*, A1394.

(23) Cahill, L. S.; Kirby, C. W.; Goward, G. R. *J. Phys. Chem. C* **2008**, *112*, 2215.

(24) Cahill, L. S., Chapman, R. P., Britten, J. F., Goward, G. R. *J. Phys. Chem. B* **2006**, *110*, 7171.

(25) Verhoeven, V. W. J.; de Schepper, I. M.; Nachtegaal, G.; Kentgens, A. P. M.; Kelder, E. M.; Schoonman, J.; Mulder, F. M. *Phys. Rev. Lett.* **2001**, *86*, 4314

(26) Xu, Z.; Stebbins, J. F. *Science* **1995**, *270*, 1332.

(27) Huang, H.; Yin, S. C.; Nazar, L. F. *Electrochem. Solid State Lett.* **2001**, *4*, A170.

(28) Yamada, A.; Takei, Y.; Koizumi, H.; Sonoyama, N.; Kanno, R.; Itoh, K.; Yonemura, M.; Kamiyama, T. *Chem. Mater.* **2006**, *18*, 804.

(29) Padhi, A. K.; Nanjundaswamy, K. S.; Masquelier, S.; Okada, S.; Goodenough, J. B. *J. Electrochem. Soc.* **1997**, *144*, 1609

(30) Masquelier, C.; Padhi, A. K.; Nanjundaswamy, K. S.; Goodenough, J. B. *J. Solid State Chem.* **1998**, *135*, 228.

(31) Huang, H.; Yin, S. C.; Kerr, T.; Taylor, N.; Nazar, L. F. *Adv. Mater.* **2002**, *14*, 1525.

(32) Saidi, M. Y.; Barker, J.; Huang, H.; Swoyer, J. L.; Adamson, G. *Electrochem. Solid State Lett.* **2002**, *5*, A149.

(33) Barker, J.; Gover, R. K. B.; Burns, P.; Bryan, A. *Electrochem. Solid State Lett.* **2005**, *8*, A285.

(34) Kerr, T. A.; Gaubicher, J.; Nazar, L. F. *Electrochem. Solid State Lett.* **2000**, *3*, 460.

(35) Song, Y. N.; Zavalij, P. Y.; Whittingham, M. S. *J. Electrochem. Soc.* **2005**, *152*, A721.

(36) Yin, S. C.; Herle, P. S.; Higgins, A.; Taylor, N. J.; Makimura, Y.; Nazar, L. F. *Chem. Mater.* **2006**, *18*, 1745.

(37) Rousse, G.; Rodriguez-Carvajal, J.; Patoux, S.; Masquelier, C. *Chem. Mater.* **2003**, *15*, 4082.

(38) Morgan, D.; Van der Ven, A.; Ceder, G. *Electrochem. Solid-State Lett.* **2004** *7*, A30

(39) Andersson, A. S.; Thomas, J. O. *J. Power Sources* **2001**, *97-8*, 498.

(40) Nishimura, S.; Kobayashi, G.; Ohoyama, K.; Kanno, R.; Yashima, M.; Yamada, A. *Nat. Mater.* **2008**, *7*, 707.

(41) Andersson, A. S.; Kalska, B.; Haggstrom, L.; Thomas, J. O. *Solid State Ionics* **2000**, *130*, 41.

(42) Srinivasan, V.; Newman, J. *Electrochem. Solid State Lett.* **2006**, *9*, A110.

(43) Delmas, C.; Maccario, M.; Croguennec, L.; Le Cras, F.; Weill, F. *Nat. Mater.* **2008**, *7*, 665.

(44) Laffont, L.; Delacourt, C.; Gibot, P.; Wu, M. Y.; Kooyman, P.; Masquelier, C.; Tarascon, J. M. *Chem. Mater.* **2006**, *18*, 5520.

(45) Delacourt, C.; Poizot, P.; Tarascon, J.-M.; Masquelier, C. *Nat. Mater.* **2005**, *4*, 254

(46) Andersson, A. S.; Thomas, J. O.; Kalska, B.; Haggstrom, L. *Electrochem. Solid State Lett.* **2000**, *3*, 66.

(47) Herle, S. P.; Ellis, B.; Coombs; N., N., L.F. *Nat. Mater.* **2004**, *3*, 147

(48) Ellis, B., Subramanya Herle, P., Rho. Y.-H., Nazar, L.F., Dunlap, R., Perry, L.K., Ryan, D.H. *Faraday Discussion* **2007**, *134*, 119

(49) Dominko, R.; Bele, M.; Gaberscek, M.; Remskar, M.; Hanzel, D.; Pejovnik, S.; Jamnik, J. *J. Electrochem. Soc.* **2005**, *152*, A607.

(50) Yang, S.; Zavalij, P. J.; Whittingham, S. M. *Electrochem. Commun.* **2001**, *3*, 505

(51) Chen, J.; Whittingham, S. M. *Electrochem. Commun.* **2006**, *8*, 855.

(52) Chen, J.; Vacchio, M. J.; Wang, S.; Chernova, N.; Zavalij, P. Y.; Whittingham, S. M. *Solid State Ionics* **2008**, *178*, 1676.

(53) Ellis, B.; Kan, W. H.; Makahnouk, W. R. M.; Nazar, L. F. *J. Mater. Chem.* **2007**, *17*, 3248.

(54) Bykov, A. B.; Chirkin, A. P.; Demyants, L. N.; Doronin, S. N.; Genkin, E. A.; Ivanov-Shits, A. K.; Kondratyuk, I. P.; Maksimov, B. A.; Mel'kinov, O. K.; Muradyan, L. N.; Simonov, V. I.; Timofeeva, V. A. *Solid State Ionics* **1990**, *38*, 31.

(55) Ohkawa, H.; Yoshida, K.; Saito, M.; Uematsu, K.; Toda, K.; Sato, M. *Chem. Lett.* **1999**, 1017.

(56) Morgan, D.; Ceder, G.; Saidi, M. Y.; Barker, J.; Swoyer, J.; Huang, H.; Adamson, G. *Chem. Mater.* **2002**, *14*, 4684.

(57) Yin, S. C.; Grondey, H.; Strobel, P.; Anne, M.; Nazar, L. F. *J. Am. Chem. Soc.* **2003**, *125*, 10402.

(58) Patoux, S.; Wurm, C.; Morcrette, M.; Rousse, G.; Masquelier, C. *J. Power Sources* **2003**, *119-121*, 278.

(59) Dutreilh, M.; Chevalier, C.; El-Ghozzi, M.; Avignant, D.; Montel, J. M. *J. Solid State Chem.* **1999**, *142*, 1.

(60) Okada, S.; Ueno, M.; Uebou, Y.; Yamaki, J. *J. Power Sources* **2005**, *146*, 565.

(61) Barker, J.; Saidi, M. Y.; Swoyer, J. L. *J. Electrochem. Soc.* **2004**, *151*, A1670.

(62) Groat, L. A.; Raudsepp, M.; Hawthorne, F. C.; Ercit, T. S.; Sherriff, B. L.; Hartman, J. S. *Am. Mineral.* **1990**, *75*, 992.

(63) Groat, L. A.; Chakoumakos, B. C.; Brouwer, D. H.; Hoffman, C. M.; Fyfe, C. A.; Morell, H.; Schultz, A. J. *Am. Mineral.* **2003**, *88*, 195.

(64) Barker, J.; Gover, R. K. B.; Burns, P.; Bryan, A.; Saidi, M. Y.; Swoyer, J. L. *J. Electrochem. Soc.* **2005**, *152*, A1776.

(65) Ellis, B. L.; Ramesh, T. N.; Davis, L. J. M.; Goward, G. R.; Nazar, L. F. *Chem. Mater.* **2011**, *23*, 5138.

(66) Lim, S. C.; Vaughey, J. T.; Harrison, W. T. A.; Dussack, L. L.; Jacobson, A. J.; Johnson, J. W. *Solid State Ionics* **1996**, *84*, 219.

(67) Lavrov, A. V.; Nikolaev, V. P.; Sadikov, G. G.; Poraikoshits, M. A. *Doklady Akademii Nauk Sssr* **1982**, *266*, 343.

(68) Long, J. R.; McCarty, L. S.; Holm, R. H. *J. Am. Chem. Soc.* **1996**, *118*, 4603.

(69) Makimura, Y.; Cahill, L. S.; Iriyama, Y.; Goward, G. R.; Nazar, L. F. *Chem. Mater.* **2008**, *20*, 4240.

(70) Cahill, L. S.; Iriyama, Y.; Nazar, L. F.; Goward, G. R. *J. Mater. Chem.* **2010**, *20*, 4340.

Chapter 2: Introduction to Solid-State NMR

2.1 Introduction

Solid-state Nuclear Magnetic Resonance (NMR) is the primary spectroscopic method utilized in this thesis to characterize the structural and ion mobility properties of the cathode materials presented in Chapter 1. The present chapter will detail the properties of nuclear spins in an applied magnetic field and the spectral features that arise from materials in the solid-state. Moreover, due to the unpaired electrons sitting on the transition metal center of the materials studied in this thesis, the properties of electron magnetic resonance and subsequent interaction with the observed nuclear spins are detailed.

2.2 Spin Properties of Nuclei in an Applied Magnetic Field

2.2.1 Definition of Nuclear Spin and Magnetic Moment

The atomic nucleus is comprised of protons and neutrons and defined by three numbers: the atomic number (Z), the mass number, and spin quantum number (I). Nuclear spin is quantified by the spin angular momentum vector ($\mathbf{I}$) which related to the magnetic moment vector ($\boldsymbol{\mu}$) of the nucleus as well as the nuclear gyromagnetic ratio (γ_N) (Equation 2-1),[1]

$$\boldsymbol{\mu} = \gamma_N \hbar \mathbf{I} = g_N \mu_N \mathbf{I} \qquad \text{Equation 2-1}$$

where γ_N is also expressed by the nuclear g factor (g_N) and the nuclear magneton (μ_N). The values for **I** and γ_N are unique to a given nucleus and allow nuclei to be distinguished from one another spectroscopically. In this thesis, two isotopes of Li, ^{6}Li and ^{7}Li, as well as ^{19}F and ^{31}P were measured. The spin numbers and gyromagnetic ratios of these nuclei are summarized in **Table 2.1**. Also included is the spin number and gyromagnetic ratio of a free electron, whose influence on nuclear spins is introduced in Section 2.3

Table 2.1 – Nuclear spins measured in this thesis with their corresponding spin number (*I*) and gyromagnetic ratio. Also included is the gyromagnetic ratio of a free electron (e^-).

Isotope	Spin number (*I*)	Gyromagnetic Ratio (10^6 rad s^{-1} T^{-1})
^{6}Li	1	39.37
^{7}Li	3/2	103.96
^{19}F	1/2	251.81
^{31}P	1/2	108.41
e^-	1/2	-176085.97

2.2.2 Zeeman Splitting in an Applied Magnetic Field

The interaction between an external magnetic field B_0 and the magnetic moments of the spin system or collection of spins results in the Zeeman interaction. For a static magnetic field applied along the *z*-axis of the laboratory frame, the Zeeman Hamiltonian, $\hat{H}_Z$, is as follows (Equation 2-2):[1]

$$\hat{H}_Z = -\gamma\hbar\hat{I}_z B_0 \qquad \text{Equation 2-2}$$

For a given nuclear spin there are $2I+1$ possible energy states each defined by the quantum number m (where $m = I, I-1, I-2, \ldots -I$). The energies for each spin state are degenerate in the absence of an applied magnetic field but lifted to a value ($E_{I,m}$) when B_0 is present. Operating the spin Hamiltonian on the spin wavefunctions (Equation 2-3),

$$\hat{H}\left|I,m\right\rangle = E_{I,m}\left|I,m\right\rangle \qquad \text{Equation 2-3}$$

gives,

$$E_{I,m} = -\gamma\hbar B_0 m \qquad \text{Equation 2-4}$$

For a nucleus with I = ½, two possible spin states of $m = +1/2$ and $m = -1/2$ give rise to the low energy +½ state (termed the α state) and a high-energy −½ state (termed the β state) (**Figure 2.1**).

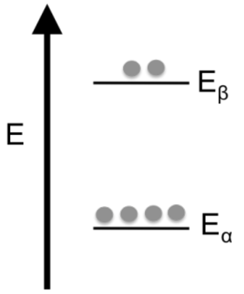

Figure 2.1 - Schematic showing the relative population of the energy levels of a spin ½ nucleus. A Boltzmann distribution governs the α and β populations (small spheres).

In a large sample of spins, the population of spins aligned with and against the applied field (N_α and N_β, respectively) is governed by a Boltzmann distribution (Equation 2-5),[2,3]

$$\frac{N_\alpha}{N_\beta} = \exp\left[\frac{-(E_\alpha - E_\beta)}{k_B T}\right] \qquad \text{Equation 2-5}$$

where E_α and E_β are the respective energies of the α and β states, k_B is the Boltzmann constant, and T is the temperature.

2.1.1 Precesssion and Larmor Frequency

The direction of the spin angular momentum is called the spin polarization axis and when placed in a static magnetic field will precess around the applied field. The rate at which the precession occurs is called the Larmor frequency (ω_0) and is governed by the gyromagnetic ratio and the strength of the applied field (Equation 2-6).

$$\omega_0 = \gamma B_0 \qquad \text{Equation 2-6}$$

For the nuclei studied in this thesis, experiments were carried out at three different applied fields of 4.70 T, 7.05 T and 11.7 T. The Larmor frequencies of ^{6,7}Li, ^{31}P, and ^{19}F nuclei at the respective fields are summarized in **Table 2.2**.

Table 2.2 – Summary of magnetic field strengths used in this thesis and the corresponding Larmor frequencies of ^{6,7}Li, ^{19}F, and ^{31}P nuclei.

Nucleus	ω_0 at 4.70 T (MHz)	ω_0 at 7.05 T (MHz)	ω_0 at 11.7 T (MHz)
^{6}Li	29.4	44.1	73.6
^{7}Li	77.3	115.9	193.2
^{19}F	188.3	282.4	470.7
^{31}P	81.1	121.6	202.6

In NMR communications the strength of the applied magnetic field is often given as the Larmor frequency of protons at that field. For applied fields of 4.70 T, 7.05 T and 11.7 T, the magnet strength is described as 200 MHz, 300 MHz, and 500 MHz, respectively.

2.2.3 The RF Pulse

The basis of the NMR experiment is the movement of the spin polarization axis by applying radiofrequency (RF) pulses tuned to the Larmor frequency. Through these pulses, a second magnetic field, B_1, is generated and able to rotate the net magnetization of the chemical sample away from the $z-$axis towards the $xy-$plane of detection. The RF pulse is defined by its flip-angle, θ_{rf}, and phase, ϕ_{rf}. For example in a single pulse experiment, rotation of the magnetization from the $+z$-axis to the $-y$-axis requires a flip angle of 90° and a phase of 0, (i.e. a $+x$-pulse). This flip-angle is calibrated by setting a RF power (in Watts) and determining the duration, τ_{rf}, of the RF pulse that maximizes the signal placement along the $-y$-axis (Equation 2-7).

$$\theta_{rf} = \gamma B_1 \tau_{rf} = \omega_1 \tau_{rf}$$ Equation 2-7

The Hamiltonian to describe the interaction of the nuclear spin with the B_1 field is similar to the description for the effect from the static field (B_0, Equation 2-2). However in this case, the B_1 field oscillates along the x-axis, leading to inclusion of the flip angle. The result is a Hamiltonian for nuclear spins under the combined influence of the static B_0 and oscillating B_1 field (Equation 2-8).

$$\hat{H} = -\gamma(\hat{I}_z B_0 + \hat{I}_x B_1 \cos(\omega_1 \tau_{rf}))$$ Equation 2-8

The length of the RF pulse also determines the range of frequencies that may be excited. For 90° flip angles generated from a short duration pulse of 2.5 μs at relatively high power, a large bandwidth of frequencies is excited. Subsequently a longer 90° pulse duration at low power leads to excitation of a smaller, more selective bandwidth. The use of selective pulses is discussed in greater detail in Chapter 3.

2.3 Spin Properties of Unpaired Electrons in an Applied Magnetic Field

A unique property of NMR studies of Li-cathode materials is the presence of unpaired electrons sitting on the transition metal center, M. Unpaired electrons are spin ½ with an electron magnetic moment (μ_e). The electron magnetic moment is dependent on the Bohr magneton, μ_B, the electron spin angular momentum, **S**, and the free electron value, g_e (Equation 2-9).

$$\mu_e = -g_e \mu_B \mathbf{S} \qquad \text{Equation 2-9}$$

The value of g_e for a free electron is 2.0023. For unpaired electrons sitting in a crystal lattice, the *g* value and subsequent magnetic moment is altered due to spin-orbit coupling between the unpaired electrons and their local environment. Therefore a tensor, **g**, is used to better represent the orientation dependence of the local field of a given electron spin. Isotropic g-tensors give rise to *g* values equal to 2.0023, while anisotropic **g**-tensors result in *g*-values that deviate from 2.0023.[1]

To describe the total electron spin value for a paramagnetic ion, the number of unpaired electrons is multiplied by the electron spin. An example of this is for octahedral coordination of V^{2+} where the three unpaired electrons give a total spin number of S = 3/2. In an applied magnetic field, the electron spins will align with or against the field, similar to a nuclear spin. The resulting Hamiltonian for the Zeeman interaction of an electron spin in an applied magnetic field is therefore expanded to include the **g**-tensor (Equation 2-10)

$$\hat{H}_{eZ} = -\mu_e \cdot B_0 = \mathbf{g} \cdot \mu_B \mathbf{S} \cdot B_0 \qquad \text{Equation 2-10}$$

Because the lifetime of the electronic spins states along or against the applied field (T_{1e}) is shorter than the nuclear spin state lifetimes, only the time averaged spin density along the +z-axis is reported and termed, $\langle S_z \rangle$. This spin density is proportional to the molar magnetic susceptibility of the transition metal, χ_M, as well as the strength of the applied field (Equation 2-11).

$$\langle S_z \rangle = -\frac{B_0}{\mu_0 g N_0 \mu_B} \chi_M \qquad \text{Equation 2-11}$$

Where μ_0 is the permeability and N_0 is Avogadro's number.

Coupling between $\langle S_z \rangle$ and the nuclear spins being measured is possible and gives rise to very distinct spectral features in NMR measurements. These couplings often dominate the NMR spectra as the electron *g* values are considerably higher than the nuclear *g* values, as shown in **Table 2.1** through comparison of γ_N and γ_e. Correlating the NMR spectral features to the spin states of the paramagnetic metal center was needed for a better understanding the local structure of the nuclei being investigated in this thesis.

2.4 NMR of Solid-state Paramagnetic Materials

For the cathode materials studied in this thesis, the most relevant phase of study is the solid phase, as the electrochemical cycling involves the movement of the Li ions in and out of a crystalline host framework. Therefore powders of each material were measured using solid-state NMR techniques where features not normally observed in the solution state were observed. The fast molecular tumbling of solute and solvent molecules averages the orientation dependence of the local fields giving rise to narrow, well-resolved spectra. In the solid-state, orientation dependent interactions such as chemical shift anisotropy (CSA) (Section 2.4.1), heteronuclear, homonuclear and electron-nuclear dipole coupling (D_{ij}) (Section 2.4.2), and quadrupole coupling (C_q) (Section 2.4.3) result in broadened spectra, where identification of distinct crystallographic environments is difficult. Application of Magic Angle Spinning (MAS) techniques can average the orientation dependent terms of the aforementioned interactions, resulting in better-resolved spectra. MAS involves the physical rotation of the sample at an angle (θ) relative to the applied magnetic field.[4,5] By setting θ to 54.74°, the geometry dependent term, ($3\cos^2\theta$-1), found in the equations describing CSA, D_{ij}, and C_q is averaged to zero. The rotation frequency must be greater than the combined magnitudes of these terms otherwise spinning sidebands are observed. These sidebands are peaks that emerge at integer multiples of the MAS frequency on either side of the isotropic peak, and have a manifold as broad as the frequency of the combined CSA, D_{ij}, and C_q contributions to the NMR spectrum.

2.4.1 Chemical Shielding and Anisotropy

The applied magnetic fields, B_0 and B_1, induce currents in the electron clouds surrounding the nuclear spins giving rise to local magnetic fields termed B_{ind}. The resonance frequencies resulting from these local fields give rise to the observed chemical shift and is what makes NMR a sensitive probe of local structure and dynamics. The chemical shielding tensor, $\boldsymbol{\sigma}$, used to describe the behaviour of the electron clouds gives rise to the chemical shielding Hamiltonian (Equation 2-12).

$$\hat{H}_{CS} = \gamma I \cdot \boldsymbol{\sigma} \cdot B_0 \qquad \text{Equation 2-12}$$

The shielding tensor, has both symmetric and asymmetric components however, only the symmetric component (σ^i) contributes to the appearance of the NMR spectrum (Equation 2-13).

$$\sigma^i = \begin{pmatrix} \sigma_{xx} & \frac{1}{2}\left(\sigma_{xy}+\sigma_{yx}\right) & \frac{1}{2}\left(\sigma_{xz}+\sigma_{zx}\right) \\ \frac{1}{2}\left(\sigma_{xy}+\sigma_{yx}\right) & \sigma_{yy} & \frac{1}{2}\left(\sigma_{yz}+\sigma_{zy}\right) \\ \frac{1}{2}\left(\sigma_{xz}+\sigma_{zx}\right) & \frac{1}{2}\left(\sigma_{yz}+\sigma_{zy}\right) & \sigma_{zz} \end{pmatrix} \qquad \text{Equation 2-13}$$

The three principal components, σ_{xx}, σ_{yy}, and σ_{zz} define the isotropic shielding, value σ_{iso} (Equation 2-14).

$$\sigma_{iso} = \frac{\sigma_{xx}+\sigma_{yy}+\sigma_{zz}}{3} \qquad \text{Equation 2-14}$$

Where the anisotropy (Δ) and asymmetry (η) of the tensor reflect the symmetry of the local nuclear environment. These values are also defined by the principal components (Equation 2-15 and Equation 2-16, respectively).

$$\Delta = \sigma_{zz} - \sigma_{iso} \qquad \text{Equation 2-15}$$

$$\eta = \frac{\sigma_{xx} - \sigma_{yy}}{\Delta}$$ Equation 2-16

The chemical shielding is manifested in the NMR spectrum through the chemical shift, where the observed NMR signal, ω_{cs}, has contributions from the isotropic, anisotropic and asymmetry parameters. (Equation 2-17),

$$\omega_{CS} = -\omega_0 \sigma_{iso} - \frac{1}{2}\omega_0 \Delta \left\{ 3\cos^2\theta - 1 + \eta \sin^2\theta \cos 2\phi \right\}$$ Equation 2-17

where, θ and ϕ are the polar angles defining the B_0 direction relative to the principal axis of the sample. In NMR experiments of solution state samples, the fast molecular tumbling averages the orientation dependence of the chemical shielding tensor, resulting in a single observed frequency. In a NMR spectrum of a powdered solid-state material, the fixed orientation of the nuclear spins for each the individual crystallites results in a distribution of shifts giving a broad powder pattern. By setting θ to 54.7° and rotating the sample, the $3\cos^2\theta$-1 term averages the anisotropic portion of ω_{CS} to zero. The result is narrowed resonances resembling a solution state spectrum. However, the shape of the powder pattern reflects the site symmetry at the nucleus, making determination of Δ and η, important tools for understanding subtle structural features of a solid material.

The observed frequency, ν, is found by adding the linear frequencies of the Larmor and ω_{CS} values and referencing it to an agreed upon chemical standard with frequency ν_{ref} (Equation 2-18). The resulting chemical shift (δ_{iso}) is reported in units of ppm and is a field independent value.

$$\delta_{iso} = \frac{\nu - \nu_{ref}}{\nu_{ref}} \qquad \text{Equation 2-18}$$

The chemical shift tensor has elements that are closely related to, but more easily observed than, the chemical shielding tensor elements. The principal values of the chemical shift tensor are labeled as, δ_{11}, δ_{22}, and δ_{33}, where by convention, $\delta_{11} \geq \delta_{22} \geq \delta_{33}$. The isotropic shift ($\delta_{iso}$) calculated from the average of the three principal components. The shift anisotropy (Δ) and the axial symmetry (η) are determined using Equation 2-19 and Equation 2-20, respectively.

$$\Delta = \delta_{11} - \delta_{iso} \qquad \text{Equation 2-19}$$

$$\eta = \frac{\delta_{xx} - \delta_{yy}}{\Delta} \qquad \text{Equation 2-20}$$

Different terminologies are used to describe the shifts of materials having different electron structures. For diamagnetic compounds a *chemical shift* is reported whereas for metals and semiconductors a *Knight shift* is given. For the highly paramagnetic materials studied in this thesis a *paramagnetic shift* is observed.[2] The influences on the paramagnetic shift are significantly more complex than the chemical shifts observed in diamagnetic solid-state compounds and will be described in greater detailed in Section 2.5.

2.4.2 Dipolar coupling

Dipolar coupling is a phenomenon that can occur between both homonuclear and heteronuclear spin pairs. In paramagnetic systems, this coupling can also take place between a nuclear spin and the local field created by the unpaired electron density. A simplified dipolar Hamiltonian ($\hat{H}_{dd}$) is given in Equation 2-21, for a dipolar coupling between an *i* and *j* spin. This interaction is dependent on both the gyromagnetic ratio of the spins as well as the internuclear distance, r_{ij}.

$$\hat{H}_{dd} = -\left(\frac{\mu_0}{4\pi}\right)\frac{\gamma_i\gamma_j\hbar}{r_{ij}^3}\hat{I}_i\hat{I}_j(3\cos^2\theta - 1) \qquad \text{Equation 2-21}$$

Similar to the treatment of large CSA's, by applying MAS techniques the ($3\cos^2\theta$-1) term is averaged to zero. However, if the frequency of spinning is not as large as the frequency of the dipolar coupling constant (Equation 2-22) combined with the broadening contribution of CSA then spinning sidebands are observed.

$$D_{ij} = \hbar\left(\frac{\mu_0}{4\pi}\right)\frac{1}{r_{ij}^3}\gamma_i\gamma_j \qquad \text{Equation 2-22}$$

As mentioned previously, the gyromagnetic ratio values of the nuclear spins studied in this thesis are significantly lower than γ_e for an electron spin ($\gamma_e = -1.760 \times 10^{11}$ rad s^{-1} T^{-1} for the free-electron *g*-value) (**Table 2.1**). This results in the effects of nuclear-electron coupling having orders of magnitude greater dipolar couplings than homonuclear or heteronuclear couplings. **Table 2.3** summarizes the dipolar coupling constants found in olivine $LiFePO_4$ for a homonuclear Li-Li contact, heteronuclear Li-P contact, and electron-nuclear contact. The value of r_{ij} for the electron-nuclear coupling was taken as the internuclear distance of the crystallographic Li and Fe sites.

Table 2.3 – Summary of homonuclear, heteronuclear, and nuclear-electron dipolar coupling constants in $LiFePO_4$

Type of Coupling	r_{ij} (Å)	D_{ij} (Hz)
Homonuclear Li-Li	3.003	670.4
Heteronuclear Li-P	2.659	1005.9
Nuclear-Electron Li-Fe	3.281	84053.1

It is evident that the nuclear-electron couplings are significantly larger than either the homonuclear and heteronuclear couplings. Moreover, this calculation is treated as an underestimate of the true electron-nuclear coupling value, as $LiFePO_4$ is Fe^{2+} with a high spin d^6 electron configuration resulting in time averaged spin density arising from 4 unpaired electrons on the metal center. The value given in **Table 2.3** is given for a single, free electron, only.

A primary consequence of this coupling is that sideband manifolds in the NMR spectra of paramagnetic spin systems are considerably more substantial than their diamagnetic counterparts. This is demonstrated in **Figure 2.2** where the ^7Li MAS spectrum of olivine $LiFePO_4$, which has Fe^{2+} in an octahedral d^6 electron configuration (giving four unpaired electrons), is compared with the MAS spectra of two isostructural compounds with different electron configurations at the M(2) metal center. The first compound is the diamagnetic analogue, $LiMgPO_4$. The second, compound $LiMnPO_4$, has a higher amount of unpaired electron spin density as Mn^{2+} in high spin d^5 octahedral coordination giving five unpaired electrons. The ^7Li MAS spectrum of $LiMgPO_4$ shows the combined influences of homonuclear and heteronuclear dipolar couplings, quadrupolar coupling and CSA. These interactions give rise to two small sidebands of low intensity. In contrast the MAS spectra of $LiFePO_4$ and $LiMnPO_4$ both have large sideband manifolds arising from the strong nuclear-electron dipolar couplings as all other parameters, C_q and CSA, would be near equivalent in these isostructural compounds. Moreover, when the manifolds of the $LiFePO_4$ and $LiMnPO_4$ are compared, the larger amount of unpaired electron spin density on the Mn^{2+} center is reflected in the larger sideband manifold of the latter. The difference in the Full-Width at Half-Maximum (FWHM) of the isotropic peaks in $LiFePO_4$ and $LiMnPO_4$ is explained in Section 2.6.2.

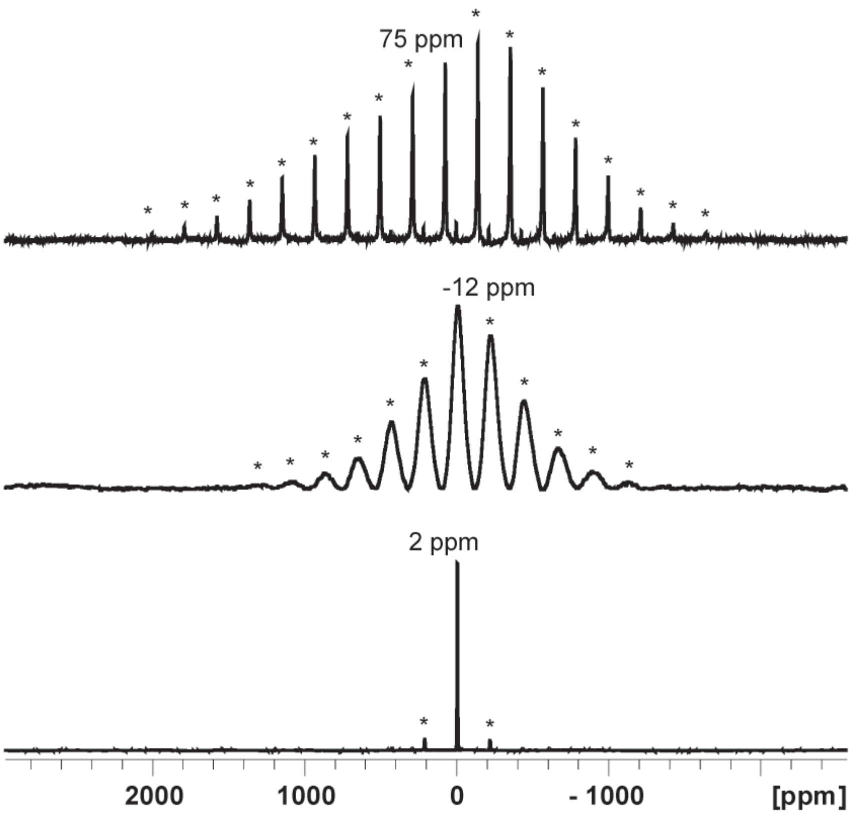

Figure 2.2 – ^{7}Li MAS spectra of $LiMgPO_4$ (bottom), $LiFePO_4$ (middle), and $LiMnPO_4$ (top) with a spinning speed of 25 kHz). The materials are isostructural with one another, differing only in the metal center. $LiMgPO_4$ is a diamagnetic analogue of the paramagnetic $LiFePO_4$ and $LiMnPO_4$. Asterisks denote spinning sidebands

A secondary consequence of nuclear spins having dipolar couplings with the unpaired electron spin density, is that structural and dynamic information relating to the magnitude of heteronuclear and homonuclear dipolar couplings is overshadowed. This leads to the use of double resonance MAS NMR techniques where ^{6}Li-^{31}P and ^{6}Li-^{19}F dipolar couplings can be reintroduced and thus probed more directly. Details of these experiments are outlined in greater detail in Chapter 3.

2.4.3 Quadrupole Coupling

Nuclei having spin greater than ½ are termed quadrupolar. For the spins identified in **Table 2.1** both ^{6}Li and ^{7}Li nuclear spins have this property and possess a nuclear electric quadrupole moment which interacts not only with the applied and local magnetic fields, but also with electric field gradients (EFG) present at the nucleus. The quadrupolar Hamiltonian, describing the coupling between a nuclear electric quadrupole moment (*eQ*) and an electric field gradient tensor (**V**) is presented in Equation 2.29,

$$\hat{H}_Q = \frac{eQ}{2I(2I-1)\hbar}\hat{\mathbf{I}}\cdot\mathbf{V}\cdot\hat{\mathbf{I}} \qquad \text{Equation 2-23}$$

where *e* is the proton charge and *Q* is the nuclear quadrupole moment. The value of *Q* is unique for each quadrupolar nuclear spin as summarized for ^{6}Li and ^{7}Li in **Table 2.4.**

Table 2.4 – Summary of spin quadrupole moments for quadrupolar nuclei measured in this thesis.

Nucleus	Quadrupole Moment (Q/m^2)
^{6}Li	-8.0 x 10^{24}
^{7}Li	-4.0 x 10^{26}

Quadrupolar coupling (C_q) gives rise to distinct spectral features in NMR spectra, allowing for interpretation of local site symmetry around the nucleus. The magnitude of C_q is calculated from Equation 2-24,

$$C_q = \frac{e^2 q_{zz} Q}{h} \qquad \text{Equation 2-24}$$

Where eq_{zz} is the largest principal axis value of the EFG tensor. The relatively low eQ values of the ^{6}Li and ^{7}Li as well as the dominance of the nuclear-electron dipolar coupling in spectra of materials (as demonstrated in **Figure 2.2**), make the contributions from quadrupolar coupling largely negligible.

2.5 Isotropic Shifts in Paramagnetic Materials

The chemical shielding that results from the interaction of the local nuclear field with electron clouds of unpaired electrons is significantly more complex. The observed paramagnetic signal (δ_P) in the cathode materials studied in the subsequent chapters is described by Equation 2-25,[6,7]

$$\delta_P = -\frac{A_H}{\omega_0 h}\langle S_z \rangle \qquad \text{Equation 2-25}$$

where the hyperfine coupling constant (A_H) is a measure of how much unpaired electron spin density has transferred to the nucleus of interest. The size and sign of A_H dictates the size and direction of the paramagnetic shift, making it an important parameter for understanding the origin of many spectral features. A_H is made up of three contributions: the Fermi-contact interaction (A_F), the dipolar coupling contribution (A_D), and the spin-orbital contribution (A_L) (Equation 2-26).

$$A_H = A_F + A_D + A_L \qquad \text{Equation 2-26}$$

The hyperfine terms are more simply separated into two contributions: the *contact* and *pseudocontact* interactions. A_F constitutes the former term as it results from the through-bond coupling between the local fields of the nuclear spin and the unpaired electron density. The combined effects of A_D and A_L arise from through-space couplings of the spin and orbital angular momentum terms, respectively, of the unpaired electron spin density to the nuclear spin.

2.5.1 The Contact Shift: Defining the Fermi-Contact Term, A_F

The Fermi-contact Hamiltonian ($\hat{H}_F$) is shown in Equation 2-27 where the geometry dependence of the interaction between the nuclear spin (**I**) and the *i*th electron spin ($\mathbf{s}_i$) is represented by a vector $\mathbf{r}_i$.

$$\hat{H}_F = \frac{16\pi\hbar\gamma_N\beta}{3}\sum_i \delta(\mathbf{r}_i)\mathbf{s}_i \cdot \mathbf{I} \qquad \text{Equation 2-27}$$

The geometry dependent mechanism of this coupling has been shown to follow the Goodenough-Kanamori rules for spin-spin super-exchange.[8,9] In this thesis, the super-exchange is between the unpaired electron spin density on the transition metal atom (M) and the nuclear spin on the Li or P nuclei being measured. These atoms are joined through the p-orbitals of an intervening anion giving a general geometry of the M-O-Li/P and/or M-F-Li/P found in the phosphate and fluorophosphates cathode materials, respectively. The transition metal centers of materials studied in this thesis, all have octahedral coordination, resulting in a split of the d-orbital into a triply degenerate t_{2g} state, (d_{xy}, d_{yz}, d_{zx}) and higher energy doubly degenerate e_g state (with orbitals $d_{x^2-y^2}$ and d_{x^2}). The coupling between the unpaired electron density to the nuclear spin is maximized when the M-O-Li/P orbital geometries are at either 90° or 180°. Two mechanisms are used to describe the geometry of the super-exchange as outlined in **Figure 2.3**.[10,11] The first mechanism involves the *delocalization* of unpaired electron spin density from the transition metal d-orbitals to the nucleus of interest via an intervening O 2p orbital. In the case of a 90^{o} orbital overlap the M t_{2g} orbitals are the source of the electron density and transferred to the s-orbital of the Li or P nuclei via an O p_{π} orbital. For the 180^{o} orbital overlap, the e_g orbitals are the electron density source which is transferred via the p_{σ}-orbital. The overall result for both of these geometries is the transfer of electron spin density to the s-orbital of the nucleus where the sign is unchanged leading to an increase in the paramagnetic shift. The second mechanism involves the *polarization* of unpaired electrons in the bonding t_{2g} or e_g orbitals by other unpaired electrons sitting on M. This results in the transfer of electron spin density with sign opposite to the metal center thus leading to a decrease in the overall paramagnetic shift at the nucleus of interest.

a) Delocalization Mechanism

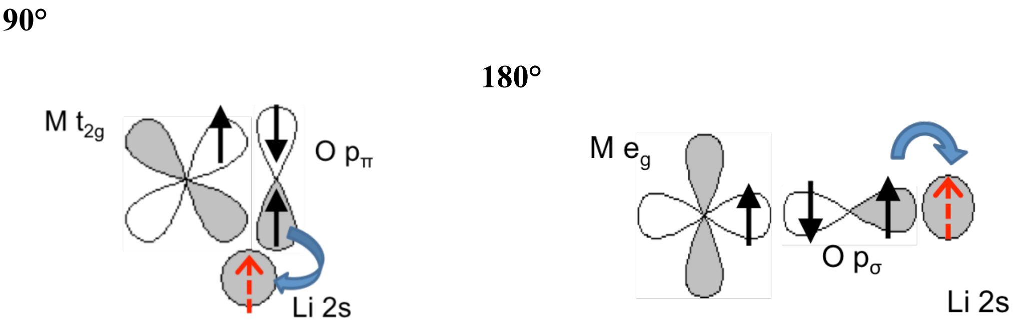

b) Polarization Mechanism

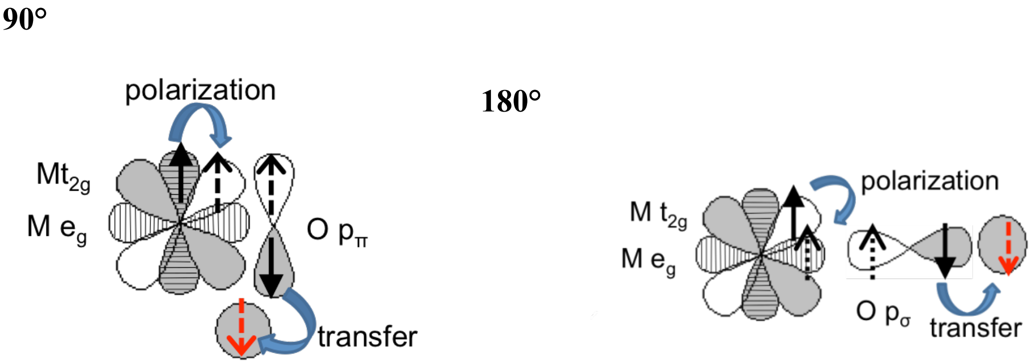

Figure 2.3 – Schematic (reproduced from Ref.[10,11] detailing two mechanisms for electron spin density transfer. a) Shows delocalization of unpaired electron spin density from the M t_{2g} to the empty Li 2s orbital either directly or via the O 2p orbital. This leads to spin density being of the same sign as that on the M center. b) Shows the 90° orbital overlap where the unpaired electron spin density in the e_g orbital (shown with hatching) polarizes the spin in the t_{2g} orbital leading to density transfer to the empty Li 2s orbital of opposite sign to that of the M center. The 180° geometry involves the polarization of the e_g spins by the t_{2g} orbitals, also leading to a transfer of spin density to the Li 2s nucleus of opposite sign to that of the metal center.

Delocalization of unpaired electron spin density onto the nucleus being measured is the more prominent mechanism and the additive nature of these effects (Equation 2-27) leads to a paramagnetic shift range that is far greater than its diamagnetic counterpart. The paramagnetic shifts arising from materials studied throughout this thesis will be discussed in the context of these mechanisms, where the crystallographic information will be relied on for justifying the size and direction of the shifts.

It is noted that this is largely a qualitative assessment of the observed shifts arising from the Fermi-contact interaction, where more quantitative interpretations are provided from Density Functional Theory (DFT) calculations. For Li-oxide materials, DFT methods were used to calculate the amount of spin density around the transition metal center with the observed shifts rationalized from the orbital geometry arguments detailed above.[10] More recent DFT calculations have extended these calculations to predict the contact shift by including the geometry dependent terms of A_{FC}. These calculations allow for contributions from metal centers at intermediate orbital overlap angles to be better incorporated into the determination of the Fermi-contact interaction leading to estimated paramagnetic shifts.[12]

2.5.2 The Pseudo-Contact Shift: Defining A_D and A_L

The first contribution to the pseudo-contact shift is the dipolar term A_D which has a Hamiltonian that is also dependent on the vector between the nuclear spin and the electron density (Equation 2-28)

$$\hat{H}_D = -\left(\frac{\mu_0}{4\pi}\right)\gamma_N\gamma_e\hbar\sum_i\left\{\frac{3(\mathbf{r}_i\cdot\mathbf{s}_i)(\mathbf{r}_i\cdot\mathbf{I})}{r_i^5}-\frac{\mathbf{s}_i\cdot\mathbf{I}}{r_i^3}\right\}$$ Equation 2-28

This term does not arise from a through-bond interaction as found in A_F, but relies on the through-space internuclear distance, r_i.. The size of the dipolar shift ($\delta^{dipolar}$) is derived to include the principal components of the electron *g*-tensor (g_{xx}, g_{yy}, and g_{zz}) (Equation 2-29)[6]

$$\delta^{dipolar} = \frac{\beta^2 S'(S+1)}{18kTr_{eN}^3}\{[2g_{zz}^2-(g_{xx}^2+g_{yy}^2)](1-3\cos^2\theta) \\ +3(g_{yy}^2-g_{zz}^2)\sin^2\theta\cos 2\Omega\}$$ Equation 2-29

where r_{eN} is the distance between the metal center and the nucleus being observed, θ is the angle between the *z*-axis and $\mathbf{r}_i$, and Ω is the angle between the *x*-axis and the projection of $\mathbf{r}_i$ onto the *xy*-plane. For isotropic g-tensors, this term vanishes to zero and there is no dipolar contribution to the observed shift.[6,13,14] Qualitative determination of the g-tensor for materials studied in this thesis, can be made through evaluation of the symmetry at the metal center. For a symmetrical metal environment, an isotropic g-tensor is presumed and there is little to no dipolar shift present.[6] For asymmetrical metal centers, the contribution from the dipolar shift is considered.

The orbital term, A_L, represents the interaction between the nuclear magnetic moment and the magnetic field generated by the orbital motion of the electrons. It is non-zero for states with net orbital angular momentum (where $\mathbf{l}_i$ is the orbital angular momentum of the *i*th electron) (Equation 2-30).

$$\hat{H}_L = 2\hbar\gamma_N\beta\sum_i \mathbf{l}_i \cdot \frac{\mathbf{I}}{r_i^3} \qquad \text{Equation 2-30}$$

Overall, the contribution of this value to the overall shift is considerably smaller as the finite NMR signal is primarily governed by the s-orbital of the nuclear spin, which has zero net angular momentum.[6,12] Therefore, only the Fermi-contact and dipolar shift contributions are considered in discussions of observed paramagnetic shifts.

2.6 Nuclear Spin Relaxation

2.6.1 Spin-Lattice Relaxation

Once the system has been perturbed by the applied RF field, it will return to thermal equilibrium by a process known as longitudinal or spin-lattice relaxation. The time constant that governs this relaxation is termed T_1, and can vary greatly depending on the local environment of the spin system being measured. The relaxation can be monitored by the exponential buildup of magnetization along the z-axis (M_z) as a function of time relative to the magnetization measured at equilibrium (M_z^{eq}) (Equation 2-31).

$$M_z(t) = M_z^{eq}(1 - \exp^{-t/T_1}) \qquad \text{Equation 2-31}$$

The total relaxation $\left(T_{1_T}^{-1}\right)$ is facilitated by a combination of the interactions with the local surroundings including, dipolar coupling $\left(T_{1_D}^{-1}\right)$, quadrupolar coupling $\left(T_{1_Q}^{-1}\right)$, chemical shift anisotropy $\left(T_{1_{CSA}}^{-1}\right)$ as well as spin-rotation $\left(T_{1_{SR}}^{-1}\right)$ (Equation 2-32).[6]

$$T_{1_T}^{-1} = T_{1_D}^{-1} + T_{1_Q}^{-1} + T_{1_{CSA}}^{-1} + T_{1_{SR}}^{-1} \qquad \text{Equation 2-32}$$

In the solid-state, the first three terms are more important, as the spins are fixed in a crystalline lattice. Moreover, for spin ½ nuclei, the quadrupolar term is dropped. For the paramagnetic systems investigated in this thesis, there is an additional relaxation contribution from the hyperfine coupling $\left(T_{1_H}^{-1}\right)$ as shown in Equation 2-33.

$$T_{1_H}^{-1} = \frac{2S(S+1)A_H^2}{3\hbar^2}\left[\frac{\tau_{e2}}{1+(\omega_I+\omega_S)^2\tau_{e2}^2}\right] \qquad \text{Equation 2-33}$$

Where τ_{e2} is the sum of the electron exchange rate and electron transverse relaxation rate, and ω_I and ω_S are the nuclear and electron resonance frequencies, respectively.[6] Overall, the dipolar term has the largest contribution, as the electron-nuclear couplings are significantly larger than any CSA, C_q, and even A_H contributions. This leads to measured T_{1_T} times on the μs – ms timescale in the paramagnetic systems investigated where in diamagnetic analogues, lattice relaxation times would range from seconds to hundreds of seconds.

When nuclei in different environments undergo site-exchange, there is the observed averaging of the spin-lattice relaxation times. This is the case for ^{6,7}Li nuclei where the Li ions hop from one crystallographic site to another. Chapter 3 outlines selective inversion experiments used to separate the ion exchange dynamics from the inherent T_1 times such that information regarding the local Li environments is accessed.

2.6.2 Spin-Spin Relaxation

Similar to longitudinal relaxation along the *z*-axis, transverse relaxation in the *xy*-plane is also observed. This relaxation has a time constant, termed T_2.

The importance of this term is highlighted by its influence on the line-width of isotropic resonances of nuclear spins. The FWHM of a peak is defined by $1/T_2$ which for paramagnetic systems, has a dependence on both the hyperfine coupling as well as the spin-lattice relaxation of the electron spins (T_{1e}) (Equation 2-34),[6]

$$FWHM = T_2^{-1} = T_{2N}^{-1} + \left(\frac{A_H}{\hbar}\right)^2 \left(\frac{T_{1e}}{8}\right) \qquad \text{Equation 2-34}$$

where T_{2N}^{-1} is the contribution to the linewidth from diamagnetic effects that are largely outweighed by effects of the Fermi-contact dominated hyperfine coupling.

2.7 Summary

The nuclear and electron resonance properties outlined in this chapter will serve to better explain the spectroscopic features that arise in the measurement of ^{6,7}Li, ^{31}P, and ^{19}F environments of cathode materials studied in subsequent chapters. Chapter 3 details specific NMR experiments used throughout this thesis that probe the structural and dynamics origins of the many spectral features observed in these materials.

2.8 References

(1) Carrington, A.; McLachlan, A. D. *Introduction to Magnetic Resonance*; Harper & Row, Publishers, Inc.: New York, 1967.

(2) Levitt, M. H. *Spin Dynamics: Basics of Nuclear Magnetic Resonance*; John Wiley & Sons, Ltd.: West Sussex, 2001.

(3) Duer, M. J. *Introduction to Solid-State NMR Spectroscopy*; Blackwell Publishing Ltd.: Oxford, 2004.

(4) Andrew, E. R.; Bradbury, A.; Eades, R. G. *Nature* **1958**, *182*, 1659.

(5) Lowe, I. J. *Phys. Rev. Lett.* **1959**, *2*, 285.

(6) La Mar, G. N., DeW. Horrocks, W., Jr., Holm, R. H. *NMR of Paramagnetic Materials*; Academic Press: New York, 1973.

(7) McConnell, H. M.; Chesnut, D. B. *J. Chem. Phys.* **1958** *28*, 107.

(8) Goodenough, J. B. *J. Phys. Chem. Solids* **1958**, *6*, 287.

(9) Kanamori, J. *Progress in Theoretical Physics* **1957**, *17*, 177.

(10) Carlier, D.; Menetrier, M.; Grey, C. P.; Delmas, C.; Ceder, G. *Phys. Rev. B* **2003**, *67*, 174103.

(11) Grey, C. P.; Dupre, N. *Chem. Rev.* **2004**, *104*, 4493.

(12) Kim, J.; Middlemiss, D. S.; Chernova, N. A.; Zhu, B. Y. X.; Masquelier, C.; Grey, C. P. *J. Am. Chem. Soc.* **2010**, *132*, 16825.

(13) McConnell, H. M.; Roberston, R. E. *J. Chem. Phys.* **1958**, *29*, 1361.

(14) Nayeem, A.; Yesinowski, J. P. *J. Chem. Phys.* **1988**, *89*, 4600.

Chapter 3: Introduction to Solid-State NMR Techniques Used in This Thesis

3.1 Introduction

This chapter outlines specific NMR techniques used throughout this thesis to characterize the structure and dynamics of cathode materials presented in Chapter 1. Rotational-echo, double-resonance (REDOR) measurements are used to reintroduce heteronuclear dipolar couplings that have been averaged by MAS. Measurements of this type allow for relative heteronuclear internuclear distances to be determined and assist in assignment of Li environments. Two-dimensional exchange spectroscopy (2D EXSY) of either ^{6}Li or ^{7}Li nuclei allow for ion-hopping pairs to be identified in samples having more than one non-equivalent crystallographic environment. Application of these experiments over a variable time and temperature range identifies Li ion hopping pairs and subsequent determination of timescales and energy barriers to be determined. This work is complemented by one-dimensional selective inversion studies (1D SI), which are a simpler means to probe ion dynamics than 2D EXSY studies and require considerably smaller amounts of spectrometer time. Overall, the determined ion-hopping timescales are compared between the materials presented in Chapter 1 where a set of structural parameters observed to enhance or inhibit ion mobility is considered.

3.2 REDOR Measurements

3.2.1 Introduction & Motivation

Assignment of ^{6,7}Li NMR resonances to the crystallographic Li sites in paramagnetic materials is an important step towards understanding ion mobility pathways in a host framework. While the Fermi-contact interaction, based on the Goodenough-Kanamori rules, can be used to rationalize the observed shifts using the crystallographic data, NMR experimental tools can be employed to support the assignment.[1-4] Rotational-echo, double-resonance (REDOR) experiments probe the relative internuclear distance between a heteronuclear spin pair, correlating the Li ions to atoms in the host framework.[5,6] REDOR in this thesis is also used to measure Li ion dynamics in $LiFePO_4$, as changes to the Li-P dipolar couplings are attributed to mobility of the Li ion within the framework.[7] In this chapter, ^{6}Li{^{31}P} REDOR measurements of $LiFePO_4$ will be used as an illustrative example, where ^{6}Li is the observed spin and ^{31}P is the dephased nucleus. However, for the Li-fluorophosphate material, Li_2VPO_4F, studied in Chapter 6, ^{6}Li{^{19}F} REDOR measurements are used to support resonance assignments made initially from the Fermi-contact interaction.

3.2.2 ^{6}Li{^{19}F} and ^{6}Li{^{31}P} REDOR Experiments

The basis of the REDOR experiment is the measurement of spectral signal intensity before and after the perturbation of a dipolar coupled heteronuclear partner. **Figure 3.1** shows the dipolar interaction between the local fields of a ^{31}P-^{6}Li spin pair separated by a distance, *r*. Here the *z*-component of the local field of the P nuclei (B^{P}_{loc})

is influenced by the Li-spin, (and *vice-versa*) whereby perturbation of one (in this case ^{31}P) using a 180° (π) pulse results in a change of sign of the ^{31}P local field felt at the ^{6}Li-spin. The resulting ^{6}Li signal is attenutated relative to its magnitude in the absence of ^{31}P perturbation.

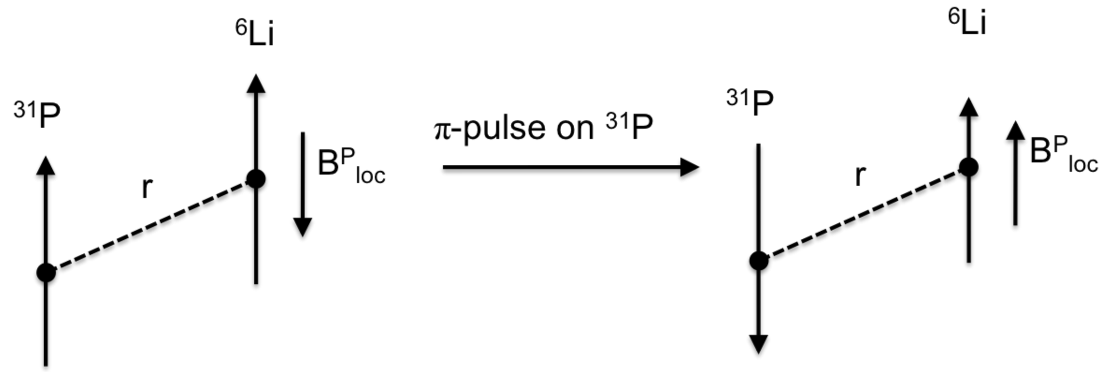

Figure 3.1 – Illustration styled after a figure from Gullion *et al.*[5] showing the influence of the ^{31}P local field on the ^{6}Li spin. Application of a π-pulse on the ^{31}P spin changes the direction of the local field at the ^{6}Li spin, causing an attenuation of the ^{6}Li magnetization aligned along the z-direction.

Initial Spin-Echo, DOuble-Resonance (SEDOR) measurements were applied to stationary samples.[8,9] where the spins being detected (in our case ^{6}Li) are measured first using a spin-echo sequence without perturbation to the heteronuclear spin partner (i.e. ^{31}P) giving rise to a spectrum with intensity S_0 (**Figure 3.2**, top). The ^{6}Li environment is then measured again, but this time with a train of π pulses applied to the ^{31}P spins giving rise to a ^{6}Li spectrum with intensity, S (**Figure 3.2**). The duration between the π-pulses is stepped over a series of experiments to probe dipolar coupling constants of different magnitudes (and therefore a range of internuclear distances). Rotational-Echo, DOuble Resonance measurements were later introduced as an expansion of SEDOR to systems where sample rotation was necessary.[5,6] This is true for our case where MAS is needed to resolve the different crystallographic Li sites. This however averages the orientation dependenece of the dipolar couplings. REDOR therefore synchronizes the spacing of the ^{31}P π-pulses as integer mutiples (N) of the rotor-period (τ_R) which reintroduces the dipolar coupling lost through MAS, while still allowing for distinction between the ^{6}Li peaks.

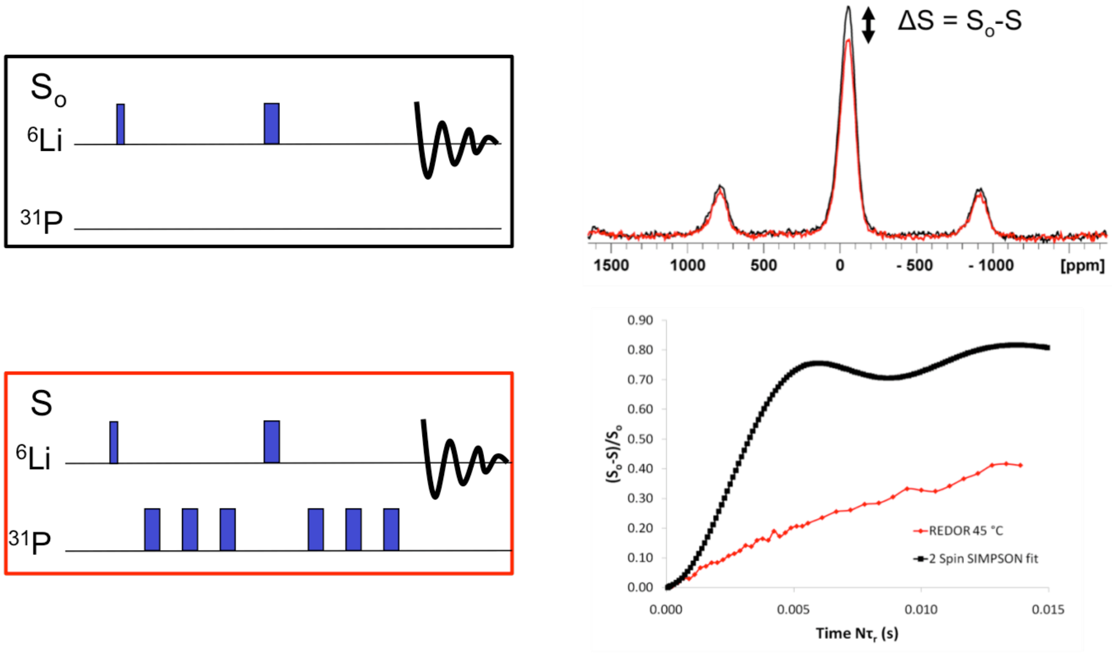

Figure 3.2 – Example of a ^{6}Li{^{31}P} REDOR experiment.

Over a series of experiments, the normalized difference in ^{6}Li signal intensity ($[S_0-S]/S_0$) is measured as a function of the dipolar evolution time ($N\tau_R$). The result is a REDOR buildup curve, shown in **Figure 3.2**, where the strength of the buildup is proportional to the strength of the dipolar coupling. For multi-site materials, this provides a relative picture of which Li resonances have the shortest and longest Li-P or Li-F contacts, and thus assists in the assignment of Li resonances to crystallographic sites in the host framework.

3.2.3 Simulations Using SIMPSON

REDOR experiments are most often used to measure the internuclear distances in materials where crystallographic data is unavailable (such as glasses).[10-14] This is determined by modeling REDOR buildup curves for a given spin system, using a program such as SIMPSON.[15] This program allows the user to refine spin systems, nuclear interactions, RF irradiation, etc. to generate simulated REDOR curves allowing for comparison to the experimental data.

For very complicated spin systems where there is more than one dipolar coupling pair, accurate modeling in SIMPSON presents a challenge. It was shown by Bertmer *et al.*[16], that SIMPSON curves are multi-spin and geometry independent in the initial portion of the buildup curve, where $0 \leq [S_0\text{-}S]/S_0 \leq 0.3$. Moreover, it was later shown that limiting the simulated curve to this region also excluded complications from pulse imperfections and finite pulse length.[17] Therefore, for spin systems studied in this thesis, only the $0 \leq [S_0\text{-}S]/S_0 \leq 0.3$ region of the experimental curve will be considered.

3.2.4 REDOR Measurements of Paramagnetic Materials

A complication that arises in ^{6}Li{^{31}P} REDOR experiments of paramagnetic materials, is that the broad resonances of the ^{31}P and ^{19}F nuclei are often not completely excited by the applied π-pulses. This is demonstrated in **Figure 3.2** where the REDOR buildup of a paramagnetic material is compared with its simulated SIMPSON curve. Even in the $0 \leq [S_0\text{-}S]/S_0 \leq 0.3$ there is considerable deviation of the experimental results from the idealized curve. We therefore only consider REDOR results as relative to one another within a single experiment and do not make absolute determinations of dipolar coupling values and or internuclear distances.

Very short T_2 and T_1 times of paramagnetic resonances leads to loss of magnetization of the perturbed and measured spins at long dipolar evolution times. This further warrants the exclusion of data found beyond the $0 \leq [S_0\text{-}S]/S_0 \leq 0.3$ limit, as magnetization at longer dipolar evolution times is less coherent.

3.2.5 REDOR for Studying Ion Dynamics

Previous studies in our group have evaluated site specific dynamics in monoclinic $Li_3V_2(PO_4)_3$.[7] The study was performed in a temperature range where Li site exchange was known to be "frozen" out based on activation energies determined from 2D NMR exchange studies.[7,18] The observed attenuation of the ^{6}Li{^{31}P} REDOR curve from the static simulated case was therefore attributed to site-specific rattling rather than from Li diffusion. In this thesis, ^{6}Li{^{31}P} REDOR measurements were performed on samples of $LiFePO_4$ in a temperature range where thermally activated Li ion diffusion (rather than site rattling) is observed in other Li intercalation compounds.[18-20] By evaluating this temperature range, thermally activated Li ion mobility in $LiFePO_4$ is monitored as a weakening of the Li-P dipolar couplings resulting in attenuated REDOR buildup curves at higher temperatures.

3.3 ^{6,7}Li MAS Two Dimensional Exchange Spectroscopy

3.3.1 Introduction & Motivation

Two-dimensional exchange spectroscopy (2D EXSY) is used throughout this thesis to identify ion hopping pairs in materials having more than one crystallographically distinct Li environment. These measurements allow for the timescales and energy barriers of the hopping processes to be determined leading to a better understanding of the structural constraints that enhance or inhibit ion mobility. This section provides an introduction to 2D NMR measurements and how they can be used to identify ion hopping pairs and quantify the timescales and energy barriers of the exchange processes.

3.3.2 2D NMR Measurements

Two dimensional NMR measurements were first introduced by Kumar *et al*. in 1975.[21,22] Since then, the field of multi-dimensional NMR spectroscopy has found widespread application in a large range of materials and biomaterials. The basic principle of the 2D NMR experiments is the measurement of two time variables, t_1 and t_2, constituting the observed signal, s, which is Fourier transformed to yield a 2D spectrum with two frequency dimensions, ω_1 and ω_2, respectively.[22,23] The duration of the two time variables is best described by partitioning the 2D experiment into three parts as shown in **Figure 3.3**.[22]

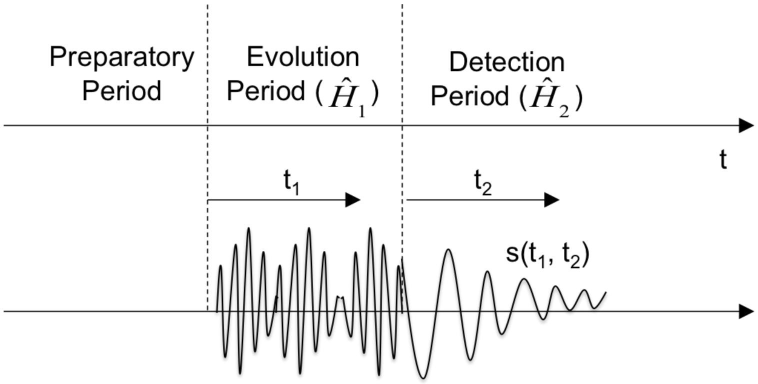

Figure 3.3 – Schematic showing the partitioning of the time axis in a 2D NMR experiment.

The preparatory period allows the system to adjust to an appropriate set of initial conditions. During the evolution period, the system evolves under the first Hamiltonian, $\hat{H}_1$, which defines the time domain, t_1. For the detection period, the spins develop further under the second time domain, t_2, with Hamiltonian, $\hat{H}_2$. During this time the transverse magnetization, $M_{xy}(t_1, t_2)$ (or $s(t_1, t_2)$) is detected and Fourier transformed giving the spectral signal, $S(\omega_1, \omega_2)$. The detection of t_2 is stepped over a series of experiments where t_1 is varied. The resulting 2D spectrum shows t_1 transformed into the indirect dimension (or F1 dimension) and t_2 producing the F2 or direct dimension.

3.3.3 2D NMR to Study Chemical Exchange

To study Li ion hopping in the materials presented in Chapter 1, the 2D Exchange Spectroscopy (EXSY) experiment, proposed by Jeener *et al.*[24] was used (**Figure 3.4**).

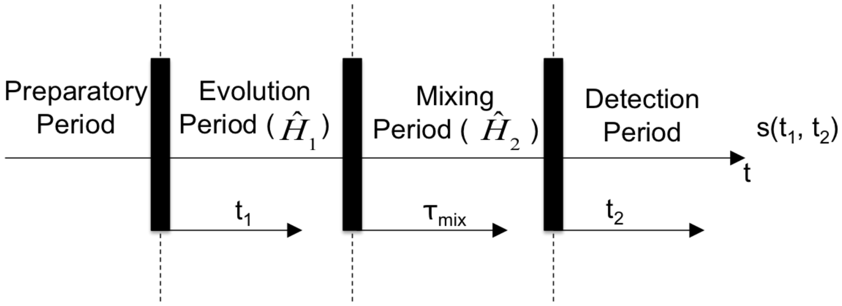

Figure 3.4 – Pulse sequence for a 2D EXSY experiment. 90° pulses are shown as black rectangles.

This experiment is an expansion of the 2D NMR experiment outlined in the previous section but has an added time domain, referred to as the mixing period (τ_{mix}), where the chemical exchange processes are allowed to evolve. The first 90° pulse creates initial transverse magnetization where the spins then evolve at their characteristic precession frequency during t_1 and are stored with their respective "spin label". The second 90° places the magnetization back onto the longitudinal axis, where during the mixing period, the chemical exchange processes take place and the spins acquire the precessional frequency of their new environment. The third 90° places the magnetization back on the *xy*-plane where detection of the new frequency takes place under t_2. The initial spin label, stored under t_1, gives rise to a 2D spectral signal of $S(\omega_1, \omega_1)$, identified as a *diagonal peak*. The signal detected after the mixing period has a 2D spectral signal of $S(\omega_1,\omega_2)$ and is referred to as a *crosspeak* (**Figure 3.5**). Crosspeaks appear on both sides of the diagonal with spectral coordinates of both $S(\omega_1, \omega_2)$ and $S(\omega_2, \omega_1)$. If no exchange takes place, then no crosspeaks evolve under τ_{mix}.

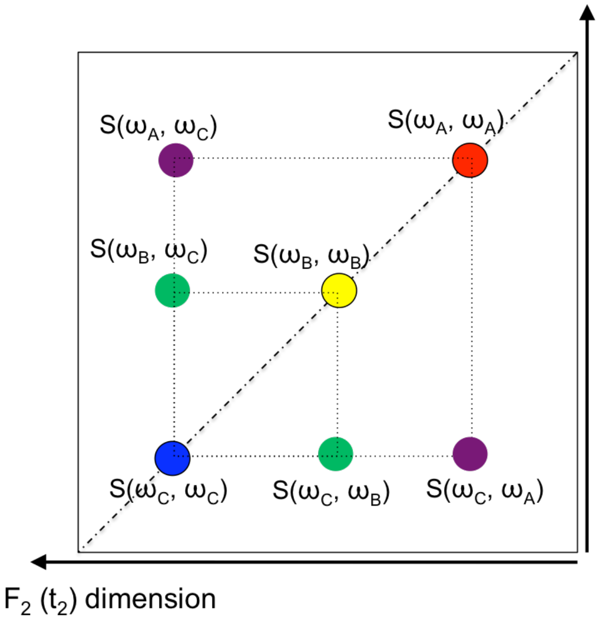

Figure 3.5 – Schematic of a 2D EXSY spectrum for a 3-site material, A, B, and C. Diagonal peaks of the A, B, and C signals stored during F_1 are shown as red, yellow, and blue circles. Crosspeaks evolving from A-C and B-C exchange are shown as green and purple circles on either side of the diagonal region.

A drawback of 2D EXSY measurements appears in systems having slow exchange where single-stage hops are difficult to distinguish from multi-site hops at long mixing times. This is not a problem for two-site materials undergoing a single exchange process, but for the three site example of **Figure 3.5**, at longer mixing times, exchange between A and B could arise from a site hop from A to B to C making an accurate, quantitative determination of the exchange rates difficult.[23] For the present thesis this is not considered an issue as the mixing times in the paramagnetic solids are limited by the short spin-lattice relaxation of the Li ions. It is a more likely scenario in the regime of slow exchange, that analysis is made less accurate by loss of signal intensity at longer mixing times.

3.3.4 Quantification of Ion-Hopping Timescales using 2D EXSY

To determine the timescales of chemical exchange from 2D EXSY measurements in systems undergoing fast ion exchange (such as $Li_3Fe_2(PO_4)_3$, Chapter 5), the mixing time is stepped over a series of experiments and the volume of the crosspeak measured. An exponential buildup of crosspeak volume as a function of mixing time is fit to yield a correlation time, τ_c, of the exchange process. An Arrhenius or Eyring analysis of the inverse correlation times over a variable temperature range produces the energy barrier. Previous work has used 2D $^{6,7}Li$ 2D EXSY as a means to understand and quantify timescales of Li ion exchange of intercalation materials that include Li_4SiO_4,[25] $LiMn_2O_4$,[19] $Li_3V_2(PO_4)_3$[18,20] and more recently Li_3VF_6.[26]

Qualitative ^6Li 2D EXSY measurements are used in Chapters 6, 7, and 8, to identify hopping pairs in Li_2VPO_4F, Li_2VOPO_4, and $Li_5V(PO_4)_2F_2$, respectively. A quantitative analysis of these systems using 2D EXSY was made difficult by the slower exchange times between the ion sites. The short T_1 times of the $^{6,7}Li$ spins limit the mixing times to regions were sufficient buildup of crosspeak intensity as a function of mixing time cannot be reached. While extension of the mixing period beyond the longest T_1 value of the spins is possible, it leads to a more complicated determination of the hopping rates and subsequent energy barriers.[27,28] The next section outlines a set of one-dimensional experiments that overcome this limitation and are a more simplified approach to determining timescales of ion hopping in materials of this type.

3.4 ^{6,7}Li One-Dimensional Selective Inversion Measurements

3.4.1 Introduction & Motivation

The 2D EXSY experiments provide a clear and visually convincing measurement of ion exchange. However, along with the complications imposed by short spin-lattice relaxation, generating enough data to determine the timescales and energy barriers of ion exchange requires hundreds of hours of spectrometer time. It was therefore a goal of this thesis to apply more time and cost effective methods for determining timescales of ion mobility where the short T_1 and T_2 times placed fewer limitations on the data analysis. This led to the use of 1D ^{6,7}Li Selective Inversion (SI) experiments as a means to expand the determination of ion-hopping timescales to more slowly exchanging materials, and also reduce the required spectrometer time to approximately one-fifth what is needed for 2D EXSY experiments. In the 1D measurements, the relaxation of a selectively inverted spin is monitored as function of both the inherent T_1 properties as well as the exchange processes taking place with non-inverted spin(s). Conversely, non-inverted spin(s) showed attenuation of signal intensity as a function of time during the period where ion exchange was the dominant mechanism for relaxation of the inverted spin.[29,30] The experimental data is modeled in a program such as CIFIT to yield accurate exchange timescales.[23,31] CIFIT is a C program based on McClung's SIFIT (Selective Inversion FIT) and is introduced in sub-section 3.4.3.[32]

This section outlines the principles of relaxation of selectively inverted spins as well as highlights the mathematical model used by CIFIT to fit the experimental data and separate the rate constant of exchange from the inherent T_1. ^{6}Li 1D selective inversion experiments are applied to quantify the timescales of ion-hopping in Li_2VPO_4F, Li_2VOPO_4, and $Li_5V(PO_4)_2F_2$ (Chapters 6, 7, and 8, respectively). This is the first application of the SI measurement to paramagnetic systems and subsequently expands the range of materials whose dynamics can be measured. Comparison of timescales arising from different frameworks gives a more comprehensive picture of the structural parameters that enhance or inhibit ion mobility in these electrochemically active materials.

3.4.2 One-Dimensional Selective Inversion Experiments

One-dimensional ^{6}Li Selective Inversion methods are relaxation-type experiments that monitor the effect of a chemical exchange process (or processes) on the magnetization's return to equilibrium. This experiment works by selectively inverting a site known to undergo exchange ion exchange with other spins in the lattice. The return to equilibrium of the inverted site is measured as a function of time (in this study it is termed the mixing time, τ_{mix}). In a multi-spin system, a selectively inverted spin (*i*) will relax (R) due to the combined effects of inherent spin-lattice (T_1) relaxation time as well as the sum of the rate constants (k) associated with each exchange process taking place with the measured spin (Equation 3-1).[33]

$$R_i = \frac{1}{T_{1i}} + \sum_{i \neq j} k_{ij}$$

Equation 3-1

Conversely, the non-inverted spin(s) (*j*) will experience an attenuation of signal intensity as a function of mixing time during the period where chemical exchange is taking place. This results in a characteristic "transient" curve for the non-inverted spin. This is shown in **Figure 3.6** for the selective inversion experiment of a two site, A-B system. Here A is the inverted site with both signals measured over a mixing time range of 5 μs to 150 ms.

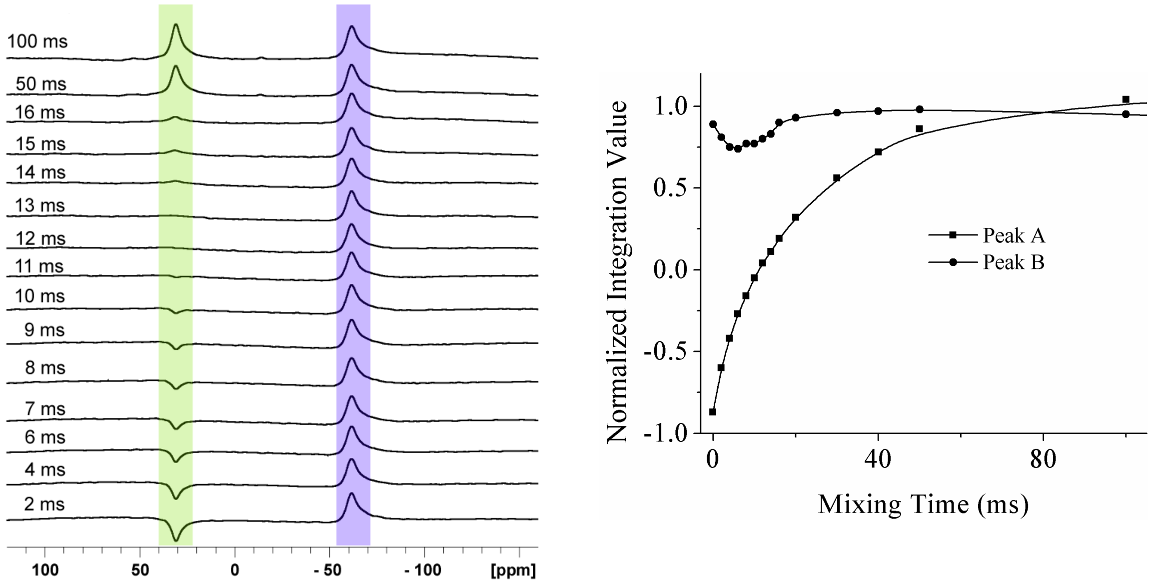

Figure 3.6 – Example of data collected using ^{6}Li SI experiments over a variable mixing time range. Inversion of Peak A (highlight in green) returns to equilibrium due to the combined effects of inherent T_1 as well as exchange with Peak B (highlighted in purple). This results in a characteristic "transient" curve for Peak B (left). Error bars on the integration values are within the size of the data points.

The initial portions of the buildup and transient curves are governed by the rate of the ion hopping process. The latter portion of the curves is dominated by the inherent T_1 of the spins. The rate information is separated from the T_1 properties by fitting the data to a simulated curve generated through a program such as CIFIT.[33] The mathematical model utilized by CIFIT for accurate determination of these parameters is outlined in section 3.4.3.

The experimental picture of a selective inversion measurement is illustrated in **Figure 3.7**. The initial inversion step is followed by a mixing period where the chemical exchange processes take place, similar to 2D EXSY measurements. Signals from both the inverted and non-inverted sites are measured as a function of mixing time over a series of 1D experiments. In this thesis, two pulse sequences having different inversion methods were used for measurement of timescales and energy barriers of ion hopping in a series of materials. The details of these methods are given in sections 3.4.4.1 and 3.4.4.2.

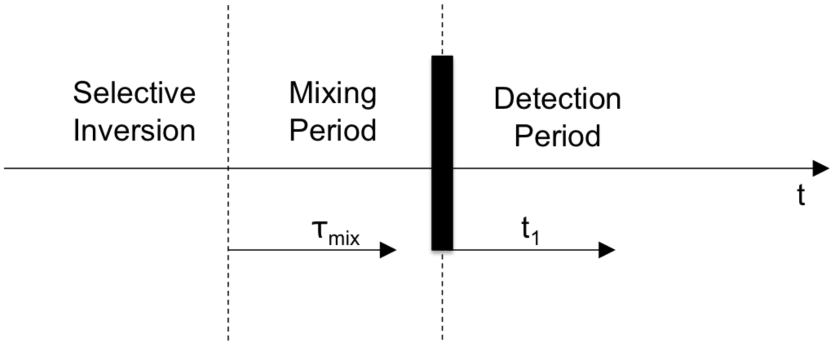

Figure 3.7 – Schematic showing the basic principle of a selective inversion experiment. The selective inversion period creates the initial conditions where one of the environments known to undergo ion-exchange is selectively inverted. This is followed by the mixing period where the return to equilibrium of the inverted peak is measured as a function of time. Detection of the signal at different mixing times gives rise to a buildup curve of the inverted site and transient curve(s) for non-inverted spin(s).

3.4.3 CIFIT

CIFIT takes a table of observed intensities for all spins as a function of mixing time and determines a key set of parameters: the jump rate (k) of each chemical exchange process, spin-lattice relaxation times in the absence of chemical exchange (T_1), and the magnetization values from initial to equilibrium conditions (i.e. from $M_i(0)$ to $M_i(\infty)$) The primary mathematical model used by the CIFIT program is a rate matrix describing the relaxation of magnetization for a system with *n* sites (Equation 3-2).

$$\begin{pmatrix} M_1(\infty)-M_1(t) \\ \vdots \\ M_n(\infty)-M_n(t) \end{pmatrix} = \exp(-\mathbf{A}t) \begin{pmatrix} M_1(\infty)-M_1(0) \\ \vdots \\ M_n(\infty)-M_n(0) \end{pmatrix} \qquad \text{Equation 3-2}$$

where,

$$\mathbf{A} = \begin{pmatrix} R_{11} & -k_{21} & -k_{31} & \cdots & -k_{n1} \\ -k_{12} & R_{22} & -k_{32} & \cdots & -k_{n2} \\ -k_{13} & -k_{23} & R_{33} & \cdots & -k_{n3} \\ \vdots & \vdots & \vdots & \ddots & \vdots \\ -k_{1n} & -k_{2n} & -k_{3n} & \cdots & R_{nn} \end{pmatrix} \qquad \text{Equation 3-3}$$

and where the relaxation (R_{nn}) is defined as the T_1 of the n^{th} spin plus the sum of the rates for each exchange process in which that spin participates (Equation 3-1).

To simplify this analysis for the 2-spin example of an ion hopping process, introduced in **Figure 3.6**, we will first define both the exchange process and the equilibrium expression (Equation 3-4 and Equation 3-5, respectively).

$$A \underset{k_{BA}}{\overset{k_{AB}}{\rightleftharpoons}} B \qquad \text{Equation 3-4}$$

$$K = \frac{[B]}{[A]} \qquad \text{Equation 3-5}$$

where k_{AB} is the rate constant for the forward hop from A to B, and k_{BA} describes the reverse hop. The solution to the exchange matrix is now simplified to give Equation 3-6

$$\begin{pmatrix} M_A(\infty) - M_A(t) \\ M_B(\infty) - M_B(t) \end{pmatrix} = \exp\left(A_{AB}t\right)\begin{pmatrix} M_A(\infty) - M_A(0) \\ M_B(\infty) - M_B(0) \end{pmatrix} \qquad \text{Equation 3-6}$$

where,

$$A_{AB} = \begin{pmatrix} -\frac{1}{T_{1(A)}} - k_{AB} & k_{BA} \\ k_{AB} & -\frac{1}{T_{1(B)}} - k_{BA} \end{pmatrix} \qquad \text{Equation 3-7}$$

When the concentrations of the two spins are equal, and the system has reached equilibrium, the rates of the forward and reverse processes are equal. The rate constants (k_{AB} and k_{BA}), therefore, will be equal as well. It is now more convenient to evaluate the exchange process from the standpoint of the equilibrium constant (K) rather than the rate constants themselves. The solution to the exchange matrix can then be written where T_1 relaxation is now ignored and the rate is fit as a single parameter (Equation 3-8).

$$\frac{\partial}{\partial t}\begin{pmatrix} M_A(\infty)-M_A(t) \\ M_A(\infty)-M_A(t) \end{pmatrix} = -k_{AB}\begin{pmatrix} K & -1 \\ -K & 1 \end{pmatrix}\begin{pmatrix} M_A(\infty)-M_A(t) \\ M_B(\infty)-M_B(t) \end{pmatrix} \qquad \text{Equation 3-8}$$

CIFIT works to adjust this mathematical model until the sum of the squares of the differences between the experimental and modeled data is minimized.

3.4.4 Experimental Methods For Selective Inversion

In this thesis, two experimental methods were used to selectively invert ^{6}Li spins known to undergo ion hopping with non-equivalent Li partners. The first inversion method evaluated is referred to as 1D EXSY and is limited to 2-site exchange systems. It is the method applied to determine the timescales and energy barriers of ion hopping in the 2-site Li_2VPO_4F (Chapter 6). The second method uses a Gaussian Shaped Pulse (SP) which is placed on resonance to a site chosen for selective inversion. This method is applicable to multi-exchange systems and is therefore used to study ion hopping timescales in the 3-site Li_2VOPO_4 (Chapter 7) and 6-site $Li_5V(PO_4)_2F_2$ (Chapter 8).

3.4.4.1 ^{6}Li 1D EXSY

Figure 3.8 illustrates the pulse sequence for selective inversion using the 1D EXSY method. Selective inversion is accomplished during the $90° - \tau_1 - 90°$ step where the carrier frequency is set on-resonance to the site chosen for inversion (*i*). The delay period, τ_1, is dependent on the frequency difference between the site of inversion (*i*) and its exchange partner (*j*) (specifically, $1/[2\Delta\nu_{ij}]$).[29,30,34] The on-resonance spin is selectively inverted following the second 90° pulse, while its exchange partner is placed along the +*z*-axis. The mixing time (τ_{mix}) is stepped over a series of experiments with the latter delay time being long enough to ensure relaxation back to equilibrium. Due to the dependence of τ_1 on the frequency difference between the two spins, it is not possible to extend this inversion technique beyond a 2-site, 1-exchange process system, as the initial conditions of a third site are not established. The next section discusses an inversion method that allows for systems having a higher number of ion-hopping processes to be measured.

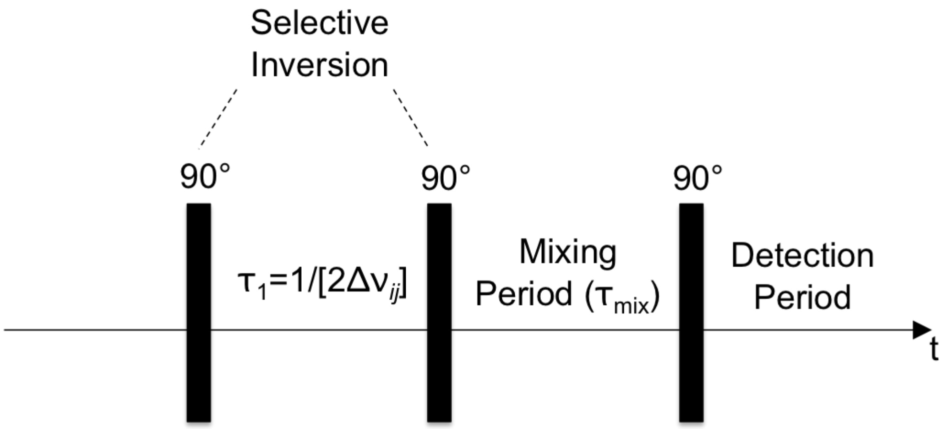

Figure 3.8 – Schematic showing the pulse sequence for a 1D EXSY experiment.

3.4.4.2 Selective Inversion Using Shaped Pulse

A second inversion method, familiar to the solution-state NMR community, is used to expand SI experiments to materials studied in this thesis that have multiple-exchange pairs.[31,33,35,36] Here the initial 90° - τ_1 - 90° of the 1D EXSY sequence, is replaced with one long, soft, Gaussian pulse, placed on-resonance to the site chosen for inversion (**Figure 3.9**). The bandwidth of the Gaussian pulse ensures inversion of only one of the sites undergoing ion exchange, leaving all other sites unperturbed. This experimental approach will be referred to as the Shaped Pulse (SP) method. A drawback to this method is that the shaped pulse can become very long (500 μs to 1 ms) for the desired bandwidth to be reached. In paramagnetic systems these pulse lengths are on the order of the relaxation time of the spin-chosen for inversion, and competition between complete inversion and relaxation results. Chapter 7 elaborates on this topic through the ^{6}Li 1D SP study of Li_2VOPO_4 and the comparative ^{6}Li 1D EXSY versus ^{6}Li 1D SP study of Li_2VPO_4F

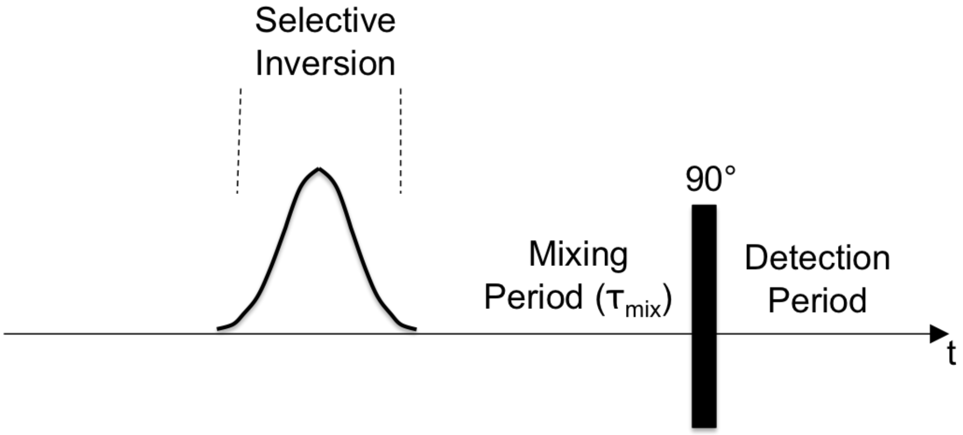

Figure 3.9 – Schematic showing the pulse sequence for selective inversion where a shaped pulse is employed to selectively invert an on-resonance pulse.

Chapter 7 uses the 3-site material, Li_2VOPO_4, to illustrate how the AB, AC, and BC hopping rates constant can be determined accurately from separate experiments where either A, B or C is inverted. Chapter 8 extends the method to a more complicated spin system, $Li_5V(PO_4)_2F_2$ where due to low resolution, only one site in an exchange pair can be selectively inverted.

Overall, the use of selective inversion experiments results in the timescales and energy barriers to be determined in materials that are of considerable interest for battery applications.

3.5 Summary

In this thesis, a combination of the three experimental methods described above is used to identify and quantify the structural and dynamic features of cathode materials for

Li ion batteries. Gathering this information for a series of Li-intercalation materials allows for a comparison of key parameters that inhibit or enhance Li ion mobility. These parameters include ion internuclear distance, area of the bottleneck for diffusion, as well the bond sum valence of the ions. $^{6}Li\{^{31}P\}$ and $^{6}Li\{^{19}F\}$ REDOR measurement are employed for Li site assignments as well providing a qualitative look at changes to dipolar couplings brought on by ion mobility in Li_2VPO_4F and $LiFePO_4$, respectively. ^{6,7}Li 2D EXSY experiments are used to identify and quantify timescales of ion exchange in many of the multi-Li site materials including $Li_3Fe_2(PO_4)_3$. Lastly, 1D ^{6,7}Li selective inversion measurements are investigated for quantification of timescales of exchange in Li_2VPO_4F, Li_2VOPO_4, and $Li_5V(PO_4)_2F_2$. This is shown to be a more accurate and time efficient method for determining these values than analogous 2D EXSY experiments.

3.6 References

(1) Goodenough, J. B. *J. Phys. Chem. Solids* **1958**, *6*, 287.

(2) Kanamori, J. *Progress in Theoretical Physics* **1957**, *17*, 177.

(3) Carlier, D.; Menetrier, M.; Grey, C. P.; Delmas, C.; Ceder, G. *Phys. Rev. B* **2003**, *67*, 174103.

(4) Grey, C. P.; Dupre, N. *Chem. Rev.* **2004**, *104*, 4493.

(5) Gullion, T. *Concepts in Magnetic Resonance* **1998**, *10*, 277

(6) Gullion, T.; Schaeffer, J. *J. Magn. Reson.* **1989**, *81*, 196

(7) Cahill, L. S.; Kirby, C. W.; Goward, G. R. *J. Phys. Chem. C* **2008**, *112*, 2215.

(8) Kaplan, D. E.; Hahn, E. L. *Journal de Physique et le Radium* **1958**, *19*.

(9) Shore, S. E.; Ansermet, J. P.; Slichter, C. P.; Sinfelt, J. H. *Phys. Rev. Lett.* **1987**, *58*, 953.

(10) van Wullen, L.; Eckert, H.; Schwering, G. *Chem. Mater.* **2000**, *12*, 1840.

(11) Ratai, E.; Chan, J. C. C.; Eckert, H. *Phys. Chem. Chem. Phys.* **2002**, *4*, 3198.

(12) Strojek, W.; Eckert, H. *Phys. Chem. Chem. Phys.* **2006**, *8*, 2276.

(13) Zhang, L.; Eckert, H. *J. Phys. Chem. B* **2006**, *110*, 8946.

(14) Zhang, L.; de Araujo, C. C.; Eckert, H. *J. Phys. Chem. B* **2007**, *111*, 10402.

(15) Bak, M.; Rasmussen, J. T.; Nielsen, N. C. *J. Magn. Reson.* **2000**, *147*, 296.

(16) Bertmer, M.; Eckert, H. *Solid State Nucl. Magn. Reson.* **1999**, *15*, 139.

(17) Chan, J. C. C.; Eckert, H. *J. Magn. Reson.* **2000**, *147*, 170.

(18) Cahill, L. S., Chapman, R. P., Britten, J. F., Goward, G. R. *J. Phys. Chem. B* **2006**, *110*, 7171.

(19) Verhoeven, V. W. J.; de Schepper, I. M.; Nachtegaal, G.; Kentgens, A. P. M.; Kelder, E. M.; Schoonman, J.; Mulder, F. M. *Phys. Rev. Lett.* **2001**, *86*, 4314

(20) Davis, L. J. M.; Heinmaa, I.; Goward, G. R. *Chem. Mater.* **2010**, *22*, 769.

(21) Kumar, A.; Welti, D.; Ernst, R. R. *J. Magn. Reson.* **1975**, *18*, 69.

(22) Aue, W. P.; Bartholdi, E.; Ernst, R. R. *J. Chem. Phys.* **1976**, *64*, 2229.

(23) Bain, A. D. *Prog. Nucl. Magn. Reson. Spectrosc.* **2003**, *43*, 63.

(24) Jeener, J.; Meier, B. H.; Bachmann, P.; Ernst, R. R. *J. Chem. Phys.* **1979**, *71*, 4546.

(25) Xu, Z.; Stebbins, J. F. *Science* **1995**, *270*, 1332.

(26) Wilkening, M.; Romanova, E. E.; Nakhal, S.; Weber, D.; Lerch, M.; Heitjans, P. *J. Phys. Chem. C* **2010**, *114*, 19083.

(27) Perrin, C. L.; Dwyer, T. J. *Chem. Rev.* **1990**, *90*, 935.

(28) Perrin, C. L. *J. Magn. Reson.* **1989**, *82*, 619.

(29) Forsen, S.; Hoffman, R. A. *J. Chem. Phys.* **1963**, *39*, 2892.

(30) Forsen, S.; Hoffman, R. A. *J. Chem. Phys.* **1964**, *40*, 1189.

(31) Bain, A. D.; Fletcher, D. A. *Mol. Phys.* **1998**, *95*, 1091.

(32) Muhandiram, D. R.; McClung, R. E. D. *J. Magn. Reson.* **1987**, *71*, 187.

(33) Bain, A. D.; Cramer, J. A. *J. Magn. Reson. Ser. A* **1996**, *118*, 21.

(34) Hampson, M. R.; Evans, J. S. O.; Hodgkinson, P. *J. Am. Chem. Soc.* **2005**, *127*, 15175.

(35) Led, J. J.; Gesmar, H. *J. Magn. Reson.* **1982**, *49*, 444.

(36) Bauer, C.; Freeman, R.; Frenkiel, T.; Keeler, J.; Shaka, A. J. *J. Magn. Reson.* **1984**, *58*, 442.

Chapter 4: Solid-State NMR Studies of the Olivine Family of Phosphate Cathode Materials

4.1 Introduction

This chapter is compromised of three sections that all together present results from ^{6,7}Li and ^{31}P MAS NMR measurements of olivine $LiMnPO_4$ and Li_xFePO_4 (x= 0, 0.5, 1.0). The first section details a comparison of the ^{7}Li and ^{31}P MAS spectra of $LiMnPO_4$ and $LiFePO_4$ phases where the different electron configurations at the transition metal center give very different spectra for these isostructural materials. The second section briefly discusses the challenges encountered when determining properties of ion mobility in the olivine phases as only a single crystallographic Li site is present and these phases are highly paramagnetic. The last section details the characterization of Li environments and phase transformations in 50% delithiated $0.5LiFePO_4$:$0.5FePO_4$. Here, the transformation of a biphasic $0.5LiFePO_4$:$0.5FePO_4$ material to the solid solution $Li_{0.5}FePO_4$ at high temperature is shown using ^{31}P static measurements.

The bulk of this latter section was published in *Physical Chemistry Chemical Physics* (**2011**, *13*, 5171-5177) with co-authors I. Heinmaa, B. L. Ellis, L.F. Nazar, and G.R. Goward. Brian Ellis prepared samples of $LiFePO_4$ (x = 0.0, 0.5, and 1.0) in the research lab of Prof. Nazar at the University of Waterloo. Ivo Heinmaa supervised NMR collection at the National Institute of Chemical Physics and Biophysics (NICPB) in Tallinn, Estonia. Prof. Goward was the principal investigator of this project.

4.2 Experimental

4.2.1 Sample Preparation

Samples studied in this thesis were prepared at McMaster University and also by collaborators at the University of Waterloo. Samples prepared at the University of Waterloo include Li_xFePO_4 (where x = 0.0, 0.5, 1.0). Here natural abundance olivine $LiFePO_4$ (92.58% ^{7}Li, 7.42% ^{6}Li) samples were prepared *via* a modified hydrothermal synthesis first described by Yang *et al.*[1] Briefly, $(NH_4)_2Fe(SO_4)_2{\bullet}6H_2O$ (Alfa Aesar), H_3PO_4 (Fisher), $LiOH{\bullet}H_2O$ (Alfa Aesar) and ascorbic acid (Sigma Aldrich) were combined in a 1:1:3:0.1 molar ratio and the reagents were stirred in a sealed 45 ml Parr autoclave at 190˚C for 8 hours. The ascorbic acid acts as an *in situ* reducing agent.[2] The solid product was filtered and dried under vacuum at 90°C for 18 hours. The as-prepared $LiFePO_4$ was oxidized to various compositions of $xLiFePO_4$:(1-x)$FePO_4$ (x = 0.5, 0.0) using *x* $NOBF_4$. The reagents were stirred in acetonitrile under an inert atmosphere for one hour. X-ray diffraction was performed on a Bruker D8-Advance powder diffractometer using Cu-Kα radiation (l = 1.5405Å) from 2θ = 10 to 70 degrees at a count rate of 1 sec per step of 0.02°. The reflections were indexed using DICVOL91 software. $LiFePO_4$ samples were gold coated and examined in a LEO 1530 field emission scanning electron microscope (FESEM) instrument equipped with an energy dispersive X-ray spectroscopy (EDX) attachment. Images were recorded at 15 kV with a back-scatter electron detector.

$LiMnPO_4$ and ^6Li enriched $LiFePO_4$ for $^6Li\{^{31}P\}$ REDOR measurements were prepared at McMaster University *via* the hydrothermal methods of Yang *et al.*[1] The starting materials, $MnSO_4{\cdot}H_2O$, $FeSO_4{\cdot}7H_2O$ (98% Sigma Aldrich), H_3PO_4 (85% Fisher), LiOH (^6Li enriched, 99 %), and ascorbic acid (Aldrich) were combined in a ratio of 3:1:1:0.1 with water added to make a 67% filled volume. ^6Li-enriched samples were prepared using ^6LiOH prepared in house (Cambridge isotopes ^6Li metal). The concentration of $MSO_4{\cdot}xH_2O$ was 0.75 M to ensure smaller particle size.[3] Samples were sealed in a 23 ml Parr reactor and placed in an oven for 5 hours at 190^{o}C. Final products were collected by vacuum filtration and dried at 60 ^{o}C under vacuum. Samples were characterized using a PANalytical diffractometer with Cu-Kα radiation ($\lambda = 1.5406$ Å). Data was collected from 15 – 70 ° in 2θ step size of 0.008 with a step time of 100 s. The reflections were indexed in agreement with the literature.[4]

4.2.2 Solid-State NMR

NMR measurements were carried out at both McMaster University and the National Institute for Chemical Physics and Biophysics (NICPB) in Tallinn, Estonia. Measurements carried out at McMaster University include room temperature 1D ^7Li and ^{31}P MAS measurements of $LiFePO_4$ and $LiMnPO_4$ presented in Sections 4.3.1, 4.3.4, and 4.3.4.1. Here, a Bruker AV300 spectrometer was used with ^{31}P and ^7Li Larmor frequencies of 121.8 MHz and 116.64 MHz, respectively. MAS measurements were made using a custom-built 1.8 mm probe with spinning speeds of 25 or 40 kHz. ^7Li and ^{31}P 1D spectra were acquired using a Hahn-echo pulse sequence ($90° - \tau - 180°$) with 90° pulses ranging from 2.0 to 2.5 μs and recycle delays of 50-200 ms. Spin-lattice relaxation times were acquired using a spin inversion recovery pulse sequence, with a variable delay list stepped over 16 experiments from 5 μs to 150 ms.

^{6}Li{^{31}P} REDOR (section 4.3.2) and ^{31}P static high temperature experiments (section 4.3.3) were carried out at the NICPB on a Bruker AMX200 spectrometer. For the REDOR measurements a custom-built double resonance wide bore probe supporting 1.8 mm rotors capable of MAS frequencies up to 45 kHz was used. ^{6}Li{^{31}P} REDOR spectra of $LiFePO_4$ were collected at MAS = 25.021 (± 0.002) kHz with a ^{31}P 180° pulse of 3.5 μs and ^{6}Li 90° pulse length of 3 μs. Spectra were collected with 600 scans and recoupling times ($N\tau_R$) incremented in 4 rotor period steps starting at N = 4 up to N = 256. This gave a maximum recoupling time of 10 ms. The ^{31}P CSAs were determined using the DMFIT program[5] with the result confirmed using a Herzfeld-Berger analysis program developed by K. Eichele and R. Wasylishen.[6,7] REDOR buildup curves were simulated using the SIMPSON (version 1.1.1) simulation program.[8]

High temperature static ^{31}P measurements were carried out on a custom built wide-bore, static, solid-state NMR probe able to reach temperatures up to 500 °C. Samples were sealed in a quartz ampoule and heated under flowing nitrogen. Temperatures were calibrated using $Pb(NO_3)_2$ as described elsewhere.[9] For all experiments, ^{7}Li shifts were referenced to 1M LiCl (0 ppm) and ^{31}P shifts were referenced to 85% H_3PO_4 (0 ppm). Due to the width of the total resonance being considerably larger than the excitation bandwidth of the ^{31}P pulse, the ^{31}P spectra were frequency-stepped over a total range of 450 kHz with a step size of 50 kHz with 16000 scans and SW of 1 MHz for each sub-spectrum. The sub-spectra were added in Topspin 2.1 to give the total spectrum.

4.3 Results and Discussion

4.3.1 ^{7}Li and ^{31}P MAS NMR of $LiMnPO_4$ and $LiFePO_4$.

In this section, the ^{7}Li and ^{31}P MAS spectra of both $LiMnPO_4$ and $LiFePO_4$ are presented. The olivine phase of cathode materials, $LiMPO_4$ (M = Mn, Fe), have received significant attention as the most commercially viable cathode materials for low-cost Li ion battery applications. Since its introduction in 1997, the landmark communication outlining the synthesis and electrochemical cycling of $LiFePO_4$ has been referenced in well over 1500 publications.[10] The high theoretical capacity, excellent reversibility, and low environmental impact make it a promising material for battery applications. As outlined in Chapter 1, the high thermal and electrochemical stability results from the strong covalent bonding of oxygen within the PO_4^{3-} moieties leaving very open channels for Li ion diffusion.[11] $LiMnPO_4$ offers higher ion conductivity as well as a higher redox potential of 4.1 V when compared to $LiFePO_4$.[12] However, the Jahn-Teller distortions around Mn^{3+} lead to poor reversibility making $LiMnPO_4$ the less preferred material for electrochemical applications.

Figure 4.1 shows the ^{7}Li MAS spectra of $LiMnPO_4$ and $LiFePO_4$ at MAS speed of 25 kHz. For $LiMnPO_4$ a higher ^{7}Li MAS paramagnetic shift (75 ppm) and larger spinning sideband manifold (Ω = 440 kHz) is attributed to an additional unpaired electron in the t_{2g} orbital as compared to $LiFePO_4$ which has $\delta_{iso} = -11$ ppm and Ω = 275 kHz.

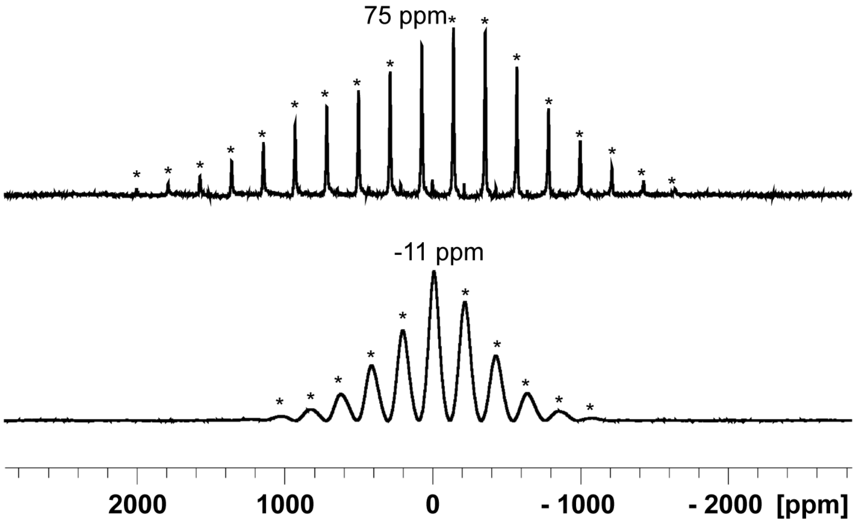

Figure 4.1 - ^{7}Li MAS NMR (25 kHz) of isostructural $LiMnPO_4$ (top) and $LiFePO_4$ (bottom). Asterisks denote spinning sidebands. This figure illustrates the changes to the Li environment when the redox center changes from a $t_{2g}^4e_g^2$ ($LiFePO_4$) to a $t_{2g}^3e_g^2$ ($LiMnPO_4$)

The Full-Width at Half-Maximum (FWHM) of the isotropic peak for $LiMnPO_4$ is 500 Hz whereas for $LiFePO_4$ it is much more broad at 9500 Hz. As outlined in Chapter 2, the lineshape in paramagnetic systems has contributions from both the hyperfine coupling value ($A/\hbar$) and the spin-lattice relaxation of the electrons (T_{1e}) to which the nucleus is coupled. This relationship is presented here again in Equation 4-1.[13,14]

$$FWHM = \frac{1}{T_{2N}} = \frac{1}{T_{2a,b}} + \frac{(A/\hbar)^2 T_{1e}}{8} \qquad \text{Equation 4-1}$$

The first portion of Equation 4-1, ($1/T_{2a,b}$), is governed by the the transverse relaxation terms arising from effects other than those induced by interaction with a paramagnetic metal center. This has a significantly smaller contribution than the portion containing terms associated with the unpaired electron spin density sitting on the metal center (T_{1e}, and the hyperfine coupling constant, $A/\hbar$).[14] Previous studies have measured the hyperfine coupling constants for both $LiMnPO_4$ and $LiFePO_4$ (0.86×10^6 rad/s and -0.48×10^6 rad/s, respectively).[15] The larger $A/\hbar$ value for $LiMnPO_4$ does not appear to affect the FWHM as this would lead to a broader resonance in the Mn materials over the Fe analogue. Therefore, the greater resolution in the $LiMnPO_4$ ^7Li spectrum is due to the shorter T_{1e} times of the spin density on the metal center as compared to $LiFePO_4$.

Similar trends for δ, FWHM, and Ω, were observed in the ^{31}P MAS spectra of the Mn and Fe phases (**Figure 4.2**). An isotropic ^{31}P shift of 7600 ppm is observed in $LiMnPO_4$ at almost 4000 ppm higher frequency than $LiFePO_4$ with $\delta = 3800$ ppm. The $LiMnPO_4$ ^{31}P FWHM is 7600 Hz while the span of the manifold, Ω, is 450 kHz. The $LiFePO_4$ ^{31}P MAS spectrum has a larger FWHM of 11600 Hz but a smaller sideband manifold of 300 kHz. Again, the T_{1e} dominates the isotropic lineshape while the total electron spin density dominates the sideband manifolds and paramagnetic shift.

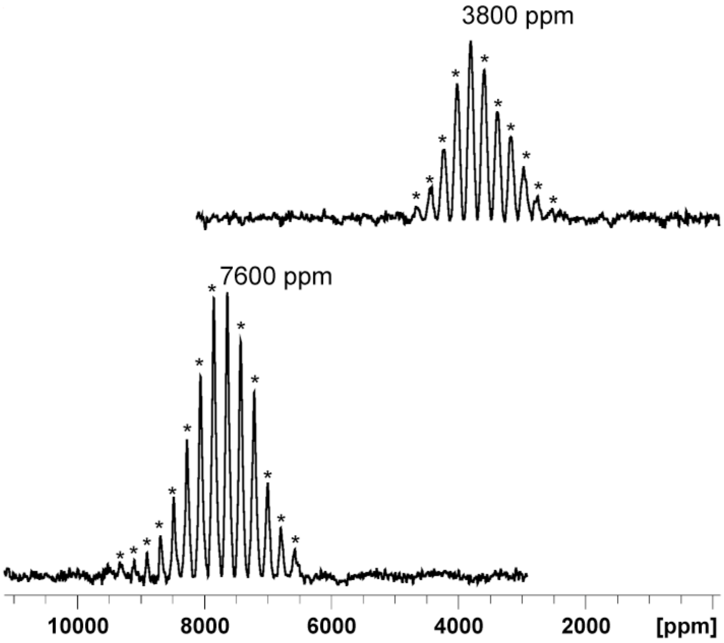

Figure 4.2 – ^{31}P MAS spectra of $LiFePO_4$ (top) and $LiMnPO_4$ bottom, with MAS speed of 25 kHz. Isotropic shifts values are given for each phase with sidebands denoted with asterisks.

4.3.2 Studying Li Dynamics in the Olivine Phases.

Here the ion dynamics in $LiFePO_4$ are investigated using $^{6}Li\{^{31}P\}$ REDOR measurements of ^{6}Li enriched samples of $LiFePO_4$. Extracting timescales of Li ion mobility is an important step towards understanding the conductivity restrictions within these phases however, many challenges are present when trying to identify and quantify Li ion mobility in the olivine phases. Firstly, the presence of a single crystallographic site means that ion mobility measurements that rely on the movement of the Li ions from one crystallographic site to another are not possible. This includes the 2D EXSY and 1D selective inversion measurements used extensively in subsequent chapters, where materials having more than one crystallographic Li site are studied. In diamagnetic systems, dynamics of single-site materials can be quantified by measuring changes in the FWHM (or $1/T_2$) mobile ion lineshape as a function of temperature.[16] This relationship is presented in (Equation 4-2).

$$k = \frac{1}{\pi T_2^*} \qquad \text{Equation 4-2}$$

Where the rate constant, k, is proportional to $1/T_2^*$ which is the FWHM of a resonance with the inhomogeneity of the magnetic field taken into account. The contributions to T_2^* in a diamagnetic system include heteronuclear and homonuclear dipolar couplings meaning that changes in the FWHM reflect changes to the average homo- or heteronuclear internuclear distances brought on by dynamics of the mobile species. As demonstrated previously, the FWHM in paramagnetic systems has contributions from both T_{1e} and the hyperfine coupling between the nucleus measured and the unpaired electron spin density on the transition metal center (Equation 4-1). The temperature dependent changes of the hyperfine coupling (due to Curie-Weiss changes to the magnetic susceptibility)[17] means that any observed changes in the FWHM of a paramagnetic resonance are likely arising not only due to changes in the nuclear dipolar couplings but also due to changes in the magnetic susceptibility of the metal center.

For the olivine phases, alternative methods to probe changes to the heteronuclear couplings resulting from movement of the mobile ion were investigated and some preliminary results are presented here. As outlined in Chapter 3, ^{6}Li{^{31}P}REDOR reintroduces ^{6}Li-^{31}P dipolar couplings that are averaged out through MAS. The observed nucleus (^{6}Li) is measured using a spin-echo sequence with (S) and without (S_0) the application of a series of π pulses on the dephased nucleus (^{31}P). The normalized difference in ^{6}Li signal intensity ($[S_0\text{-}S]/S_0$) is then plotted as a function of the dipolar evolution time ($N\tau_R$ = number of rotor periods times the rotor period). This experiment is more often used to determine internuclear distances in systems where diffraction studies are not possible. For our purposes, this technique is applied over a variable temperature range to monitor changes to the ^{6}Li-^{31}P dipolar coupling brought on by mobility of the Li ion. Previous studies in our group have evaluated site specific dynamics in the cathode material $Li_3V_2(PO_4)_3$.[18] The study of $Li_3V_2(PO_4)_3$ was performed in a temperature range where Li site exchange was known to be "frozen" out based on activation energies determined from 2D NMR exchange studies.[18,19] The observed attenuation of the ^{6}Li{^{31}P} REDOR curve from the static simulated case was therefore attributed to site specific rattling rather than from Li diffusion. For the present study, ^{6}Li{^{31}P} REDOR measurements were performed in a temperature range where thermally activated Li ion diffusion (rather than site-rattling) is observed in related Li-intercalation compounds.[19-21]

Experimental ^{6}Li{^{31}P} REDOR curves were therefore measured over a temperature range of 250 K to 350 K with MAS of 25 kHz. Several complications arise from the broad paramagnetic ^{31}P resonance which must be accounted for within this set of experiments. A 1D ^{31}P MAS spectrum was collected for each temperature at which a ^{6}Li{^{31}P} REDOR experiment was acquired. It is clear from **Figure 4.3** that the ^{31}P isotropic shift moves to lower frequency as the temperature is increased. This is consistent with Curie-Weiss changes to the magnetic susceptibility in paramagnetic materials where, in this temperature range, there is a near linear dependence (**Figure 4.3** inset) of the shift on sample temperature.[17]

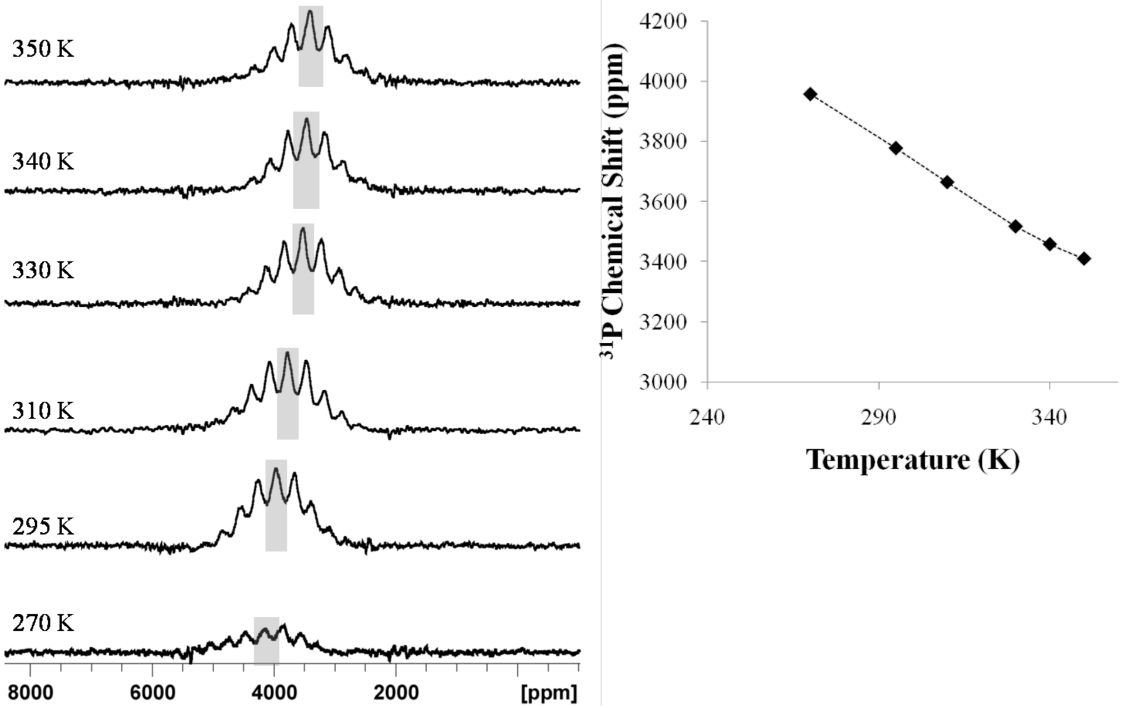

Figure 4.3 – Changes to the ^{31}P MAS resonance of $LiFePO_4$ as a function of temperature.

Due to the migration of the resonance, the frequency of the ^{31}P π pulse was adjusted for each REDOR experiment such that the excitation was on resonance (**Table 4.1**). **Figure 4.4** shows the ^{6}Li{^{31}P} REDOR buildup curves acquired over a variable temperature range (250 K to 350 K).

Table 4.1 - Summary of changes to transmitter frequency due to migration of the ^{31}P resonance as temperature is increased.

Temperature (K)	^{31}P π transmitter frequency (MHz)
270	81.3173770
298	81.3060000
310	81.2870000
330	81.2667129
340	81.2615890
350	81.2579238

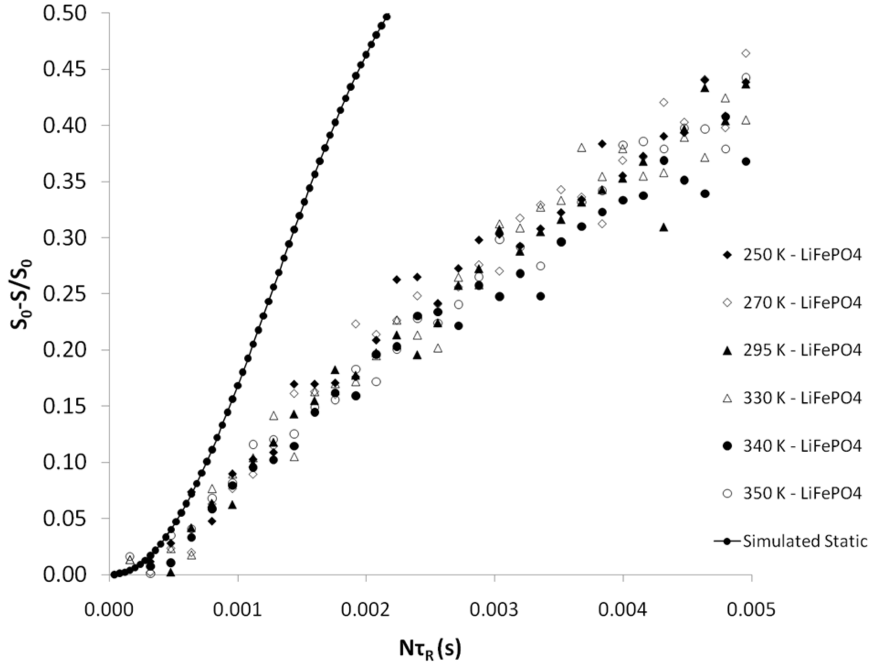

Figure 4.4 – ^{6}Li{^{31}P} REDOR curve of $LiFePO_4$ over a variable temperature range. The static simulated curve from SIMPSON is also shown as the data points connected by a line.

Overall, there are no observable changes to the ^{6}Li{^{31}P} REDOR buildup curve as the temperature is increased. It is difficult to assess whether this is from an inherent lack of Li ion diffusion below 350 K or if a systematic error is present within the experiment.

The shortest Li−P contact of 2.659 Å gives rise to dipolar coupling value of 381 Hz which is 2.4 % of the FWHM of the isotropic (16000 Hz at 300 K) and 0.2 % of the total ^{31}P signal (250000 Hz over the entire sideband manifold). The transmitter frequency is chosen by identifying the frequency at which the maximum intensity of isotropic signal is found. Based on the width of the isotropic peak being close to 16000 Hz, if a 1% error is alloted to this selection then the error on the transmitter frequency would be ± 160 Hz. This consitutes close to 50% of the total dipolar coupling value and illustrates how changes to the measured couplings may fall within the error values of experimental parameters.

Changes in the magnetic susceptibility of the Fe center over a variable temperature range may also introduce a systematic error within this experiment. As the temperature is raised, the magnetic susceptibility decreases and the paramagnetic character of the resonances decreases. This leads not only to the migration of the isotropic shift towards the diamagnetic region of the spectrum, (**Figure 4.3**) but also to a narrowing of the resonance. This is not a problem if the total signal falls within the bandwidth of the pulse as 100% of the signal is excited regardless of span. However, in the highly paramagnetic systems studied here, the width of the signal (250 kHz) is larger than the bandwidth of the applied pulse (142 kHz) and incomplete excitation of the ^{31}P signal occurs. Previous studies have shown that a base attenuation of the REDOR buildup is observed and related to this incomplete excitation of the ^{31}P signal.[18] This base attenuation is not a problem at measurements carried out over a single temperature, but for a variable temperature range where changes to the REDOR buildup indicate mobility of the Li ions, a narrowing of the shift leads to more complete excitation of the ^{31}P signal meaning stronger REDOR buildup curve are measured at higher temperatures. This increase in REDOR buildup from improved excitation may offset the weakening of the REDOR buildup from movement of the mobile ion, making interpretation of the results non-trivial. While neutron diffraction results have shown that there is limited lithium diffusion below 620 K (prior to the onset of solid solution formation)[22] it is unclear if the REDOR results presented here can be interpreted to support this claim. It is therefore the focus of ongoing work to measure nuclei whose full signal falls within the bandwidth of the applied pulse such that narrowing of the resonances brought on by susceptibility changes has no effect on the total excitation. This includes use of ^{6}Li{^{7}Li} REDOR and ^{7}Li{^{6}Li} REDOR measurements where dephasing of the narrower ^{7}Li and ^{6}Li resonances has fewer complications from excitation disparities over a variable temperature range.

4.3.3 Phase Transformation in Li_xFePO_4 (x = 0.5)

The section details the solid solution formation at high temperature in biphasic $0.5LiFePO_4$:$0.5FePO_4$ characterized using static ^{31}P measurements. To date, the conductivity restrictions in the olivine phases are ascribed to a one-dimensional Li ion diffusion pathway coupled with limited electronic conduction owing to small polaron hopping conductivity.[22-24] This results in a two-phase redox reaction during electrochemical cycling and a voltage plateau corresponding to the phase transition between them.[10,11,25-28] In order to enhance the cycling capabilities, particularly for $LiFePO_4$, generation of single phase or “solid-solution” properties at temperatures amenable to the operation of the Li ion battery have been investigated either through chemical or mechanical manipulation of the parent compound.[27-32]

The present work evaluates the temperature driven formation of solid solution phases in samples of partially delithiated Li_xFePO_4 using static ^{31}P variable temperature NMR experiments. The ^{31}P paramagnetic shift proves to be an ideal tool for monitoring electronic changes taking place at the Fe redox center as it has a very strong hyperfine coupling to the unpaired electrons on the transition metal center.[15] The use of static NMR measurements in this case provides access to a broad temperature range, such that the phase transformation can be performed *in-situ* providing a complementary NMR picture to the previous *in-situ* diffraction and Mossbauer studies of Li_xFePO_4.[28,29] For this study, $Li_{0.5}FePO_4$ was the chosen composition as it allows for well-balanced ^{31}P signal intensity from the separate $FePO_4$ and $LiFePO_4$ domains.

4.3.3.1 XRD of $0.5LiFePO_4$:$0.5FePO_4$

Complete chemical and electrochemical oxidation of triphylite Li_xFePO_4 produces orthorhombic $FePO_4$ (heterosite), while partial oxidation to $x = 0.5$ results in mixtures of the two end-members. The diffraction pattern of biphasic $0.5LiFePO_4$:$0.5FePO_4$, produced by the oxidation of $LiFePO_4$ with a stoichiometric amount of $NOBF_4$ by collaborators at the University of Waterloo is shown in **Figure 4.5**. The lattice parameters of $LiFePO_4$ were indexed to be $a = 10.323$ Å, $b = 6.002$ Å, $c = 4.696$ Å with a unit cell volume of 291.0 Å^3, in good accord with several other reports of $LiFePO_4$ bulk crystallites. The lattice parameters of the oxidized phase were determined to be $a = 9.833$

Å, *b* = 5.801 Å, *c* = 4.771 Å with a unit cell volume of 272.1 Å^3, also in good accord with previous reports.

An SEM micrograph (inset **Figure 4.5**) shows the particle size of the crystallites to be 200-500 nm in dimension.

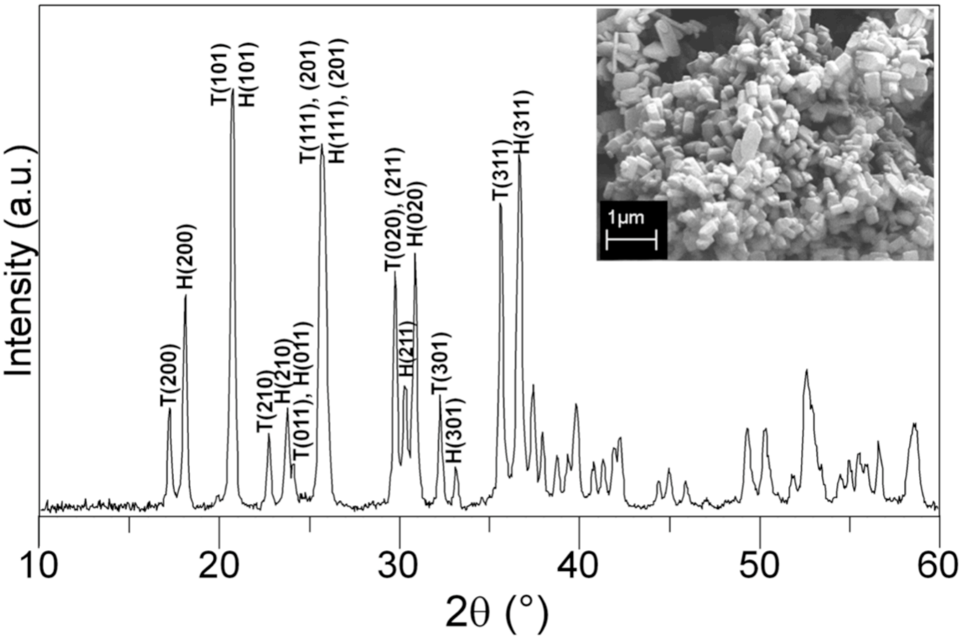

Figure 4.5 - Powder X-ray diffraction pattern of biphasic $Li_{0.5}FePO_4$ prepared from chemical oxidation of $LiFePO_4$. Selected reflections of $LiFePO_4$ (triphylite, **T**) and $FePO_4$ (heterosite, **H**) are indexed. Inset: SEM micrograph of the $Li_{0.5}FePO_4$ material which consists of uniform sub-micron sized particles, with a narrow particle size distribution.

4.3.3.2 ^{31}P MAS NMR of $0.5LiFePO_4$:$0.5FePO_4$

The sample of half-delithiated, hydrothermally prepared, $0.5LiFePO_4$:$0.5FePO_4$ was first evaluated using ^{31}P MAS NMR. **Figure 4.6** (bottom) shows the room temperature ^{31}P MAS NMR spectrum of 0.5LiFePO$_4$:0.5FePO$_4$ where two distinct domains with resonances centered around ~ 3800 and 5800 ppm are observed. **Figure 4.6** also shows the ^{31}P MAS NMR spectrum of fully lithiated LiFePO$_4$ and with an Fe^{2+} electron configuration of $t_{2g}^4e_g^2$ giving a ^{31}P isotropic resonance centered at 3800 ppm. In contrast, for the ^{31}P MAS spectrum of FePO$_4$, where the oxidation state of the iron center is raised to Fe^{3+} giving a $t_{2g}^3e_g^2$ electron configuration, the paramagnetic shift increases to 5800 ppm (**Figure 4.6** top). This shift information is in agreement with previous reports of the olivine Li$_x$FePO$_4$ family.[15,33,34] The cause of this increase in paramagnetic shift is similar to what was observed for the LiMnPO$_4$ - LiFePO$_4$ comparison in Section 4.3.1. The unpairing of an electron in the t_{2g} orbital of both FePO$_4$ and LiMnPO$_4$ (which both have a d^5 electron configuration of $t_{2g}^3e_g^2$) leads to an increased amount of unpaired electron spin density able to delocalize onto the phosphorus nucleus and hence an increased paramagnetic shift relative to LiFePO$_4$.

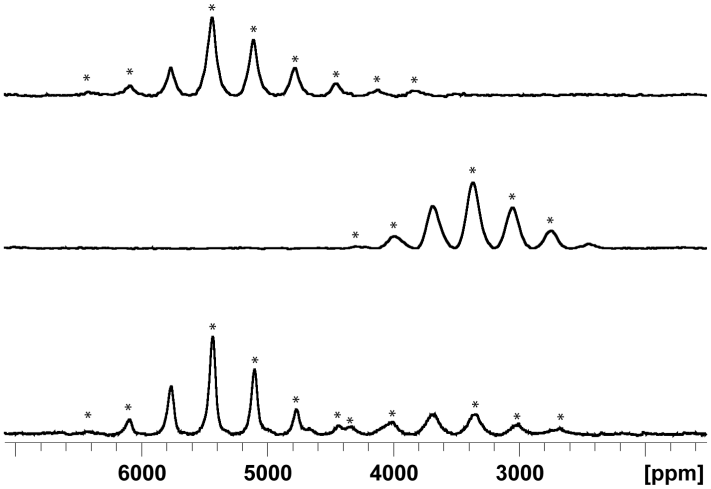

Figure 4.6 - ^{31}P MAS NMR of $FePO_4$ (top), $LiFePO_4$ (middle) and biphasic $0.5LiFePO_4$:$0.5FePO_4$ (bottom) all at room temperature. Isotropic shifts for $FePO_4$, $LiFePO_4$ found at 5800 and 3800 ppm respectively. Asterisks denote spinning sidebands.

Although $LiMnPO_4$ and $FePO_4$ are isoelectronic, the overall higher shift observed in $LiMnPO_4$ is attributed to slightly better orbital overlap within this phase. Figure 4.7 shows the P environment found within the olivine phases. Five metal centers coordinate to the P atom via the oxygen atoms creating both edge- and corner-sharing geometries between the phosphate tetrahedra and metal octahedra. Table 4.2 lists the P-O-M orbital overlap angles where the edge shared geometries give the best overlap angles ranging from 92.05° for $LiMnPO_4$ to 94.75° for $FePO_4$. The higher ^{31}P paramagnetic shift for $LiMnPO_4$ is attributed to this phase having an overlap angle closer to 90° than $FePO_4$. Moreover, this highlights how the geometry dependent contact shift dominates the observed paramagnetic shift, as the pseudo-contact interaction would be near equivalent in these materials.

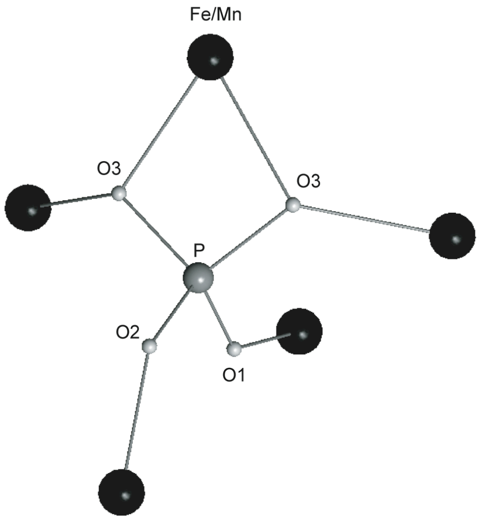

Figure 4.7 – Schematic showing the P environment as coordinated via oxygen to the metal centers (either Mn or Fe) in the olivine phases of $LiMnPO_4$, $LiFePO_4$ and $FePO_4$.

Table 4.2 – Summary of M-O-P orbital overlap angles in $LiFePO_4$,[35] $FePO_4$,[35] and $LiMnPO_4$.[36]

O Label	$LiFePO_4$ Fe-O-P Angle (°)	$FePO_4$ Fe-O-P Angle (°)	$LiMnPO_4$ M-O-P Angle (°)
O3-edge	94.74	94.75	92.05
O3-edge	94.74	94.75	92.05
O1-corner	3.244	3.202	121.58
O2-corner	3.275	3.370	123.22
O3-corner	3.269	3.302	124.96

4.3.3.3 *In-Situ* ^{31}P NMR Study of the Thermally Driven Solid Solution in $Li_{0.5}FePO_4$

The sensitivity of the ^{31}P resonance to changes at the redox center allow for an *in-situ* ^{31}P NMR study of the thermally driven phase transformation from biphasic $0.5LiFePO_4{:}0.5FePO_4$ to solid solution $Li_{0.5}FePO_4$. In order to reach temperatures where full electron delocalization occurs (~ 400 °C), NMR experiments were acquired in the absence of magic angle spinning. The static ^{31}P NMR spectra (**Figure 4.8**) were collected as a series of frequency stepped sub-spectra and added. The room temperature spectrum (**Figure 4.8,** bottom 26 °C) clearly shows the separate domains of phosphorous nuclei near Fe^{3+} and Fe^{2+} similar to that observed in the MAS NMR experiments. When the temperature is raised to 250 °C, there is a loss of resolution between the two phases consistent with the expected onset of electron and lithium delocalization leading to a larger phase interface region.[28,29] The migration of the $FePO_4$ and $LiFePO_4$ resonances to lower frequency with increased temperature results from to Curie-Weiss behaviour of paramagnetic resonances whereby the overall magnetic susceptibility of each metal center decreases as the temperature is raised. This leads to a decrease in the hyperfine coupling constant and thus a lower chemical shift.[17] When temperatures of 400 °C are reached, a single resonance centered at 3200 ppm appears. The ^{31}P nuclei now “see” the Fe transition metal in a single, average oxidation state due the complete delocalization of electrons of the solid solution phase.

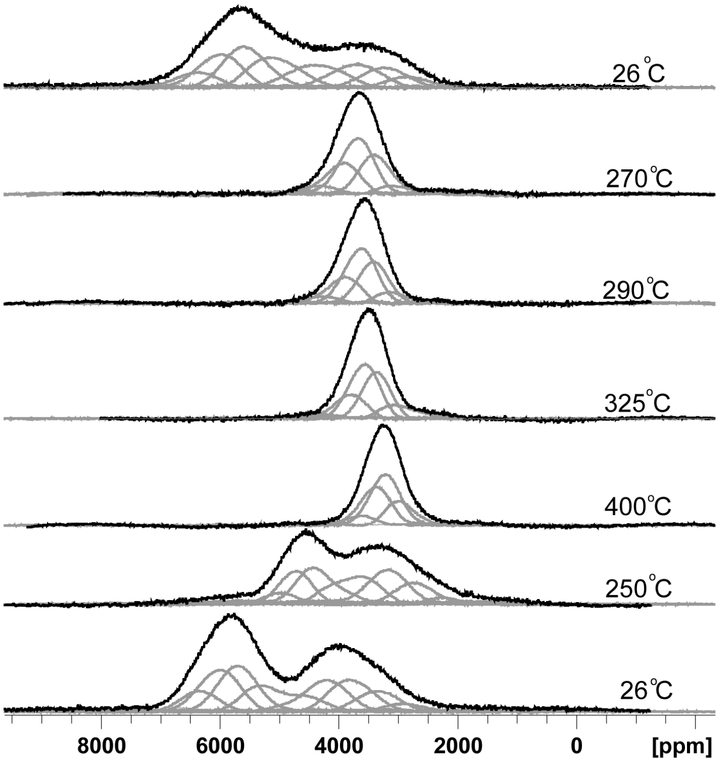

Figure 4.8 – ^{31}P static solid-state NMR spectra under variable temperature conditions. Frequency stepped sub-spectra (grey) added to yield total spectrum (black).

The sample was then cooled in small increments to observe the re-emergence of the two domains. Between temperatures of 400 °C and 270 °C, the sample retains single phase features but with slight broadening. At this stage it is difficult to determine whether this is caused by the slowing of electron mobility or increased paramagnetism at lower temperatures. At 250 °C, where reappearance of the separate domains is expected, the spectrum continues to appear single phase. **Figure 4.9** shows two sub-spectra with the excitation frequency set to 81.28 MHz collected at 250 °C before and after the solid solution was formed. The pre-solid solution sub-spectrum shows features that indicate that two domains are present. For the same sub-spectrum collected 24 hours after formation of the solid solution, these features are no longer present and only single phase $Li_{0.5}FePO_4$ is observed. Upon cooling and allowing the sample to sit at room temperature for 72 hours, the separation into two domains is apparent (**Figure 4.8** top 26 °C). This separation however, is not as well defined as the 26 °C spectrum collected prior to heat treatment and thus suggests that there is a considerable increase in the number of P nuclei residing at the phase interface following treatment at high temperature.

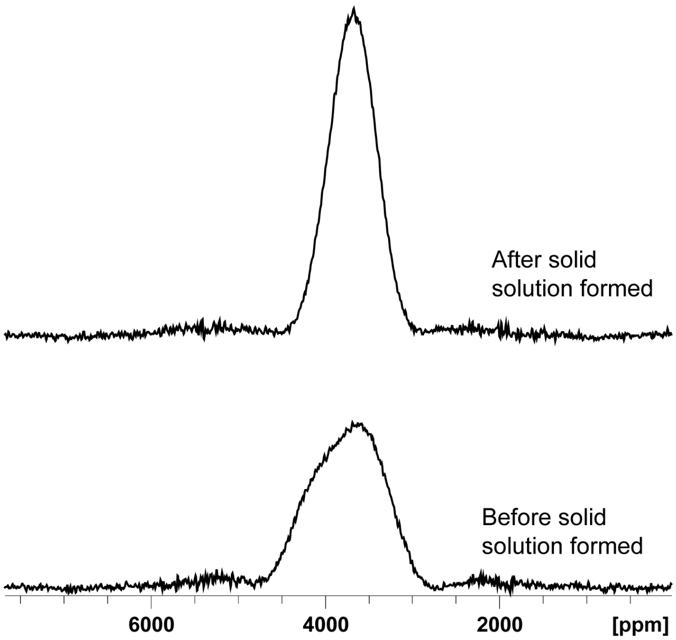

Figure 4.9 – Static ^{31}P sub-spectra of $Li_{0.5}FePO_4$ at 250 °C measured before and after the solid solution phase was reached. The two-phase features observed before the solid solution was formed do not reappear in the cooled sample on a timescale of 24 hr following heat treatment.

4.3.4 ^{7}Li MAS NMR Investigation of Phase Boundary Regions in Nanoparticles

Here, detailed information regarding the $FePO_4$/$LiFePO_4$ phase interface is obtained from room temperature ^{7}Li MAS NMR spectra of biphasic $Li_{0.5}FePO_4$ that has not undergone any heat treatements. For comparison, a ^{7}Li MAS NMR spectrum of pristine, fully lithiated, $LiFePO_4$ is also presented which shows a single isotropic resonance centered at -11 ppm (**Figure 4.10** a) consistent with previous reports.[15,34] The isotropic lineshape has a FWHM of 9500 Hz. Following chemical delithiation, the ^{7}Li MAS NMR spectrum of biphasic $Li_{0.5}FePO_4$ (**Figure 4.10** b) shows an isotropic resonance centered at -12 ppm which deconvolutes to 5 peaks labelled as A, B, C, D, and E. The deconvolution resulting in the appearance of multiple peaks is somewhat surprising as only the $LiFePO_4$ domain should contain observable Li. The $FePO_4$ domain is not expected to give rise to any Li signals. These newer peaks are therefore resulting either from Li ion disorder and/or Li belonging to the $LiFePO_4$ domain but sitting at the interface with the $FePO_4$ domain. The deconvolution presented here is the minimum number of peaks needed to obtain a goodness of fit of 95% in the Topspin 2.1 program. Peak A is broad with parameters similar to that of the ^{7}Li MAS NMR spectrum of pristine $LiFePO_4$ (**Table 3**) and is thus confidently assigned as Li sitting in the fully lithiated domain. Peak B is very narrow and centered at -7 ppm. This peak does not contribute to the lineshape of the spinning sidebands meaning it is a non-paramagnetic Li environment (possibly a Li-salt impurity arising from the oxidation of $LiFePO_4$ with NO_2BF_4). Peaks C, D, and E, deconvolute with varying degrees of broadening and also appear in the 1st order sidebands suggesting these resonances belong to paramagnetic phases. Peaks C and D have chemical shifts slightly higher than the $LiFePO_4$ domain (−8 ppm and −6 ppm, respectively).

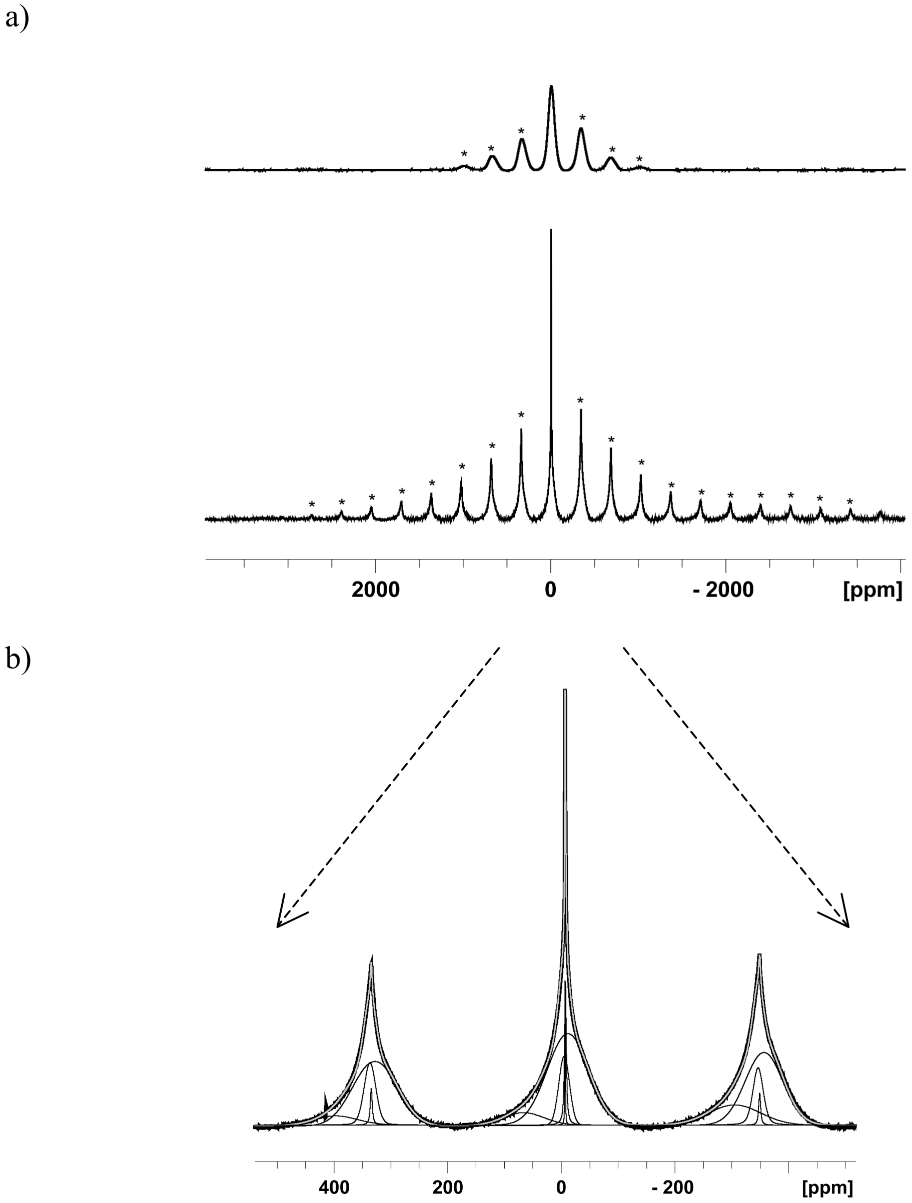

Figure 4.10 – a) ^7Li MAS NMR spectra of $LiFePO_4$ (top, MAS = 40 kHz) and biphasic $Li_{0.5}FePO_4$ ($0.5LiFePO_4$:$0.5FePO_4$) (bottom, MAS = 40 kHz). Asterisks denote spinning sidebands. b) Deconvolution of biphasic $Li_{0.5}FePO_4$ with MAS = 40 kHz. Fitted spectrum (grey) sits on top of experimental spectrum (black). Deconvoluted peaks shown in black.

Table 4.3 - Summary of deconvolution parameters for the ^{7}Li MAS NMR spectrum of biphasic $Li_{0.5}FePO_4$ (**Figure 4.10**)

Peak	Chemical shift (ppm)	FWHM (Hz)
A	-12	9998
B	-7	114
C	-8	427
D	-6	2598
E	65	9827

The narrowness and appearance in higher order sidebands suggests that these resonances arise due to their closeness to an Fe^{3+} environment (i.e. proximity to the phase interface as purely Fe^{3+} regions would have no Li ions present). This conclusion is made in consideration of the through-space nuclear-electron spin interactions for paramagnetic materials. Increasing the unpaired electron spin density significantly impacts not only the paramagnetic shifts, but also the span of the chemical shift anisotropy (CSA) and the broadness of the isotropic resonance.[37,38] Li sitting close to Fe^{3+} experiences a larger electron-nuclear dipolar coupling as compared to Li sitting close to Fe^{2+}. This leads to a larger CSA which is now observed for biphasic $Li_{0.5}FePO_4$ (span of the CSA is now close to ^{7}Li 8000 ppm). There is also a characteristic narrowness to the ^{7}Li lineshapes that we have assigned to Li near Fe in oxidation 3+. This is justified based on the contributions from both the hyperfine coupling value ($A/\hbar$) and the spin-lattice relaxation of the electrons (T_{1e}) to which the nucleus is coupled on the FWHM of paramagnetic resonance identified in (Equation 4-1). In the $LiFePO_4$:$FePO_4$ system, the increase in chemical shift from -11 ppm for Li in a Fe^{2+} environment to -6 ppm for Li near Fe^{3+} is due to a modest increase in the $A/\hbar$ value. This increase alone would then lead to broadening of the resonance for any Li near Fe^{3+}. However, the opposite trend is observed in this system

(**Figure 4.10**) thus indicating that the changes in the linewidth are governed, rather, by the T_{1e} term. As the redox charge is raised from Fe^{2+} to Fe^{3+} (or as the spin number goes from S = 2 to S = 5/2) the T_{1e}s decrease, resulting in the observed narrower resonances. This trend was also observed when comparing the ^{7}Li MAS spectra of $LiFePO_4$ and $LiMnPO_4$ (**Figure 4.1).** In $LiMnPO_4$, all Li nuclei are surrounded by transition metals with a spin state of S = 5/2 (isoelectronic with Fe^{3+}). The resultant ^{7}Li MAS NMR spectrum (with δ = 75 ppm, FWHM of ~ 500 Hz, **Figure 4.1**) strongly resembles the new, narrower resonances, assigned to Fe^{3+} Li environments in biphasic $0.5LiFePO_4$:$0.5FePO_4$.

Overall, there is sufficient evidence to confirm that a fraction of the Li nuclei are sitting close to a more paramagnetic Fe^{3+} ($t_{2g}^3e_g^2$) center. This thereby results in phase interface Li being observable in these materials. However, due to the large number of possible Li sites that could be produced, caution is emphasized when attempting site specific assignments of the remaining deconvoluted peaks (C, D, and E). **Figure 4.11** shows the local lithium environment in $LiFePO_4$ where each Li ion is connected via O to 6 Fe atoms. Two of the Fe atoms have Li-O-Fe overlap angles close to 90° while the other 4 Fe atoms overlap at angles of either 110° or 120°. Oxidation of an Fe atom involved in the 90° orbital configuration (**Figure 4.11** left) would lead to the greatest increase in the paramagnetic shifts based on the geometry dependent delocalization of unpaired electron spin density discussed previously. Alternatively, oxidation of Fe atoms in the 110° or 120° configurations (**Figure 4.11** right) would have a less significant impact on the paramagnetic shift but through-space effects including changes to the CSA would still be observed. These represent the two extreme cases of numerous possible combinations of Fe^{2+}/Fe^{3+} neighbours to the crystallographic Li site. Together these lead to a large number of Li environments with varying degrees of paramagnetic shift and broadness.

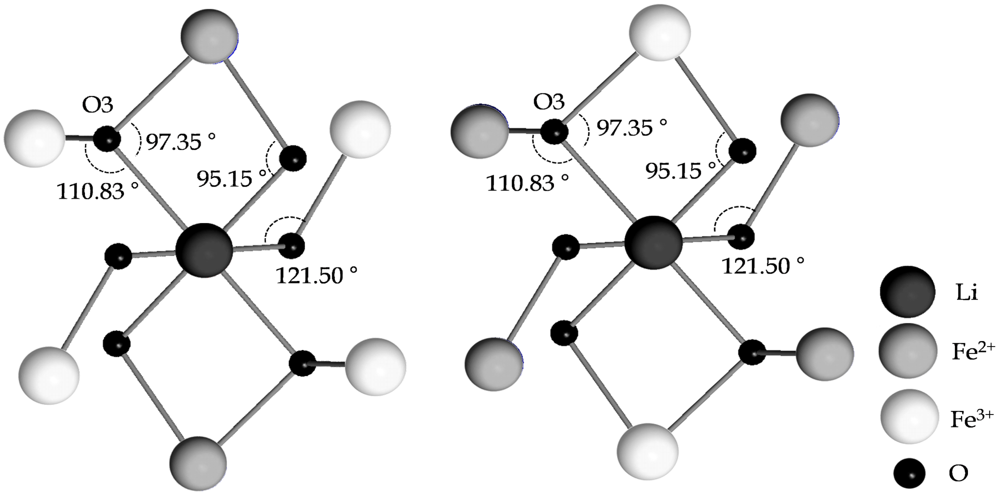

Figure 4.11 – Schematic detailing the local Li environment with respect to Fe transition metal center proximity. **Left**. Oxidation of Fe centers that have orbital overlap close to 90° leading to Li environments with high paramagnetic shift. **Right**. Oxidation of Li environments with orbital overlap of 110-122° leading to a smaller impact on paramagnetic shift but similar impact on lineshape and breadth of CSA.

An exception is made for Peak E which was deconvoluted with a shift of 65 ppm and large FWHM of ~ 9800 Hz. While the paramagnetic shift is considerably higher, the linewidth is virtually unchanged from the parent $LiFePO_4$ thus suggesting that this Li envrionment is still in an Fe^{2+} environment. This peak is therefore assigned as a Li environment generated where there is a larger number of Fe^{2+} atoms in the Li-coordination sphere. This scenario is best represented by the anti-site defect commonly generated in this system.[39,40] **Figure 4.12** shows the local Li environment generated if an Fe is found along the diffusion channel. The Li ion now has 7, rather than 6, Fe^{2+} in its coordination sphere where the defect Fe^{2+} (Fe_{defect}) edge shares with the Li-atom at two Li-O-Fe overlap angles of 87.5 and 92.2°. Due to the additive nature of the Fermi-contact interaction, this would lead to the observed increase in the Li-paramagnetic shift value but with minimal changes to the lineshape. This anti-site defect was not observed in the fully lithiated parent compound. This is attributed to the the difficulty in deconvolution of such a broad isotropic resonance which is made worse by the increased concentration of Li in the crystallographic, -11 ppm, environment. Future work will look to overcome this obstacle through the use of ^{6}Li MAS NMR on enriched samples of $Li_{1-x}FePO_4$.

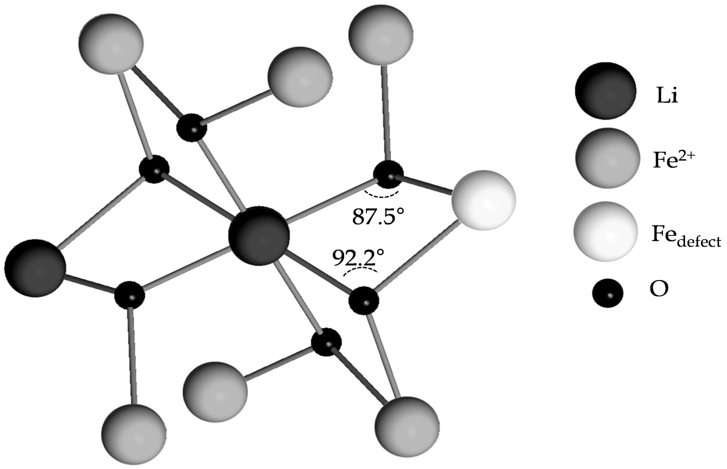

Figure 4.12 – Schematic detailing the new Li environment generated if a Fe atom was found along the Li diffusion channel. The Fe_{defect}-O-Li orbital overlap angles are very close to 90° resulting in a further increase of the paramagnetic shift value.

4.3.4.1 ^{7}Li MAS NMR Investigation of Phase Boundary Regions in Microparticles

Confirmation of the influence of particle size on the ability to detect the phase boundary following delithiation is provided through parallel studies of electrochemically cycled $LiFePO_4$. It is shown that observation of phase boundary lithium is limited as the particle size increases. **Figure 4.13** shows ^{7}Li MAS spectra of large particle (1-1.5 μm) $LiFePO_4$ before and after cycling to a composition of $Li_{0.43}FePO_4$. The post-cycled spectrum is unchanged relative to the parent material and, no new Fe^{3+} environment is observed. Therefore, although the material is delithiated to an equivalent, or slightly greater degree than the nanoparticles studied above, there is not sufficient lithium in the interface region to allow detection by NMR. Similarily in a recent resport from, Cabana *et al.*,[33] a ^{6}Li MAS NMR spectrum of chemically delithiated, large particle (>2 μm) $LiFePO_4$ did not reveal features of phase boundary Li.

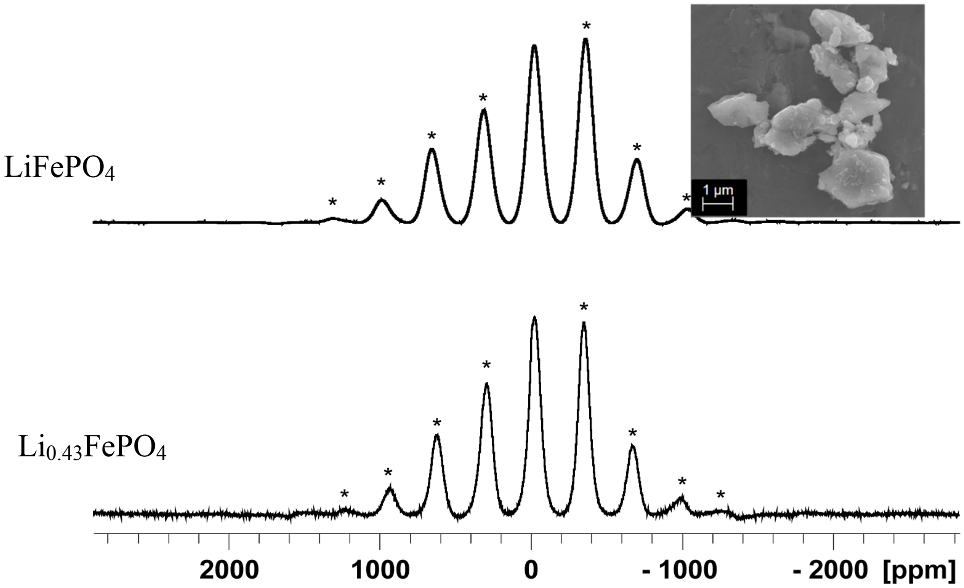

Figure 4.13 - ^{7}Li MAS NMR (40 kHz) of micro-diameter $LiFePO_4$ before (top) and after (bottom) electrochemically cycling to a composition of $Li_{0.43}FePO_4$. Asterisks denote spinning sidebands. Inset is SEM image of pristine particles.

In both cases, there is certainly Li residing at the $FePO_4$/$LiFePO_4$ interface, however because of the larger particle diameter, the fraction of this lithium (relative to Li in the fully lithiated $LiFePO_4$ domain) would be significantly smaller. The interface regions are proposed to be only a few nanometers thick.[10] In smaller diameter particles, these few nanometers carry greater significance than in particles of micrometer diameter. From a ^{7}Li NMR standpoint, signals arising from Li residing in the fully lithated domain would overtake the NMR spectrum in the microdiamater samples making the small region of interface Li unobservable. Due to the larger relative impact of the interface in nanodimension particles, both the fully lithiated domain as well as interface Li is observed.

4.4 Concluding Remarks

Significant differences in paramagnetic shift, isotropic lineshape and sideband manifold were observed when comparing the ^{7}Li and ^{31}P MAS spectra of $LiMnPO_4$ and $LiFePO_4$. This is attributed to the different electron configurations at the transition metal center of these isostructural compounds where $LiMnPO_4$ has a d^5, $t_{2g}{}^3e_g{}^2$, configuration while $LiFePO_4$ has a d^6, $t_{2g}{}^4e_g{}^2$ configuration. This sensitivity of the nuclear spins to electron configuration is exploited to characterize phase transformations and phase interface environments in $Li_{0.5}FePO_4$ where room temperature MAS and static ^{31}P spectra show the presence of two distinct domains arising from the $Fe^{3+}PO_4$ and $LiFe^{2+}PO_4$ domains. The P nuclei show extreme sensitivity to electronic changes taking place at the transition metal center yielding ^{31}P paramagnetic shifts of 5800 ppm and 3800 ppm, respectively. At 400 °C, these resonances coalesce into a single P-site centered at 3200 ppm. This is due to complete electron delocalization resulting in a single, average Fe oxidation state. Upon cooling back to room temperature, the two domains of $FePO_4$ and $LiFePO_4$ are not as clearly resolved suggesting that some P nuclei continue to sit in an environment where the average Fe oxidation state is between 2+ and 3+. ^{7}Li MAS NMR spectra of biphasic $Li_{0.5}FePO_4$ (or $0.5LiFePO_4$:$0.5FePO_4$) reveal phase interface regions as sites deconvolute into resonances attributable to the distribution of Fe^{3+} and Fe^{2+} around a lithium center. This is based on the extent of orbital overlap, and the resulting magnitude of the chemical shift at one extreme, and alternatively, the lack of orbital overlap, but the significant influence of T_{1e}, on the narrowness of the lineshape. These details allow for a clear distinction between NMR spectra of samples with larger particle size from those with submicron particle sizes. The latter uniform, small particles have been shown to have excellent electrochemical performance, and the utility of NMR in elucidating properties of the lithiated/delithiated phase boundary will provide ongoing insight into the development of similar phases.

4.5 References

(1) Yang, S. F.; Song, Y. N.; Zavalij, P. Y.; Whittingham, M. S. *Electrochem. Commun.* **2002**, *4*, 239.

(2) Ellis, B.; Kan, W. H.; Makahnouk, W. R. M.; Nazar, L. F. *J. Mater. Chem.* **2007**, *17*, 3248.

(3) Ellis, B.; Kan, W. H.; Makahnouk, W. R. M.; Nazar, L. F. *J. Mater. Chem.* **2007**, *17*, 3248

(4) Bykov, A. B.; Chirkin, A. P.; Demyants, L. N.; Doronin, S. N.; Genkin, E. A.; Ivanov-Shits, A. K.; Kondratyuk, I. P.; Maksimov, B. A.; Mel'kinov, O. K.; Muradyan, L. N.; Simonov, V. I.; Timofeeva, V. A. *Solid State Ionics* **1990**, *38*, 31.

(5) Massiot, D.; Fayon, F.; Capron, M.; King, I.; Le Calve, S.; Alonso, B.; Durand, J. O.; Bujoli, B.; Gan, Z. H.; Hoatson, G. *Magn. Reson. Chem.* **2002**, *40*, 70.

(6) Herzfeld, J.; Berger, A. E. *J. Chem. Phys.* **1980**, *73*, 6021

(7) Eichele, K.; Wasylishen, E. *Dalhousie University and Universität Tübingen* **2006**.

(8) Bak, M.; Rasmussen, J. T.; Nilesen, N. C. *Journal of Magnetic Resonance Chemistry* **2002**, *147*, 296.

(9) Takahashi, T. K., Hiroe; Sugisawa, Hishashi; Baba, Toshihide; *Solid State Nuclear Magnetic Resonance* **1999**, *15*, `119.

(10) Padhi, A. K.; Nanjundaswamy, K. S.; Goodenough, J. B. *J. Electrochem. Soc.* **1997**, *144*, 1188

(11) Andersson, A. S.; Kalska, B.; Haggstrom, L.; Thomas, J. O. *Solid State Ionics* **2000**, *130*, 41.

(12) Kobayashi, G.; Yamada, A.; Nishimura, S.; Kanno, R.; Kobayashi, Y.; Seki, S.; Ohno, Y.; Miyashiro, H. *J. Power Sources* **2009**, *189*, 397.

(13) La Mar, G. N., DeW. Horrocks, W., Jr., Holm, R. H. *NMR of Paramagnetic Materials*; Academic Press: New York, 1973.

(14) Miller, J. S., Drillon, M. Kohler, F. H. *Magnetism: Molecules to Materials*; Wiley-VCH, 2001; Vol. 1.

(15) Tucker, M. C., Doeff, Marca M., Richardson, Thomas J., Finones, Rita, Reimer, Jeffrey A., Cairns, Elton J. *Electrochemical and Solid-State Lettters* **2002**, *5*, A95

(16) Goward, G. R.; Schuster, M. F. H.; Sebastini, D.; Schnell, I.; Spiess, H. W. *J. Phys. Chem. B* **2002**, *106*, 9322.

(17) Gee, B.; Horne, C. R.; Cairns, E. J.; Reimer, J. A. *J. Phys. Chem. B* **1998**, *102*, 10142.

(18) Cahill, L. S.; Kirby, C. W.; Goward, G. R. *J. Phys. Chem. C* **2008**, *112*, 2215.

(19) Cahill, L. S., Chapman, R. P., Britten, J. F., Goward, G. R. *J. Phys. Chem. B* **2006**, *110*, 7171.

(20) Verhoeven, V. W. J.; de Schepper, I. M.; Nachtegaal, G.; Kentgens, A. P. M.; Kelder, E. M.; Schoonman, J.; Mulder, F. M. *Phys. Rev. Lett.* **2001**, *86*, 4314

(21) Davis, L. J. M.; Heinmaa, I.; Goward, G. R. *Chem. Mater.* **2010**, *22*, 769.

(22) Nishimura, S.; Kobayashi, G.; Ohoyama, K.; Kanno, R.; Yashima, M.; Yamada, A. *Nat. Mater.* **2008**, *7*, 707.

(23) Morgan, D.; Van der Ven, A.; Ceder, G. *Electrochem. Solid-State Lett.* **2004** *7*, A30

(24) Andersson, A. S.; Thomas, J. O. *J. Power Sources* **2001**, *97-8*, 498.

(25) Srinivasan, V.; Newman, J. *Electrochem. Solid State Lett.* **2006**, *9*, A110.

(26) Delmas, C.; Maccario, M.; Croguennec, L.; Le Cras, F.; Weill, F. *Nat. Mater.* **2008**, *7*, 665.

(27) Laffont, L.; Delacourt, C.; Gibot, P.; Wu, M. Y.; Kooyman, P.; Masquelier, C.; Tarascon, J. M. *Chem. Mater.* **2006**, *18*, 5520.

(28) Delacourt, C.; Poizot, P.; Tarascon, J.-M.; Masquelier, C. *Nat. Mater.* **2005**, *4*, 254

(29) Ellis, B.; Perry, L. K.; Ryan, D. H.; Nazar, L. F. *J. Am. Chem. Soc.* **2006**, *128*, 11416.

(30) Dodd, J. L.; Yazami, R.; Fultz, B. *Electrochem. Solid-State Lett.* **2006**, *9*, A151.

(31) Yamada, A.; Koizumi, H.; Nishimura, S.-I.; Sonoyama, N.; Kanno, R.; Yonemura, M.; Nakamura, T.; Kobayashi, Y. *Nat. Mater.* **2006**, *5*, 357.

(32) Tan, H. J.; Dodd, J. L.; Fultz, B. *J. Phys. Chem. C* **2009**, *113*, 2526.

(33) Cabana, J.; Shirakawa, J.; Chen, G.; Richardson, T. J.; Grey, C. P. *Chem. Mater.* **2010**, *22*, 1249.

(34) Hamelet, S.; Gibot, P.; Casas-Cabanas, M.; Bonnin, D.; Grey, C. P.; Cabana, J.; Leriche, J. B.; Rodriguez-Carvajal, J.; Courty, M.; Levasseur, S.; Carlach, P.; van Thournout, M.; Tarascon, J. M.; Masquelier, C. *J. Mater. Chem.* **2009**, *19*, 3979.

(35) Rousse, G.; Rodriguez-Carvajal, J.; Patoux, S.; Masquelier, C. *Chem. Mater.* **2003**, *15*, 4082.

(36) Arcon, D.; Zorko, A.; Dominko, R.; Jaglicic, Z. *J. Phys.-Condes. Matter* **2004**, *16*, 5531.

(37) Nayeem, A.; Yesinowski, J. P. *J. Chem. Phys.* **1988**, *89*, 4600.

(38) Grey, C. P.; Dupre, N. *Chem. Rev.* **2004**, *104*, 4493.

(39) Malik, R.; Zhou, F.; Ceder, G. In *217th ECS Meeting*; The Electrochemical Society: Vancouver, Canada, 2010.

(40) Gardiner, G. R.; Islam, M. S. *Chem. Mater.* **2010**, *22*, 1242.

Chapter 5: Quantification of Li Ion Mobility in α−$Li_3Fe_2(PO_4)_3$ using Variable Temperature ^{6}Li 2D EXSY Measurements

5.1 Introduction

This chapter is divided into two studies detailing the ion dynamics and electrochemical performance of the monoclinic α-$Li_3M_2(PO_4)_3$ (M = V, Fe) family of cathode materials. The first study elucidates timescales of Li-mobility in $Li_3Fe_2(PO_4)_3$ using ^{6}Li 2D EXSY measurements. Three crystallographically unique Li sites were resolved under magic angle spinning (25 kHz) with paramagnetic shifts arising at 45 ppm, 102 ppm, and 216 ppm. These resonances were assigned to the crystallographic positions based on the degree of the Fermi-contact interaction with the paramagnetic iron center. ^{6}Li 2D exchange NMR experiments were performed under variable temperature conditions in order to determine the activation energies for hopping between lithium sites. Activation energies ranged from 0.59 (± 0.05) eV to 0.81 (± 0.04) eV, where shorter Li internuclear distances, yet larger Li-O bottlenecks, yielded higher activation energies. These results are opposite in trend from the previous study of isostructural $Li_3V_2(PO_4)_3$ which showed that increased internuclear distance and constricted bottlenecks yield larger energy barriers for Li-Li exchange. In the Fe-case, the geometry of the polyhedral faces of the Li environments plays a more critical role in the ion dynamics as there is a blocking of the diffusion pathway by the Fe atoms in the edge-shared geometries. This latter result is better illustrated through evaluation of bond valence sum maps which reveal a large amount of bond valence density in the lone edge-shared geometry giving this pair the highest energy barrier for hopping. This work was published in *Chemistry of Materials* (**2010**, *22*, 769-775) with co-authors I. Heinmaa, and G. R. Goward. For this work, NMR data was collected at the National Institute of Chemical Physics and Biophysics in Tallinn Estonia, under the supervision of Dr. Ivo Heinmaa. All data was processed at McMaster University with supervision from Prof. Goward.

The second part of this chapter studies changes to Li ion mobility in $Li_xV_2(PO_4)_3$ using variable temperature ^{6}Li MAS NMR as it is electrochemically cycled from x = 3 to x = 2. Preliminary results show the Li ion mobility is slowed in the cycled product relative to the as-prepared $Li_3V_2(PO_4)_3$ phase.

5.2 Experimental

5.2.1 Sample Preparation.

$Li_3Fe_2(PO_4)_3$ was prepared by solid state reaction as described by Padhi et al.[1] Stoichiometric amounts of $NH_4H_2PO_4$ (Sigma Aldrich, 99%), ^6LiOH (prepared in house using Cambridge isotopes ^6Li metal), and Fe_2O_3 (Sigma Aldrich, 99%) were ground together and heated to 250 °C to drive off ammonia and water. The mixture was reground and fired again, this time bringing the sample to 850 °C over a period of 24 hours and then holding for 2 days. The sample was reground, pelletized, and sintered at 930 °C for 24 hours.

$Li_3V_2(PO_4)_3$ was prepared by solid state reaction described by Yin et al.[2] Stoichiometric amounts of ^6Li enriched Li_2CO_3 (Sigma Aldrich, 95% atom ^6Li), V_2O_5 (Alfa Aesar, 99.6%), and $NH_4H_2PO_4$ (Sigma Aldrich, 99%) were ground together and heated to 300°C for 3 hours. The mixture was reground and fired at 850°C for 12 hours under a flow of 5% H_2/N_2.

Synthesized samples were characterized using a PANalytical diffractometer with Cu $K\alpha_1$ radiation ($\lambda = 1.5406$ Å). Data was collected from 10 – 90 ° in 2θ step size of 0.016 with a step time of 100 s. The reflections were indexed in agreement with the literature.[2,3]

5.2.2 Solid-State NMR.

For the SSNMR study of $Li_3Fe_2(PO_4)_3$, variable temperature 1D ^6Li MAS NMR and 2D EXSY spectra were acquired at a Larmor frequency of 29.4 MHz on a Bruker AMX 200 spectrometer. A custom-built double resonance probe supporting 1.8 mm rotors capable of MAS frequencies of 25 kHz up to 45 kHz was used. Temperatures were calibrated using $Pb(NO_3)_2$ as described elsewhere.[4] The spectra were referenced to 1 M ^6LiCl (aq) (0 ppm). ^6Li 1D spectra were acquired using a Hahn-echo pulse sequence with a 90° pulse of 2.5 μs and recycle delay of 50 ms. T_1 relaxation times were determined using a standard saturation recovery sequence. 2D exchange spectra were acquired using mixing times from 100 μs to 8 ms. The number of slices in the indirect dimension was 512. Phase-sensitive detection in t_1 was achieved through the use of States-TPPI.[5]

For the variable temperature study of electrochemically cycled $Li_3V_2(PO_4)_3$, ^6Li MAS spectra were acquired at a Larmor frequency of 44.1 MHz on a Bruker AV300 spectrometer. A custom-built double resonance probe supporting 1.8 mm rotors capable of MAS frequencies of 25 kHz up to 45 kHz was used. Temperatures were calibrated using $Sm_2Sn_2O_7$ as described elsewhere.[6] The spectra were referenced to 1 M ^6LiCl (aq) (0 ppm). ^6Li 1D spectra were acquired using a Hahn-echo pulse sequence with a 90° pulse of 2.5 μs and recycle delay of 200 ms.

5.2.3 Electrochemical Measurements

The positive electrode material was prepared by combining the active material ($Li_3V_2(PO_4)_3$) in a 75:15:10 weight ratio with carbon black (CB) and polyvinylidene fluoride (PVDF). This mixture was made into a slurry with N-methl-2-pyrrolidine (NMP) (Sigma Aldrich) as a solvent and cast onto Al foil. Cathode discs of 1.27 cm in diameter were assembled in coin cell casings with $LiPF_6$ as the electrolyte (1M $LiPF_6$ in a 1:1wt% ethylene carbonate:dimethylcarbonate solvent, Novolyte) and Li-metal as the negative electrode. Cells were cycled on a VMP multichannel potentiostat at a rate of C/100 using a Galvanostatic Intermittent Titration Technique (GITT).

5.2.4 Bond Valence Density Maps

Bond valence density maps were generated for each crystal structure using the *VALMAP* program developed by Gonzalez-Platas *et al.*[7] This program takes the crystallographic input data including unit cell parameters and atomic coordinates, and calculates the bond valences density within a three-dimensional unit cell using the empirical parameters of Brown *et al.*[8,9] In this work, two-dimensional planes of bond valence density were extracted using the atomic coordinates of atoms defining a Li ion diffusion pathway. For each map, a 1.5 Å radius is shown with a bond valence density contour level increment is 0.485.

5.3 Results and Discussion

5.3.1 ^{6}Li 2D EXSY Study of $Li_3Fe_2(PO_4)_3$

The iron phosphate family of materials including the olivine $LiFePO_4$,[10] NASICON $Li_3Fe_2(PO_4)_3$,[11] and monoclinic $Li_3Fe_2(PO_4)_3$,[1,12] have been an exceptional point of interest due to their low cost and low environmental impact. The appreciable redox potentials of the Fe^{3+}/Fe^{2+} redox couple for these materials occur at approximately 3.43, 3.55, and 2.8 V vs. Li^+, respectively. Despite the advantages of using the iron phosphate materials, overall these compounds exhibit surprisingly poor electronic and ionic conductivity, which has limited their commercial success. Lithium NMR is well known to be an in-depth tool for studying structural and dynamic factors that can lead to poor electrochemical performance.[13-16] Lithium in these materials is directly involved in the electrochemical process and moreover, shows sensitivity to electronic changes that may take place in the surrounding lattice during lithium extraction, making it an interesting nucleus for solid-state NMR studies.

$Li_3Fe_2(PO_4)_3$ crystallizes in a structure similar to the open framework NASICON structure with space group $P2_1/n$.[3] The structure is a three dimensional framework of FeO_6-octahedra and PO_4-tetrahedra (**Figure 5.1**). There are three crystallographically unique Li sites where Li1 occupies the tetrahedral position and Li2 and Li3 both occupy the distorted trigonal bipyramidal sites.

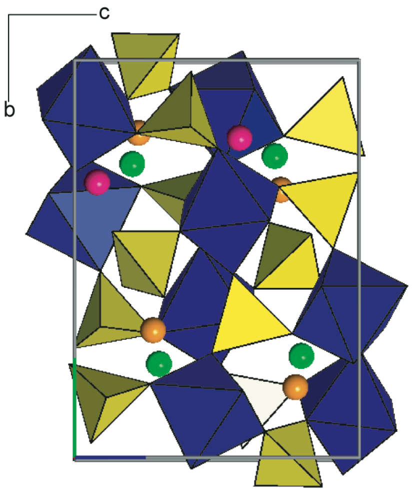

Figure 5.1 - Unit cell of monoclinic $Li_3Fe_2(PO_4)_3$ along the *a*-axis. FeO_6 octahedra (blue) are connected to PO_4^{3-} tetrahedra (yellow) at oxygen vertices. Li1 (orange), Li2 (pink) and Li3 (green) sit in channels formed by the PO_4 and FeO_6 units.

5.3.1.1 ^{6}Li MAS NMR and Site Assignment of $Li_3Fe_2(PO_4)_3$

The three Li crystallographic positions of $Li_3Fe_2(PO_4)_3$ (**Figure 5.1**) were resolved in the 1D ^{6}Li NMR spectrum with MAS of 25 kHz (**Figure 5.2**). Resonances which arise at 45 ppm, 102 ppm, and 216 ppm, are designated as sites A, B, and C, respectively. An assignment of the ^{6}Li resonances to the crystallographic positions was made based on the geometry dependent electron spin density transfer from the paramagnetic iron center to the Li and P atoms.[8,17] Note that the assignment presented here differs from the assignment made in the original manuscript.[18] This amendment is made in light of the density functional results of Kim *et al.* as well as the assignment presented by Castets *et al.*[19,20]

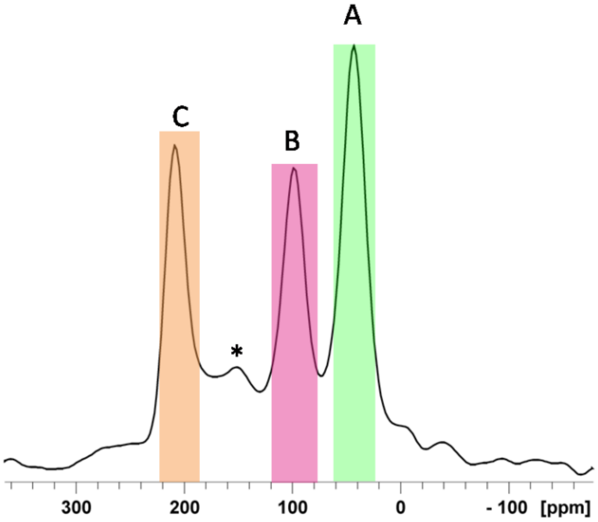

Figure 5.2 - ^{6}Li MAS NMR spectrum of $Li_3Fe_2(PO_4)_3$ with MAS = 25 kHz. Asterisk denotes peak belonging to impure phase.

The assignment of the Li shifts is rationalized based on the Fermi-contact rules outlined in Chapter 2. For $Li_3Fe_2(PO_4)_3$, the Fe^{3+} has an electron configuration of high spin $t_{2g}^3e_g^2$. The overall chemical shift range (Table 2) for the three Li crystallographic sites of $Li_3Fe_2(PO_4)_3$ is significantly higher (45 – 216 ppm) than that of the vanadium analogue (17-107 ppm).[2,13] This is consistent with the addition of one more unpaired electron in the t_{2g} orbitals and the assertion that the delocalization mechanism is often dominant over the polarization mechanism.[21] Therefore, the 1D ^{6}Li MAS NMR spectrum was assigned based on the crystallographic data, using a similar approach to the $Li_3V_2(PO_4)_3$ case.[13] The highest chemical shift, C, is assigned to Li2 which showed orbital interactions with the strongest 90° overlap (90.28° and 89.47°) (**Table 5.1**). The lowest resonance, A, at 45 ppm is assigned to Li3 which has the poorest Li-O-Fe overlap.

Site B is therefore assigned to the four coordinate Li1 site which has two sites close to 90° (93.98° and 92.61°).

Table 5.1 – Summary of crystallographic data for $Li_3Fe_2(PO_4)_3$with assignment to the A, B, and C, resonance provided.[22]

Li Site	O label	Li-O Distance (Å)	Li-Fe Distance (Å)	Li-O-Fe Angle
Li1 (C)	O1	1.9568	2.869	92.61
	O9	1.9395	2.869	93.98
	O3	1.9598	3.055	98.26
	O11	1.9838	3.055	97.91
Li2 (B)	O3	2.1878	3.025	90.28
	O7	1.8989	3.025	102.47
	O2	2.5040	2.870	77.41
	O4	2.0924	2.870	85.10
	O12	1.9720	2.870	89.47
Li3 (A)	O2	1.9384	3.538	126.61
	O4	1.9613	2.739	83.39
	O12	2.5084	2.739	72.27
	O8	1.9508	2.739	87.73
	O11	2.2549	3.582	111.90

5.3.1.2 ^{6}Li 2D EXSY Over a Variable Temperature Range

^{6}Li 2D EXSY experiments were used for determining the timescales and activation energies of ion hopping in $Li_3Fe_2(PO_4)$. As outlined in Chapter 3, in a 2D EXSY experiment each spin is frequency labeled during the evolution period, t_1. The exchange processes are allowed to take place during the following mixing period of set length, τ_m. Through successive experiments, the integrated volume of the cross peaks plotted as a function of mixing time yields a correlation time for the exchange process. Since the mixing period is limited by the spin-lattice relaxation time (T_1) of the spins, the increased number of unpaired electrons had a profound effect on the T_1 times when comparing the Fe and V compounds. For $Li_3V_2(PO_4)_3$ ^{7}Li relaxation times for all three resonance were on the order of 6.0 ± 0.2 ms. For $Li_3Fe_2(PO_4)_3$, ^{7}Li T_1 times for all resonances were shortened significantly to 1.1 ± 0.2 ms due to the addition of 3 unpaired electrons at the Fe metal center. In order to achieve a first-order exponential buildup to extract an accurate correlation time, mixing times longer than 1 ms were needed. A smaller quadrupole moment and lower magnetogyric ratio for ^{6}Li gives weaker dipolar coupling values than the ^{7}Li counterpart, resulting in longer T_1 relaxation values. Therefore, samples of $Li_3Fe_2(PO_4)_3$ were prepared with ^{6}Li enriched LiOH which increased T_1 times for all three sites to 8.0 ± 0.2 ms and allowed for longer mixing times to be used.

Figure 5.3 shows ^{6}Li 2D EXSY spectra acquired at 311 K at two different mixing times. For the shorter mixing time of 0.5 ms, exchange was not observed (**Figure 5.3**.a). When the mixing time was increased to 3.0 ms (**Figure 5.3**.b), exchange is observed between all three resonances giving AB, BC, and AC crosspeaks.

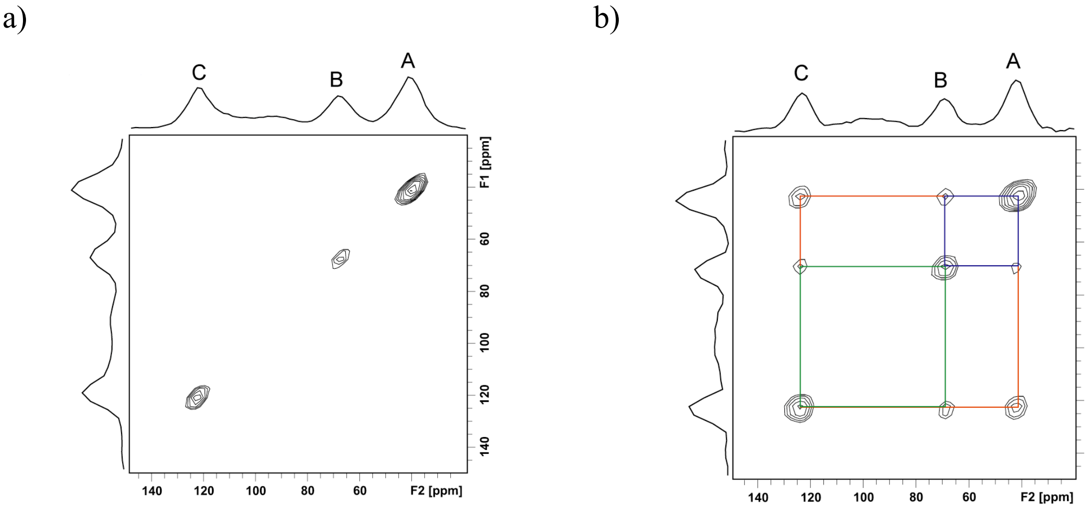

Figure 5.3 – ^{6}Li 2D EXSY spectrum at MAS = 25 kHz, T = 311 K, with a) τ_{mix} = 0.5 ms and b) τ_{mix} = 3.0 ms

Hopping rates for each exchange pair were determined by measuring the cross peak intensity (normalized to the sum of the intensities of the diagonal peaks) as a function of mixing time (**Figure 5.4**). By fitting this data to a first order exponential function, correlation times, τ_c, and jump rates (k) were extracted at each temperature (**Table 5.2**).

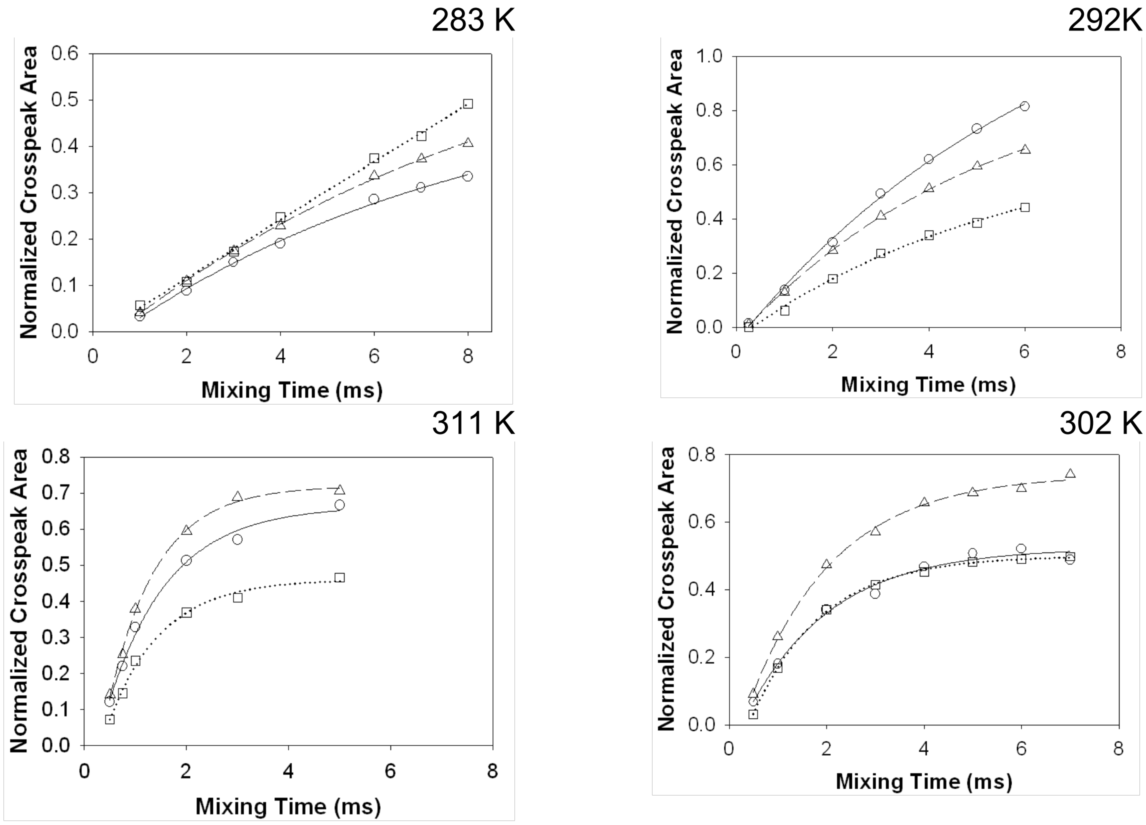

Figure 5.4 – Normalized cross peak volume as a function of mixing time for exchange pair AB (□), BC (○), and AC (△) for $Li_3Fe_2(PO_4)_3$. Clockwise from top left acquisition temperatures for each data set are 283 K, 292 K, 302 K, and 311 K. Due to T_1 limitations, plateaus, for lower temperature data sets were not achieved.

Table 5.2 – Summary of exchange rates determined from ^{6}Li 2D EXSY measurements over a variable temperature range for $Li_3Fe_2(PO_4)_3$.

Temperature (K)	k_{AB} (s^{-1})	k_{BC} (s^{-1})	k_{AC} (s^{-1})
283	8 ± 16	100 ± 50	100 ± 50
292	200 ± 100	150 ± 50	200 ± 100
302	700 ± 200	600 ±100	600 ± 100
311	1000 ± 200	800 ± 200	1000 ± 200

The large relative error on the lowest temperature rate (283 K) for the AB exchange pair is due to the linear appearance of the cross peak build-up prior to the onset of T_1 relaxation (**Figure 5.4** top left). Due to the dynamic limitations within this material, the range of temperatures for the exchange experiments was limited. At temperatures below 283 K, the dynamics were too slow for a sufficient buildup curve to be attained within the limits of the T_1 times. At higher temperatures, the three resonances began to coalesce due to fast mobility making accurate integration of the crosspeaks difficult. The jump rates from multiple integrations were averaged and error determined at the 95% confidence level. This error was insignificant as compared to the error from the first order exponential fit and therefore this latter error was propagated into the Arrhenius analysis.

The activation energies, E_a, for each exchange pair were determined by plotting natural log of the rates as a function of 1000/T in an Arrhenius analysis (**Figure 5.5**). Errors for the E_a values were calculated from the standard error of the slope from the regression analysis. Exchange between sites AC and BC is the most energetically favourable having activation energies of 0.63 (±0.03) eV and 0.59 (± 0.05) eV. A higher energy barrier is observed for the AB exchange pair, however it is noted that a poor linear fit is found when the low temperature data point (carrying the large error) is used. The energy barrier was therefore calculated again but this time with the AB 283 K data point set to the uppermost limit of the error bound. The result is a better linear fit and an activation energy of 0.81 ± 0.04 eV that is still considerably higher than the AC and BC ion hops.

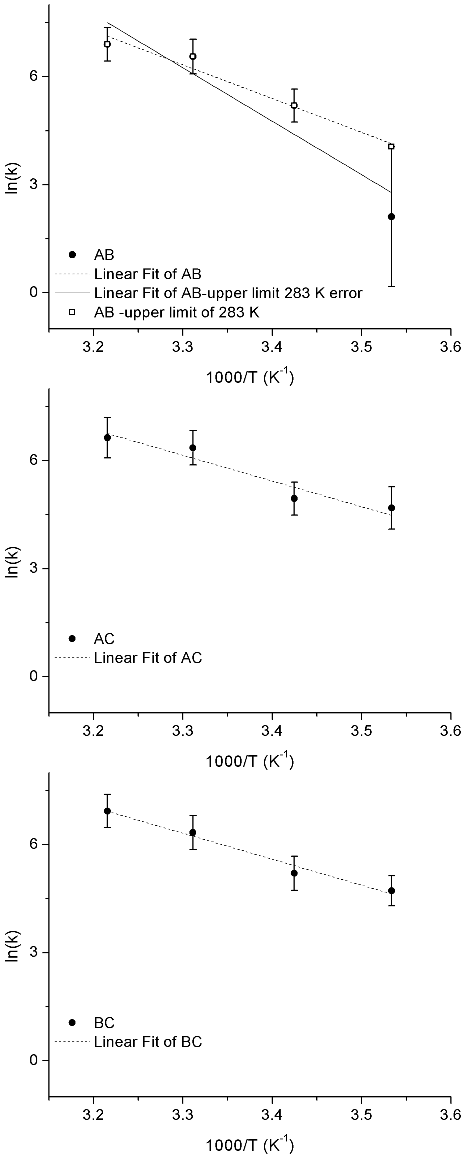

Figure 5.5 – Arrhenius analysis for determination of activation energies for Li-Li hopping between exchange pairs AB (top), AC (middle), and BC (bottom). For the AB exchange pair (top), the large error bar of the lowest temperature data point (283K) obscures the fit significantly. The analysis was therefore performed with the 283 K data point set to the uppermost limit of the error bar to yield a better linear fit (open squares with dashed linear fit (top)).

5.3.1.3 Correlating E_a to Structural Constraints in $Li_3Fe_2(PO_4)_3$

The energy barriers observed in $Li_3Fe_2(PO_4)_3$ were evaluated in relation to structural constraints present in the host framework. In the previous report of the ion dynamics in $Li_3V_2(PO_4)_3$, the energy barriers of the ion hopping were found to be higher in ion pairs where longer internuclear distances coupled with smaller bottlenecks of diffusion (summarized in **Table 5.3**).[13] Bottlenecks of diffusion in both $Li_3Fe_2(PO_4)_3$ and $Li_3V_2(PO_4)_3$ were defined as the area created by O vertices of PO_4 and FeO_6 polyhedra that were found along the pathway of a Li-Li exchange pair.[16]

Table 5.3 - Summary of activation energy values for the three Li-Li exchange pairs as well as the calculated Li-O bottlenecks of diffusion for $Li_3V_2(PO_4)_3$.[13]

NMR Sites	Li Site	E_a (eV)[13]	Li-O bottleneck (Å^2)	Li-Li distance (Å)
BC	Li1-Li2	0.83 ± 0.01	3.69	3.43(3)
AB	Li1-Li3	0.73 ± 0.01	4.10	3.08(3)
AC	Li2-Li3	0.79 ± 0.01	3.79	3.28(3)

For $Li_3Fe_2(PO)_3$, no such correlation exists. Rather, the highest energy barrier observed has the most open bottleneck area and the shortest internuclear distance (**Table 5.4**).

Table 5.4 - Summary of activation energy values for the three Li-Li exchange pairs as well as the calculated Li-O bottlenecks of diffusion for $Li_3Fe_2(PO_4)_3$.

NMR Sites	Li Site	E_a (eV)	Li-O bottleneck (Å^2)	Li-Li distance (Å)
BC	Li1-Li2	0.59 ±0.05	3.96	3.139
AC	Li1-Li3	0.63 ±0.03	3.61	3.417
AB	Li2-Li3	0.81 ± 0.04	4.22	3.110

To better explain the observed trends of the energy barriers within $Li_3Fe_2(PO_4)_3$, the influence that bond valence sum (BVS) values have on ion mobility was investigated. BVS values are a measure of how tightly bound a Li ion is within its crystallographic position. High BVS values indicate a tightly bound Li environment while more loosely bound Li will have lower BVS values.[9,23] In $Li_3Fe_2(PO_4)_3$ the BVS values of each Li ion at the crystallographic positions fall very close to one another with Li1, Li2, and Li3 BVS values of 1.054, 0.952, and 0.989, respectively and subsequently do not shed light on the observed trends in exchange energy barriers. Bond valence density maps were therefore calculated for each of the exchange pathways given in **Table 5.4**. In these maps, regions of high bond valence density are less amenable to Li ion diffusion while low bond valence density leads to favourable pathways for Li mobility.[23,24]

Figure 5.6 shows the bond valence density maps where for a given exchange pair, a plane was defined by the coordinates of the O-atoms that create the faces of each ion that are directed towards one another. Using Li1-Li2 exchange as an example, the face of the Li1 atom directed towards the Li2 face is defined by atoms O1, O11, and O3. The O3 atom is shared with the Li2 polyhedron with O7 and O12 atoms completing the Li2 face. By calculating the midpoint between the unshared oxygen atoms arising from each face (i.e. the midpoints between the O1-O12 atoms and the O7-O11 atoms) a plane between the Li1 and Li2 faces is defined (**Figure 5.6** left column). In each BVS map, lines are drawn on the bond valence map to show the angles at which the diffusion region extends from the shared atoms to the coordinates of the mid-point for the unshared atoms.

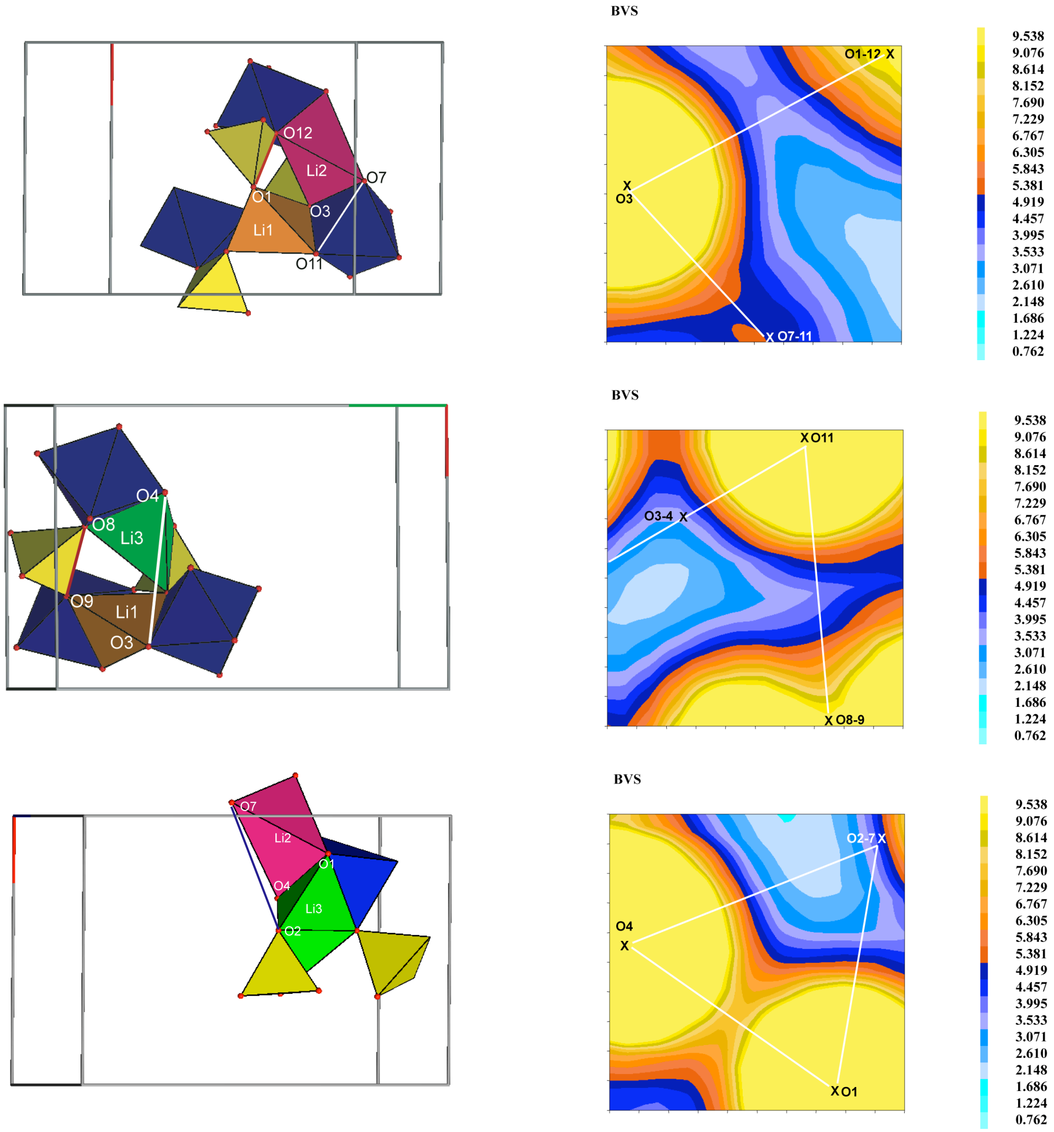

Figure 5.6 – Bond valence maps (right column) for the Li1-Li2 (top), Li1-Li3 (middle), and Li2-Li3 (bottom) exchange pathways. The maps shown were defined by the plane of the vertices of the faces of the Li-polyhedra orientated towards each other for exchange, with a 1.5 Å radius and contour increment of 0.485. A schematic showing how these panes were defined is shown in the right column for the Li1-Li2 (top), Li1-Li3 (middle), and Li2-Li3 (bottom) exchange pathways. On each map the coordinates of shared atoms and midpoints are given with lines radiating from shared atoms to midpoints of unshared atoms.

The geometries of the Li1-Li2 and Li1-Li3 pathways have an appreciable region of low bond valence density available for the Li ions to diffuse. The similarity in appearance of the bond valance maps corresponds well to these two ion hopping pairs having energy barriers equivalent within error (0.59 ±0.05 and 0.63 ± 0.03 for Li1-Li2 and Li1-Li3, respectively). For Li2-Li3 on the other hand, the anchoring of the Li2 and Li3 atoms to the edge of a Fe octahedral environment (via O4 and O1), leads to a high-density region dominating the diffusion pathway which does not have the "open" features observed in the Li1-Li2 and Li1-Li3 maps. This highlights why a higher energy barrier is found for the Li2-Li3 exchange process. Moreover, the position of the edge-shared Fe octahedron relative to the Li ions (as shown in the spherical representation of the Li ions) shows the Fe obstruction along the Li-pathway **Figure 5.7**. For the corner-shared geometries, the prominence of the Fe atoms along the pathway is less severe.

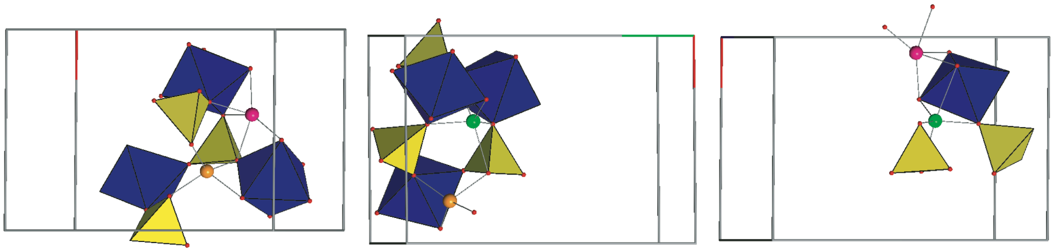

Figure 5.7 - Schematic showing the geomtries of the shared polyhedra of the Li ion sites undergiong ion exchange in $Li_3Fe_2(PO_4)_3$, Li1-Li2 left, Li1-Li3 middle and Li2-Li3 left.

Correlation of the exchange information of $Li_3Fe_2(PO_4)_3$ to the available electrochemical data remains the focus of ongoing work. While these results show that the dynamics in the parent $Li_3Fe_2(PO_4)_3$ compound are more energetically favourable than in the parent $Li_3V_2(PO_4)_3$ material, overall the Fe intercalation cathode is not as interesting from a commercial standpoint as the vanadium analogue. Not only does $Li_3V_2(PO_4)_3$ have an overall higher operating potential with three reversible voltage plateaus of 3.59, 3.67, and 4.06 V but it also has one of the highest theoretical capacities of all the phosphates (about 197 mAh/g).[25,26] In the case of $Li_3V_2(PO_4)_3$, results from the 2D EXSY study correlated well to the order in which the Li ions are extracted from the parent material. In the case of $Li_3Fe_2(PO_4)_3$, the potential of the Fe^{3+}/Fe^{4+} redox pair lies well outside the operating voltage window of a typical Li ion battery meaning that extraction of Li1, Li2, and Li3 from the iron material studied here is not possible for electrochemical applications. Instead, electrochemists exploit the Fe^{3+}/Fe^{2+} redox pair through insertion of fourth and fifth lithium ions into the structure, giving two voltage plateaus at 2.65 V and 2.85 V. Therefore, a direct correlation of the activation energies for ion hopping in the parent material to electrochemical extraction of lithium is not possible for $Li_3Fe_2(PO_4)_3$. Rather, we anticipate significant changes in local lithium dynamics upon chemical or electrochemical insertion of excess lithium.

5.3.2 ^{6}Li MAS Study of Electrochemically Cycled $Li_xV_2(PO_4)_3$

Here preliminary results demonstrating changes to ion mobility in $Li_xV_2(PO)_3$ as it is electrochemically cycled from x = 3 to x = 2 are presented. Previous reports have linked the ion dynamics of the as-prepared phase to the order in which the Li ions are extracted from the lattice, giving rise to new, intermediate phases. Specifically, Yin *et al.* showed the existence of new, single phases, when $Li_xV_2(PO_4)_3$ was cycled to points found midway between voltage plateaus.[2] These results showed that Li3 is extracted first while Li1 and Li2 are more energetically costly and therefore removed as second and third sites, respectively. This analysis agreed well with the energy barriers found from the 2D EXSY work of Cahill *et al.* and highlighted how the dynamics of the as-prepared phase influences the electrochemical performance.[13]

Here ^{6}Li MAS NMR measurements are used to characterize Li environments in $Li_xV_2(PO_4)_3$ after being electrochemically cycled to points along the voltage plateaus (not midway between). **Figure 5.8** shows the Galvanostatic Intermittent Titration Technique (GITT) experiments used to extract 0.8 Li from $Li_3V_2(PO_4)_3$. GITT experiments have current applied for a set time before being switched off to allow the system to reach equilibrium. This method ensures a 1:1 Li:electron removal. In this experiment, due to the low sample size of electrochemically cycled cathode materials, two separate coin cells were combined after being cycled to near equivalent compositions (**Figure 5.8**, left). The MAS spectra of the pristine and cycled samples are shown in **Figure 5.8**, right. There is an observed narrowness of the cycled peaks not observed in the as-prepared sample. We attribute this to a mixing of the active material with carbon black and binder as this same narrowing was observed in a ^{6}Li NMR spectrum of the uncycled cast (**Figure 5.9** middle). There is no observed change to the paramagnetic shift of the cycled sample indicating that no new Li environments have emerged in spite of electron changes at the transition metal center. This is not entirely unexpected as the flat voltage plateau indicates a two-phase extraction and although removal may be initiated from a preferred site, the fast ion exchange allows the sites to equilibrate over the crystallographic positions. The cycled sample with x = 2.2 is therefore more accurately described as the two-phase $0.73Li_3V_2(PO_4)_3$:$0.27V_2(PO_4)_3$.

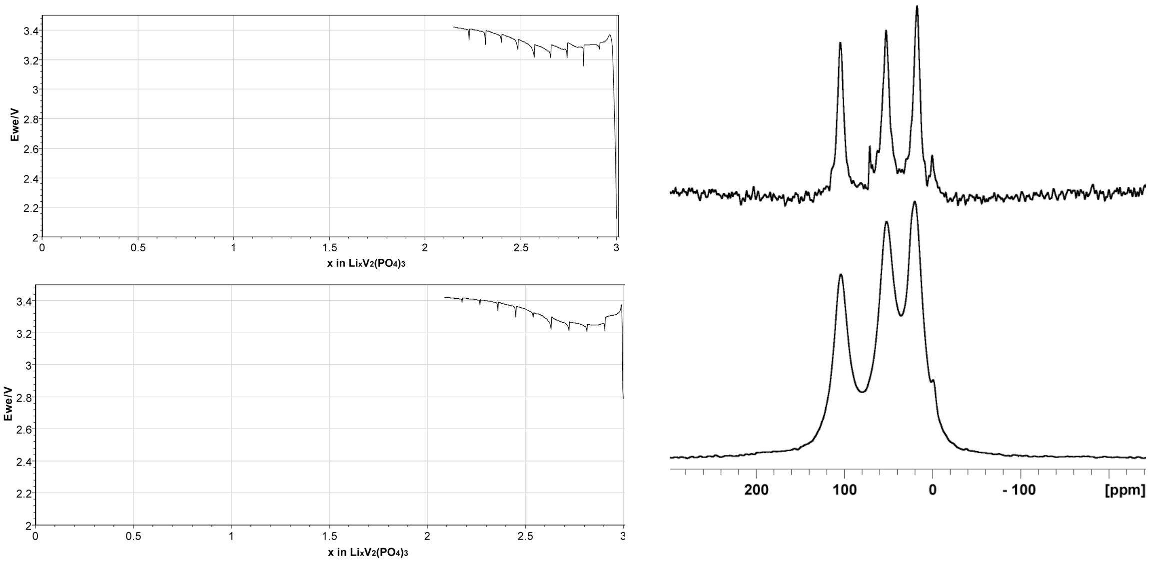

Figure 5.8 – Right: GITT experiments of the two coin cells combined for NMR measurements. Cells were each cycled to x ~ 2.2. Left: ^{6}Li MAS spectra of the as-prepared $Li_3V(PO_4)_3$ (bottom) and the cycled material.

The sample size from the two coin cells was too small for quantitative methods such as 2D EXSY to be used for determination of ion dynamics. Therefore, a preliminary qualitative picture of the ion dynamics was made through variable temperature ^{6}Li 1D MAS measurements of the pristine sample as compared to the uncycled cast and the cycled material (**Figure 5.9**).

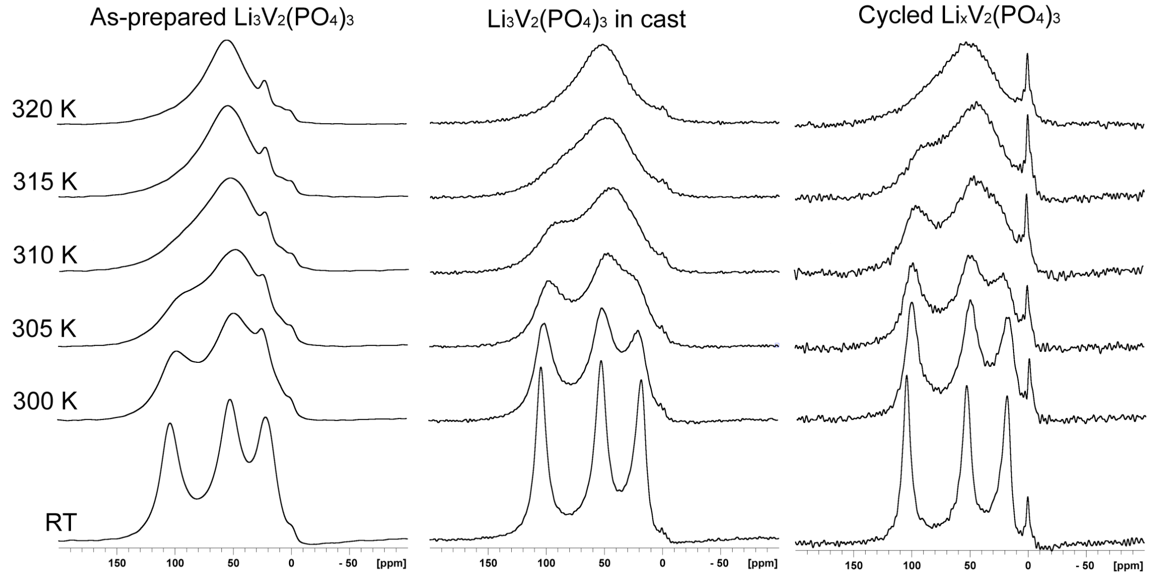

Figure 5.9 – ^{6}Li MAS spectra under variable conditions of as-prepared $Li_3V_2(PO_4)_3$, an uncycled cast of $Li_3V_2(PO_4)_3$ with carbon black and PVDF (middle) and a sample cycled to x =2.2 giving $0.73Li_3V_2(PO_4)_3:V_2(PO_4)_3$

For the as-prepared $Li_3V_2(PO_4)_3$, the coalescence of the three environments gives a resonance with single site features at 315 K. Two small diamagnetic impurities centered at 0 and 20 ppm are also observed but do not interact with the phase of interest and are therefore ignored. When $Li_3V_2(PO_4)_3$ is cast with CB and PVDF to form a positive electrode, the dynamics slow, and single site features do not definitively appear until 320 K. This result is presumably from increased grain boundary effects due to the introduction of the additives. After the material has been cycled to a composition of x ~ 2.2, the dynamics are slowed further, where complete coalescence has not been reached by 320 K. A diamagnetic peak is also observed here at ~ 0 ppm and is attributed to residual electrolyte from the battery casing. The slowing of the ion mobility in the cycled sample is surprising result, as the presence of a larger number of Li site vacancies is expected to increase the ion mobility. Slow dynamics may arise from immobility of the phase interface regions, which is a known problem in the phosphate family of cathode materials. Studies are currently underway to investigate this system further including measurements of samples cycled to lower Li content and applying more quantitative measurements of the ion dynamics.

5.4 Summary and Outlook

This chapter presents the first study of Li^+ dynamics in monoclinic $Li_3Fe_2(PO_4)_3$. Exchange between the crystallographic Li sites was found to be on the millisecond timescale. By plotting the change in jump rate as a function of temperature the activation barriers for Li ion exchange were determined. The activation energies, ranging from 0.59 (± 0.05) eV to 0.81 (± 0.04) eV, did not correlate to Li-Li internuclear distances nor the Li-O bottlenecks along the diffusion pathway. The energy barriers were more simply described by the bond valence density found along the plane defining the midpoint between the faces of the Li poyhedra undergoing ion exchange.

This chapter also presents preliminary results on the ion dynamics of $Li_3V_2(PO_4)_3$ as it is cycled to lower Li content using GITT experiments. Here, coalescence data showed a slowing of the ion mobility as the Li ions were removed from the host framework. Due to the low sample size of the cathodes used in the current coin cell design, 2D EXSY measurements are not possible for quantification of ion hopping timescales. Future studies could not only increase the number of cathodes that are combined for an experiment, but also utilize 1D selective inversion methods which are a more time-efficient method for determining ion hopping rates than 2D EXSY. Details of the selective inversion experiments and how they can be applied to paramagnetic systems are outlined in the next chapter.

5.5 References

(1) Padhi, A. K.; Nanjundaswamy, K. S.; Masquelier, S.; Okada, S.; Goodenough, J. B. *J. Electrochem. Soc.* **1997**, *144*, 1609

(2) Yin, S. C.; Grondey, H.; Strobel, P.; Anne, M.; Nazar, L. F. *J. Am. Chem. Soc.* **2003**, *125*, 10402.

(3) Bykov, A. B.; Chirkin, A. P.; Demyants, L. N.; Doronin, S. N.; Genkin, E. A.; Ivanov-Shits, A. K.; Kondratyuk, I. P.; Maksimov, B. A.; Mel'kinov, O. K.; Muradyan, L. N.; Simonov, V. I.; Timofeeva, V. A. *Solid State Ionics* **1990**, *38*, 31.

(4) Takahashi, T.; Kawashima, H.; Sugisawa, H.; Bab, T. *Solid State Nucl. Magn. Reson.* **1999**, *15*, 119.

(5) Marion, D.; Ikura, M.; Tschudin, R.; Bax, A. *J. Magn. Reson.* **1989**, *85*, 393.

(6) Grey, C. P.; Cheetham, A. K.; Dobson, C. M. *J. Magn. Reson. Ser. A* **1993**, *101*, 299.

(7) Gonzalez-Platas, J.; Gonzalez-Silgo, C.; Ruiz-Perez, C. *J. Appl. Crystallogr.* **1999**, *32*, 341.

(8) Brown, I. D.; Wu, K. K. *Acta Crystallogr. Sect. B-Struct. Commun.* **1976**, *32*, 1957.

(9) Brown, I. D. *Chem. Soc. Rev.* **1978**, *7*, 359.

(10) Padhi, A. K.; Nanjundaswamy, K. S.; Goodenough, J. B. *J. Electrochem. Soc.* **1997**, *144*, 1188

(11) Padhi, A. K.; Manivannan, V.; Goodenough, J. B. *J. Electrochem. Soc.* **1998**, *145*, 1518.

(12) Masquelier, C.; Padhi, A. K.; Nanjundaswamy, K. S.; Goodenough, J. B. *J. Solid State Chem.* **1998**, *135*, 228.

(13) Cahill, L. S., Chapman, R. P., Britten, J. F., Goward, G. R. *J. Phys. Chem. B* **2006**, *110*, 7171.

(14) Grey, C. P.; Lee, Y. J. *Solid State Sci.* **2003**, *5*, 883.

(15) Cahill, L. S.; Kirby, C. W.; Goward, G. R. *J. Phys. Chem. C* **2008**, *112*, 2215.

(16) Makimura, Y.; Cahill, L. S.; Iriyama, Y.; Goward, G. R.; Nazar, L. F. *Chem. Mater.* **2008**, *20*, 4240.

(17) Grey, C. P.; Dupre, N. *Chem. Rev.* **2004**, *104*, 4493.

(18) Davis, L. J. M.; Heinmaa, I.; Goward, G. R. *Chem. Mater.* **2010**, *22*, 769.

(19) Kim, J.; Middlemiss, D. S.; Chernova, N. A.; Zhu, B. Y. X.; Masquelier, C.; Grey, C. P. *J. Am. Chem. Soc.* **2010**, *132*, 16825.

(20) Castets, A.; Carlier, D.; Trad, K.; Delmas, C.; Menetrier, M. *J. Phys. Chem. C* **2010**, *114*, 19141.

(21) Grey, C. P., Dupree, Nicolas *Chemical Reviews* **2004**, *104*, 4493.

(22) Bykov, A. B.; Chirkin, A. P.; Demyanets, L. N.; Doronin, S. N.; Genkina, E. A.; Ivanovshits, A. K.; Kondratyuk, I. P.; Maksimov, B. A.; Melnikov, O. K.; Muradyan, L. N.; Simonov, V. I.; Timofeeva, V. A. *Solid State Ionics* **1990**, *38*, 31.

(23) Brown, I. D. *Chem Rev* **2009**, *109*, 6858.

(24) Schindler, M.; Hawthorne, F. C.; Alexander, M. A.; Kutluoglu, R. A.; Mandaliev, P.; Halden, N. M.; Mitchell, R. H. *J. Solid State Chem.* **2006**, *179*, 2616.

(25) Morgan, D.; Ceder, G.; Saidi, M. Y.; Barker, J.; Swoyer, J.; Huang, H.; Adamson, G. *Chem. Mater.* **2002**, *14*, 4684.

(26) Huang, H.; Yin, S. C.; Kerr, T.; Taylor, N.; Nazar, L. F. *Adv. Mater.* **2002**, *14*, 1525.

Chapter 6 : Structural Features and Li Ion Hopping Timescales in Li_xVPO_4F from ^{6}Li MAS Measurements

6.1 Introduction

In this chapter ^{6,7}Li MAS NMR measurements are used to characterize Li environments in three samples of Li_xVPO_4F (where x = 1.0, 1.5, or 2.0). Timescales of ion hopping are quantified in the final phase, Li_2VPO_4F, using ^{6}Li 1D Selective Inversion (SI) measurements over a variable temperature range.

The tavorite-based $LiVPO_4F$ was first reported by Barker *et al.* as a high capacity (155 mAh/g) 4.1 V positive electrode material for Li ion batteries.[1] Intercalation of a second lithium to create Li_2VPO_4F takes place with a V^{3+}–V^{2+} redox potential of 1.8 V.[2] Our collaborators at the University of Waterloo have chemically prepared L_xVPO_4F (x = 1.0, 1.5, 2.0) and used powder XRD to characterize the structural changes of the host framework as $LiVPO_4F$ transforms from triclinic space group P -1 (isostructural to many known fluorophosphates)[3,4] to monoclinic Li_2VPO_4F (space group C 2/c). This structure is proposed to have three-dimensional conduction pathways which is considerably advantageous over more well-known cathode materials including olivine $LiFePO_4$ which is restricted to 1D tunnels for conduction.[5] Here we evaluate the new Li environments generated through lithiation using ^{6,7}Li MAS NMR and determine the propensity for 3D diffusion within the reduced phase.

This thesis also introduces the use of one-dimensional selective inversion (1D SI) methods to determine the ion hopping rates in the fully lithiated, Li_2VPO_4F, phase. As outlined in Chapter 3, 1D SI experiments monitor the return of magnetization to equilibrium conditions following the selective inversion of a single lithium environment. The ion relaxation is governed not only by the inherent spin-lattice relaxation of the nuclei, but also by the rate of ion exchange with non-inverted spins. Conversely, non-inverted spin(s) show attenuation of signal intensity as a function of time during the period where ion exchange is the dominant mechanism for relaxation of the inverted spin.[6,7] By fitting the experimental data in a program such as CIFIT, timescales of ion exchange can reliably be separated from inherent T_1 properties[8,9]. These 1D experiments are more efficient in terms of spectrometer time as compared to their 2D counterparts and thus warrant investigation. Moreover, this method reveals timescales of ion hopping in materials where the Li ions exchange slowly relative to their T_1 spin-lattice relaxation. As was shown in the ^{6}Li 2D EXSY study of Chapter 5, considerable error was introduced in the EXSY buildup curves as the dynamics slowed and the mixing times were limited to the longest $T_{1.}$ This situation is particularly relevant to cathode materials for lithium ion batteries, where the unpaired electrons of the transition metal centers provide a dominant mechanism for rapid relaxation. The aim of the remainder of this thesis is to expand the use of 1D selective inversion experiments to allow for ion hopping timescales to be quantified in a larger range of materials that were previously excluded due to T_1 limitations.

The results of this chapter were published in two different manuscripts. The first paper was submitted to the journal, *Chemistry of Materials* (2011, in press, cm-2011-01773n.R1) with authorship of B. Ellis, T. N. Ramesh, L. J. M. Davis, G. R. Goward, L. F. Nazar. Researchers from Prof. Nazar's group at the University of Waterloo, B. Ellis and T.N. Ramesh, prepared samples of Li_xVPO_4F (x = 0, 1.5, 2.0). Electrochemical measurements as well as Rietveld analysis of crystallographic data were also carried out in the Nazar group. All NMR measurements and analysis was carried out at McMaster University under the supervision of Prof. Goward. A second manuscript of the ^{6}Li 1D EXSY measurements on Li_2VPO_4F was submitted to the *Journal of Physical Chemistry C*, (2011, in press, DOI 10.1021/jp2059408). The authorship on this work was L.J.M. Davis, B. L. Ellis, T. N. Ramesh, L. F. Nazar, A. D. Bain, G. R. Goward. Here, I collected and analyzed all NMR data under the supervision of Prof. Bain and Prof. Goward. Members of Prof. Nazar's research group, B. L. Ellis and T. N. Ramesh, prepared the samples studied in this work.

6.2 Experimental

6.2.1 Sample Preparation

Samples of Li_xVPO_4F were prepared by collaborators at the University of Waterloo. Briefly, $LiVPO_4F$ was prepared by the method reported by Barker *et al.*:[1] V_2O_5 (Aldrich, 99%+), $NH_4H_2PO_4$ (BDH, 99%) and carbon black were mixed in a 0.5:1:1.5 molar ratio and fired at 750 °C under a flowing Ar atmosphere to produce carbon-coated VPO_4. VPO_4 and LiF were combined in stoichiometric amounts and milled with zirconia milling media for 4-6 hours. The powder was fired at 600 °C for 1 hour under an Ar atmosphere to form $LiVPO_4F$. $LiVPO_4F$ was then stirred with a stoichiometric amount of $LiAlH_4$ in tetrahydrofuran in an argon-filled glove box for 44 hours. The final product, Li_2VPO_4F, was washed with tetrahydrofuran and stored under argon.

6.2.2 Solid State NMR.

All experiments with the exception of the $^{6}Li\{^{19}F\}$ REDOR and ^{6}Li 1D EXSY measurements were carried out at field strength of 7.0 T with ^{6}Li and ^{7}Li Larmor frequencies of 44.1 and 116.6 MHz on a Bruker AV300 spectrometer. A custom built probe supporting 1.8 mm rotors was used with MAS frequencies ranging from 25-40 kHz. By adjusting spinning speeds from 25 kHz to 40 kHz, a temperature range of 303 K to 330 K was available. Both ^{6}Li and ^{7}Li 1D spectra were acquired using 90° pulse lengths ranging from 2.0 to 2.5 μs and recycle delay of 100 ms. Spin-lattice relaxation times (T_1) were determined using the standard inversion recovery sequence included in the Bruker software package. Two-dimensional exchange (EXSY) spectra were acquired using mixing times ranging from 2 ms to 17 ms. The number of slices in the indirect dimension was 2048. Phase-sensitive detection in t_1 was achieved through the use of States-TPPI.[10]

^{6}Li{^{19}F} REDOR studies were carried out on a Bruker AV500 spectrometer (11.7 T) with ^{6}Li and ^{19}F Larmor frequencies of 73.6 MHz and 469.5 MHz, respectively. The same 1.8 mm probe as described above was used for these experiments with the ^{1}H channel modified to allow for ^{19}F dephasing. A ^{19}F π pulse length of 4.40 μs was used.

1D ^{6}Li EXSY was also performed on a Bruker AV500 spectrometer with a Bruker MAS probe supporting 2.5 mm rotors. 1D EXSY experiments were performed using a 90° - τ_1 - 90° - τ_{mix} - 90° sequence, also with a 90° pulse of 2.5 μs, recycle delay of 200 ms, and 10240 scans for each slice. For our two-site system, selective inversion of the lower frequency A spin was accomplished using a 90° pulse, set on resonance to spin A. During the first [90° - τ_1- 90°] portion of the sequence, where τ_1 is set to $1/(2\Delta\nu_{AB})$, the on-resonance spin is selectively inverted following the second 90° pulse. Mixing times (τ_{mix}) were stepped over a series of 16 experiments from 5 μs to 100 ms (the latter delay time being well beyond the relaxation rates of both spins to ensure that both spins had magnetization measured at equilibrium). Nonselective Inversion (NSI) experiments were performed using the standard inversion-recovery sequence. The same variable delay list was used in the NSI as was used in the 1D EXSY experiments. In both the SI and NSI studies, a digital filter was applied to allow for acquisition and analysis of the centerband region only.

All spectra were referenced to 1 M ^{6,7}LiCl (aq) (0 ppm), and $CFCl_3$ for ^{19}F experiments. Temperatures were calibrated using $Sm_2Sn_2O_7$ as described elsewhere.[11]

6.2.3 1D EXSY Data Analysis

In each data set, slices for each mixing time/variable delay were extracted and baseline corrected. After integrating both spins involved in the exchange process, these values were normalized to the integration value of the slice collected at the longest mixing time/variable delay (where the magnetization of each spin was fully relaxed). The data was fit using the CIFIT program developed by A.D. Bain.[12] This program utilizes a table of observed intensities for all spins as a function of mixing time and determines a key set of parameters: the jump rates (k) of each chemical exchange process, spin-lattice relaxation times in the absence of chemical exchange (T_1), and the magnetization values from initial to equilibrium conditions (i.e. from $M_i(0)$ to $M_i(\infty)$). The rate matrix used to describe spin relaxation under the influence of chemical exchange is the primary mathematical model used by the CIFIT program and is described in greater detail elsewhere.[9,12,13] CIFIT adjusts the free parameters, T_1, k, $M_i(0)$ and M_i (∞), using a Levenberg-Marquardt algorithm until the sum of the squares of the differences between the experimental and calculated data is minimized. Error values of the exchange rates were approximated in the CIFIT program by the variance-covariance matrix of the fit to the data.[12]

6.2.4 Bond Valence Density Maps

Bond valence density maps were generated for each crystal structure using the VALMAP program, developed by Gonzalez-Platas *et al.*[14] This program takes crystallographic data including unit cell parameters and atomic coordinates, and calculates the bond valences density within a three-dimensional unit cell using the empirical parameters of Brown *et al.*[15,16] In this work, two-dimensional planes of bond valence density were extracted using the atomic coordinates of atoms defining a Li ion diffusion pathway. For each map, a 2 Å radius is shown with a bond valence density contour level increment is 0.485.

6.3 Results and Discussion

6.3.1 ^{6}Li MAS NMR of Li_xVPO_4F ($1 \leq x \leq 2$)

The single crystallographic site for $LiVPO_4F$ was resolved in the ^{7}Li MAS NMR spectrum collected at 330 K (MAS = 40 kHz) with a paramagnetic shift centered at 111 ppm (**Figure 6.1**). The high value for the observed shift is attributed to the geometry dependent hyperfine coupling of the Li nuclei with the unpaired electron density sitting on the V^{3+} transition metal center.[17,18] The relatively short spin-lattice relaxation time (T_1) of this resonance (6.5 ± 0.2 ms) also reflects the paramagnetic nature of the Li-resonance.

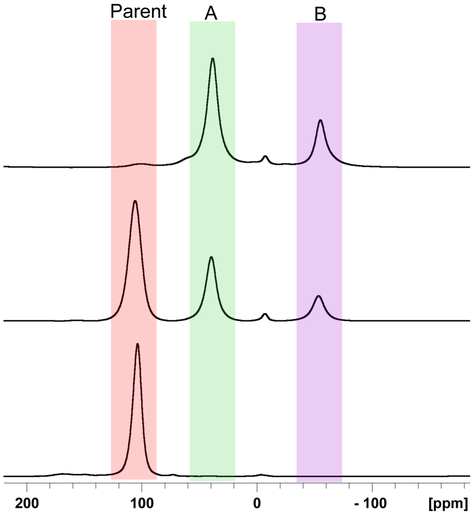

Figure 6.1 – ^{7}Li MAS (40 kHz, 330 K) spectra of Li_xVPO_4F at various stages of lithiation resulting in single site $LiVPO_4F$ (bottom), two-phase $0.5LiVPO_4F$:$0.5Li_2VPO_4F$ (middle), and single-phase Li_2VPO_4F (top)

The isotropic resonance of $LiVPO_4F$ deconvoluted to reveal a small shoulder at higher frequency (**Figure 6.2**). This is consistent with the Rietveld refinement results performed by our collaborators at the University of Waterloo. Here they refined the splitting of the Li site in $LiVPO_4F$ as a Li1:Li2 occupancy of 0.18:0.82 (**Figure 6.3**). Our NMR results deconvoluted to similar values however we assign an error of ± 0.1 giving an approximate Li1:Li2 ratio of 0.2:0.8. This site splitting is commonly observed in other lithium fluorophosphates materials as the large octahedral environments yield high thermal parameters for the Li atoms.[3,19]

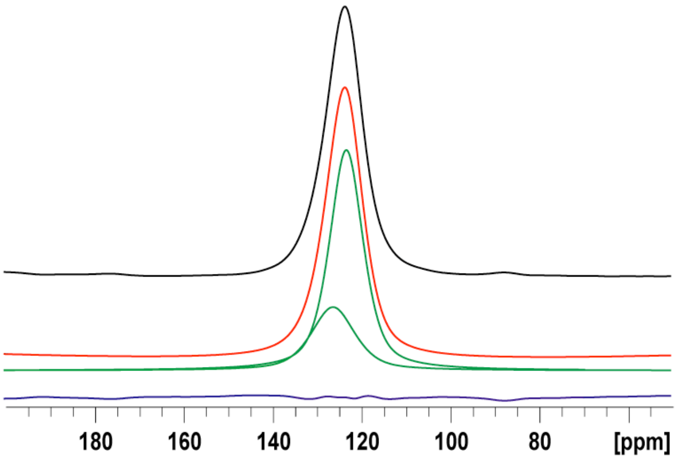

Figure 6.2 – Deconvolution of ^{7}Li MAS isotropic resonance of $LiVPO_4F$ (MAS 40 kHz, 330 K). The Li1:Li2 sites integrate in a ratio of 0.2(±0.1):0.8(±0.1).

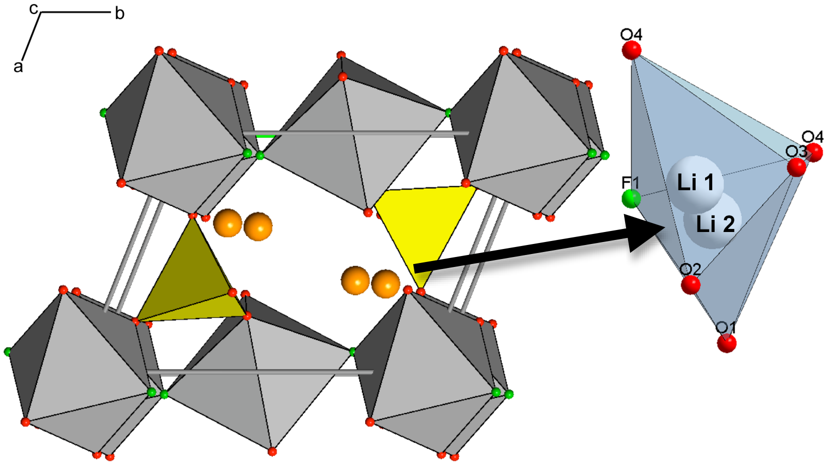

Figure 6.3 – Schematic showing the split site in $LiVPO_4F$ which both Rietveld refinement and NMR showed to be a Li1:Li2 0.18:0.82 occupancy.

Upon 50% lithiation of $LiVPO_4F$ to x = 1.5, two new resonances emerge (**Figure 6.1** middle). The first is centered at 50 ppm and the second at -52 ppm (at 330 K) (herein referred to as sites A and B, respectively). The peak belonging to the parent $LiVPO_4F$ phase remains but broadens slightly. A resonance centered at 0 ppm is also observed and is attributed to a diamagnetic Li impurity as it has a considerably longer T_1 relaxation time (> 60 s). After lithiation to Li_2VPO_4F, a slight amount of the parent $LiVPO_4F$ remains but resonances belonging to the A and B sites now dominate the spectrum. Over the entire sideband manifold, a 1:1 integration for the A:B sites is found and clearly correspond to the two independent lithium ions in the fully reduced phase. The phase at x =1.5 therefore is better described as biphasic $0.5LiVPO_4F$:$0.5Li_2VPO_4F$.

The ^7Li spin lattice relaxation times for sites A and B were 3.2 ± 0.2 ms and 2.0 ± 0.2 ms, respectively. The lower times *vis a vis* the parent $LiVPO_4F$ are consistent with the increase in unpaired electron spin density observed in these systems that leads to stronger electron-Li dipolar coupling values (**Table 6.1**).

Table 6.1 - Summary of ^7Li spin-lattice relaxation times (T_1) for $LiVPO_4F$ and Li_2VPO_4F at 4.7 T

Sample	T_1 times (ms)		
	Parent $LiVPO_4F$	A	B
$LiVPO_4F$	6.5 ± 0.2	-	-
Li_2VPO_4F	-	3.2 ± 0.2	2.0 ± 0.2

6.3.2 ^{6}Li 2D EXSY Measurements of Li_2VPO_4F

Exchange of the Li^+ between these two sites was explored using ^{6}Li 2D EXSY experiments. In these studies, each spin is frequency labeled during the evolution period, t_1. The exchange processes are allowed to take place during a mixing period of set length, τ_m which is limited by the T_1 times of the nuclei. Cross peaks appear at off-diagonal sites corresponding to the sites involved in the exchange process. Samples partially enriched with ^{6}Li (which has an inherently longer T_1, see **Table 6.1** and **Table 6.2**) were used for the exchange experiments in order to probe mixing times long enough for exchange processes to occur. Spin-lattice relaxation times of both spins were determined at room temperature for ^{6}Li using a nonselective inversion recovery experiment, and found to be 22.7 ± 0.5 ms and 16.3 ± 0.5 ms for sites A and B respectively (**Table 6.2**).

Table 6.2 – Summary of ^{6}Li spin-lattice relaxation times (T_1) for $Li_{1.5}VPO_4F$ and Li_2VPO_4 at 4.7 T

Sample	T_1 times (ms)		
	Parent $LiVPO_4F$	A	B
$Li_{1.5}VPO_4F$	44.2 ± 0.5	22.9 ± 0.5	16.8 ± 0.5
Li_2VPO_4F	-	22.7 ± 0.5	16.3 ± 0.5

Figure 6.4.a shows ^{6}Li 2D EXSY spectra acquired at 303 K for the $0.5LiVPO_4F{:}0.5Li_2VPO_4F$ sample. Although no ion exchange between the crystallographic sites takes place at this temperature, crosspeaks between the A and B sites are clearly evident at 330 K (**Figure 6.4**.b). The mixing time in these experiments was extended to 15 ms, which provided sufficient time for the exchange process to take place. This confirms that the two new resonances appearing in the reduced compound belong to the same phase and undergo thermally activated chemical exchange. The

timescales and energy barriers of this observed ion hopping were quantified using ^{6}Li 1D EXSY measurement in Section 6.3.4.

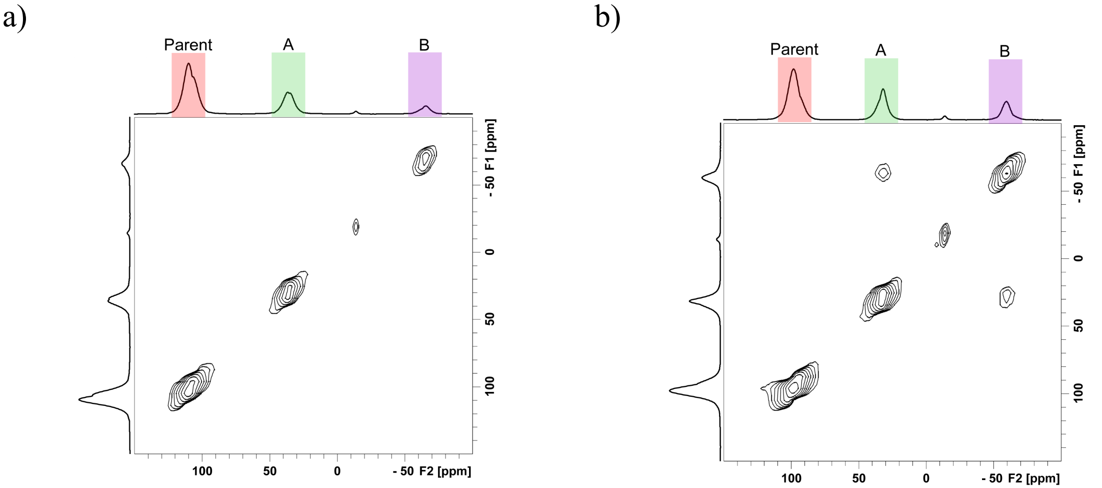

Figure 6.4 - ^{6}Li 2D EXSY spectrum over a variable temperature range shows evidence of thermally activated chemical exchange in the Li_2VPO_4F phase. On left a) T = 303 K (MAS = 25 kHz) and b) T = 330 K (MAS = 40 kHz). For both experiments, τ_{mix} = 15 ms

6.3.3 Site Assignment of Li_2VPO_4F

6.3.3.1 Site Assignment Based on the Fermi-Contact Interaction

To answer the question of which Li sites in the Li_2VPO_4F structure correlate to the A and B resonances, the geometry dependent hyperfine coupling between the unpaired electron spin density and the Li atoms was analyzed.[17,18] There are two mechanisms for electron spin density transfer which are found to be most effective when the Li-O-V (or Li-F-V) orbitals overlap at angles close to 90° or 180°.[9,10] Since Li_2VPO_4F has orbital overlap angles closer to 90°, the 180° interactions are ignored. For the mechanisms involving 90° orbital overlap, unpaired electron spin density sitting in the t_{2g} orbital of V in an octahedral environment is able to delocalize onto the Li s orbital leading to an increase in the paramagnetic shift. Comparison of the local Li environments of Li1 and

Li2 in reference to the V centers clearly shows that Li1 has a larger number of Li-O-V angles closer to 90° than does Li2 (**Table 6.3**). A greater amount of electron density spin density is localized onto the Li nucleus meaning a higher paramagnetic shift is observed. Therefore resonance A is assigned to Li1. Conversely, Li2 has much poorer Li-O-V and Li-F-V overlap and gives rise to the lower frequency resonance labeled B.

Table 6.3 - Summary of Li-X-V bond angles for the Li1 and Li2 environments in Li_2VPO_4F.

	Angle (°)	**Li-V Distance (Å)**
Li1-X-V		
Li1-O1a-V1a	108.30	3.681
Li1-O1b-V1b	89.61	3.046
Li1-O2b-V1b	91.45	3.046
Li1-O1c-V1c	135.00	4.268
Li1-F1-V1d	146.35	4.006
Li1-F1-V1e	87.86	2.904
Li1-O2e-V1e	87.72	2.904
Li2-X-V		
Li2-F1a-V1a	123.77	4.074
Li2-F1a-V1b	73.10	2.764
Li2-O1b-V1b	83.86	2.764
Li2-O2b-V1b	84.05	2.764
Li2-F1c-V1c	134.62	3.643
Li2-F1c-V1d	86.92	2.724
Li2-O1d-V1d	66.15	2.724
Li2-O2d-V1d	86.99	2.724

It is unclear however, why the Li2 resonance falls at such a low shift value of −52 ppm. We therefore turn to more experimental evidence to support the assignment of Li1 to resonance A, and Li2 to resonance B, which includes ^{6}Li{^{19}F} REDOR measurements and determination of the ^{7}Li CSA parameters for each of the resonances.

6.3.3.2 Site Assignment in Li_2VPO_4F from $^6Li\{^{19}F\}$ REDOR NMR

The assignment made using the Fermi-contact interaction was further confirmed by correlating each of the Li sites to the single F environment using ^{6}Li-^{19}F rotational echo, double resonance (REDOR) measurements. As outlined in Chapter 3, ^{6}Li{^{19}F}REDOR reintroduces ^{6}Li-^{19}F dipolar couplings that are averaged through MAS. The observed nucleus (^{6}Li) is measured using a spin-echo sequence with (S) and without (S_0) the application of a series of π pulses on the dephased nucleus (^{19}F). The normalized difference in ^{6}Li signal intensity ($[S_0\text{-}S]/S_0$) is then plotted as a function of the dipolar evolution time ($N\tau_R$ = number of rotor periods times the rotor period). Stronger REDOR buildup curves arise from stronger dipolar couplings (D_{ij}) which are inversely dependent on the internuclear distance between the two spins (*i* and *j*) (Equation 2.4-11). **Figure 6.5** shows the ^{6}Li{^{19}F} REDOR curves observed for resonances A and B.

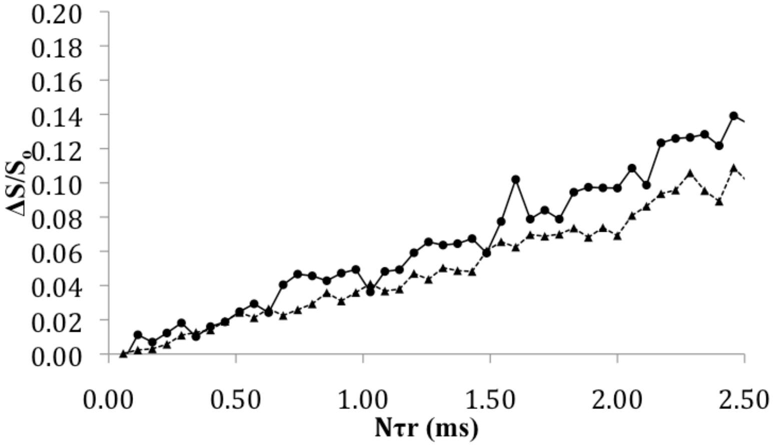

Figure 6.5 – ^{6}Li{^{19}F} REDOR buildup curves for resonances A (triangles) and B (circles). MAS = 35 kHz

The stronger REDOR buildup for the B resonance (Li2) is consistent with this site having one short Li-F internuclear distance of 1.82 Å, and a second Li-F contact at 2.49 Å

(**Table 6.4**). The single Li1-F distance of 2.06 Å gives rise to the weaker REDOR buildup curve for resonance A (Li1).

Table 6.4 - Summary of bond distances for the Li environments in Li_2VPO_4F.

Atom	**Ligand**	**Distance (Å)**
Li1	F1	2.062
	O2e	2.071
	O2b	2.135
	O1b	2.183
	O1a	2.399
	O1c	2.479
Li2	F1c	1.824
	O2d	1.826
	O1b	1.994
	O2b	2.008
	F1a	2.492
	O1d	2.759

6.3.3.3 Site Assignment Using ^7Li Sideband Manifolds of $0.5LiVPO_4F:0.5Li_2VPO_4F$

For a more detailed analysis of the Li environments within this system, the sideband manifolds belonging to the different Li sites were isolated and the respective CSA parameters determined. A ^7Li MAS spectrum showing the full sideband manifold of $Li_{1.5}VPO_4F$ is shown in **Figure 6.6**. Using the DMFit program, the sideband manifolds of each Li site were modeled.[20] This allowed for determination of the chemical shift anisotropy (Δ_{cs}), axial symmetry (η), and span (Ω) of each site (**Table 6.5**). The substantial increase in the span of the sideband manifolds of A and B (Ω = 2400 and 2700 ppm, respectively) as compared to the parent $LiVPO_4F$ (Ω = 1350 ppm) is consistent with the increase in electron spin density sitting on the transition metal center. This increase leads to stronger electron-Li dipolar coupling interaction which largely governs the span of CSA in paramagnetic systems.[17] When comparing the Li1 and Li2 sites, the larger anisotropy of the Li2 site *vs* the Li1 site (Δ_{cs} = 1205 ppm vs 705 ppm) is expected as Li1 is a six coordinate site (LiO5F), whereas the Li2 sits in a much more asymmetric environment composed of a five coordinate LiO_3F_2 polyhedron with an additional long Li-O bond of 2.759Å (**Table 6.4**).

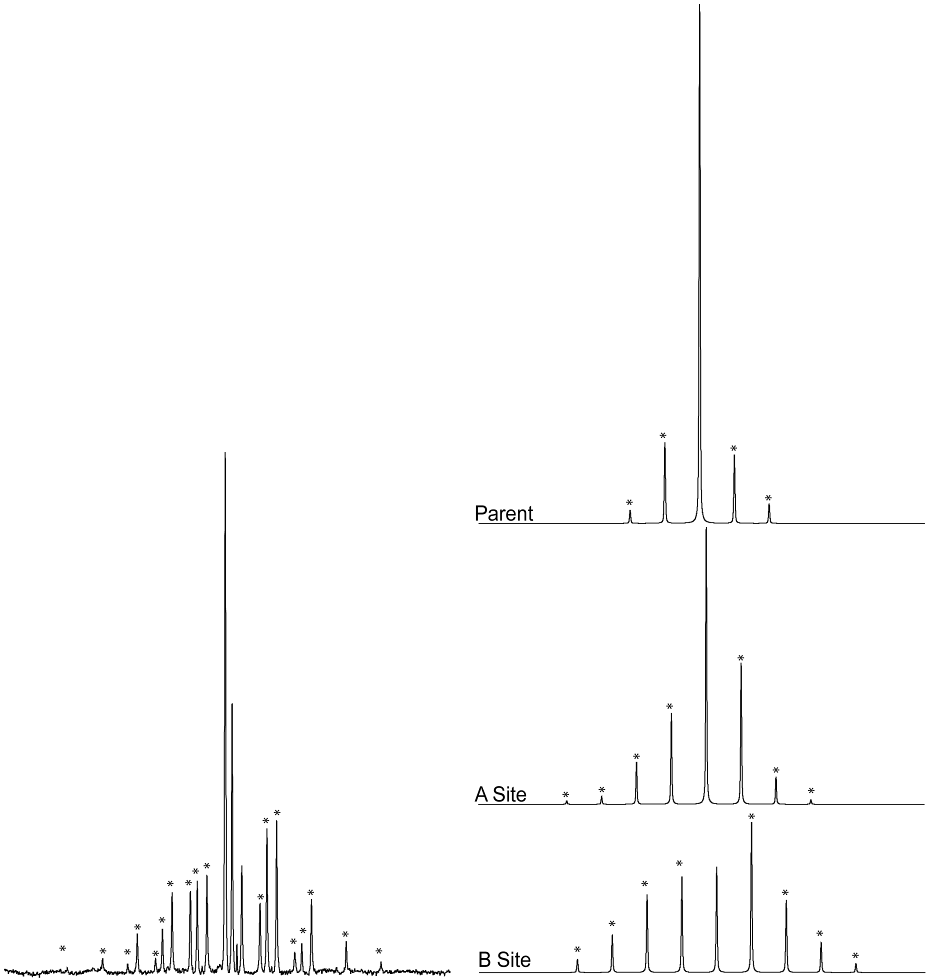

Figure 6.6 – Deconvolution of sideband manifold for ^{7}Li MAS spectrum of $0.5LiVPO_4F{:}0.5Li_2VPO_4F$. Experimental spectrum shown on left. Sideband manifolds for each of the crystallographic Li sites (as modeled in DMfit) on right from top to bottom–Parent $LiVPO_4F$, A site, and B site. Asterisks denote spinning sidebands.

Table 6.5 - Summary of CSA parameters for individual sites of $Li_{1.5}VPO_4F$

Li site	Ω (ppm)	Δ_{cs} (ppm)	η
Parent $LiVPO_4F$	1350 (± 20)	440 (± 20)	0.80 (± 0.05)
A	2400 (± 20)	740 (± 20)	0.50 (± 0.05)
B	2700 (± 20)	1200 (± 20)	0.75 (± 0.05)

6.3.4 Quantification of Ion Dynamics in Li_2VPO_4F Using ^{6}Li 1D EXSY

Our earlier investigations confirmed the lithium ion dynamics within the Li_2VPO_4F, using a qualitative 2D EXSY experiment, where the expected cross peaks were observed for the doubly lithiated phase, whereas no cross peak between the doubly and singly lithiated phases was detected, confirming the two-phase nature of the lithiation process (**Figure 6.4**). To determine the timescales and energy barriers of exchange in the doubly lithiated phase, ^{6}Li 1D EXSY experiments were applied over a variable temperature range. For the two-spin system found in Li_2VPO_4F, resonance A was chosen for inversion while resonance B was left unperturbed. Data collected from ^{6}Li 1D EXSY experiments over a variable temperature range are shown in **Figure 6.7** a. At all temperatures, the strong buildup of the inverted A spin, is accompanied by a transient "well" in the intensity of the B spin. This clearly shows the expected chemical exchange between the two sites.

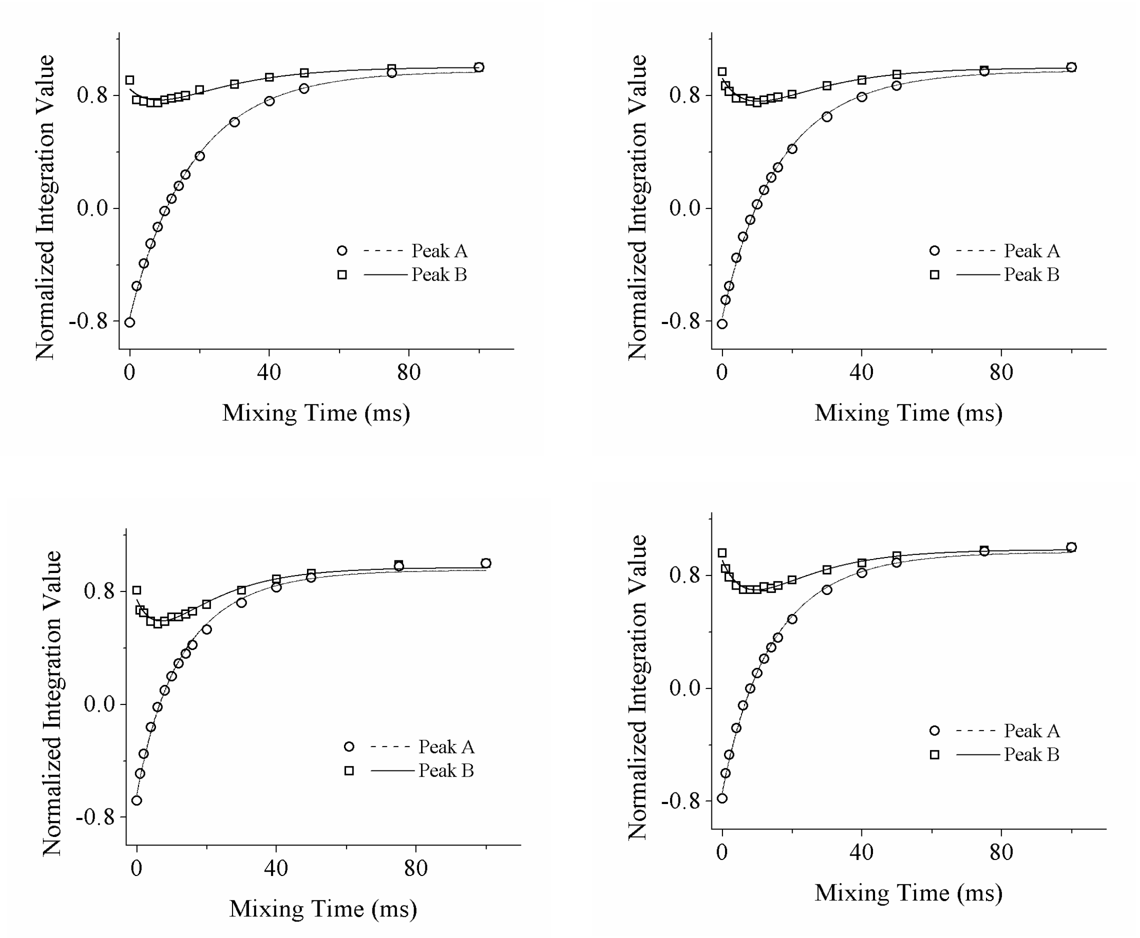

Figure 6.7 – Results of the ^{6}Li 1D EXSY experiments over a variable temperature range. Clockwise from the top left, 331 K, 337 K, 343 K and 350 K. The points represent measured values and the lines are the best fit to the data from the CIFIT program. The depth of the transient well increases with increasing temperature.

The effect of temperature, on both the buildup of the A spin as well as the transient well of the B spin, is better illustrated in **Figure 6.8**. Here the A and B curves are separated and then each plotted over the entire temperature range. This *x*-axis has been adjusted to show the shorter mixing times where the influence of the ion dynamics is more prominent. The lines drawn show the best fit to the data from the CIFIT program.

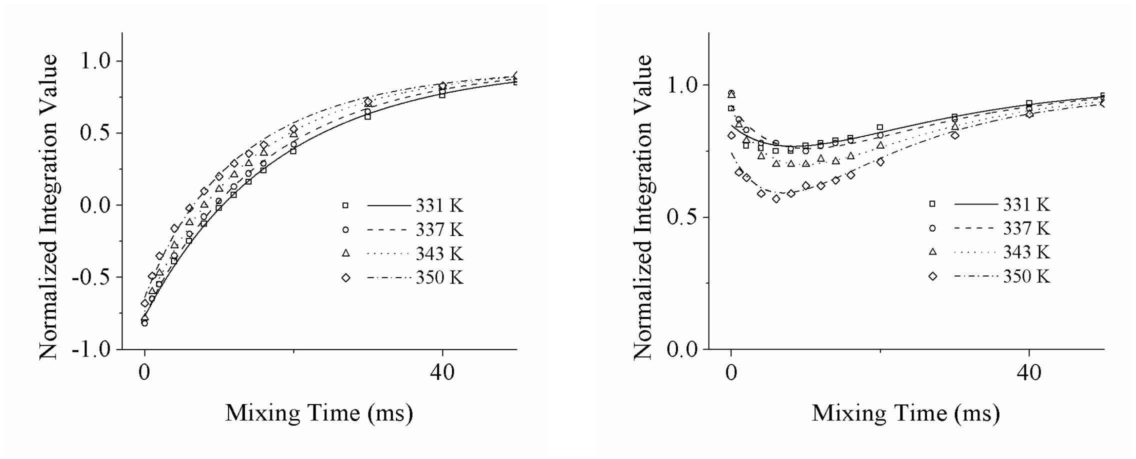

Figure 6.8 - Results of the ^{6}Li 1D EXSY experiments over a variable temperature range. Plots are separated into the inverted A spin (left) and non-inverted B spin (right). Data points represent measured values and the lines are the best fit to the data from the CIFIT program.

As the temperature is raised from 331 K to 350 K, the exchange rate is increased from 24 ± 1 to 55 ± 4 Hz (**Table 6.6**). The lower limit of the temperature range in this experiment was governed by the ion dynamics of this material where no exchange was observed at temperatures below 330 K. The upper limit of the temperature range was governed by the instrumentation where 350 K was the highest possible temperature for the probe.

Table 6.6 – Summary of CIFIT results for ^{6}Li 1D EXSY measurements of Li_2VPO_4F

Temperature (K)	Exchange rate (Hz)	Correlation time (ms)
331 K	24 (± 1)	41 (± 2)
337 K	30 (± 1)	34 (± 1)
343 K	40 (± 2)	25 (± 1)
350 K	55 (± 4)	18 (± 1)
Activation energy	0.44 (±0.06) eV	

The effectiveness of ^{6}Li 1D EXSY experiments in separating rate information from inherent T_1 properties is demonstrated in **Figure 6.9**. Here ^{6}Li 1D Nonselective Inversion (NSI) experiments, recorded over the same temperature range and mixing time period, are plotted beside the ^{6}Li 1D SI counterparts. Only the A resonance is evaluated as it was the environment chosen for selective inversion in the ^{6}Li 1D SI study. **Figure 6.9** clearly shows that the initial portion of the EXSY buildup curves are influence by changes in the ion dynamics while the NSI data remains relatively unchanged. This further confirms that thermally driven chemical exchange is taking place between the two Li environments of Li_2VPO_4F.

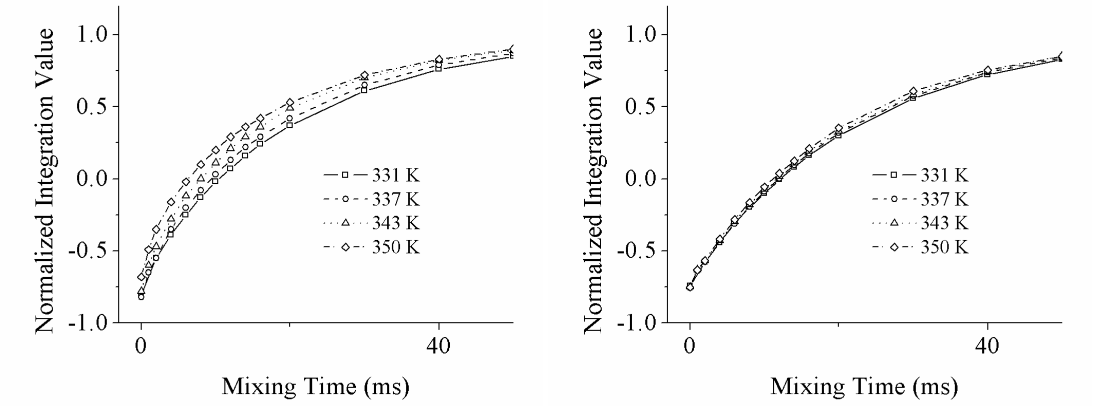

Figure 6.9 – Results of selective 1D ^{6}Li EXSY (left) and nonselective inversion (NSI) recovery (right) experiments of the A resonance over the same temperature range. The x-axis is minimized to the time region where chemical exchange is expected to dominate the buildup curves. The 1D EXSY results show an increase in buildup intensity as the temperature is raised. The NSI recovery shows only a slight variation with temperature.

The NSI data however, cannot be taken as a true measurement of the inherent T_1 times of each environment. The T_1 values reported earlier, from the NSI experiments at

331 K (herein referred to a T_1^{NSI}) were 23 ± 1 ms and 18 ± 1 ms for spins A and B, respectively (note that these T_1 values were collected at a field of 11.7 T and differ from result given in **Table 6.2** which were collected at 7.0 T). By fitting the 1D EXSY data (also at 331 K) using CIFIT, a new set of T_1 values (abbreviated as T_1^{SI}) were generated. These values were determined from single component fits as the primary mechanism of relaxation in ^{6}Li MAS NMR is from dipolar coupling with the unpaired electrons sitting on the paramagnetic center. T_{1Q} and spin diffusion have negligible effects on these values.[21] For spins A and B, the fitted T_1^{SI} values of 29 ± 2 ms and 11 ± 1 ms, respectively, were determined. The T_1^{SI} are a more faithful representation of the inherent T_1 times of each environment in the absence of chemical exchange, which is further emphasized when the modeled T_1^{SI} values are compared to the experimentally measured T_1^{NSI} values. For the A spin, T_1^{SI} is longer than the T_1^{NSI} while for the B spin, the opposite is true: the T_1^{SI} is shorter than the experimentally measured T_1^{NSI} value. This is a result of equilibration of the spin-lattice relaxation times for spins undergoing chemical exchange and further emphasizes how the T_1^{SI} values are a more accurate timescale of the spin-lattice relaxation in the absence of chemical exchange. The T_1^{SI} values were therefore held as a constant in the CIFIT models of ^{6}Li 1D EXSY data over the remaining variable temperature range.

Determination of jump rates for the Li1-Li2 exchange pair at different temperatures allowed for the calculation of the activation energy, E_a, as the natural log of the exchange rates was plotted as a function of inverse temperature in an Arrhenius plot (**Figure 6.10**). An energy barrier value of 0.44 ± 0.06 eV was calculated from the slope of the graph, where the error bounds on the ln(k) values were included in the regression analysis. The error value of the energy barrier was calculated from the standard error of the slope from the regression analysis.

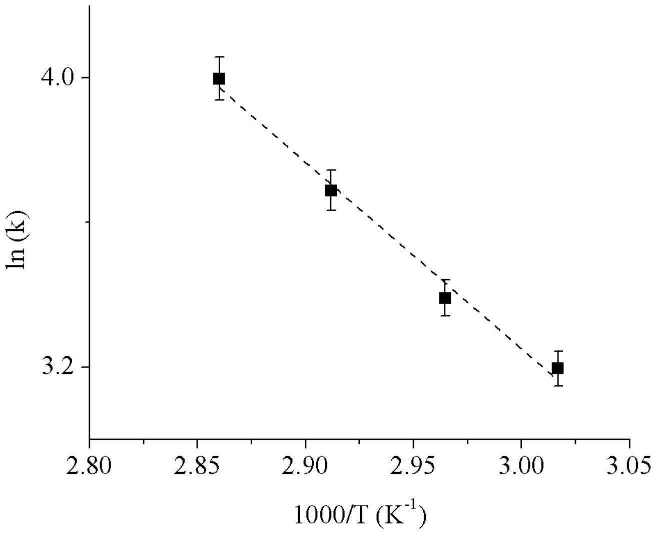

Figure 6.10 – Arrhenius plot of ion exchange rates as a function of temperature for Li1-Li2 ion exchange in Li_2VPO_4F.

6.3.5 Correlating the Timescales of Exchange to Structural Constraints

This activation energy was correlated to structural constraints within the lattice in a similar approach to the one taken in Chapter 5 for $Li_3Fe_2(PO_4)_3$ and to previous studies where mechanisms of Li-transport were identified.[22-24] The lithiated tavorite structure has the two crystallographically unique Li sites, both of which were previously determined to be half occupied.[2] **Figure 6.11** shows a simplified unit cell, where the two most probable pathways for Li ion hopping are identified as face shared geometries between the Li1-Li2 polyhedral environments.

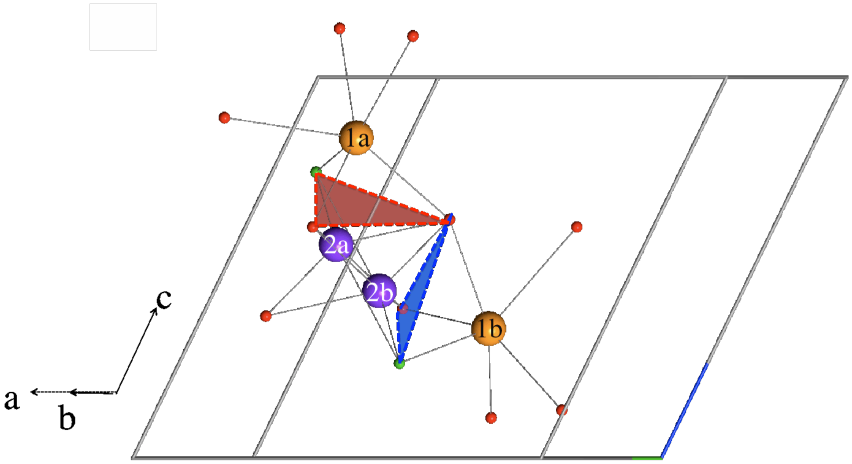

Figure 6.11 - Schematic of the simplified unit cell highlighting the two face-shared Li1-Li2 (orange-lilac) diffusion pathways. Each has a bottleneck area (shaded triangle) created by 1 F atom (green) and 2 O atoms (red). Depending on the population of the half occupancy Li1 and Li2 environments, the α-bottleneck (red triangle) is present as either α1 (Li1a-Li2a) or α2 (Li1a-Li2b). Similarly, the β-bottleneck (blue triangle) exists as either β1 (Li1b-Li2b) or β2 (Li1b-Li2a). The coordination environments and pathways lend themselves to 3D ion transport.

The bottlenecks for diffusion along each pathway were quantified by calculating the area of the triangular face created by the 2 O atoms and 1 F atom shared by the two exchanging Li sites. The first triangular window which we term the α-bottleneck (red triangle, **Figure 6.11**) has a smaller area of 3.92 Å^2. The second triangular window which we term the β-bottleneck (blue triangle, **Figure 6.11**) is more open with an area of 4.22 Å^2 (**Table 6.7).** The internuclear distances between the ions passing through the α and β bottlenecks, is complicated by the half-occupancy of the Li environments. For each bottleneck there is one short and one long Li1-Li2 internuclear distance. For the case of the α bottleneck, the shorter Li1-Li2 distance of 1.938 Å is referred to as the α_1 pathway, whereas the longer 2.791 Å distance is the α_2-pathway (**Table 6.7**). Similarly for the β-bottleneck, β_1 identifies the Li1-Li2 distance of 1.979 Å whereas β_2 indicates the pathway with a 2.993 Å Li1-Li2 distance. In order to minimize electrostatic repulsion between the Li environments, it is expected that a longer internuclear distance separates the Li ions. Based on this assumption, the two plausible exchange pathways occur such that the shorter internuclear distance is paired with the tighter bottleneck (α_2 pathway), as compared to the longer internuclear distance that is paired with the wider bottleneck (β_2 pathway).

Table 6.7 - Summary of face-shared Li1-Li2 pathways in Li_2VPO_4F with the corresponding bottlenecks for diffusion and internuclear distances.

Li1-Li2 pathway	Area of bottleneck (Å^2)	Li1-Li2 distance (Å)
α_1	3.92	1.938
α_2	3.92	2.791
β_1	4.22	1.979
β_2	4.22	2.993

This makes differentiation between these two possible pathways non-trivial, and the single rate determined here at each temperature is attributable to either of these exchange routes. Bond valence maps of the α_2 and β_2 faces also do not indicate a preferred pathway either, as they both show very similar density along the planes defined by the shared face of each pathway (**Figure 6.12**).

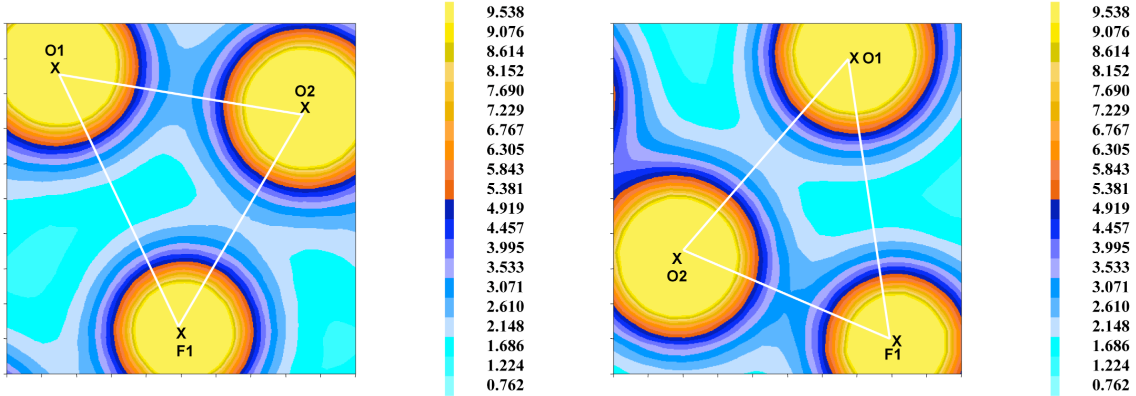

Figure 6.12 – Bond valence maps of the planes defining the shared face of the α2 (left) and β2 (right) pathways. Atoms that define the space are marked with an X.

Overall, the similarity between the pathways, which are fitted to a single ion exchange rate for the 1D EXSY data at each temperature, is a strong indication of the propensity for 3D ion transport in this material.

6.4 Conclusions

This work identifies new Li environments generated as Li_xVPO_4F is lithiated from x = 1.0 up to x = 2.0 and confirms that this takes place in a two-phase fashion. This chapter also presents the first quantitative study of Li^+ dynamics in tavorite Li_2VPO_4F. It also is the first quantitative study of ion dynamics in a solid-state paramagnetic system using 1D EXSY experiments. This is an example of a material where the spin-lattice relaxation rates are faster than the ion dynamics, and thus a 2D EXSY approach is non-trivial. Exchange between the two crystallographic Li sites was found to be on the millisecond timescale with an energy barrier of 0.44 ± 0.06 eV. Two pathways of ion exchange between Li1 and Li2 were identified, with similar structural constraints. The next chapter extends the use of 1D selective inversion methods to systems having multiple exchange processes allowing this NMR tool to be expanded to systems with more complex ion conduction pathways.

6.5 References

(1) Barker, J.; Saidi, M. Y.; Swoyer, J. L. *J. Electrochem. Soc.* **2003**, *150*, A1394.

(2) Ellis, B. L.; Ramesh, T. N.; Davis, L. J. M.; Goward, G. R.; Nazar, L. F. *Chem. Mater.* **2011**, *23*, 5138.

(3) Groat, L. A.; Raudsepp, M.; Hawthorne, F. C.; Ercit, T. S.; Sherriff, B. L.; Hartman, J. S. *Am. Mineral.* **1990**, *75*, 992.

(4) Ramesh, T. N.; Lee, K. T.; Ellis, B. L.; Nazar, L. F. *Electrochem. Solid State Lett.* **2010**, *13*, A43.

(5) Morgan, D.; Van der Ven, A.; Ceder, G. *Electrochem. Solid-State Lett.* **2004** *7*, A30

(6) Forsen, S.; Hoffman, R. A. *J. Chem. Phys.* **1963**, *39*, 2892.

(7) Forsen, S.; Hoffman, R. A. *J. Chem. Phys.* **1964**, *40*, 1189.

(8) Bain, A. D.; Fletcher, D. A. *Mol. Phys.* **1998**, *95*, 1091.

(9) Bain, A. D. *Prog. Nucl. Magn. Reson. Spectrosc.* **2003**, *43*, 63.

(10) Marion, D.; Ikura, M.; Tschudin, R.; Bax, A. *J. Magn. Reson.* **1989**, *85*, 393.

(11) Grey, C. P.; Cheetham, A. K.; Dobson, C. M. *J. Magn. Reson. Ser. A* **1993**, *101*, 299.

(12) Bain, A. D.; Cramer, J. A. *J. Magn. Reson. Ser. A* **1996**, *118*, 21.

(13) Bain, A. D.; Berno, B. *Prog. Nucl. Magn. Reson. Spectrosc.* **2011**, *59*, 223.

(14) Gonzalez-Platas, J.; Gonzalez-Silgo, C.; Ruiz-Perez, C. *J. Appl. Crystallogr.* **1999**, *32*, 341.

(15) Brown, I. D.; Wu, K. K. *Acta Crystallogr. Sect. B-Struct. Commun.* **1976**, *32*, 1957.

(16) Brown, I. D. *Chem. Soc. Rev.* **1978**, *7*, 359.

(17) Grey, C. P.; Dupre, N. *Chem. Rev.* **2004**, *104*, 4493.

(18) Carlier, D.; Menetrier, M.; Grey, C. P.; Delmas, C.; Ceder, G. *Phys. Rev. B* **2003**, *67*, 174103.

(19) Groat, L. A.; Chakoumakos, B. C.; Brouwer, D. H.; Hoffman, C. M.; Fyfe, C. A.; Morell, H.; Schultz, A. J. *Am. Mineral.* **2003**, *88*, 195.

(20) Massiot, D.; Fayon, F.; Capron, M.; King, I.; Le Calve, S.; Alonso, B.; Durand, J. O.; Bujoli, B.; Gan, Z. H.; Hoatson, G. *Magn. Reson. Chem.* **2002**, *40*, 70.

(21) Xu, Z.; Stebbins, J. F. *Solid State Nucl. Magn. Reson.* **1995**, *5*, 103.

(22) Cahill, L. S., Chapman, R. P., Britten, J. F., Goward, G. R. *J. Phys. Chem. B* **2006**, *110*, 7171.

(23) Wilkening, M.; Romanova, E. E.; Nakhal, S.; Weber, D.; Lerch, M.; Heitjans, P. *J. Phys. Chem. C* **2010**, *114*, 19083.

(24) Makimura, Y.; Cahill, L. S.; Iriyama, Y.; Goward, G. R.; Nazar, L. F. *Chem. Mater.* **2008**, *20*, 4240.

Chapter 7:Expansion of ^{6}Li 1D Selective Inversion Methods to Multi-Spin Systems

7.1 Introduction

In the previous chapter, ^{6}Li 1D EXSY measurements were used to probe the timescales of ion hopping in Li_2VPO_4F, which had a single exchange process between its two crystallographically distinct Li environments. Here we expand the use of selective inversion techniques to paramagnetic materials that have more than one ion hopping pathway. The selective inversion method of Chapter 6 was 1D EXSY which uses a $90°-\tau_1-90°$ sequence for selective inversion of a Li resonance undergoing site exchange. The first delay period, τ_1, is determined by the frequency difference between two resonances undergoing ion exchange which subsequently limits the experiment to probe the timescales of single exchange pair systems. To overcome this limitation, a second selective inversion method is used in this chapter where the $90°-\tau_1-90°$ portion of 1D EXSY is replaced with a long, selective Shaped Pulse (SP). This work has been accepted to a special issue of the journal, *Solid State NMR* (*SSNMR-11-39*) with the authorship of X. (−J). He, L. J. M. Davis, A. D. Bain, and G. R. Goward. My contribution to this work was the collection of NMR data and supervision of undergraduate thesis student, Xuilan (Janice) He as she carried out the data analysis in CIFIT. Prof. Bain and Prof. Goward were the principal investigators of the project.

The two paramagnetic cathode materials chosen for analysis using the 1D SI methods are Li_2VPO_4F and Li_2VOPO_4. The first compound, monoclinic Li_2VPO_4F, is the same reduced phase of the tavorite-based triclinic compound studied in Chapter 6.[1-3] The two crystallographically unique lithium sites mean only a single exchange pair is present. Both selective inversion methods are applied to this simple exchange system in order to evaluate the agreement between the two methods. The second compound, Li_2VOPO_4, is the reduced phase of triclinic α−$LiVOPO_4$, a structure first reported by Lavrov *et al.*[4] The V^{5+}/V^{4+} redox potential sits at 3.95 V with a reversible capacity of 100 mAh/g.[5] Fewer details regarding the V^{4+}/V^{3+} redox potential and electrochemical performance are available at present and thus remain the focus of ongoing work. Lithiation to form the reduced phase results in three crystallographically unique Li environments with three ion-exchange pairs. The higher number of ion exchange pairs led to determination of timescales and energy barriers using the SP method only.

7.1.1 Selective Inversion Using 1D EXSY

As outlined in the previous chapter, 1D EXSY, uses a 90° - τ_1 - 90° - τ_{mix} - 90° pulse sequence to selectively invert the on-resonance spin.[6-8] The first delay period, τ_1, is set to a value governed by the frequency difference between the site of inversion (spin *i*) and its exchange partner (spin *j*) (specifically, $1/[2\Delta\nu_{ij}]$). The on-resonance spin (*i*) is selectively inverted following the second 90° pulse, while its exchange partner, *j*, is placed along the +*z*-axis. The mixing time (τ_{mix}) is stepped over a series of experiments with the longest delay time set to ensure relaxation back to equilibrium. Due to the dependence of τ_1 on the frequency difference between the two of spins it is not appropriate to extend this inversion technique beyond a 2-site, 1-exchange process and is therefore only applied to the monoclinic phase of Li_2VPO_4F.

7.1.2 Selective Inversion Using Shaped Pulses

A second inversion method is investigated and tested on both materials having either single or multiple-exchange processes. This second method replaces the initial 90° - τ_1 - 90° of the 1D EXSY sequence, with one long, soft, Gaussian pulse, placed on-resonance to the site chosen for inversion. The bandwidth of the Gaussian pulse ensures inversion of only one of the sites undergoing ion exchange, leaving all other sites unperturbed.[9] This experimental approach will be referred to as the Shaped Pulse (SP) method. Previous studies have shown this to be an effective technique for determining timescales in systems undergoing multiple chemical exchange processes in solution-state systems.[9-12] This method is applied to the single-exchange material, Li_2VPO_4F, in addition to the 1D EXSY method in order to determine the agreement between the two methods. The SP method was then used to quantify the timescales of ion hopping in a multiple-exchange system, Li_2VOPO_4, over a variable temperature range.

7.2 Experimental

7.2.1 Sample Preparation.

Collaborators at the University of Waterloo provided samples of ^{6}Li enriched Li_2VPO_4F and Li_2VOPO_4.

7.2.2 Solid State NMR.

For both materials, a custom built 1.8 mm probe with MAS speed of 40 kHz was used for initial characterization of the ^{6}Li environments, at a Larmor frequency of 44.1 MHz. **Li_2VPO_4F.** Variable temperature experiments of Li_2VPO_4F were carried out using a Bruker 2.5 mm probe with MAS of 25 kHz at a Larmor frequency of 76.7 MHz. ^{6}Li 1D MAS spectra were acquired using a 90° pulse of 2.5 μs and recycle delay of 200 ms. **Li_2VOPO_4.** Variable temperature experiments of Li_2VOPO_4 were performed using a custom built probe supporting 1.8 mm rotors with MAS frequencies ranging from 25 − 40 kHz at a Larmor frequency of 44.1 MHz. ^{6}Li 1D MAS spectra were acquired using a 90° pulse of 3.5 μs and recycle delay of 300 ms.

7.2.3 1D EXSY.

^{6}Li 1D EXSY experiments were performed using a $90° - \tau_1 - 90° - \tau_{mix} - 90°$ sequence. Selective inversion was accomplished by setting the carrier frequency on-resonance to a chosen spin *i* and setting τ_1 to one-half the frequency difference with the resonance frequency of an ion-exchange partner ($1/[2\Delta\nu_{ij}]$). This experiment was applied to Li_2VPO_4F with the mixing time (τ_{mix}) stepped over a series of 16 experiments from 5 μs to 100 ms.

7.2.4 Shaped Pulse Experiments.

Shaped Pulse experiments used a 180° - τ_{mix} - 90°, where the 180° pulse was a long (500 μs), soft, Gaussian pulse set on resonance to the site chosen for inversion. To calibrate the Gaussian pulse, the pulse length is fixed at 500 μs while the power level is adjusted to get maximum inversion of the on-resonance signal. The mixing time (τ_{mix}) was stepped over a series of 16 experiments from 5 μs to 100 ms for Li_2VPO_4F and 5 μs to 200 ms for Li_2VOPO_4. For Li_2VPO_4F, the same variable/mixing time list used in the 1D EXSY experiments is used here in order to facilitate the comparison of the two methods. A hard, short, 90° pulse was used to acquire the final magnetization.

7.2.5 Nonselective Inversion Recovery.

Nonselective Inversion (NSI) recovery experiments used a standard inversion-recovery sequence with the variable delay list set equivalent to the variable mixing time list of the SP and 1D EXSY experiments.

7.2.6 Data Analysis.

In each data set, slices for each mixing time/variable delay were extracted and baseline corrected. All spins involved in the exchange process, were integrated and normalized to data collected with longest mixing time/variable delay (where the magnetization of each spin was fully relaxed). The data was modeled using the CIFIT program developed by A.D. Bain of McMaster University.[10] This program takes the table of observed areas for all spins as a function of mixing time and determines a key set of parameters: the jump rates (k) of each chemical exchange process, spin-lattice relaxation times in the absence of chemical exchange (T_1), and the magnetization values from initial ($M_i(0)$) to equilibrium conditions ($M_i(\infty)$). The rate matrix used to describe spin relaxation under the influence of chemical exchange is the primary mathematical model used by the CIFIT program and is described in greater detail elsewhere.[10,13,14] CIFIT adjusts the free parameters, T_1, k, $M_i(0)$ and $M_i(\infty)$, using a Levenberg-Marquardt algorithm until the sum of the squares of the differences between the experimental and calculated data is minimized. Error values of the exchange rates were approximated in the CIFIT program by the variance-covariance matrix of the fit to the data.

7.3 Results and Discussion

Figure 7.1 shows the ^{6}Li MAS spectra of the two-site material, Li_2VPO_4F, and three-site compound, Li_2VOPO_4. For Li_2VPO_4F the paramagnetic shifts arising at 46 ppm and − 47 ppm were labeled A and B, respectively respectively and integrated to give a 1:1 ratio over the entire sideband manifold. There is a small diamagnetic impurity centered at 0 ppm. The higher frequency resonance centered at ~ 112 ppm is the known parent phase of $LiVPO_4F$.[2] In the ^{6}Li MAS spectrum of Li_2VOPO_4, the resonances centered at 190 ppm, 75 ppm and -105 ppm were labeled A, B, and C, respectively and integrated to give a 1:0.5:0.5 A:B:C occupancy over the entire sideband manifold. The lithiation process ($LiVOPO_4 \rightarrow Li_2VOPO_4$) is found to create two new, partially-occupied lithium environments, which is often seen in lithiation of cathode materials.[15] Again, there is a diamagnetic impurity centered at 0 ppm along with a broad resonance centered at 10 ppm. Neither of these resonances participates in ion exchange, as determined through the 2D EXSY data set, and were therefore omitted from the analysis.

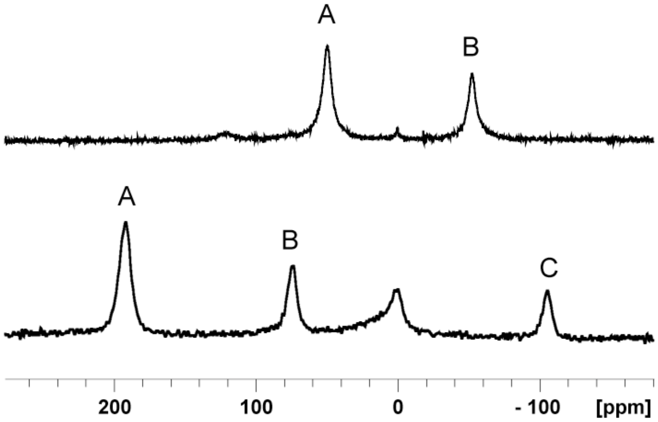

Figure 7.1 – ^{6}Li MAS (25 kHz) spectra of Li_2VPO_4F (top) and Li_2VOPO_4 (bottom). Labeling of sites A, B, and C, indicate spins involved in ion hopping processes. The resonances at zero ppm arise from diamagnetic impurities from the lithiation process.

^{6,7}Li MAS 2D EXSY spectra of each sample confirm ion hopping between each of the labeled Li environments (**Figure 7.2**). For the ^{6}Li 2D EXSY spectrum of Li_2VPO_4F, exchange between the A and B spins confirms that Li_2VPO_4F is a 2-site, 1-exchange process system. The ^{7}Li 2D EXSY spectrum of Li_2VOPO_4 shows crosspeaks between the A-B, B-C, and A-C resonances, confirming a 3-site, 3-exchange system. The 2D EXSY spectra provided an initial indication that the timescales of ion mobility between the fluorophosphate Li_2VPO_4F and oxyphosphate Li_2VOPO_4 are significantly different. For the oxyphosphate, prominent cross peaks at MAS 40 kHz (calibrated to a temperature of 330 K), were observed with a mixing time of 6 ms. In contrast, for

Li_2VPO_4F, at an equivalent temperature, only weak crosspeaks appeared at an extended mixing time of 15 ms, indicating a more slowly exchanging system.

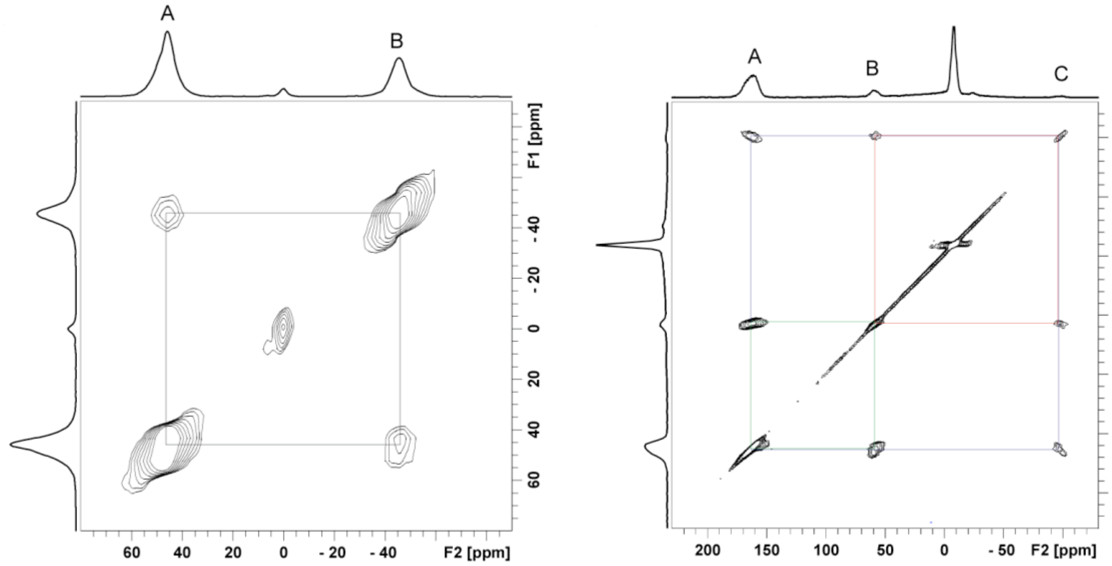

Figure 7.2 - 2D EXSY spectra of Li_2VPO_4F (left, ^{6}Li MAS 40 kHz, τ_{mix} = 15 ms) and Li_2VOPO_4 (right, ^{7}Li MAS 40 kHz, τ_{mix} = 6 ms). A 2-site, 1-exchange process system is shown in Li_2VPO_4F as crosspeaks between the A and B Li ion crystallographic positions are present. Similarly, a 3-site, 3-exchange process system in Li_2VOPO_4, is proven with observation of A–B, A–C, and B–C, crosspeaks.

Figure 7.3 shows the results of ^{6}Li selective inversion of Li_2VPO_4F using both the 1D EXSY and SP methods. The magnetization of the selectively inverted site (the A resonance) from both the SP, and 1D EXSY experiments is also plotted alongside results from a NSI recovery experiment at the same temperature. The stronger buildup of both the selectively inverted curves, as compared to the NSI recovery, highlights the influence of chemical exchange on the relaxation of selectively inverted magnetization. Comparing the 1D EXSY and SP results only, a slightly stronger buildup of the A magnetization is observed. The discrepancy between the data from the two methods is more evident when the transient curves of resonance B are examined (**Figure 7.3,** right). In this case, the transient of the 1D EXSY data is slightly deeper than the SP data. We attribute this difference to the timescales of the inversion processes leading to different initial conditions for selective inversion. For the 1D EXSY method, the total time of the $90^\circ-\tau_1-90^\circ$ inversion step is 78.3 μs whereas for the shaped pulse experiments, the length of the shaped pulse needed for inversion is 500 μs in length. Despite the differences in experimental timescales, CIFIT is able to fit the data from each experiment to yield comparable timescales of exchange. Li-hopping rates of $59 \pm 2\ s^{-1}$ and $64 \pm 4\ s^{-1}$, for the shaped pulse and 1D EXSY methods, respectively, are equivalent within error (**Table 7.1**). A complete analysis of the timescales of Li_2VPO_4F using the 1D EXSY method over a variable temperature range has been reported in the previous chapter.[3]

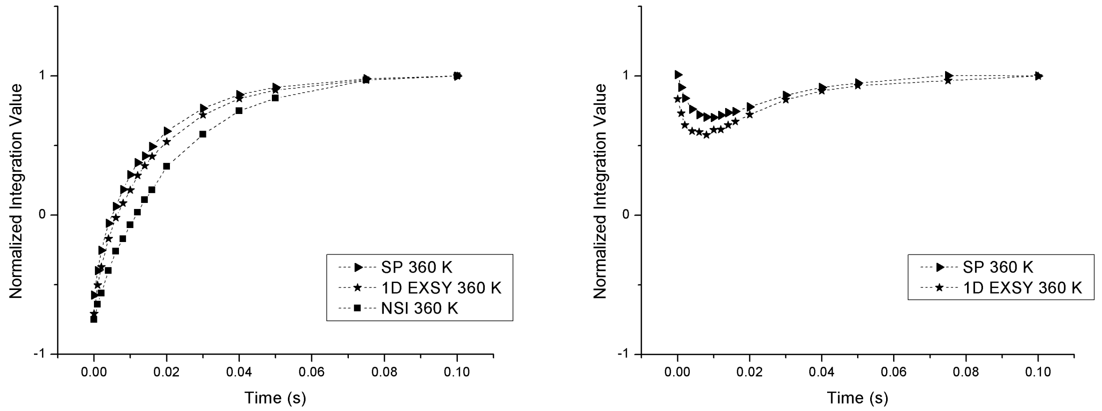

Figure 7.3 – Selective inversion results of the 2-site, 1-exchange material, Li_2VPO_4F, at 360 K. Left: Comparison of NSI recovery, 1D EXSY, and SP experiments of the inverted A resonance. Right: 1D EXSY and SP results of the non-inverted B resonance.

Table 7.1 – Summary of Li-hopping rates in Li_2VPO_4F as determined from the SP and 1D EXSY inversion methods.

	k_{AB} (s^{-1}) (T = 360 K)
SP	58 ± 2
1D EXSY	64 ± 4

The equivalent results observed from the 1D EXSY and SP experiments of the single-exchange system, allows us to extend the SP method to systems with a higher number of exchange pairs. The timescales and energy barriers in the 3-site, 3-exchange model compound, Li_2VOPO_4, were measured using SP experiments over a variable temperature range (304 K – 327 K). For each exchange process, a forward and backward ion-hopping rate coefficient exists. For exchange between B and C, the populations of these sites is equal meaning that under a steady-state approximation, the forward and backward rate coefficients (labeled k_{BC} and k_{CB}), respectively, are equal. For ion hopping between A and C, the 2:1 occupancy of A to C means that under steady-state conditions, k_{AC} (forward) will not be equal to k_{CA} (backward) (more specifically, $k_{CA} = 2k_{AC}$). A similar situation arises for A and B exchange where the population of A:B is also 1:0.5, meaning that again the reverse (k_{BA}) is twice that of the forward (k_{AB}) rate coefficient ($k_{BA} = 2k_{AB}$). In this study therefore, the CIFIT parameters were set such that only the three backward rates of ion-exchange, k_{BA}, k_{CA}, and k_{CB} were determined for the exchange pairs, A-B, A-C and B-C, respectively, while the reverse rates k_{AB}, k_{AC}, and k_{BC}, were predicted, based on the site-populations. Details on the treatment of unequal populations in CIFIT is outlined in greater detail elsewhere.[16]

Here, the rate coefficients for each exchange process were determined reproducibly from two separate experiments where either site in an exchange pair was selectively inverted. Therefore, a total of three experiments were carried out at each temperature where either A, B or C was inverted. To identify which site was inverted in each experiment, an $\bar{X}Y$ notation for the exchange pairs is used, where $\bar{X}$ is the inverted site and Y is the unperturbed, transient peak. As an example, for determination of ion exchange rate k_{BA}, the $\bar{A}B$ experiment indicates that results are from the inversion of A whereas the $A\bar{B}$ experiment is from the inversion of B. The results for inversion of A, B, and C, over a variable temperature range are shown in **Figure 7.4**. For all temperatures, there is a clear increase in the depth of the transient well as the temperature is raised. This is accompanied by an increase in the buildup of the inverted magnetization of each experiment. Results from CIFIT show agreement between the rates of ion exchange regardless of the site chosen for inversion (**Table 7.2**). The values of k_{BA} at 304 K were determined from both $\bar{A}B$ and $A\bar{B}$ experiments, giving ion exchange rates of 63 ± 7 s^{-1} and 55 ± 6 s^{-1}, respectively. Similarly for k_{CA}, values of 58 ± 7 s^{-1} and 64 ± 5 s^{-1} were found from $\bar{A}C$ and $A\bar{C}$ experiments, respectively. The equivalency of the ion hopping rates from different inversion sites will allow this inversion method to be extended to systems where only one of the exchange sites is well enough resolved for selective inversion.

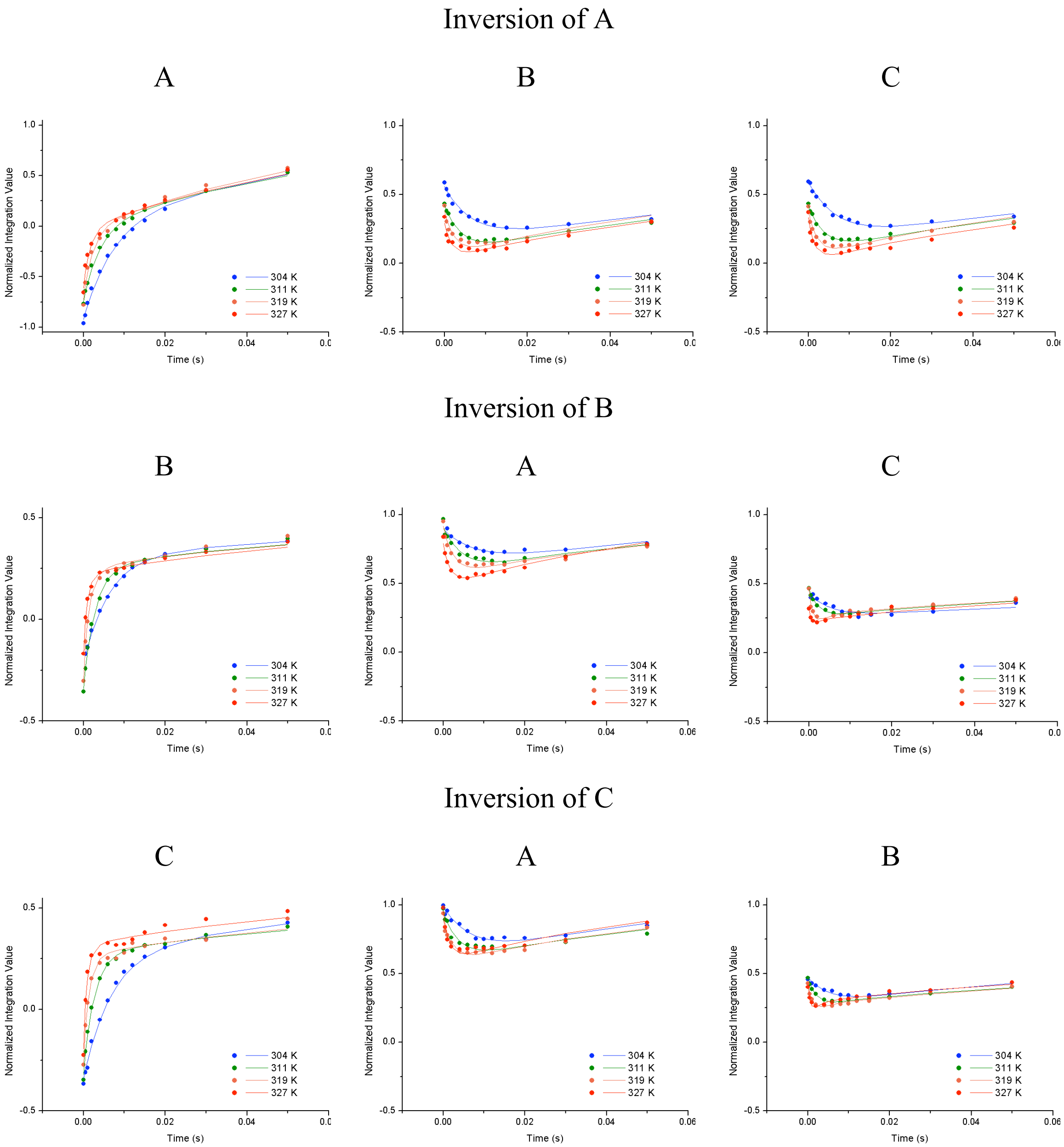

Figure 7.4 – ^{6}Li SP results over a variable temperature range (304 K – 327 K) of the 3-site, 3-exchange material, Li_2VOPO_4, Top row shows results from the inversion of A with A, B, and C magnetization curves plotted from left to right. The middle row contains results from the inversion of B where the B, A, and C, magnetization curves are plotted from left to right. Results from the inversion of C are shown in the bottom row where from left to right the C, A, and B magnetization curves are given.

Table 7.2 – Summary of exchange rates determined from ^{6}Li SP measurements of Li_2VOPO_4. Each rate of ion exchange was determined twice from separate inversion of each resonance involved in the ion exchange process. Example: $\bar{A}B$ indicates the results from inversion of A, whereas $A\bar{B}$ is from inversion of B.

Temp (K)	$\bar{A}B$ k_{BA} (s^{-1})	$A\bar{B}$ k_{BA} (s^{-1})	$\bar{A}C$ k_{CA} (s^{-1})	$A\bar{C}$ k_{CA} (s^{-1})	$\bar{B}C$ k_{CB} (s^{-1})	$B\bar{C}$ k_{CB} (s^{-1})
304	63 ± 7	55 ± 6	58 ± 7	64 ± 5	90 ± 10	110 ± 10
311	110 ± 10	100 ± 10	130 ± 20	130 ± 10	320 ± 40	210 ± 30
319	200 ± 50	190 ± 30	230 ± 50	210 ± 30	750 ± 90	710 ± 90
327	290 ± 90	280 ± 70	300 ± 90	370 ± 60	1100 ± 200	900 ± 200

Jump rates for A-B, A-C, and B-C exchange pairs at different temperatures were determined making the calculation of the activation energy, E_a, possible. **Figure 7.5** shows Eyring plots of the natural log of the averaged exchange rates over temperature plotted as a function of inverse temperature for the A-B, A-C, and B-C exchange pairs. The energy barriers were reported in three separate ways, to ensure accuracy between the different inversion methods (**Table 7.3**). For example, the energy barrier of the A−B hopping pair was determined first using the rates determined from experiments where A was inverted $(\bar{A}B)$, then using the results from measurements where B was inverted $(A\bar{B})$, and lastly, using the average ion hopping rates from both experiments. **Figure 7.5** shows only the Eyring plots using the latter, averaged results where the A−B, A−C, and B−C ion hopping energy barriers were 0.6 ± 0.1 eV, 0.6 ± 0.1 eV, and 0.9 ± 0.2 eV, respectively (**Table 7.3**). Refinement data from powder x-ray diffraction measurements is not yet available. Therefore correlation of these energy barriers and timescales to structural constraints within the lattice is ongoing.

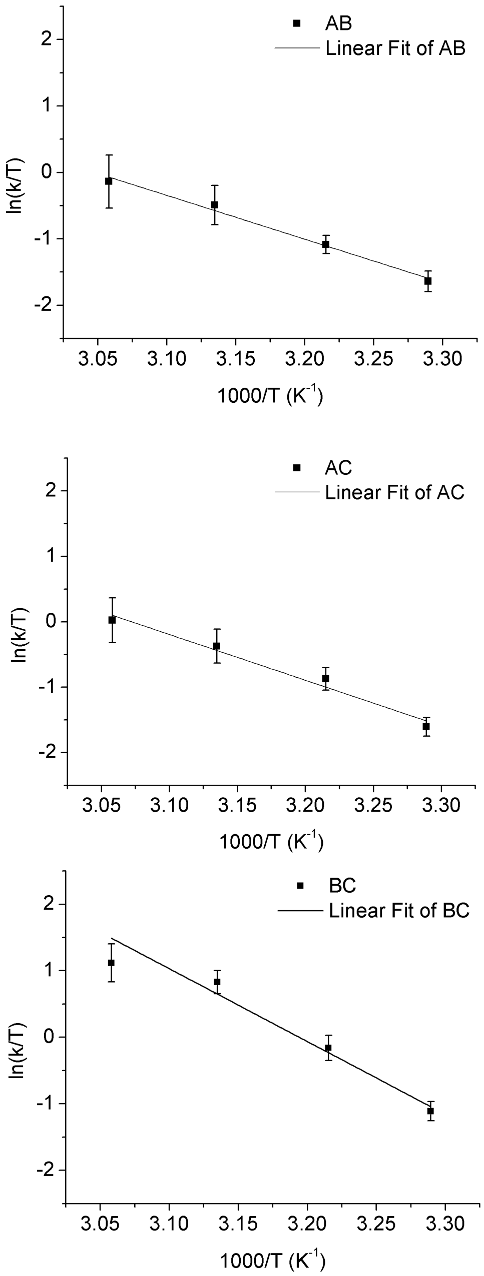

Figure 7.5 - Eyring plots where the slope of the natural log of the averaged ion hopping rate over temperature plotted against inverse temperature gives the energy barrier for the A-B, (top), A-C (middle), and B-C (bottom) exchange processes.

Table 7.3 - Summary of activation energies for Li ion hopping from the variable temperature ^{6}Li SP studies of Li_2VOPO_4.

Experiment	A-B hop E_a (eV)	A-C hop E_a (eV)	B-C hop E_a (eV)
Inversion of A	0.57 ± 0.04	0.7 ± 0.1	N/A
Inversion of B	0.62 ± 0.03	N/A	1.0 ± 0.2
Inversion of C	N/A	0.63 ± 0.05	0.9 ± 0.1
Average	0.6 ± 0.1	0.6 ± 0.1	0.9 ± 0.2

7.4 Conclusions

The present work compares the effectiveness of different inversion methods for accurate determination of timescale and energy barriers of Li ion hopping in solid-state paramagnetic Li-intercalation materials. Inversion using both 1D EXSY and SP methods was performed on a 2-site, 1-exchange example, Li_2VPO_4F. The 3-site, 3-exchange example, Li_2VOPO_4 was measured with the SP method only. As expected, in the 2-site, 1-exchange example, the 1D EXSY and SP methods gave equivalent timescales of exchange. However the longer duration of the inversion pulse in the SP method leads to different initial conditions of the inversion resulting in slightly different features of the transient well. For the 3-site, 3-exchange material, Li_2VOPO_4, only the SP method was applied with timescales of ion hopping determined over a variable temperature range. Ion hopping rates from AB, AC, and BC, experiments at 304 K were 55 ± 6 s^{-1}, 58 ± 7 s^{-1}, and 90 ± 10 s^{-1}, respectively. These rates increased at higher temperature (327 K) to $\bar{A}B$, $\bar{A}C$, and $\bar{B}C$, of 290 ± 90 s^{-1}, 300 ± 90 s^{-1}, 1100 ± 200 s^{-1}, respectively. These timescales were found to be equivalent within error to hopping rates determined from $A\bar{B}$, $A\bar{C}$, and $B\bar{C}$, experiments at all temperatures. An Eyring analysis of the averaged ion hopping rates as function of temperature gave A–B, A–C, and B–C, energy barriers of 0.6 ± 0.1 eV, 0.6 ± 0.1 eV, and 0.9 ± 0.2 eV, respectively.

7.5 References

(1) Barker, J.; Saidi, M. Y.; Swoyer, J. L. *J. Electrochem. Soc.* **2003**, *150*, A1394.

(2) Ellis, B. L.; Ramesh, T. N.; Davis, L. J. M.; Goward, G. R.; Nazar, L. F. *Chem. Mater.* **2011**, *23*, 5138.

(3) Davis, L. J. M.; Ellis, B. L.; Ramesh, T. N.; Nazar, L. F.; Bain, A. D.; Goward, G. R. *J. Phys. Chem. C* **2011**, *115*, 22603.

(4) Lavrov, A. V.; Nikolaev, V. P.; Sadikov, G. G.; Poraikoshits, M. A. *Doklady Akademii Nauk Sssr* **1982**, *266*, 343.

(5) Kerr, T. A.; Gaubicher, J.; Nazar, L. F. *Electrochem. Solid State Lett.* **2000**, *3*, 460.

(6) Forsen, S.; Hoffman, R. A. *J. Chem. Phys.* **1963**, *39*, 2892.

(7) Forsen, S.; Hoffman, R. A. *J. Chem. Phys.* **1964**, *40*, 1189.

(8) Hampson, M. R.; Evans, J. S. O.; Hodgkinson, P. *J. Am. Chem. Soc.* **2005**, *127*, 15175.

(9) Bauer, C.; Freeman, R.; Frenkiel, T.; Keeler, J.; Shaka, A. J. *J. Magn. Reson.* **1984**, *58*, 442.

(10) Bain, A. D.; Cramer, J. A. *J. Magn. Reson. Ser. A* **1996**, *118*, 21.

(11) Bain, A. D.; Fletcher, D. A. *Mol. Phys.* **1998**, *95*, 1091.

(12) Led, J. J.; Gesmar, H. *J. Magn. Reson.* **1982**, *49*, 444.

(13) Bain, A. D. *Prog. Nucl. Magn. Reson. Spectrosc.* **2003**, *43*, 63.

(14) Bain, A. D.; Berno, B. *Prog. Nucl. Magn. Reson. Spectrosc.* **2011**, *59*, 223.

(15) Makimura, Y.; Cahill, L. S.; Iriyama, Y.; Goward, G. R.; Nazar, L. F. *Chem. Mater.* **2008**, *20*, 4240.

(16) Bain, A. D.; Cramer, J. A. *J. Magn. Reson. Ser. A* **1993**, *103*, 217.

Chapter 8: Quantification of Li Ion Hopping Timescales in $Li_5V(PO_4)_2F_2$

8.1 Introduction

This chapter characterizes Li ion hopping rates and energy barriers in the novel layered phase, $Li_5V(PO_4)_2F_2$, using ^{6}Li Selective Inversion (SI) NMR measurements. $Li_5V(PO_4)_2F_2$ has six crystallographically distinct lithium sites giving the possibility of fifteen exchange partners between non-equivalent lithium environments. Previous studies have qualitatively observed ion hopping in five pairs of ions using ^{6}Li 2D EXSY measurements.[1] Higher temperature and lower field ^{6}Li 2D EXSY measurements presented in this chapter revealed a sixth ion hopping pair, confirming that ion hopping is found only between Li sites which have polyhedral sharing either through an edge or face geometry. ^{6}Li 1D SI measurements over a variable temperature range were used to quantify the timescales and energy barriers of ion mobility for three of the six ion pairs observed to participate in ion hopping. Limiting the analysis to only three of the six pairs was brought on by the poor resolution of the exchanging sites found in the lower part of the ^{6}Li MAS spectrum, making selective inversion a challenge.

8.2 Experimental

8.2.1 Sample Preparation.

Samples of ^{6}Li enriched $Li_5V(PO_4)_2F_2$ were provided by collaborators at the University of Waterloo and is the same material studied in previous publications.[1]

8.2.2 Bond Valence Density Maps

Bond valence density maps were generated for each crystal structure using the VALMAP program, developed by Gonzalez-Platas *et al.*[2] This program takes crystallographic data including unit cell parameters and atomic coordinates, and calculates the bond valences density within a three-dimensional unit cell using the empirical parameters of Brown *et al.*[3,4] In this work, two-dimensional planes of bond valence density were extracted using the atomic coordinates of atoms defining a Li ion diffusion pathway. For each map, a 2 Å radius is shown with a bond valence density contour level increment is 0.485.

8.2.3 Solid State NMR.

^{6}Li 2D EXSY spectra were acquired at a Larmor frequency of 29.4 MHz on a Bruker AMX 200 spectrometer at the National Institute of Chemical Physics and Biophysics (NICPB), Tallinn, Estonia. A custom-built double resonance probe supporting 1.8 mm rotors capable of MAS frequencies of 25 kHz up to 45 kHz was used. Temperatures were calibrated using $Pb(NO_3)_2$ as described elsewhere.[5] The spectra were referenced to 1 M ^{6}LiCl (aq) (0 ppm). Two-dimensional exchange spectra were acquired with mixing time set to 2 ms, 608 scans, and a recycle delay of 50 ms. The number of slices in the indirect dimension was 512. Phase-sensitive detection in t_1 was achieved through the use of States-TPPI.[6]

Variable temperature ^{6}Li MAS NMR experiments were acquired at a Larmor frequency of 73.6 MHz on a Bruker AV500 spectrometer at McMaster University. Temperatures were calibrated using $Sm_2Sn_2O_7$ as described elsewhere.[7] ^{6}Li 1D MAS spectra were acquired with a 90° pulse length of 2.5 μs and recycle delay of 200 ms. 1D ^{6}Li Selective Inversion (SI) experiments were performed using a 180° - τ_{mix} - 90° sequence. Selectivity for a particular resonance was accomplished using a soft, long, Gaussian pulse for the 180° pulse. The duration of the low power (0.159 W) shaped pulse was 1 ms. The mixing time (τ_{mix}) was stepped over a series of 16 experiments from 5 μs to 100 ms (the latter delay time being well beyond the relaxation rates of both spins reached equilibrium). A recycle delay of 200 ms was used with a total of 2048 scans collected for each slice, Nonselective Inversion (NSI) experiments were performed using the standard inversion-recovery sequence included in the Bruker software package. The same variable delay list, scan number, and recycle delay, was used in the NSI as was used in the 1D SI experiments.

8.2.4 Data Analysis.

A Mathematica notebook developed by Darren Brouwer of Redeemer University was used for deconvolution and integration of the pseudo two-dimensional data sets produced by the arrayed 1D selective and non-selective inversion recovery experiments. The integrals were normalized to the integration value of the slice collected at the longest mixing time/variable delay (where the magnetization of each spin was fully relaxed). The experimental data was fit using the CIFIT program developed by A.D. Bain of McMaster University.[8] CIFIT uses as an input table of observed integrated intensities for all spins as a function of mixing time and determines a key set of parameters: the jump rates (k) of each chemical exchange process, spin-lattice relaxation times in the absence of chemical exchange (T_1), and the magnetization values from initial to equilibrium conditions (i.e. from M_0 to M_∞). The rate matrix used to describe spin relaxation under the influence of chemical exchange is the primary mathematical model used by the CIFIT program and is described in greater detail elsewhere.[8-10] CIFIT adjusts the free parameters, k, T_1, M_0 and M_∞ using a Levenberg-Marquardt algorithm until the sum of the squares of the differences between the experimental and modeled data is minimized. Error values of the exchange rates were approximated in the CIFIT program by the variance-covariance matrix of the fit to the data.

8.3 Results and Discussion

The six Li crystallographic positions in $Li_5V(PO_4)_2F_2$ (**Figure 8.1**) were resolved in the 1D ^{6}Li NMR spectrum with MAS of 25 kHz at a calibrated temperature of 312 K (**Figure 8.2**). Resonances centered at 110 ppm, 83 ppm, 49 ppm, 16 ppm, 11 ppm, and 7 ppm, were labeled as A-F in order of highest to lowest frequency. The assignment of these resonances to the crystallographic positions is detailed in a previous publication based on the Fermi-contact interaction with the transition metal as well as the exchange pathways observed from ^{6}Li 2D EXSY experiments.[1]

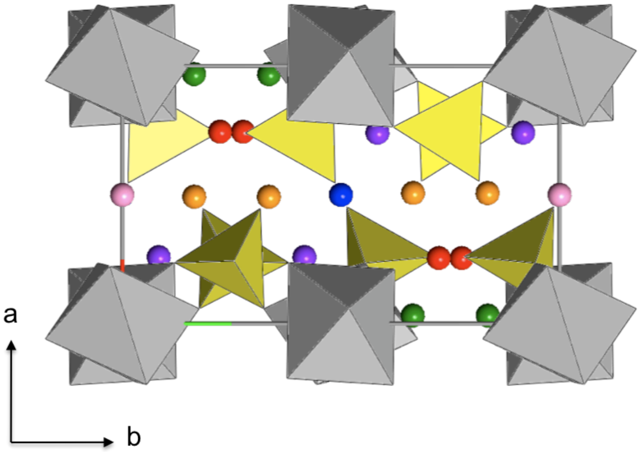

Figure 8.1 – Structure of $Li_5V(PO_4)_2F_2$, which crystallizes in the monoclinic space group, $P2_1/c$. Corner shared vanadium octahedra (grey) and phosphate tetrahedra create a two-dimensional sheet that sandwiches layers of lithium ions (coloured spheres). $Li1_A$ (pink) and $Li2_B$ (blue) sit on the *2b* and *2d* Wyckoff positions, respectively, each with occupancy of 0.5. The remaining lithium environments, $Li3_E$ (purple), $Li4_C$ (red), $Li5_F$ (orange), and $Li6_D$ (green), all sit on the *4e* Wyckoff position with full occupancy.[11]

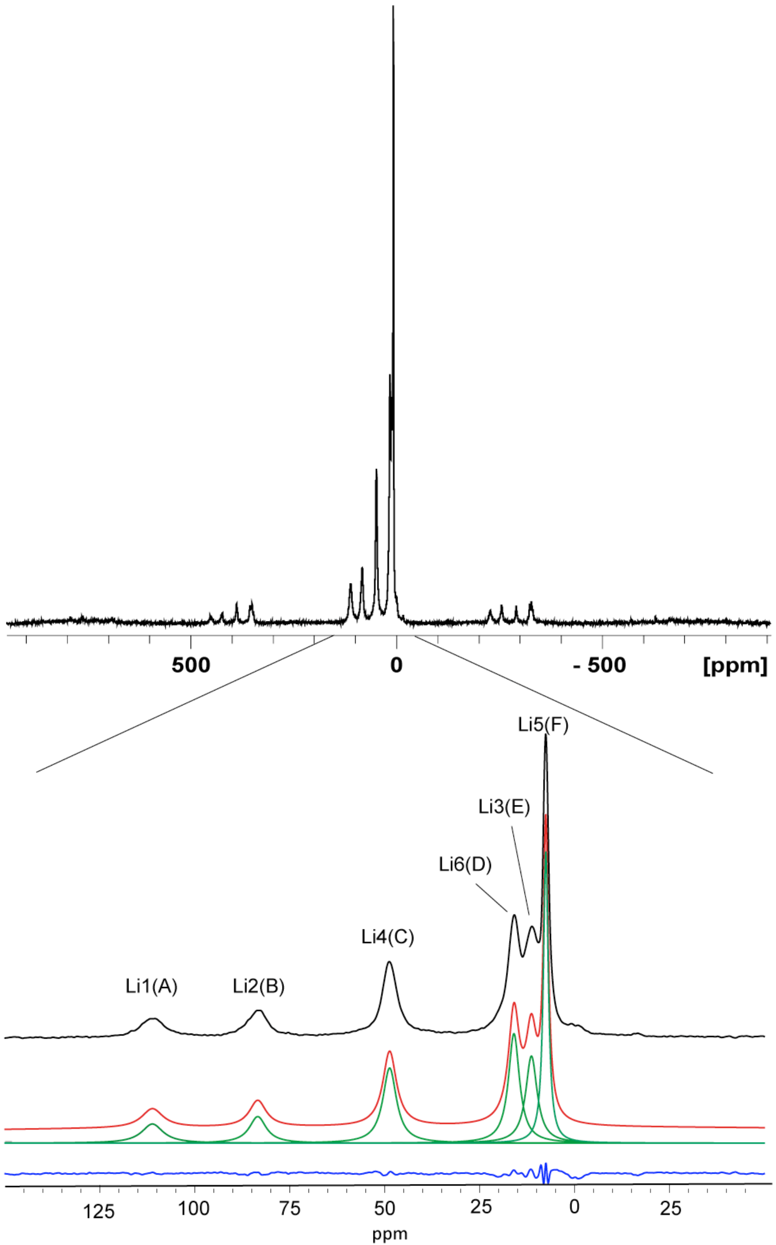

Figure 8.2 – Top: ^{6}Li MAS NMR spectrum of $Li_5V(PO4_4)_2F_2$ at MAS frequency of 25 kHz and temperature of 312 K. Deconvolution of the isotropic region is shown as the bottom spectrum. The experimental spectrum (black) was deconvoluted into the known six crystallographic sites (green). The difference map (blue) between the experimental (back) and modeled spectrum (red) is shown at the bottom of the spectrum.

Previous studies in our group identified five Li ion hopping pairs between $Li3_E$-$Li5_F$, $Li3_E$-$Li6_D$, $Li4_C$-$Li5_F$, $Li4_C$-$Li6_D$, and $Li5_F$-$Li6_D$, in $Li_5V(PO_4)_2F_2$, using ^6Li 2D EXSY measurements at 327 K and magnetic field strength of 7.0 T. The sharing of the Li polyhedral environments for each exchange pair is summarized here (**Table 8.2**).[1] The $Li4_C$-$Li5_F$ and $Li4_C$-$Li6_D$ polyhedra are face shared with internuclear distances of 2.749 Å and 2.831 Å, respectively. Triangular bottlenecks created by the O and F atoms along the ion hopping pathway have areas of 3.59 Å^2 and 3.43 Å^2, for the $Li4_C$-$Li5_F$, $Li4_C$-$Li6_D$ pairs, respectively. For the exchange pairs with edge-shared Li polyhedra, extension of the Li bond radius from 2.80 Å to 3.00 Å in a crystal structure visualization software program such as xtaldraw, a pseudo-face-shared geometry can be visualized. This also allowed for bottleneck areas of, 3.80 Å^2, 3.70 Å^2, and 3.97 Å^2 to be calculated for exchange pairs $Li3_E$-$Li5_F$, $Li3_E$-$Li6_D$, and $Li5_F$-$Li6_D$, respectively. The corresponding internuclear distances for these pairs are 3.133 Å, 3.041 Å, and 3.027 Å, as listed in **Table 8.1**.

Table 8.1 – Summary of the five exchange pairs/pathways in $Li_5V(PO_4)_2F_2$ identified previously in the Goward group using ^6Li 2D EXSY measurements.[1]

Exchange pair	Geometry of Li Ion Polyhedra	Li-Li Internuclear Distance (Å)	Bottleneck Area (Å^2)
$Li3_E$-$Li5_F$	Edge	3.133	3.80
$Li3_E$-$Li6_D$	Edge	3.041	3.70
$Li4_C$-$Li5_F$	Face	2.749	3.59
$Li4_C$-$Li6_D$	Face	2.831	3.43
$Li5_F$-$Li6_D$	Edge	3.027	3.97

In this work, a ^6Li 2D EXSY study carried out at lower field (4.7 T) with higher temperature of 349 K (**Figure 8.3**) revealed a sixth exchange pair between $Li1_A$-$Li5_F$.

This is another edge-shared geometry with internuclear distance of 2.988 Å. Extension of the Li bond radius to 3.1 Å for both Li1$_A$ and Li5$_F$, in the crystal structure drawing program, allows for pseudo-face geometry to be visualized with a calculated bottleneck area of 4.17 Å^2.

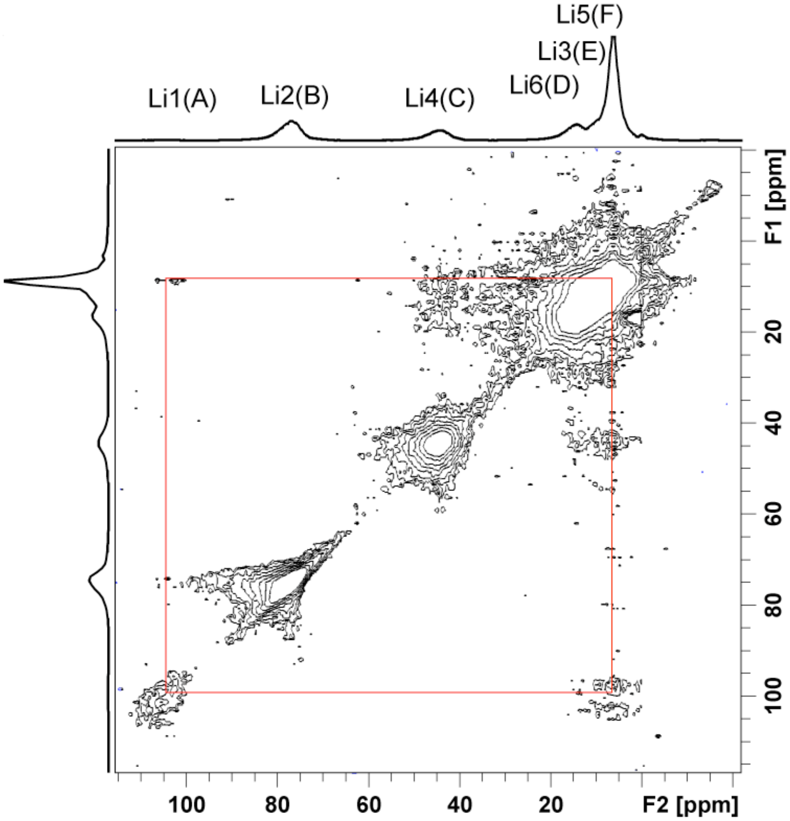

Figure 8.3 – ^{6}Li 2D EXSY spectrum of $Li_5V(PO_4)_2F_2$ collected at the NICPB. MAS = 40 K, T = 349 K, and τ_{mix} = 2 ms.

While only six exchange pairs were observed from the ^{6}Li 2D EXSY studies, a total of fifteen ion hopping pairs are possible between the six crystallographic positions within $Li_5V(PO_4)_2F_2$. All fifteen pairs are listed in (**Table 8.2**) along with their respective polyhedral sharing geometry, internuclear distance, and bottleneck area of diffusion (if applicable). *Italicized* typeface indicates that exchange has been observed between that pair from ^{6}Li 2D EXSY measurements.

Table 8.2 – Summary of all possible exchange pairs/pathways in Li$_5$V(PO$_4$)$_2$F$_2$. Pairs where ion exchange has been observed are presented in *italicized* typeface.

Exchange pair	Geometry of Li Ion Polyhedra	Li-Li Internuclear Distance (Å)	Bottleneck Area (Å^2)	BSV values (Lix−Liy)
Li1$_A$-Li2$_B$	None	5.192	n/a	0.953 - 0.883
Li1$_A$-Li3$_E$	Corner	3.331	n/a	0.953 - 0.988
Li1$_A$-Li4$_C$	Face	2.882	3.34	0.953 - 1.080
Li1$_A$-Li5$_F$	*Edge*	*2.988*	*4.17*	*0.953 - 0.805*
Li1$_A$-Li6$_D$	Corner	4.344	n/a	0.953 - 0.819
Li2$_B$-Li3$_E$	Edge	2.964	3.47	0.884 - 0.988
Li2$_B$-Li4$_C$	Corner	3.371	n/a	0.884 - 1.080
Li2$_B$-Li5$_F$	Corner	3.308	n/a	0.884 - 0.805
Li2$_B$-Li6$_D$	Corner	4.310	n/a	0.884 - 0.819
Li3$_E$-Li4$_C$	Corner	4.185	n/a	0.988 - 1.080
Li3$_E$-Li5$_F$	*Edge*	*3.133*	*3.80*	*0.988 - 0.805*
Li3$_E$-Li6$_D$	*Edge*	*3.041*	*3.70*	*0.988 - 0.819*
Li4$_C$-Li5$_F$	*Face*	*2.749*	*3.59*	*1.080 - 0.805*
Li4$_C$-Li6$_D$	*Face*	*2.831*	*3.43*	*1.080 - 0.819*
Li5$_F$-Li6$_D$	*Edge*	*3.027*	*3.97*	*0.805 - 0.819*

This provides an opportunity to identify which structural constraints are most critical for ion exchange to take place. As was demonstrated in previous chapters, parameters that have strong influence on the probability of ion exchange include Li-Li internuclear distance, sharing geometry of the Li polyhedra site within an exchange pair (corner-, edge-, or face-shared), area of the bottleneck for face-sharing or pseudo-face sharing geometries, and bond valence density along the diffusion pathway. When evaluating **Table 8.2**, it is noted that ion exchange is not observed between Li polyhedra sharing only a corner (Li1$_A$-Li3$_E$, Li2$_B$-Li4$_C$, Li2$_B$-Li5$_F$, Li2$_B$-Li6$_D$, and Li3$_E$-Li4$_C$) or in pairs where no common atoms are shared between their polyhedra ($Li1_A$-$Li2_B$). For the edge-shared interactions, ion exchange was observed between $Li1_A$-$Li5_F$, $Li3_E$-$Li5_F$, $Li3_E$-$Li6_D$, and $Li5_F$-$Li6_D$. Here the pseudo-face-sharing geometries have bottlenecks ranging from 3.70 $Å^2$ to 4.17 $Å^2$ and internuclear distances from 2.749 Å to 3.133 Å. For the non-exchanging $Li2_B$-$Li3_E$ edge-shared pair, the structural parameters (bottleneck of 3.47 $Å^2$ and Li-Li distance of 2.964 Å) fall within the range of pairs where exchange has been observed. Similarly for the non-exchanging $Li1_A$-$Li4_C$ pair, which has face-shared Li polyhedra, the structural constraints of the internuclear distance and bottleneck suggest that exchange is possible between these two Li sites. However, exchange has not been observed in either $Li1_A$-$Li4_C$ and $Li2_B$-$Li3_{E.}$ We therefore turn to bond valence density maps to better explain why ion hopping is not observed in these otherwise promising pathways for ion diffusion. **Figure 8.4** shows bond valence (BV) maps of $Li1_A$-$Li4_C$, $Li1_A$-$Li5_F$, $Li2_B$-$Li3_E$, $Li3_E$-$Li5_F$, $Li3_E$-$Li6_D$, $Li4_C$-$Li5_F$, $Li4_C$-$Li6_D$, and $Li5_F$-$Li6_D$ (from **Table 8.2**). The plane of each BV density map was defined by the atomic coordinates of the O and F atoms that create the bottleneck of diffusion for a given exchange pair.

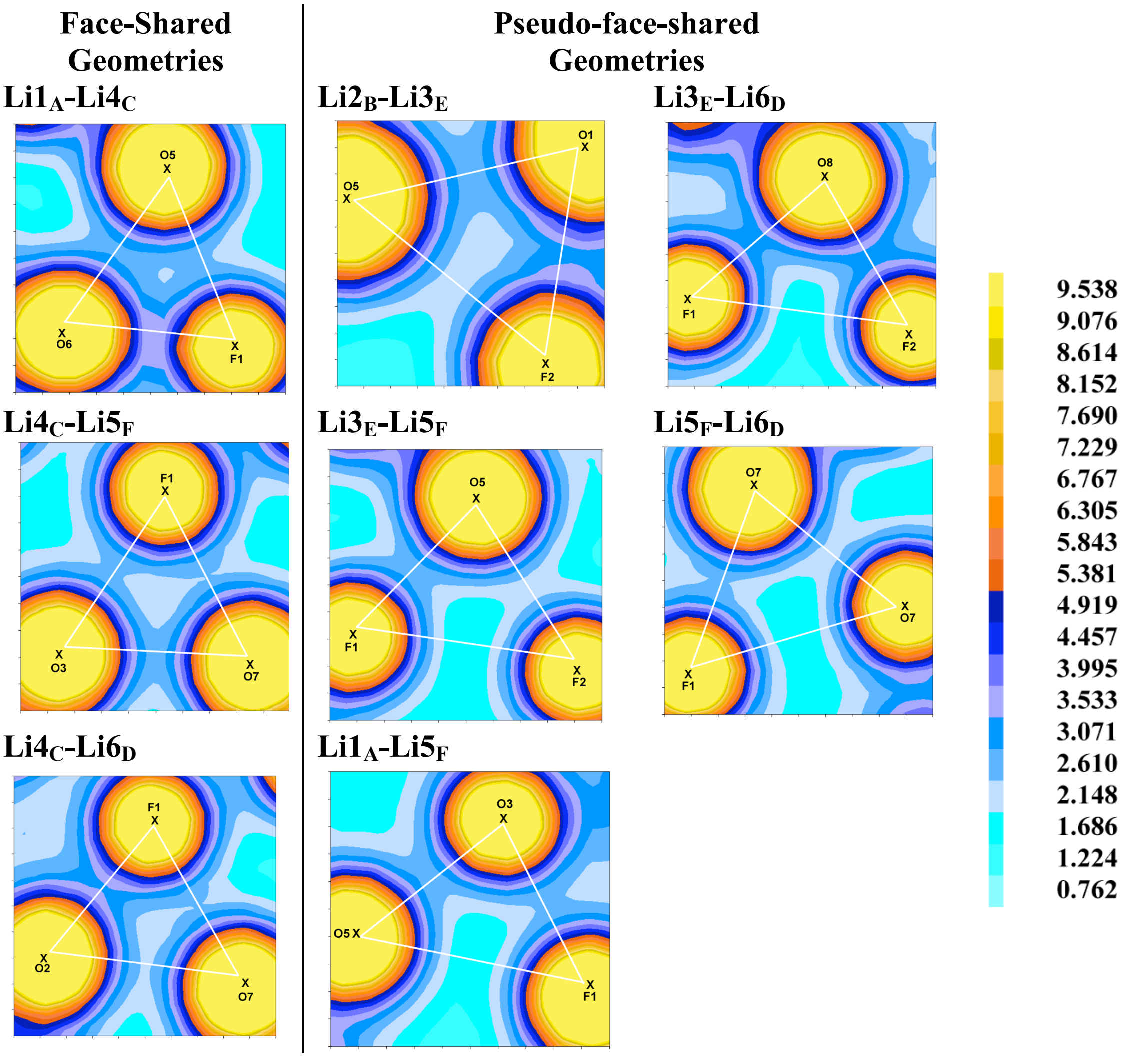

Figure 8.4 – Bond valence maps of ion exchange pathways in $Li_5V(PO_4)_2F_2$ for the ion hopping pairs that have either face-shared (left) or pseudo-face-shared (right) Li polyhedral geometries.

The exchange pairs with face-shared Li polyhedra have pathways with higher BV density than the pairs with pseudo-face-shared polyhedra. As will be shown in the next section, the timescales of ion hopping between pairs with pseudo-face-shared polyhedra are considerably slower than the pairs having face-shared geometry. This is attributed to the less direct pathway found in the pseudo-face-shared geometries created by the open edge. Therefore, the comparison of BV density is restricted to ion pairs with similar geometries of polyhedral sharing. For the Li exchange pairs with face-shared polyhedral environments, the map of the non-exchanging Li1$_A$-Li4$_C$ pair has much higher bond valence density relative to the maps of the exchanging Li4$_C$-Li5$_F$ and Li4$_C$–Li6$_D$ pairs. Similarly in the maps of the exchange pairs with edge-shared (or pseudo-face-shared) Li polyhedra, the non-exchanging Li2$_B$–Li3$_E$ has higher bond valence density when compared to the maps of Li1$_A$-Li5$_F$, Li3$_E$-Li5$_F$, Li3$_E$-Li6$_D$, and Li5$_F$-Li6$_D$, where exchange has been observed. Overall, there is a strong correlation between the BV density found along the diffusion pathway and the propensity for ion exchange to take place within a host framework.

8.3.1 Timescales of Ion Hopping Determined from ^{6}Li SI Experiments

The influence of bond valence density on the timescales of ion exchange was investigated using ^{6}Li 1D selective inversion measurements over a variable temperature range. Only Li1$_A$ and Li4$_C$ were chosen for selective inversion out of the six Li sites in $Li_5V(PO_4)_2F_2$. (**Figure 8.2**) as these resonances were the best resolved in the spectrum and observed to participate in chemical exchange from the 2D EXSY studies. Inverting Li1$_A$ allowed for the timescales and energy barriers of the exchange pair Li1$_A$-Li5$_F$, to be determined. Inversion of Li4$_C$ in a second set of experiments gave quantitative results for Li4$_C$-Li5$_F$, and Li4$_C$-Li6$_D$ ion hopping. The exchange timescales in Li5$_F$-Li6$_D$, Li3$_E$-

$Li5_F$, and $Li3_E$-$Li6_D$ were not determined due to low resolution of the crystallographic sites within this set of exchange pairs (**Figure 8.2**). The CIFIT model was designed to include the ion hopping rate matrices from all six exchange pairs. However, because the $Li3_E$-$Li6_D$, $Li3_E$-$Li5_F$, and $Li5_F$-$Li6_D$ hopping rates could not be measured experimentally, the influence that they have on the resolved $Li4_C$-$Li5_F$, $Li4_C$-$Li6_D$, and $Li1_A$-$Li5_F$ rates is difficult to determine. Therefore, rates of the measureable $Li4_C$-$Li5_F$, $Li4_C$-$Li6_D$, and $Li1_A$-$Li5_F$ were fit initially with the rates of $Li3_E$–$Li6_D$ (k_{36}), $Li3_E$–$Li5_F$ (k_{35}), and $Li5_F$–$Li6_D$ (k_{56}) set to zero. The ion hopping rates of $Li4_C$-$Li5_F$ (k_{45}) and $Li4_C$-$Li6_D$ (k_{46}) at 348 K were then fit again with non-zero values input for k_{35}, k_{36}, and k_{56}. A more detailed presentation of this latter strategy is given in section 8.3.1.3 while the results from the zero value fits are given herein.

8.3.1.1 ^{6}Li Selective Inversion Results for Inversion of $Li1_A$

Data collected from inversion of $Li1_A$ in the ^{6}Li 1D SI experiments over a variable temperature range is shown in **Figure 6.7**. The magnetization curves of $Li3_E$, $Li4_C$, and $Li6_D$ do not have transient features that indicate ion exchange is taking place with the inverted $Li1_A$ site. Only $Li5_F$ shows transient features attributable to ion exchange, which is consistent with the ^{6}Li 2D EXSY results of **Figure 8.3**.

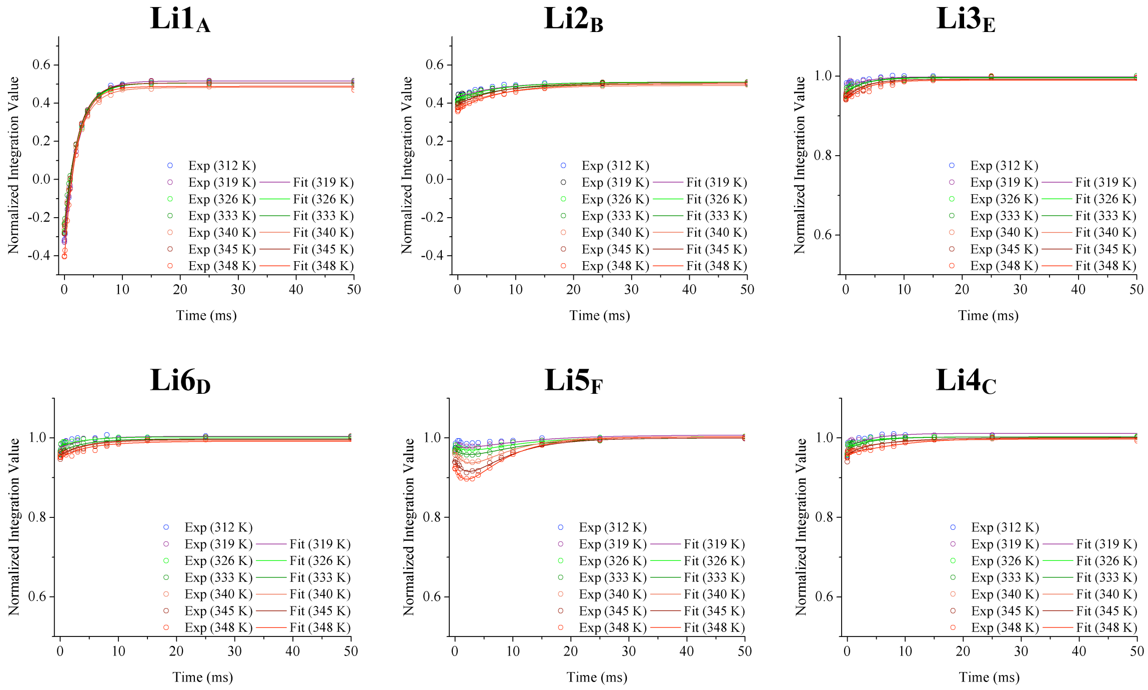

Figure 8.5 – Results of the ^{6}Li 1D selective inversion of Li1$_A$ (resonance A) over a variable temperature range (312 K – 348 K as indicated on legend on each plot). Clockwise from the top left, magnetization curves of Li1$_A$, Li2$_B$, Li3$_E$, Li4$_C$, Li5$_F$ and Li6$_D$. The points represent measured values and the lines are the best fit to the data from the CIFIT program. For the non-inverted resonances, the depth of the transient well increases with increasing temperature, as expected for the ion exchange process.

Li2$_B$ does show a temperature dependent attenuation of its magnetization with inversion of Li1$_A$. This attenuation however, is not attributed to Li1$_A$-Li2$_B$ exchange as these two sites are 5.912 Å apart and do not share any atoms between their respective polyhedral environments (**Table 8.2**). Rather, the attenuation is attributed to the proximity of the Li2$_B$ resonance to the site selected for inversion. **Figure 8.6** shows the slight inversion (~ 5%) of the Li2$_B$ resonance at the lowest (312 K) and highest (348 K) experimental temperatures. As the temperature is raised, the paramagnetic resonances migrate towards 0 ppm, (due to Curie-Weiss changes in the magnetic susceptibility)[12] creating a less resolved spectrum. The attenuation of the neighbouring Li2$_B$ magnetization has now increased to ~ 15 % relative to the signal observed at a mixing time where all spins are at equilibrium.

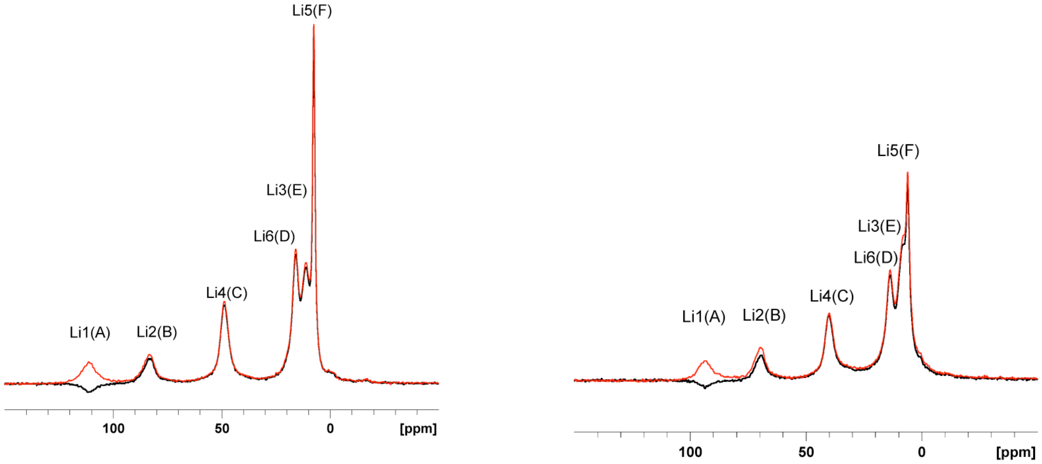

Figure 8.6 – ^{6}Li SI spectra showing the inversion of Li1$_A$ at different mixing times and temperatures. Left: inversion of Li1$_A$ at 312 K. Right: Inversion of Li1$_A$ at 348 K The red spectra are at a mixing time of 100 ms, where complete relaxation of the inverted peak is accomplished. The black spectra are at mixing times of 5 µs where maximum inversion is observed.

The rate coefficients for the Li1$_A$Li5$_F$ exchange process were determined by fitting the experimental results in CIFIT. For this exchange process a forward and backward rate coefficient exists, (k$_{15}$ and k$_{51}$, respectively). Because the Li1$_A$:Li5$_F$ occupancy is 0.5:1.0, under a steady-state approximation, $k_{15} = 2k_{51}$. In this study, the CIFIT parameters were set such that the faster coefficient, k$_{15}$, was found while the reverse coefficient, k$_{51}$, was predicted based on the site-populations (**Table 8.3**). Detail on the treatment of unequal populations in CIFIT is outlined in greater detail elsewhere.[13]

The forward rate coefficients for $Li1_A$-$Li5_F$ ranged from 14 ± 4 s^{-1} at 326 K up to 49 ± 6 s^{-1} at 348 K (Table 8.3). Data collected at temperatures below 326 K, had timescales that could not be accurately fit using CIFIT and were therefore excluded from the analysis of the energy barriers.

Table 8.3 – Summary of CIFIT results over a variable temperature range of ^{6}Li SI measurements where $Li1_A$ was the site chosen for inversion. The forward rate coefficients (k_{15}) are reported from CIFIT while the backward coefficients (k_{51}) are predicted from the site-populations

Temperature (K)	**k_{15} (s^{-1}) $Li1_A$-$Li5_F$**	**k_{51} (s^{-1}) $Li1_A$-$Li5_F$**
312 K	Not Determined	Not Determined
319 K	Not Determined	Not Determined
326 K	14 (± 4)	7 (± 2)
333 K	18 (± 5)	9 (± 3)
340 K	40 (± 5)	20 (± 3)
345 K	45 (± 5)	23 (± 3)
348 K	49 (± 6)	25 (± 3)
Energy Barrier (eV)	0.6 ± 0.1	0.6 ± 0.1

The activation energy of $Li1_A$-$Li5_F$ hopping was calculated from the slope of the natural log of (k/T) plotted against the inverse temperature in an Eyring analysis (**Figure 8.7**). An energy barrier value of 0.6 ± 0.1 eV was calculated with the error determined from the standard error of the slope from the regression analysis. The large error on the energy barriers is attributed to the large relative error for the ion hopping rates determined at 326 K and 333 K (**Table 8.3**). It is noteworthy that the overall timescales measured for this exchange pair in $Li_5V(PO_4)_2F_2$ are considerably slower than those measured for Li ion hops between corner-shared polyhedra of $Li_3Fe_2(PO_4)_3$ (from ^{6}Li 2D

EXSY measurements, Chapter 5) and $Li_3V_2(PO_4)_3$ (from ^{7}Li 2D EXSY study of Cahill *et al.*[14]). This difference is discussed in greater detail in 8.3.2.

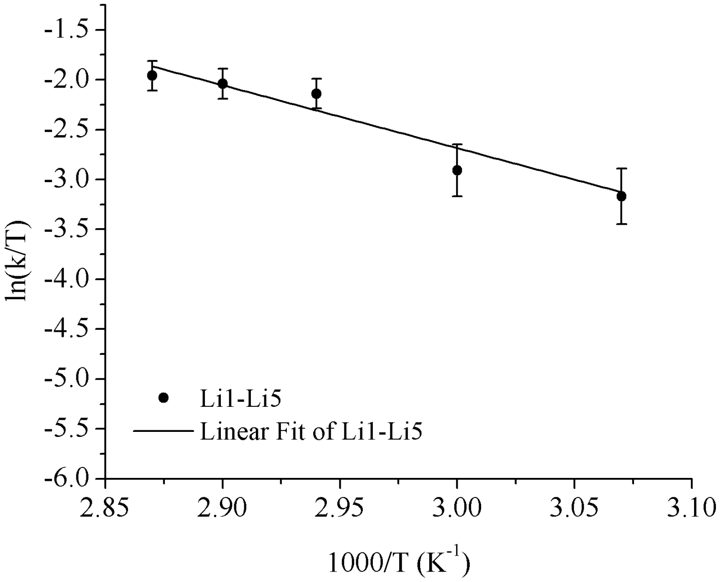

Figure 8.7 – Eyring plot of the natural log of the $Li1_A$-$Li5_F$ ion hopping rate (k) over temperature plotted against 1000/T.

8.3.1.2 ^{6}Li Selective Inversion Results for Inversion of $Li4_C$

Results from the inversion of $Li4_C$ over a variable temperature range are given in **Figure 6.7**. Here, both $Li5_F$ and $Li6_D$ show well-developed transients attributed to ion exchange with $Li4_C$. This is supported by the previous reports of $Li4_C$-$Li5_F$, and $Li4_C$-$Li6_D$ exchange observed in the ^{6}Li 2D EXSY studies.[1]

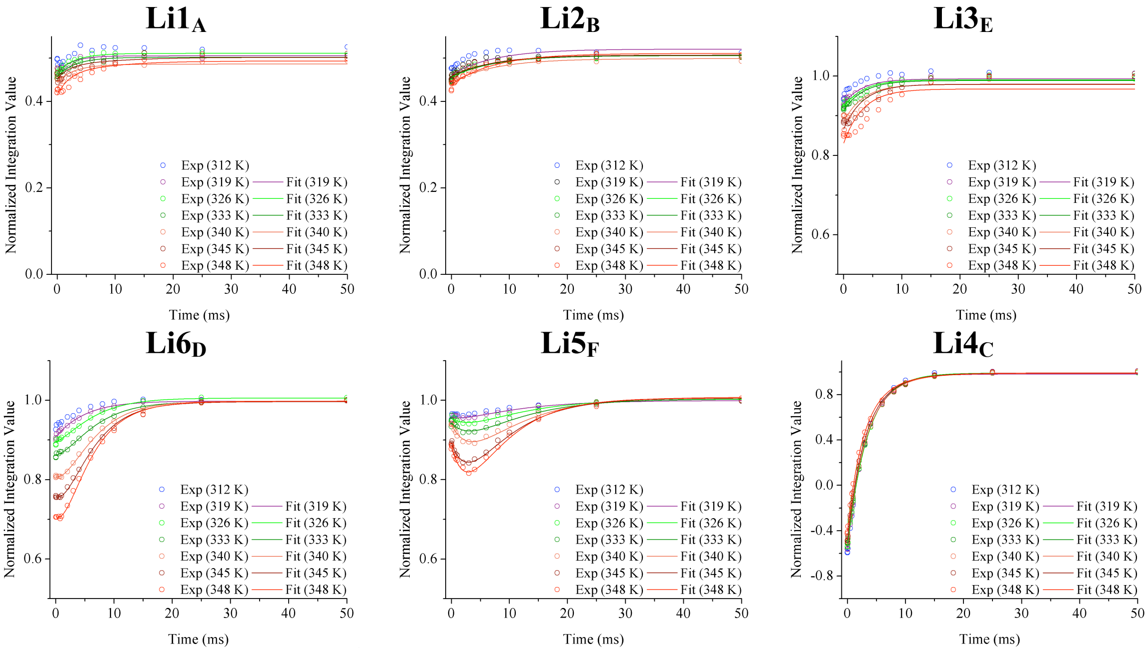

Figure 8.8 – Results of the ^{6}Li 1D selective inversion of Li4$_C$ over a variable temperature range. Clockwise from the top left, magnetization curves of Li1$_A$, Li2$_B$, Li3$_E$, Li4$_C$, Li5$_F$ and Li6$_D$. The points represent measured values and the lines are the best fit to the data from the CIFIT program. For the non-inverted resonances, the depth of the transient well increases with increasing temperature, as expected for ion exchange processes.

Slight transient features also appear in the magnetization curves of Li3$_E$. This transient is not attributed to Li4$_C$-Li3$_E$ exchange but more to Li3$_E$-Li6$_D$ exchange. Due to the proximity of the Li6$_D$ resonance (δ = 16 ppm at 312 K, **Figure 8.2**) to the Li4$_C$ inversion site (δ = 11 ppm, at 312 K), slight inversion (~ 5 %) of the Li6$_D$ site is observed (**Figure 8.9**). As the temperature is raised, the paramagnetic resonances migrate towards 0 ppm, (due to Curie-Weiss changes in the magnetic susceptibility)[12] creating a less resolved spectrum. The attenuation of the neighbouring Li6$_D$ magnetization has now increased to ~ 30% relative to the signal observed at a mixing time where all spins are at equilibrium.

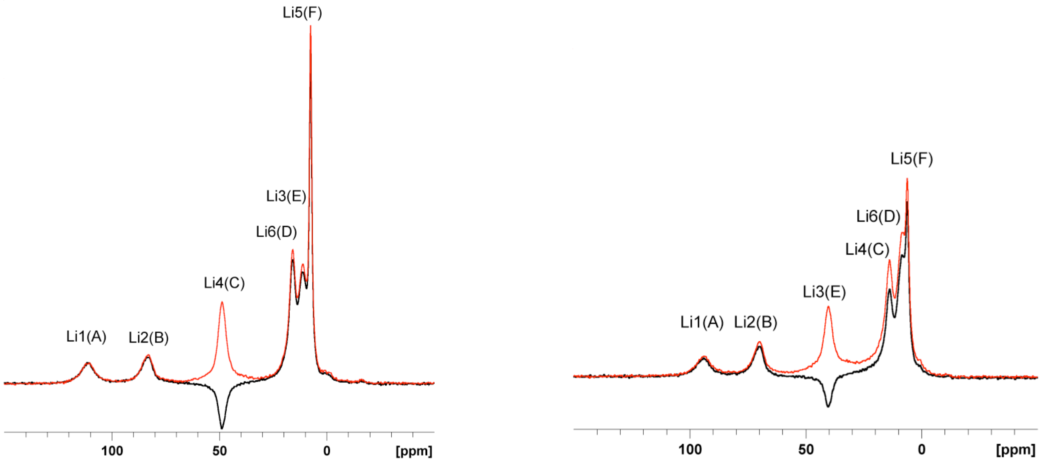

Figure 8.9 – ^{6}Li SI spectra showing the inversion of Li4$_C$ at different mixing times and temperatures. The red spectra are at a mixing time of 100 ms, where complete relaxation of the inverted peak is accomplished. The black spectra are at mixing times of 5 μs where maximum inversion is observed. Left: inversion of Li4$_C$ at 312 K Right: Inversion of Li4$_C$ at 348 K

Therefore, the determined timescales of ion hopping for Li4$_C$-Li5$_F$ and Li4$_C$-Li6$_D$ are treated with some caution. This is not only due to the slight inversion of the neighbouring Li6$_D$ resonance, but also due to the unknown influence that the un-measureable Li3$_E$-Li6$_D$, Li3$_E$-Li5$_F$, and Li5$_F$-Li6$_D$ exchange pairs has on the hopping rates of the measureable exchange pairs, Li4$_C$-Li5$_F$, Li4$_C$-Li6$_D$, and Li1$_A$-Li5$_F$. As stated previously, the CIFIT model includes the ion hopping rate matrices from all six exchange pairs. However, because the Li3$_E$-Li6$_D$, Li3$_E$-Li5$_F$, and Li5$_F$-Li6$_D$ hopping rates cannot be measured experimentally, the influence that they have on the measureable Li4$_C$-Li5$_F$, Li4$_C$-Li6$_D$, and Li1$_A$-Li5$_F$ rates is difficult to determine. A more detailed presentation of this latter strategy is given in section 8.3.1.3.

Rates of $Li4_C$-$Li5_F$ extend from 9 ± 2 s^{-1} at 326 K up to 58 ± 7 s^{-1} at 348 K. Slightly faster kinetics were observed for the $Li4_C$-$Li6_D$ exchange with timescales ranging from 12 ± 4 s^{-1} at 326 K up to 71 ± 11 s^{-1} at 348 K (**Table 8.4**). In both exchange pairs, data collected at 312 K had dynamics too slow to be accurately determined. This temperature was therefore excluded from the Eyring analysis of the energy barriers. Plots of the natural log of the rate constant over temperature as a function of inverse temperature in an Eyring analysis yielded energy barriers of 0.79 ± 0.04 eV for $Li4_C$-$Li5_F$ and 0.76 ± 0.04 eV for $Li4_C$-$Li6_D$ (**Figure 8.10**). These energy barriers are equivalent within error and reflect the similarity in bottleneck dimensions and internuclear distances (**Table 8.2**) as well as bond valance density maps (**Figure 8.4**), for these two hopping pairs.

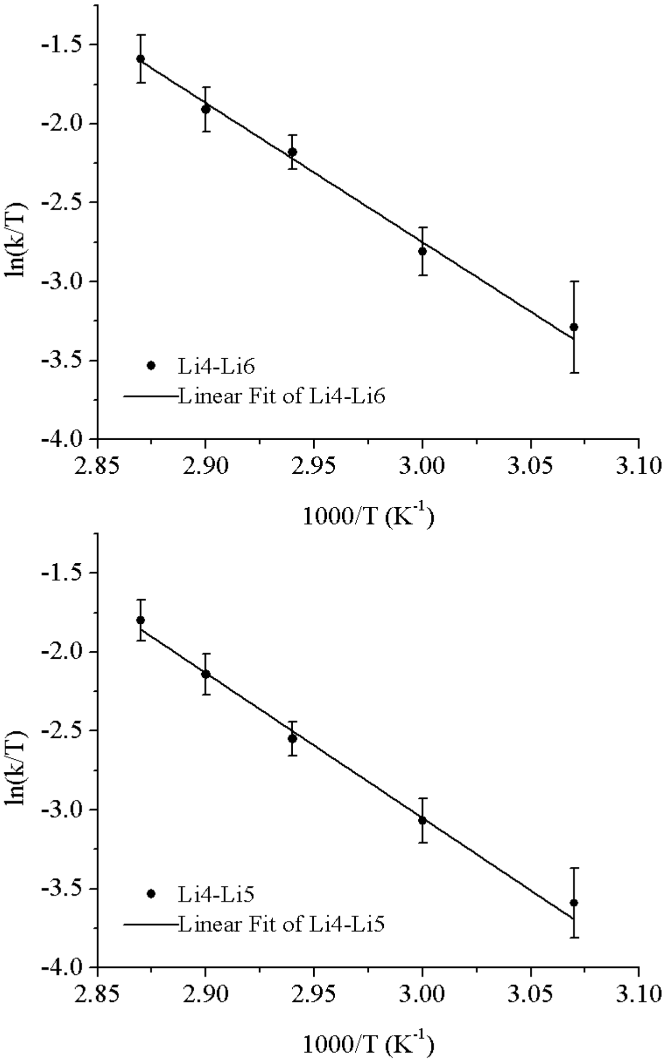

Figure 8.10 – Eyring plots of the natural log of the Li4$_C$-Li6$_D$ (top) and Li4$_C$-Li5$_F$ (bottom) ion hopping rates (k) over temperature against 1000/T.

Here the timescales and energy barriers of ion hopping in the face-shared polyhedra, Li4$_C$-Li5$_F$ and Li4$_C$-Li6$_D$, are compared to that of the edge-shared polyhedral pair Li1$_A$-Li5$_F$. This comparison is made more complex by the unequal populations of the Li1$_A$ and Li1$_F$ sites of this pair as compared to the equal population of the face-shared pairs. Comparing the backward (k_{51}) and forward rate (k_{15}) coefficients for the Li1$_A$-Li5$_F$

(where $k_{15} = 2k_{51}$), k_{15} is higher due to the lower concentration of the $Li1_A$ site, while k_{51} is lower due to the higher population of the $Li5_F$ site. If the $Li1_A$ and $Li5_F$ populations were equal, the rate coefficients would both sit at the lower, k_{51}, value, as there would no longer be an overcompensation of the coefficient for the low population. Therefore, the reverse rate coefficients of the $Li1_A$-$Li5_F$ (which are of half-value to those solved for in CIFIT) are more suitable for comparison to the rate coefficients of the $Li4_C$-$Li5_F$, $Li4_C$-$Li6_D$ exchange pairs where occupancy is 1:1. Therefore, comparing timescales found at 348 K, the edge-shared rate coefficient (25 ± 3 s^{-1}) is considerably slower than the timescales found for the either of face-share ion-hopping pairs (71 ± 11 s^{-1} and 58 ± 7 s^{-1} for $Li4_C$–$Li6_D$ and $Li4_C$–$Li5_F$, respectively). Furthermore, ion pairs having face-shared polyhedral geometries have significantly higher energy barriers to the site hop than the edge-shared $Li1_A$-$Li5_F$ pair. Returning to the BSV maps of these three exchange pairs in **Figure 8.4**, the face-shared geometries have a more confined pathway for diffusion resulting in a more direct and therefore faster exchange rate. A higher energy threshold however, accompanies this tighter, but more direct pathway. The edge-shared interaction, while having a more open bottleneck for diffusion, results in a less direct pathway for the ion to diffuse giving longer correlation times.

Table 8.4 – Summary of exchange rates and activation energies of Li ion hopping as determined from ^{6}Li selective inversion studies of $Li_5V(PO_4)_2F_2$.

Temperature (K)	k_{51} (=0.5 k_{51}) (s^{-1}) Li1$_A$-Li5$_F$ (edge)	k_{46} (=k_{64}) (s^{-1}) Li4$_C$-Li6$_D$ (face)	k_{45} = (k_{54}) (Hz) Li4$_C$-Li5$_F$ (face)
312 K	Not Determined	Not Determined	Not Determined
319 K	Not Determined	3 (± 3)	4 (± 2)
326 K	7 (± 2)	12 (± 4)	9 (± 2)
333 K	9 (± 3)	20 (± 3)	15 (± 2)
340 K	20 (± 3)	38 (± 4)	26 (± 3)
345 K	23 (± 3)	51 (± 7)	41 (± 5)
348 K	25 (± 3)	71 (± 11)	58 (± 7)
Energy Barrier (eV)	0.6 ± 0.1	0.76 ± 0.04	0.79 ± 0.04

8.3.1.3 CIFIT Results for Unresolved Exchange Pairs

The results presented in **Table 8.4** of the previous section, are the k_{45}, k_{46} and k_{15} values determined from CIFIT where the rates of exchange between the unresolved sites, Li3$_E$-Li5$_F$, Li3$_E$-Li6$_D$, and Li5$_F$-Li6$_D$ (k_{35}, k_{36}, and k_{56}, respectively) were set to zero. Here, the effect that non-zero values for k_{35}, k_{36}, and k_{56} has on the fit of the measureable data ion hopping rates (k_{45}, k_{46}) is investigated. **Table 8.5** summarizes the values of k_{45} and k_{46} given from a series of fit procedures (labeled LD1 through LD12) where the values of k_{35}, k_{36}, k_{56} values were varied from 0 s^{-1} to 300 s^{-1}, in different combinations.

Table 8.5 – Summary of fits for k_{45} and k_{46} rates at 348 K when the values of k_{36}, k_{35} and k_{56}, are held at non-zero values.

Fit Name	χ^2	Fit Variables k_{36} (s^{-1})	 k_{35} (s^{-1})	 k_{56} (s^{-1})	Held Variables k_{45} (s^{-1})	 k_{46} (s^{-1})	 Sum of k_{45} and k_{46} (s^{-1})
LD1	0.0253	0	0	0	58 (±7)	71 (±11)	128 (±13)
LD2	0.0252	0	0	50	53 (±6)	83 (±9)	130 (±11)
LD3	0.0211	50	0	0	49 (±6)	80 (±10)	129 (±13)
LD4	0.0231	0	50	0	64 (±7)	67 (±9)	135 (±11)
LD5	0.0203	50	50	50	50 (±7)	88 (±10)	137 (±11)
LD6	0.0209	50	0	50	45 (±7)	92 (±10)	137 (±12)
LD7	0.0232	0	50	50	55 (±8)	77 (±10)	132 (±13)
LD8	0.0203	50	50	0	58 (±7)	78 (±9)	138 (±11)
LD9	0.0219	25	25	25	54 (±7)	80 (± 9)	134 (±12)
LD10	0.0192	100	100	100	40 (±8)	104 (± 11)	145 (±14)
LD11	0.0197	200	200	200	17 (±10)	135 (± 14)	152 (±17)
LD12	0.0206	300	300	300	- 7 (±12)	165 (±17)	158 (±20)

An initial set of fits (LD2, LD3, and LD4) have only one of k_{35}, k_{36}, or k_{56} set to 50 s^{-1}, while the others were held at 0 s^{-1}. These were compared to the fits from LD1 where k_{35}, k_{36}, or k_{56} are all at set to zero and LD5 where k_{35}, k_{36}, and k_{56} are all set to 50 s^{-1}. A value of 50 s^{-1} was chosen for the rates of the unresolved sites as it is of the same magnitude of values determined from the initial fits of k_{45}, k_{46} and k_{15} and is comparable to other fluorophosphate frameworks studied in this thesis (Li_2VPO_4F, Chapter 6). It is evident that having only one of k_{35}, k_{36}, and k_{56} rates set to a non-zero value does not alter k_{45} and k_{46} beyond the error bounds given from LD1. The fits of the transient wells of the $Li5_F$ and $Li6_D$ magnetization under these different fitting conditions (**Figure 8.11**), maintain a χ^2 value close to, or better than, the one given for LD1 (**Table 8.5**)

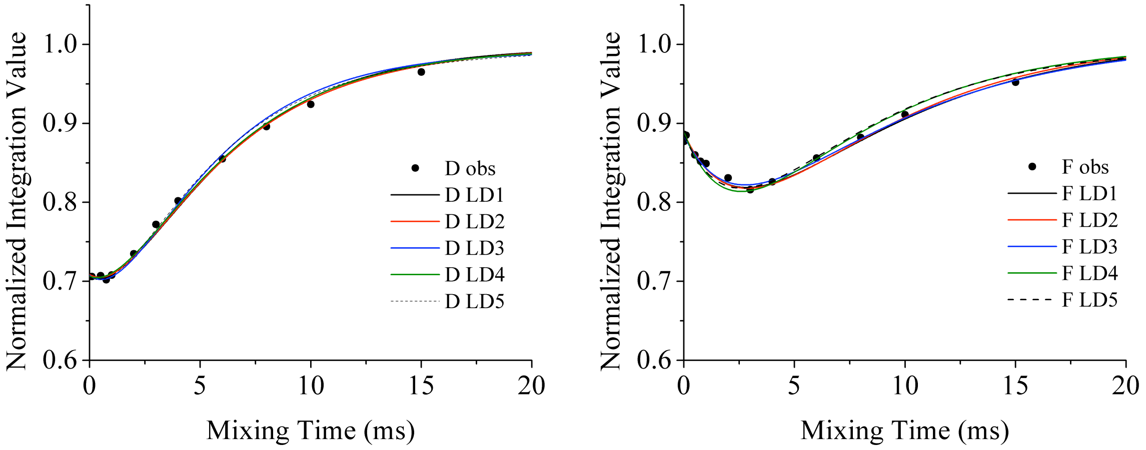

Figure 8.11 - Fit of Li6$_D$ (left) and Li5$_F$ (right) transient wells at 348 K as the values of k_{36}, k_{35} and k_{56} are varied in the fitting regimes of LD1, LD2, LD3, LD4, and LD5. Parameters for each fit are summarized in **Table 8.5**

When two out of the three rates are set to 50 s^{-1}, the values of k_{45} and k_{46} are impacted to a greater extent (outlined in fits LD6, LD7, and LD8). When k_{36} and k_{56} are both set to 50 s^{-1} while k_{35} is left at 0 s^{-1} (LD6), the fitted values for k_{45} and k_{46} are pushed further away from the LD1 results, than the rates given in the LD2, LD3, and LD4 fits. However, these values are still equivalent within error to the LD1 results with fits of the transient wells of the Li5$_F$ and Li6$_D$ magnetization (**Figure 8.12**) under the different fitting conditions giving χ^2 values close to, or better than, those for LD1 (**Table 8.5**).

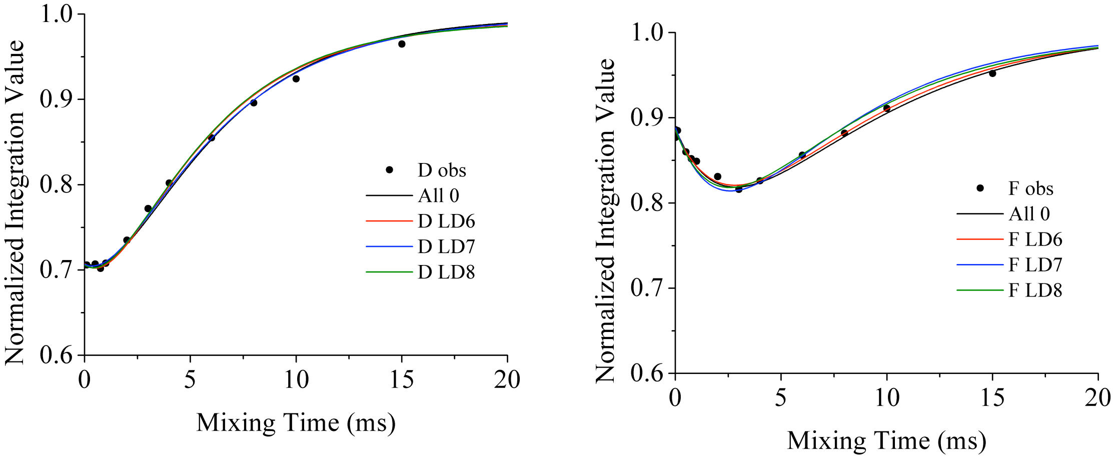

Figure 8.12 - Fit of $Li6_D$ (left) and $Li5_F$ (right) transient wells at 348 K as the values of k_{36}, k_{35} and k_{56} are varied in the fitting regimes of LD1, LD6, LD7, and LD8. Parameters for each fit are summarized in **Table 8.5**.

When all three rates, k_{35}, k_{36}, and k_{56} are set to 50 s^{-1} (LD5), there is minimal change to the values of k_{45} and k_{46} than those determined from LD1. When the k_{35}, k_{36}, and k_{56} are set to values slightly lower (25 s^{-1}(LD9)) there is still no movement of the fit values of k_{45} and k_{46} outside the error limits of the LD1 results. Only when much higher values of k_{35}, k_{36}, and k_{56} are selected, do the fit values of k_{45} and k_{46} begin to move outside the error limits of the LD1 results (**Table 8.5**). This was the case when k_{35}, k_{36}, and k_{56} were set to 100 s^{-1} (LD10), 200 s^{-1} (LD11) and 300 s^{-1} (LD12). For this set of conditions, the transient wells of the $Li5_F$ and $Li6_D$ magnetization for fits LD1, LD5, and LD9-12 are given in **Figure 8.13**. The χ^2 values for this last group of fits also does not deviate from the goodness of fit given in the LD1 calculations (**Table 8.5**)

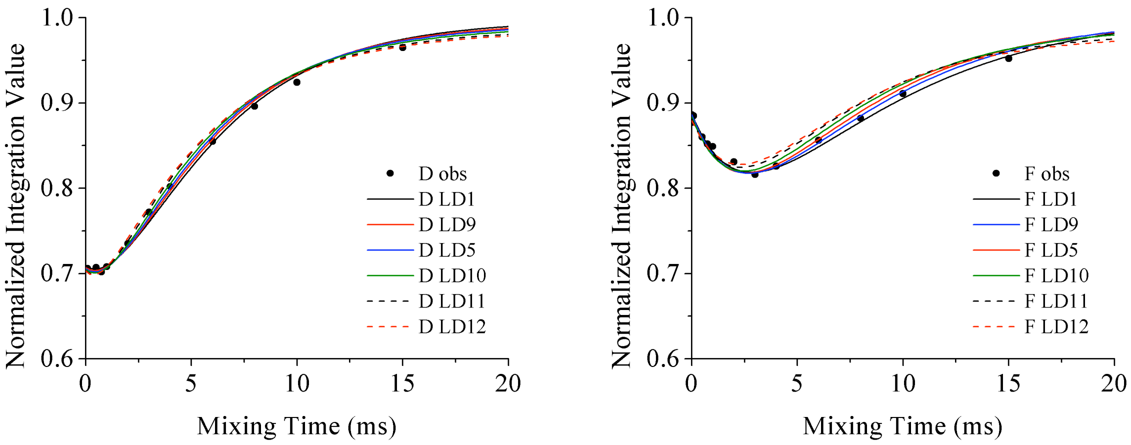

Figure 8.13 – Fit of Li6$_{\mathrm{D}}$ (left) and Li5$_{\mathrm{F}}$ (right) transient wells at 348 K as the values of k_{36}, k_{35} and k_{56} are varied in the fitting regimes of LD1, LD9, LD10, LD11, and LD12. Parameters for each fit are summarized in **Table 8.5**.

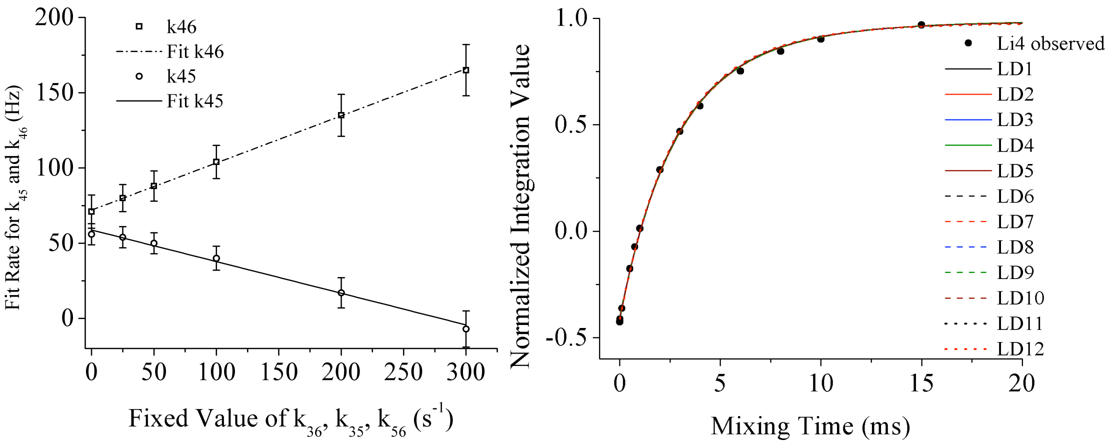

Figure 8.14 - Left: Plot of the fit values of k_{45} and k_{46} at 348 K against the held values of k_{35}, k_{36} and k_{56} (from fitting regimes LD1, LD5, LD9-12). Right: Fit of Li4C over all fitting regimes (LD1-LD12). Parameters for each fit are summarized in **Table 8.5**.

It is noteworthy that in this last fitting procedure, the k_{45} and k_{46} values diverge away from one another with a linear dependence on the held value of k_{35}, k_{36}, and k_{56} (**Figure 8.14**, left). Moreover, the sum of the k_{45} and k_{46} rates remains consistent (within error) over all possible fitting regimes. This shows that although the distribution of the k_{45} and

k_{46} values may change, the total contribution of the ion mobility to the relaxation of Li4_C is unchanged. This is more clearly demonstrated when the fits of Li4_C are shown over the entire set of fitting parameters (LD1-LD12) (**Figure 8.14**, right).

Overall, the results from this series of fitting procedures (LD1-LD12) show that the values of k_{45} and k_{46} are accurately determined when the values of, k_{35}, k_{36}, and k_{56}, are set to 0 s^{-1} in the CIFIT rate matrices. For the ion hopping rates of the unresolved exchange processes k_{35}, k_{36}, and k_{56}, little information regarding the magnitude of these values can be extracted from this set of initial conditions.

8.3.2 Comparison to Materials Studied in this Thesis and Other Works

Here we compare the timescales and energy barriers of ion hopping within the set of materials studied in this thesis and other works. **Table 8.6** summarizes the timescales, energy barriers, and key parameters that influence ion mobility in $Li_3M_2(PO_4)_3$ (M = Fe and V), [14,15] Li_2VPO_4F, $Li_5V(PO_4)_2F_2$ and Li_3VF_6.[16]

Table 8.6 – Summary of Li ion hopping rates, energy barriers, internuclear distances, bottleneck area, bond sum valence (BSV) values and bond sum value distribution (ΔBSV) for ion hopping pairs in a series of Li intercalation compounds.

Material and Hopping Pairs	**k Range (s^{-1})**	**E_a (eV)**	**Li-Li distance (Å)**	**Bottleneck (Å^2)**	**BSV Lix-Liy**	**ΔBSV**
$Li_3Fe_2(PO_4)_3$	**Temperature Range = 283 – 311 K**					
Li1-Li2	108 − 760	0.59 ± 0.05	3.139	3.96	1.054-0.952	0.102
Li1-Li3	112−1025	0.63 ± 0.03	3.417	3.42	1.054-0.989	0.065
Li2-Li3	8 −990	0.81 ± 0.04	3.110	4.22	0.952- 0.989	0.037
$Li_3V_2(PO_4)_3$[14]	**Temperature Range = 278 K**					
Li1-Li2	142 (± 7)	0.83 ± 0.01	3.4	3.69	1.057-0.909	0.148
Li1-Li3	155 (± 10)	0.73 ± 0.01	3.08	4.10	1.057- 1.064	0.007
Li2-Li3	130 (± 10)	0.79 ± 0.01	3.28	3.79	0.909 -1.064	0.155
Li_2VPO_4F	Temperature Range = 331 – 350 K					
Li1-Li2 α_2	24 –55	0.44 ± 0.06	2.791	3.92	0.799 – 1.029	0.230
Li1-Li2 β_2	24 –55	0.44 ± 0.06	2.993	4.22	0.799 – 1.029	0.230
$Li_5V(PO_4)_3$	**Temperature Range = 326 − 348 K**					
$Li1_A$-$Li5_F$	4–25	0.6 ± 0.2	2.988	4.17	0.953 - 0.805	0.148
$Li4_C$-$Li5_F$	9 −58	0.76 ± 0.04	2.749	3.59	1.080 - 0.805	0.275
$Li4_C$-$Li6_D$	12 −71	0.79 ± 0.04	2.831	3.43	1.080 - 0.819	0.261
Li_3VF_6[16]	**Temperature = 340 K**					
Li1-Li2	49	N/A	2.72	3.78	1.045 – 0.959	0.086
Li1-Li3	225	N/A	2.72	3.83	1.045 – 0.901	0.144
Li2-Li3	31	N/A	3.51	Edge	0.959 – 0.901	0.058

First, the results from the fluorophosphates, $Li_5V(PO_4)_2F_2$ and $Li_2VPO_4F_2$ are compared. In Chapter 6, two ion exchange pathways with face-shared polyhedral geometries were identified as the most probable pathways for ion exchange in Li_2VPO_4F and labeled as the α- and β-pathways, respectively. The range of ion hopping rates of these pathways is similar to those found for the $Li4_C$-$Li5_F$ and $Li5_F$-$Li6_D$ partners, of $Li_5V(PO_4)_2F_2$, which also have face-shared polyhedra. However, a lower energy barrier of exchange was found in Li_2VPO_4F which we attribute to the more open diffusion bottlenecks (~ 4 Å^2) whereas in $Li_5V(PO_4)_2F_2$ the $Li4_C$-$Li5_F$ and $Li5_F$-$Li6_D$ bottlenecks are smaller at 3.59 Å^2 and 3.43 Å^2, respectively. The energy barrier of the face-shared

Li_2VPO_4F pathways is closer to that of the $Li1_A$-$Li5_F$ pair in $Li_5V(PO_4)F_2$ which is an edge-shared polyhedral exchange pair. This is consistent with the similar appearance of the bond valence maps of the two exchange pathways (**Figure 8.15**) and the bottleneck dimensions of the two being much closer. The α- and β-pathways of Li_2VPO_4F have areas of 3.92 Å^2 and 4.22 Å^2 respectively, while the $Li1_A$-$Li5_F$ exchange pair in $Li_5V(PO_4)F_2$ has a pseudo-face sharing geometry bottleneck area of 4.17 Å^2.

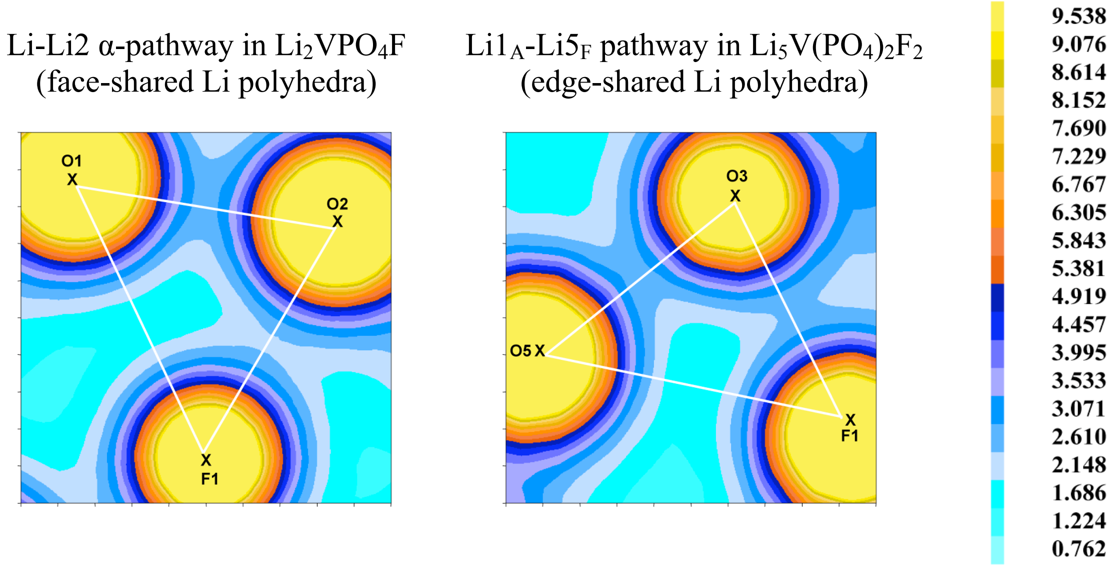
Li-Li2 α-pathway in Li_2VPO_4F
(face-shared Li polyhedra)

$Li1_A$-$Li5_F$ pathway in $Li_5V(PO_4)_2F_2$
(edge-shared Li polyhedra)

Figure 8.15 – Comparison of bond valence density maps of the Li1-Li2 α-pathway in Li_2VPO_4F (left) and the $Li1_A$-$Li5_F$ exchange pathway in $Li_5V(PO_4)_2F_2$. Each map shown has a viewing radius of 2 Å and contour increment of 0.485.

Comparing the fluorophosphates to other fluorinated polyanion frameworks, we turn to the recently published report on the ion hopping rates in Li_3VF_6 from a ^{6}Li 2D EXSY study by Wilkening *et al.*[16] Between the three crystallographic sites, three exchange pairs were identified with ion hopping rates for Li1-Li2, Li2-Li3, and Li2-Li3 as 49 s^{-1}, 225 s^{-1} and 35 s^{-1}, respectively, at 340 K. Results from only a single temperature were presented, meaning a comparison of the energy barriers of this system to other frameworks is not possible. In terms of ion hopping rates, within Li_3VF_6, the authors attributed the slow (31 s^{-1}) Li2-Li3 ion hop to the Li ion possibly occupying an intermediate tetrahedral interstitial site. This is more simply referred to in our work as an edge-shared polyhedral geometry, where a less direct pathway and subsequent longer ion diffusion time is expected. The more quickly exchanging, Li1-Li2 and Li1-Li3 pairs have face-shared polyhedra with similar internuclear distances and bottleneck areas, giving more direct pathways for ion hopping and faster ion hopping rates of 41 s^{-1} and 225 s^{-2}, respectively. We attribute the very fast hopping rate of the Li1-Li3 to a region of low bond valence density observed in its BV density map, that is not observed in the Li1-Li2 pair (**Figure 8.16**).

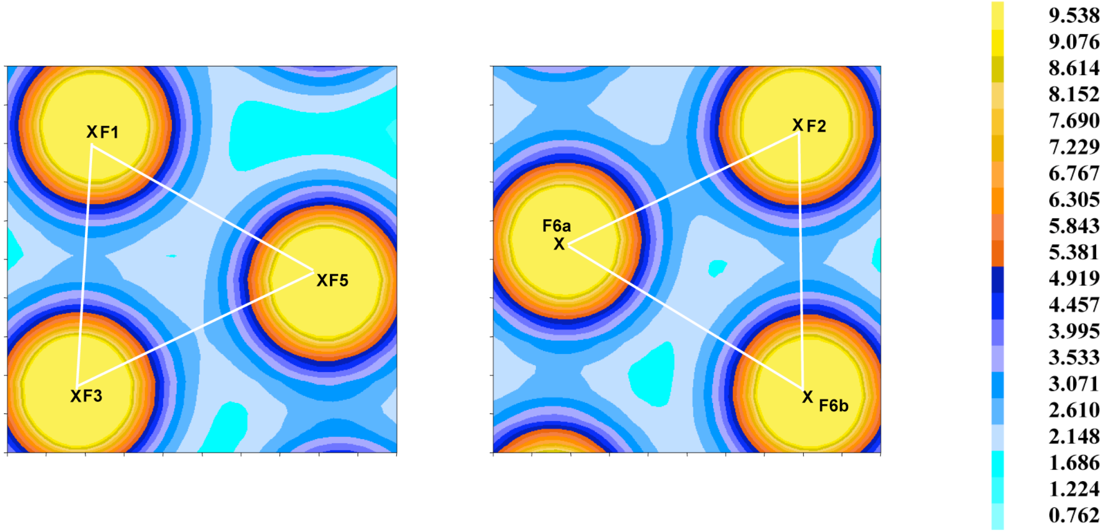

Figure 8.16 – Bond valence density maps of the Li1-Li2 (left) and Li1-Li3 (right) exchange pathways in Li_3VF_6. Contour increment is 0.485 with a 2 Å radius shown.

Comparing the fluorophosphates to Li_3VF_6, the timescales of the $Li4_C$-$Li5_F$ and $Li4_C$-$Li6_D$ pairs (with face-shared polyhedra) in $Li_5V(PO_4)_2F_2$ (at $26 \pm 3\ s^{-1}$ and $38 \pm 4\ s^{-1}$, respectively at 340 K) are quite close to the Li1-Li2 pair of Li_3VF_6 (41 s^{-1} at 340 K). Returning to the $Li4_C$-$Li5_F$ and $Li4_C$-$Li6_D$ bond valence maps for $Li_5V(PO_4)_2F_2$ of **Figure 8.4**, these maps closely resemble the map belonging to the Li1-Li2 pair of Li_3VF_6 (**Figure 8.16**). This again illustrates the usefulness of bond valence density maps in interpreting measured timescales of ion mobility in Li intercalation compounds.

Li ion hopping in the fluorophosphates and metal fluoride (Li_3VF_6) frameworks are much slower relative to those in the phosphates, $Li_3Fe_2(PO_4)_3$ and $Li_3V_2(PO_4)_3$. Not only are the measured rates of ion hopping in the phosphates ~ 10 times faster than the fluorophosphates and Li_3VF_6, but this is observed within a much lower temperature range. This fast exchange is not explained by the geometry of the exchange pairs as the phosphates host only corner- and edge-shared geometries of ion hopping pathways, which are less favourable for fast ion mobility than the face-shared geometries found in Li_3VF_6 and fluorophosphates. It is evident that the introduction of fluorine atoms to the anion within the framework contributes to the slow ion exchange in Li_3VF_6, Li_2VPO_4F and $Li_5V(PO_4)_2F_2$. It is proposed that the ion dynamics in a larger set of materials having different phosphate, fluorophosphates, and fluorosulfate anion compositions be studied in order to further investigate the role that the anion composition plays on the Li ion mobility properties. This study should include the tavorite based Li_2FePO_4F[17] as its structure and dynamics are easily compared to the isostructural Li_2VPO_4F as well as $Li_3Fe_2(PO_4)_3$.

8.4 Conclusions

This chapter highlights the influence of bond valence density on the probability of ion hopping in fluorophosphates. ^{6}Li Selective Inversion measurements revealed the timescales and energy barriers of ion hopping between Li1$_A$-Li4$_C$, Li4$_C$-Li5$_F$, and Li4$_C$-Li6$_D$ in $Li_5V(PO_4)_2F_2$. Faster ion hopping with a higher energy barrier was observed in the face-shared Li4$_C$-Li5$_F$ and Li4$_C$-Li6$_D$ pairs, where more direct bottlenecks were revealed in the bond valence density maps. The more open bottleneck of the Li1$_A$-Li5$_F$ pathway gives a lower energy barrier but a less direct pathway giving a longer correlation time for exchange. These results were compared to frameworks having different anion structures including phosphates ($Li_3Fe_2(PO_4)_3$ and $Li_3V_2(PO_4)_3$) and the metal fluoride (Li_3VF_6). The fluorinated structures have restricted ion mobility relative to the phosphates, indicating that the introduction of fluorine atoms influences the Li ions significantly.

8.5 References

(1) Makimura, Y.; Cahill, L. S.; Iriyama, Y.; Goward, G. R.; Nazar, L. F. *Chem. Mater.* **2008**, *20*, 4240.

(2) Gonzalez-Platas, J.; Gonzalez-Silgo, C.; Ruiz-Perez, C. *J. Appl. Crystallogr.* **1999**, *32*, 341.

(3) Brown, I. D.; Wu, K. K. *Acta Crystallogr. Sect. B-Struct. Commun.* **1976**, *32*, 1957.

(4) Brown, I. D. *Chem. Soc. Rev.* **1978**, *7*, 359.

(5) Takahashi, T. K., Hiroe; Sugisawa, Hishashi; Baba, Toshihide; *Solid State Nuclear Magnetic Resonance* **1999**, *15*, `119.

(6) Marion, D.; Ikura, M.; Tschudin, R.; Bax, A. *J. Magn. Reson.* **1989**, *85*, 393.

(7) Grey, C. P.; Cheetham, A. K.; Dobson, C. M. *J. Magn. Reson. Ser. A* **1993**, *101*, 299.

(8) Bain, A. D.; Cramer, J. A. *J. Magn. Reson. Ser. A* **1996**, *118*, 21.

(9) Bain, A. D. *Prog. Nucl. Magn. Reson. Spectrosc.* **2003**, *43*, 63.

(10) Bain, A. D.; Berno, B. *Prog. Nucl. Magn. Reson. Spectrosc.* **2011**, *59*, 223.

(11) Yin, S. C.; Herle, P. S.; Higgins, A.; Taylor, N. J.; Makimura, Y.; Nazar, L. F. *Chem. Mater.* **2006**, *18*, 1745.

(12) Gee, B.; Horne, C. R.; Cairns, E. J.; Reimer, J. A. *J. Phys. Chem. B* **1998**, *102*, 10142.

(13) Bain, A. D.; Cramer, J. A. *J. Phys. Chem.* **1993**, *97*, 2884.

(14) Cahill, L. S., Chapman, R. P., Britten, J. F., Goward, G. R. *J. Phys. Chem. B* **2006**, *110*, 7171.

(15) Davis, L. J. M.; Heinmaa, I.; Goward, G. R. *Chem. Mater.* **2010**, *22*, 769.

(16) Wilkening, M.; Romanova, E. E.; Nakhal, S.; Weber, D.; Lerch, M.; Heitjans, P. *J. Phys. Chem. C* **2010**, *114*, 19083.

(17) Ramesh, T. N.; Lee, K. T.; Ellis, B. L.; Nazar, L. F. *Electrochem. Solid State Lett.* **2010**, *13*, A43.

Chapter 9: Summary and Outlook

9.1 Summary

This thesis presented multinuclear solid-state NMR results that elucidated the structural and Li ion mobility properties in a series of phosphate and fluorophosphate Li intercalation compounds used as cathode materials for Li ion batteries. NMR of these materials is made non-trivial by the strong through-bond and through-space coupling between the nuclei being measured and the unpaired electron spin density sitting on the transition metal center. While this coupling can lead to complications in the NMR spectra, it also allows for subtle changes in the electronic structure of the redox active center to be easily identified through changes in the paramagnetic shift, isotropic lineshapes, and span of the sideband manifolds. This thesis also sought to expand the number of NMR tools available to study ion dynamics in this class of materials. Previous studies of Li ion mobility have used ^{6,7}Li 2D EXSY measurements over a variable temperature range to quantify ion hopping rates and energy barriers in paramagnetic Li intercalation compounds including $Li_3Fe_2(PO_4)_3$ studied in Chapter 5.[1-4] Analysis of this data is most accurate when the longest mixing time extends well beyond the correlation time of the exchange process(es). However, in strongly paramagnetic systems such as those studied here, short spin-lattice relaxation of the Li nuclei limits the range of mixing times available leading to a more complicated data analysis. This thesis showed that ^{6}Li Selective Inversion (SI) experiments are an excellent alternative means to measure ion dynamics in solid-state paramagnetic materials, especially in systems where the ion hopping rates are slow relative to the spin-lattice time of the Li nuclei. As a result, a combination of ^{6}Li 2D EXSY and ^{6}Li 1D SI measurements led to quantification of the ion hopping timescales in $Li_3Fe_2(PO_4)_3$, Li_2VPO_4F, Li_2VOPO_4 and $Li_5V(PO_4)_2F_2$. This gave a more detailed picture of the structural factors that enhance or inhibit ion mobility in a framework including Li-Li internuclear distance, atomic bottlenecks for diffusion and bond valence density along the ion hopping pathway. Here, a chapter-by-chapter breakdown of the key results from each section is given with suggestions for future work included.

In Chapter 4, the influence of the paramagnetic centers on the appearance of both the ^{7}Li and ^{31}P MAS NMR spectra of $LiMnPO_4$ and $LiFePO_4$ was investigated. Significant differences in paramagnetic shift, span of the sideband manifold, and full-width half-maximum (FWHM) of the isotropic peak of these isostructural frameworks was observed and attributed to the different electron configuration at the transition metal center where, Mn^{2+} is a $d^5\,t_{2g}^3e_g^2$ configuration and Fe^{2+} is a $d^6\,t_{2g}^4e_g^2$ configurations. This sensitivity to electronic changes at the transition metal center was used to monitor the high-temperature phase transformation in Li_xFePO_4 from biphasic $0.5LiFePO_4$:$0.5FePO_4$ to the solid solution $Li_{0.5}FePO_4$. Here the large difference in the ^{31}P paramagnetic shift of the $Fe^{3+}PO_4$ and $LiFe^{2+}PO_4$ domains allowed the coalescence of these two domains to be monitored as a function of temperature. This was the first *in-situ* NMR study of the high-temperature phase transformation in this electrochemically important material. Moreover, this chapter also showed the presence of phase-interface Li regions in $0.5LiFePO_4$:$0.5FePO_4$, using solid-state ^{7}Li MAS measurements. Lack of site mixing in the phase boundary regions are often attributed to poor cycling rates in the phosphate family of cathode materials. Our identification of distinct Li environments at these regions confirms that the Li ions are not hopping between the lithiated and delithitiated regions on a timescale faster than that of the NMR acquisition.

The focus of ongoing work is the quantification of Li ion mobility timescales in the olivine phases. Only a single crystallographic Li site is found within these frameworks meaning exchange measurements, which rely on the movement of Li ions from one crystallographic environment to another, cannot be used effectively. Similarly, measurements which rely on changes to the ^{6,7}Li NMR lineshape over a variable temperature, also cannot be used to quantify ion dynamics. This is due to temperature-dependent changes to the magnetic susceptibility having a larger influence on the appearance on the NMR spectra than any changes to the average homo- or heteronuclear dipolar couplings brought on by Li ion mobility. In this thesis, an attempt to probe heteronuclear dipolar couplings was made by using ^{6}Li{^{31}P} REDOR measurements. However, the incomplete excitation of the broad ^{31}P resonance introduces a large number of variables that makes accurate interpretation of the resulting REDOR buildup curves non-trivial. Therefore, it is proposed that future studies focus on REDOR measurements that investigate changes in ^{6}Li-^{7}Li dipolar couplings as both ^{6}Li and ^{7}Li resonances are narrow relative to the ^{31}P meaning fewer complications from incomplete excitation are encountered.

In Chapter 5, the timescales and energy barriers of ion hopping in α-$Li_3Fe_2(PO_4)_3$ were quantified using ^{6}Li 2D EXSY measurements. Unlike previous reports on the ^{7}Li 2D EXSY measurements of isostructural $Li_3V_2(PO_4)_3$,[2] the measured timescales and energy barriers did not correlate to trends in internuclear distances and atomic bottlenecks for diffusion. Rather, for $Li_3Fe_2(PO_4)_3$, bond valence density maps revealed a significant obstruction of valence density from an Fe atom along the diffusion pathway leading to the highest energy barrier for the Li2-Li3 pair despite it having an open bottleneck and short internuclear distance. This highlighted the importance of considering the three-dimensional bond valence density along the Li-Li exchange route when discussing possible pathways for Li ion diffusion.

Chapter 5 also demonstrated how the ion dynamics are changed in samples of as-prepared $Li_xV_2(PO_4)_3$ (x = 3) as it first cast as a cathode slurry and then as it is cycled to a composition of x = 1.2. Preliminary results show that coalescence of the three isotropic peaks (A, B, and C) takes place at lower temperature in the cycled materials than in either the cast material or the as-prepared compound. Similar to the case for $0.5LiFePO_4{:}0.5FePO_4$, the presence of phase interface regions may be hindering the ion mobility in this phase as well. Quantification of these timescales using ^{6}Li Selective Inversion (SI) measurements are proposed as a continuation of this project, as the low signal to noise of the cycled samples makes ^{6,7}Li 2D EXSY measurements impractical from the standpoint of spectrometer time.

Proposed future work for $Li_3Fe_2(PO_4)_3$, is based on the recent work of Cabana *et al.* where insertion of a fourth and fifth Li ion was characterized using ^{6}Li MAS measurements.[5] Here, the isotropic peaks were broadened significantly which the authors attribute to enhanced mobility and/or Li ion disorder of the newly prepared phases $Li_{3+x}Fe_2(PO)_3$ ($1 \leq x \leq 2$). It is possible however, that this broadening is due to changes in T_{1e} at the paramagnetic center brought on by the change in Fe oxidation state. A lengthened T_{1e} could greatly increase the FWHM of the isotropic Li lineshapes, as was shown in our study of the FWHM of Li near a Fe^{3+} site versus a Fe^{2+} site in biphasic $0.5LiFePO_4$:$0.5FePO_4$ (Chapter 4). Therefore, it is proposed that quantification of the ion dynamics in the electrochemically intercalated phases be made either through ^{6}Li SI or ^{6}Li 2D EXSY measurements. This will allow for the source of the line broadening to be properly identified as arising either from the changes in ion dynamics brought on by Li insertion, or because of electronic changes at the paramagnetic center leading to different electron spin relaxation properties. This differentiation is critical as faster ion mobility at higher lithiation levels would make $Li_{3+x}Fe_2(PO_4)_3$ a very high-capacity material for Li ion battery applications.

Chapter 6 detailed the characterization of the structure and ion mobility properties of the fluorophosphate phase Li_xVPO_4F ($x = 0.0, 1.5, 2.0$) using ^{19}F, ^{31}P and ^{6,7}Li NMR measurements. Collaborators from the University of Waterloo provided samples of Li_xVPO_4F allowing for ^{6,7}Li MAS NMR measurements to map an *ex-situ* lithiation of the host framework from x = 0.0 to 1.5 to 2.0. The two new environments in the Li_2VPO_4F phase were assigned initially based on the Fermi-contact interaction with the paramagnetic V center, and then through analysis of the sideband manifolds where CSA parameters were extracted and correlated to the symmetry of each site. ^{6}Li{^{19}F}REDOR measurements further confirmed the assignment where the Li site having shortest Li-F contact (as given from the crystallographic data) gave rise to the strongest REDOR buildup. ^{6}Li 1D EXSY measurements were applied to Li_2VPO_4F in order to determine the ion hopping rates over a variable temperature range. This was the first application of selective inversion NMR methods to quantify ion mobility timescales in paramagnetic solid-state materials. It has subsequently expanded the NMR tools available to study ion mobility timescales in this class of materials. The timescales measured were correlated to one of two possible pathways for ion hopping. However, due to similarities in internuclear distance, bottleneck area, and bond valence density, distinguishing between the equally favourable pathways was not possible.

While the ^{6}Li 1D EXSY method used in Chapter 6, was an excellent selective inversion method for determining the timescales and energy barriers in Li_2VPO_4F, it is limited to systems having only a single exchange process. This is due to the delay period (τ_1) in the $90° - \tau_1 - 90°$ inversion step being dependent on the frequency difference between the two sites observed to exchange. In Chapter 7, the use of selective inversion methods was expanded from a two-site, single exchange system to the three-site, three exchange system by replacing the $90° - \tau_1 - 90°$ step of 1D EXSY with a selective shaped pulse. In the three-site material, Li_2VOPO_4, the A, B, and C resonances were observed to participate in AB, BC, and AC exchange first from ^{7}Li 2D EXSY measurements. ^{6}Li selective inversion measurements using shaped pulses (^{6}Li 1D SP) were used to quantify the hopping rates through a series of experiments over a variable temperature range. The exchange rate for each hopping pair was determined twice, where each site in an exchange pair was selectively inverted in separate experiments. For example, the rate of AB exchange was first determined from the inversion of A and then again from the inversion of B where the timescales were found to be within error of one another from each experiment over a variable temperature range. It was concluded that selective inversion measurements using shaped pulses is an accurate method for determining ion exchange rates in solid-state paramagnetic materials. This method therefore, becomes a powerful tool for elucidating the timescales and structural constrains for high capacity battery materials, which more than likely, have multiple crystallographic Li sites.

^{6}Li SP methods were then applied to quantify the ion hopping rates in the novel layered cathode material, $Li_5V(PO_4)_2F_2$. Here, six crystallographic sites were observed to participate in six different exchange processes from ^{6}Li 2D EXSY measurements in previous studies[3] and this work. ^{6}Li selective inversion of the A and C resonances (Li1 and Li4, respectively) gave ion hopping rates for three out of the six exchange pairs, over a variable temperature range. The CIFIT rate matrix used to fit the experimental data included variables for all six exchange processes, meaning the effect of the exchange rates arising from the unresolved pairs on the resolved exchange processes need to be considered. A series of fits were performed where the rates of ion hopping between unresolved pairs were held anywhere from 0 s^{-1} to 300 s^{-1} and the rates of the resolved pairs determined. It was shown that the ion hopping rates of the resolved pairs were not altered outside the errors bounds given when the hopping rates of unresolved pairs were held at zero. The ion hopping rates in $Li_5V(PO_4)_2F_2$ were found to be on a similar timescale to those determined for Li_2VPO_4F, where bond valence density maps of the diffusion pathways correlated well to the measured ion dynamics. Our results show that the fluorophosphates have considerably slower timescales of ion mobility than the phosphates $Li_3Fe_2(PO)_3$, $Li_3V_2(PO_4)_3$.[2,4] The fluorophosphates have been introduced as a class of positive electrode materials that have higher redox potentials over their phosphate counterparts. This thesis has shown that the gains in redox potential come at the expense of fast ion mobility, meaning that any improvements to the power output of the battery through higher voltage may be lost due to slow charge/discharge rates.

These results showed that the anion plays a significant role the ion mobility timescales, and subsequently opens an avenue for future studies. Measurement of the ion mobility timescales in a larger number of Li intercalation materials using solid-state NMR methods will better reveal trends in ion mobility as they correlate to the properties of anion species. This includes study of the tavorite-based materials, $LiFePO_4F$ and Li_2FePO_4F recently reported by Ramesh *et al.*[6] $LiFePO_4F$ is isostructural with $LiVPO_4F$, meaning any information gained from NMR studies would compare well to those already studied in our group. Study of the ion mobility timescales in the silicate family of cathode materials, including Li_2FeSiO_4[7] and Li_2MnSiO_4,[8] would reveal whether a change in polyanion has a significant effect on the ion dynamics relative to those observed in the phosphates. Both ^{6,7}Li 2D EXSY and ^{6,7}Li 1D selective inversion methods over a variable temperature range are proposed for investigating the ion dynamics in these frameworks. As this thesis and other works have shown, these methods prove to be very reliable for studying Li ion exchange processes between different crystallographic sites. However, for materials having only a single crystallographic site, methods to quantify the ion hopping timescales in are still needed. As stated previously, ^{6}Li{^{7}Li} REDOR measurements should be investigated as a possible method for studying ion mobility in single site materials. These experiments will initially be carried out on systems where the ion mobility timescales are known. Materials such as Li_2VPO_4F or $Li_3V_2(PO_4)_3$, are proposed as they are well characterized from this thesis and previous works.[2,9] Overall, development of this experimental method will allow for mobility timescales of single-site materials including tavorite $LiVPO_4F$ and olivine $LiFePO_4$, to be probed.

Despite the challenges posed by the strong paramagnetic influences of the transition metal centers, multinuclear NMR methods continue to be an effective tool for characterizing both the structural and ion mobility properties of solid-state Li intercalation compounds. This thesis focused on unraveling the structural details that give fast charge-discharge rates in Li ion cathode materials with either phosphate or fluorophosphate anion compositions, by measuring the ion mobility timescales in using solid state NMR methods. Information of this type will assist materials development in bringing cost-effective and environmentally benign cathode materials to battery applications.

9.2 References

(1) Verhoeven, V. W. J.; de Schepper, I. M.; Nachtegaal, G.; Kentgens, A. P. M.; Kelder, E. M.; Schoonman, J.; Mulder, F. M. *Phys. Rev. Lett.* **2001**, *86*, 4314

(2) Cahill, L. S., Chapman, R. P., Britten, J. F., Goward, G. R. *J. Phys. Chem. B* **2006**, *110*, 7171.

(3) Makimura, Y.; Cahill, L. S.; Iriyama, Y.; Goward, G. R.; Nazar, L. F. *Chem. Mater.* **2008**, *20*, 4240.

(4) Davis, L. J. M.; Heinmaa, I.; Goward, G. R. *Chem. Mater.* **2010**, *22*, 769.

(5) Cabana, J.; Shirakawa, J.; Nakayama, M.; Wakihara, M.; Grey, C. P. *J. Mater. Chem.* **2011**, *21*, 10012.

(6) Ramesh, T. N.; Lee, K. T.; Ellis, B. L.; Nazar, L. F. *Electrochem. Solid State Lett.* **2010**, *13*, A43.

(7) Nyten, A.; Abouimrane, A.; Armand, M.; Gustafsson, T.; Thomas, J. O. *Electrochem. Commun.* **2005**, *7*, 156.

(8) Dominko, R.; Bele, M.; Gaberscek, M.; Meden, A.; Remskar, M.; Jamnik, J. *Electrochem. Commun.* **2006**, *8*, 217.

(9) Cahill, L. S.; Kirby, C. W.; Goward, G. R. *J. Phys. Chem. C* **2008**, *112*, 2215.